Graphene Hydrogel/Aerogel Based Nanohybrids for the Application in Energy Storage and Catalysis

A thesis submitted in partial fulfilment of the requirements for the degree of doctor of philosophy

By

Anirban Sikdar

Under the Supervision of

Dr. Uday Narayan Maiti

Department of Physics

Indian Institute of Technology Guwahati
Guwahati-781039, India
December 2020

March 2021

Department of Physics
Indian Institute of Technology
Guwahati
Guwahati-781039, India

Declaration

I hereby declare that the thesis work entitled "Graphene Hydrogel/Aerogel Based Nanohybrids for the Application in Energy Storage and Catalysis" has been entirely carried out by me at Department of Physics, Indian Institute of Technology Guwahati under the supervision of Dr. Uday Narayan Maiti and neither this work nor any part of it has been submitted elsewhere for any degree/diploma or other academic award.

Anirban Sikdar

Anirban Sikdar

Roll no. : 156121012
Senior research fellow
Department of Physics
Indian Institute of
Technology
Guwahati

Department of Physics
Indian Institute of Technology
Guwahati
Guwahati-781039, India

Certificate

It is certified that the work contained in the thesis titled "Graphene Hydrogel/Aerogel Based Nanohybrids for the Application in Energy Storage and Catalysis" has been carried out by Mr. Anirban Sikdar (roll no. 156121012) at Indian Institute of Technology Guwahati under my supervision and neither this work nor any part of it has been submitted elsewhere for any degree/diploma or other academic award.

Dr. Uday Narayan Maiti

Assistant professor
Department of Physics
Indian Institute of Technology
Guwahati

Acknowledgement

To me PhD is an enduring journey to quench the thirst for knowledge and now standing at the verge of my PhD journey, I feel grateful to a number of people, without the constant support and help of whom this journey would not become a reality.

Firstly, I would like to express my deepest appreciation to my thesis supervisor Dr. Uday Narayan Maiti for his guidance, relentless support and continuous encouragement throughout my PhD journey. It has been a great opportunity to be a part of his group and work with him which helped me in building great scientific knowledge. I have the greatest admiration for his immense knowledge, enthusiasm and dedication for the science. Without his motivation and guidance this thesis work would remain incomplete.

I would like to extend my gratitude to my doctoral committee members, Dr. Gagan Kumar, Dr. Subhas Thota and Dr. K. Anki Reddy for their invaluable suggestions, constructive advices throughout my research work. I would like to thank Prof. Subhradip Ghsosh, Head of the Department, Physics, IIT Guwahati and Central Instruments Facility (CIF), IIT Guwahati for providing laboratory and instrumental facilities. I deeply acknowledge the financial assistance provided by the IIT Guwahati through institute fellowship. I am also thankful to all the faculty members, technical/scientific officers and non-teaching stuffs of the department of Physics for their support and cooperation.

I am really greatful to Dr. K. Anki Reddy (Department of Chemical Engineering, IIT Guwahati), Abhijit Gogoi (Department of Mechanical Engineering, IIT Guwahati), Dr. Youngtak Oh (Center for Environment, Health, and Welfare Research, Korea Institute of Science and Technology), Dr. Soumen Maiti (St. Thomas College of Engineering & Technology) and Chiranjib Gogoi (Department of Chemistry, IIT Guwahati) for contributing to my research work through conducting theoretical studies, providing instrumental facitlities and giving insightful suggestions.

It has been a real pleasure to get a wonderful research ambience in the laboratory. I am extremely grateful to my present and past lab members Abhisek, Pronoy, Nasim, Sujit, Golam, Dr. Munu Borah and Amalika for their good company and continous help in so many ways. Thanks to my dear friends Dr. Krishnakanta, Dr. Joydip, Rishav, Sunil for being a part of my PhD journey. I would like to recognize some of my jouniors Sumit, Surojit, Swarup, Dibyendu, Niloy, Arindam and Milan for building a brotherly relationship. Special appreciations to my

hostel mates Aritra, Amritava, Dipowjjal, Subhajit, Saptarshi, Dr. Bandhan with whom I shared a lot of wonderful memories. I very much appriciate the joyful company of my close friends Tanmoy, Bishnu, Sayantan, Subhajit, Barun and Nilanajan.

I am deeply indebted to my father Late Akhil Chandra Sikdar and my mother Anita Sikdar. I feel strong with their blessings. I am immensely greatful to my sisters Arpita and Sima and brothers-in-law Suraj da and Sambad da for their love and continual motivatons. I wish to thank my wife Dipa for her endless love, beleif in my abilities and unparalleled support through the ups and downs of my life.

Finally, I express my sincere apology to those people who helped me during my research work but forgot to mention their name.

Anirban Sikdar

IIT Guwahati

Contents

Chapter 2

Scalable Fabrication of Graphene Polyaniline Hybrid Hydrogel for Customized Performance Supercapacitors

Chapter 3

Diffusion Limited Surface Polymerization over Graphene-hydrogel framework for High Area and Mass Specific Energy Storage

Chapter 4

Large Scale Ambient Casting of Graphene-MXene 3D Hydrogel for High Energy Density Asymmetric Supercapacitor

Chapter 5

A General Morphological Tuning and Hybridization of MOF with Grpahene Hydrogel for Highly Active OER Electrocatalysts

Abstract

Conversion of renewable energy, and its storage either in terms of electrochemical energy in battery/supercapacitors or in the form of chemical fuel hydrogen via converted energy driven water splitting promises to offer a clean and sustainable future. Battery/supercapacitors are also inevitable technology to power portable electronics, whose requirement is increasing at an astonishingly rapid rate. Graphene, a 2D nanosheets of carbon atoms, has been considered as ideal material for electrodes of supercapacitor devices and as active catalyst or conductive support in water electrolysis on behalf of its unique properties including very high specific surface area and excellent conductivity. Despite significant successes, intrinsic face–to–face restacking tendency of graphene has made it challenging to keep its surface accessible for these two electrochemical processes. Together with the processing challenge, the restacking issue in graphene or graphene nanohybrids based electrodes is known to significantly reduce the energy density of supercapacitors and to lower the performance of water splitting. In particular, high area and mass specific energy density with high rate performance is very tough to attain in supercapacitors. On the other hand, requirement of high overpotential for oxygen evolution reaction (OER) is the main hurdle for hydrogen generation by water splitting, which concurrently happens at the other electrode. For practical adaptability, not only restacking controlled graphene and its tunable hybrids are required to address the above–mentioned challenge, but also the processing should be done though facile, scalable and cost–effective way. The present thesis work comprehensively addresses these major challenges in the field of energy storage and catalysis through systematically developing high performing graphene hydrogel and hydrogel based diverse hybrids. For instance, a facile and scalable strategy for the room temperature co–assembly of graphene and polyaniline (PANI) nanowires resulted in a porous hydrogel–hybrid structure where the embedded water molecules helped to avoid face–to–face restacking. The hybrid exhibited a maximum areal capacitance of 2.2 F cm^{-2} at an electrode mass loading of 15.3 mg cm^{-2}. Further, a compressed gel hybrid obtained by controlling the hydration level of the hybrid hydrogel (< 35 wt%) resulted in an excellent volumetric capacitance of 560 F cm^{-3}, while retaining high rate performances (81.3% at 20 mA cm^{-2}). Importantly, by down–sizing PANI nanostructure following a bio–mimicking "graphene hydrogel–organic medium" interfacial surface polymerization process at room temperature, a PANI–graphene hybrid with PANI sizes < 50 nm was developed which exhibited high specific capacitance (503 F g^{-1}) and excellent rate performance (88.6% at a current density of 30 A g^{-1}) even at commercial level of mass loading (8.8 mg cm^{-2}). The versatile processability and the

issue of low energy density were further addressed by developing a graphene–MXene hybrid via facile gel–casting based approach. The asymmetric supercapacitor device consisting of graphene–MXene–hydrogel as negative electrode and a graphene–PANI–hydrogel hybrid as positive electrode demonstrated a large operating voltage window of 1.4 V and an ultra–high energy density of 30.3 Wh kg^{-1}. The high areal and specific capacitances of the PANI/MXene based graphene hybrids were associated with the uniform hybridization of the pseudocapacitive PANI/MXene with the conducting graphene hydrogel framework. Such uniform hybridization without bulk aggregation facilitated ion transportation and effective utilization of the redox active surface of PANI/MXene. Furthermore, the low OER activity of the electrocatalysts was addressed by developing size and shape tuned versatile MOF–graphene heterostructures by adopting "graphene hydrogel–organic medium" interfacial reaction system. As–developed rod–like nickel–cobalt–iron tri–metallic MOF–graphene structure exhibited a remarkably low overpotential of 255 mV to achieve a current density of 10 mA cm^{-2} and a small Tafel slope of 44.3 mV dec^{-1} surpassing the performance of other MOF based OER catalysts. The excellent OER activity of the MOF–graphene hybrid was attributed to the presence of conducting graphene backbone and the high surface area with abundant exposed active sites due the morphology tuning of the MOF nanostructure. Moreover, the easy processing with large scalability, the two practical criteria from the material development perspectives, have been taken care during the synthesis of all the graphene and graphene based hybrids. Importantly, all the developed processes are versatile that could be applicable for hybridizing graphene with diverse functional nanomaterials. We believe, the present thesis work will provide a guideline to develop versatile graphene based functional nanohybrids via large scale facile processing, and will find widespread applications not only in energy storage but in other fields namely oxygen reduction reaction, gas storage, oil adsorption, or adsorption of contaminants from water.

List of Abbreviations

HER	Hydrogen evolution reaction
OER	Oxygen evolution reaction
GO	Graphene oxide
EDLC	Electrolytic double layer capacitance
IHP	Inner Helmholtz plane
OHP	Outer Helmholtz plane
CV	Cyclic voltammetry
GCD	Galvanostatic charge/discharge
EIS	Electrochemical impedance spectroscopy
RGO	Reduced graphene oxide
GH	Graphene hydrogel
PANI	Polyaniline
MOF	Metal organic framework
ECSA	Electrochemical surface area
EDAX	Energy Dispersive X–ray Spectroscopy
FESEM	Field emission scanning electron microscopy
FETEM	Field emission transmission electron microscopy
HRTEM	High resolution transmission electron microscopy
STEM	Scanning Transmission Electron Microscopy
FTIR	Fourier transform infra–red spectrometer
BET	Brunauere–Emmette–Teller
XRD	X–ray diffraction
XPS	X–ray photoelectron spectroscopy

List of Publications

Journal publications:

1. Anirban Sikdar, Abhisek Majumdar, Pronoy Dutta, Munu Borah, Sang Ouk Kim, Uday Narayan Maiti, "Ultra–large area graphene hybrid hydrogel for customized performance supercapacitors: High volumetric, areal energy density and potential wearability", ***Electrochim Acta***, 332 (2020), pp. 135492.

2. Anirban Sikdar, Sujit Kumar Deb, Abhijit Gogoi, Abhisek Majumdar, Pronoy Dutta, K. Anki Reddy, Uday Narayan Maiti, "Polyaniline–Graphene Hydrogel Hybrids via Diffusion Controlled Surface Polymerization for High Performance Supercapacitor", ***ACS Appl. Nano Mater.*** 3 (2020), pp. 12278

3. Anirban Sikdar, Abhisek Majumdar, Abhijit Gogoi, Pronoy Dutta, Munu Borah, Soumen Maiti, Chiranjib Gogoi, K. Anki Reddy, Youngtak Oh, Uday Narayan Maiti, "Diffusion driven nanostructuring of metal–organic frameworks (MOFs) for graphene hydrogel based tunable heterostructures: Highly active electrocatalyst for efficient water oxidation", ***J. Mater. Chem A***, 2021, DOI: 10.1039/D0TA09077H

4. Anirban Sikdar, Sujit Kumar Deb, Abhisek Majumdar, Pronoy Dutta, Uday Narayan Maiti, "MXene–graphene interpenetrating 3D hydrogel via facile room temperature casting and metal particle induced self–assembly for high energy density supercapacitors", (Comunicated).

5. Pronoy Dutta, Anirban Sikdar, Abhisek Majumdar, Munu Borah, N. Padma, Subhradip Ghosh, Uday Narayan Maiti, "Graphene aided gelation of MXene with oxidation protected surface for supercapacitor electrodes with excellent gravimetric performance", ***Carbon***, 169(2020), pp. 225.

6. Munu Borah, Anirban Sikdar, Samadhan Kapse, Abhisek Majumdar, Pronoy Dutta, Golam Masud Karim, Sujit Deb, Ranjit Thapa, Uday Narayan Maiti, Stable and boosted oxygen evolution efficiency of mixed metal oxide and borate planner heterostructure over heteroatom (N) doped electrochemically exfoliated graphite foam ***Catal. Today***, 2021, DOI: 10.1016/j.cattod.2021.01.007

7. Pradip Kumar, Uday Narayan Maiti, Anirban Sikdar, Tapas Kumar Das, Asheesh Kumar, V Sudarsan, "Recent advances in polymer and polymer composites for electromagnetic interference shielding: review and future prospects", ***Polym Rev***, 59(2019), pp. 687.

Works presented in conference:

1. Anirban Sikdar, Uday Narayan Maiti, "Spontaneously assembled 3D graphene monolith with microwave induced improved graphitization for high areal mass loading supercapacitor", International Conference on Optoelectronic and Nano Materials for Advanced Technology (ICONMAT–2019), January 3– 5, 2019, CUSAT, Kochi, India.

2. Anirban Sikdar, Uday Narayan Maiti, "Hydration controlled densely packed graphene polyaniline hybrid hydrogel for high volumetric and high power supercapacitor", International Conference on Nano Science and Technology (ICONSAT–2020), March 5–7, 2020, S.N. Bose National Centre for Basic Sciences, Kolkata, India.

Workshop attended:

3rd National Workshop on NEMS/MEMS and Theranostic devices (NWNTD–2017), March 21–23, 2017, IIT Guwahati, Guwahati, India.

Chapter 1

Introduction

Chapter 1

Introduction

1.1 Introduction:

The global demand for energy has increased quite rapidly due to the advances in industrial activities and growth in population. Fossil fuels e.g. coal, crude oil, natural gas etc. contribute to the major portion of the global energy generation. [1, 2] However, the continuous depletion of fossil fuels and their serious environmental concerns have forced us to rely more on renewable energy sources like solar power, wind power, hydro–power etc. [3-5] Despite their clean energy generation, the major challenges associated with these energy sources are their efficient production and on demand usage. For instance, the renewable energy sources are intermittent in nature which limits their on demand usability. As a result, for the effective use of renewable sources efficient storage devices are required.

To efficiently store the converted renewable energy two prominent technologies are in the forefront, electrochemical energy storage and storage in terms of chemical fuel, hydrogen. [6-8] Battery and supercapacitors are the main candidates in the category of electrochemical energy storage. Facile development of electrode materials with optimized structural, chemical and electronic properties are of foremost important for battery/supercapacitors to attain high energy storage metric in a cost efficient way. On the other hand, harvested renewable energy can be used to produce green fuel hydrogen by electrochemically splitting water, thus this technology offers a direct route to store energy in the form of fuel. [9-14] Success of this direct fuel based storage technology relies on availability of efficient catalysts not only for cathodic hydrogen evolution (HER) but also for oxygen evolution reaction (OER) that concurrently happens at the other electrode. In fact, sluggish OER reaction mainly limits the hydrogen production efficiency. [15-17] Moreover, OER remains one of the core reactions in energy storage devices like rechargeable metal–air batteries. [18, 19] Therefore, for the practical and widespread utilization of renewable energy, much research interests must be paid to develop efficient energy storage systems.

Both of these energy storage technologies involving electrochemical processes have been greatly benefited by the introduction of two–dimensional (2D) atomic thin materials due to their high surface area and tunable physiochemical properties. [20-25] Among the large pool of 2D nanomaterials, graphene has emerged as the most promising material for energy applications due to its unique characteristics like extraordinary electrical conductivity (0.5–100

S m^{-1}) at room temperature, large specific surface area (2675 m^2 g^{-1}) and good mechanical stability. [26, 27] As a result, graphene has been used extensively as an electrode material for various energy storage devices, and as active catalyst or support of other catalytic nanomaterials for electrocatalytic applications including OER. [28-32]

This chapter highlights a brief introduction to the two important aspects of energy technology i.e. energy storage via electrochemical supercapacitors and energy storage/generation via electrocatalytic OER process. Recent advances in the graphene and graphene based nanohybrids for the application in supercapacitor and electrocatalytic OER technologies have also been discussed. We have further focussed the design principle of electrode architectures for commercial level applications. A brief characterization techniques are also included. The motivation and objectives of this work have also been presented in this chapter.

1.2 Fundamentals of electrochemical supercapacitors:

Among various electrochemical energy storage devices like batteries, supercapacitors and fuel cells, recently, electrochemical supercapacitors have gained much research interests owing to their high power density, low cost, usability in portable devices and bridging the energy–power gap between the conventional dielectric capacitors (high power output) and the batteries/fuel cells (high energy density). [33-37] Although supercapacitors deliver lower energy than batteries, they are superior to batteries in terms of high power density (hundred to several thousand times higher power than conventional batteries of the same size), capability to be charged and discharged for tens of thousand times without significant performance decay (for battery, performance decreases significantly after few hundred times of charge and discharge) and safety. [38] Therefore, supercapacitors are ideal for using where power boost is needed like power grid, heavy electric vehicles etc. where batteries (e.g. lead-acid batteries) cannot serve the desired purpose. [39] Nowadays one extensive use of supercapacitor could be found in capturing regenerative breaking energy, where kinetic energy of a system is captured and stored for later use which would otherwise be lost as heat energy (for physical breaks).

A supercapacitor consists of an electrolyte, two–electrodes and a separator to electrically separate the electrodes (Figure 1.1.a). Electrode materials play an important role in determining the performance of a supercapacitor. Before discussing the state–of–art graphene based nanomaterials used in supercapacitor electrodes, a brief discussion about the different

charge storage processes of a supercapacitor and some of its basic characterization techniques are presented.

1.3 Charge storage mechanism of supercapacitor:

The charge storage mechanism of a supercapacitor either involves the adsorption of electrolyte ions (electrolytic double layer capacitance) or surface redox reaction (pseudocapacitance). [40] In case of electrolytic double layer capacitance (EDLC), the electrode materials are not electrochemically active and therefore no electrochemical reaction occurs in EDLC. Carbon materials are the examples of EDLC type capacitors. While for the case of pseudocapacitance, the electrode material is electrochemically active, undergoes redox reaction during charging and discharging of the capacitor. Metal oxides and conducting polymers are the most commonly used pseudocapacitive materials. A brief discussion of both the charge storage mechanisms is presented below.

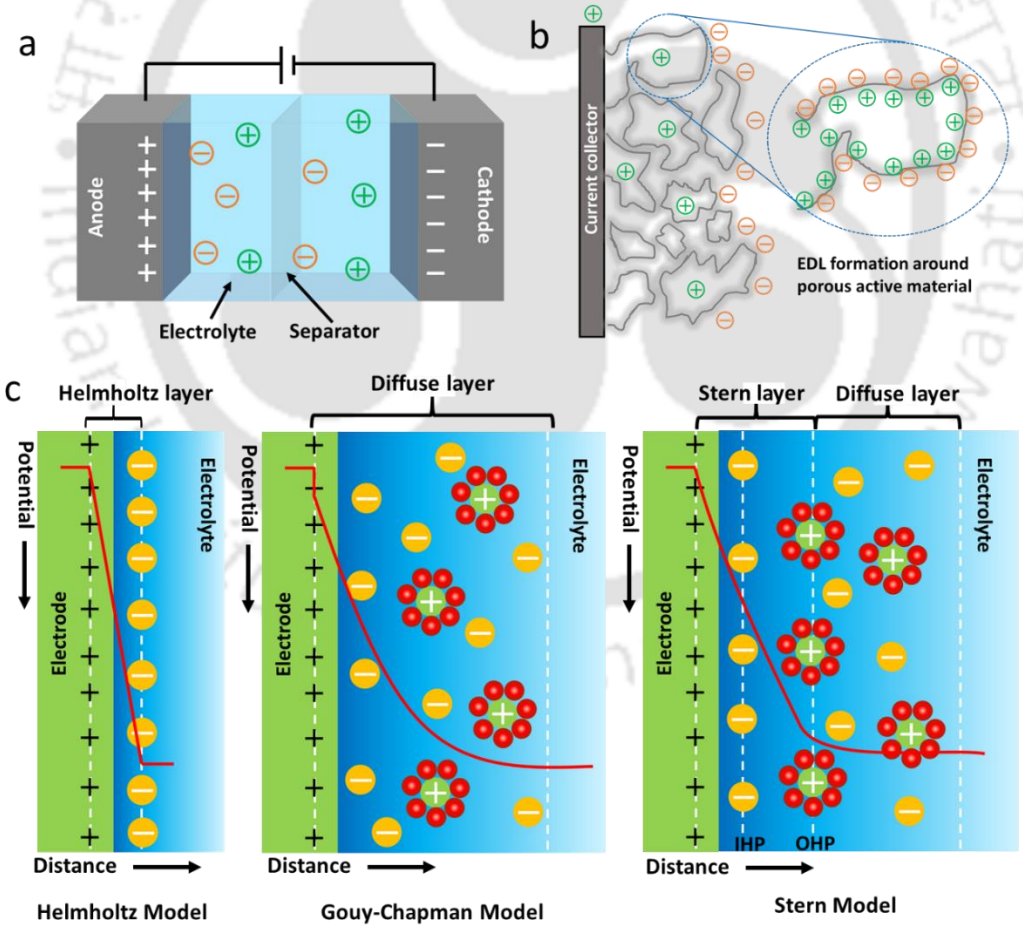

Figure 1.1. Schematic illustrations of (a) basic construction of a supercapacitor; (b) EDL type charge storage mechanism in porous electrode and (c) Helmholtz, Gouy–Chapman and Stern model of EDL supercapacitor.

1.3.1 Electrolytic double layer capacitance (EDLC):

In EDLC type capacitors, the charge is being stored via reversible adsorption of electrolyte ions onto the electrode surface (Figure 1.1.b). Several models are proposed for the charge accumulation in electrode/electrolyte interface (Figure 1.1.c). The first model was proposed by Helmholtz in 1853. [41] According to this model, the charge of the solid electrode is counterbalanced by a rigid layer of electrolyte ions at a distance d from the electrode thereby forming the double–layer. Gouy and Chapman extended this model by considering that the electrolyte ions do not form a rigid layer but they tend to diffuse inside the liquid phase forming a diffuse layer. [42, 43] The counter potential developed as a result of the diffusion of ions restricts their further diffusion. In this theory, the electrolyte ion concentration near the surface of the electrode follows the Boltzmann distribution. This theory however fails in the case of highly charged double layers. Stern further modified Gouy and Chapman model by merging it with Helmholtz model. Consequently, EDLC, based on this model is formed by two layers namely Stern layer and diffuse layer. [44, 45] The Stern layer is a compact layer and is formed by the two layers namely, (i) Inner Helmholtz plane (IHP), consisting of specifically adsorbed electrolyte ions on the surface of electrode and (ii) Outer Helmholtz plane (OHP), consisting of non–specifically adsorbed solvated ions. The ions forming the Stern layer are strongly adsorbed via electrostatic interactions with the electrode surface. As the formation of double layer involves only electrostatic adsorption/desorption of ions without involving any chemical reaction, the charge storage process of EDL usually occurs instantaneously (~ 10^{-8} s). [44]

1.3.2 Pseudocapacitance:

Pseudocapacitors, the other type of capacitors store energy by reversible Faradaic/redox reaction occurring at the surface of the electrode. The pseudocapacitance charge storage mechanism is entirely different from the EDLC mechanism and usually occurs in the following two ways depending upon the type of physical process and the electrode material, namely (i) the surface redox pseudocapacitance and (ii) the intercalation type pseudocapacitance. [40]

In surface redox pseudocapacitance, the electrochemical adsorption/desorption of electrolyte ions occurs on the surface or near surface of electrode accompanied by a reversible faradaic reaction. The typical examples where surface redox type pseudocapacitance occur are oxide materials e.g. RuO_2, MnO_2, conductive polymers etc. [46-49] The surface redox mechanism can be understood by the following reaction process occurring in metal oxide surface: [50]

$$Ox + zC^+ + ze^- \leftrightarrow Red(C_z)$$

where Ox is the oxide species, C^+ is the ion adsorbed on surface, z is the number of electron transferred in the redox process and $Red(C_z)$ is the reduced species.

In case of intercalation type pseudocapacitance, where ions intercalate/de–intercalate into the channels of a layered redox–type materials along with faradaic charge transfer process without any structural/phase transformation of the material. This type of pseudocapacitance is described by the following reaction: [50]

$$MA_y + xLi^+ + xe^- \leftrightarrow Li_xMA_y$$

where MA_y is the layered material (one typical example is Nb_2O_5), Li^+ is the intercalating ion and x is the number of electrons transferred. [50-52] Although the mechanism of intercalating pseudocapacitance closely resembles that of batteries, the main difference is that, in contrast to batteries intercalation pseudocapacitance mechanism is not limited by the solid–state diffusion process which resulted in a high rate performance and power density in pseudocapacitance. [53]

1.4 Characterization techniques for supercapacitors:

The electrochemical characterization of a supercapacitor is estimated by several techniques e.g. cyclic voltammetry (CV), galvanostatic (constant current) charge/discharge (GCD) characteristics and electrochemical impedance spectroscopy (EIS). From these characterizations, various parameters (e.g. current, voltage, time etc.) are measured which are used to evaluate energy and power densities. The basic electrochemical cell of a supercapacitor is either operated in a three–electrode configuration (Figure 1.2), which comprises a working electrode (WE), a reference electrode (RE) and a counter electrode (CE), or in a two–electrode configuration (Figure 1.1.a), where the two–electrodes comprise of active materials. However, the performance measurement in two–electrode configuration is more reliable as the configuration is close to the practical devices which are of two–electrode type. [54]

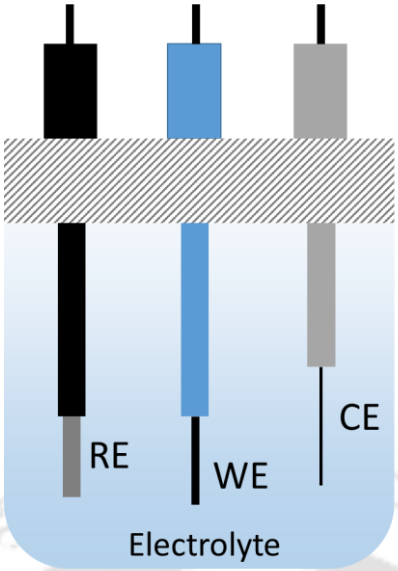

Figure 1.2. Schematic illustration of three–electrode configuration of an electrochemical cell.

1.4.1 Cyclic voltammetry (CV):

A CV curve is basically the current response of a supercapacitor with the change in applied potential between two fixed limits (potential window) at a constant scan rate (mV s^{-1}). Before discussing the details of CV, let us discuss some points about the voltage window of a supercapacitor. Theoretically the energy density of a supercapacitor is expressed as, $E = {}^{1}/_{2}\, CV^{2}$, where C is the capacitance and V is the voltage window. Therefore, to enhance the energy density of a supercapacitor, ideally we should have a greater voltage window. Unfortunately, the voltage window of a supercapacitor cannot be increased arbitrarily, and it is actually determined by the nature of the electrode material and the stability window of the electrolyte. For example, for carbon based material e.g. graphene, CNT with aqueous electrolyte (e.g. 1 M H_2SO_4) the voltage window is set to 1 V to avoid any polarization effect due to oxygen evolution (a sharp rise in current in CV profile). For faradaic materials like transition metal hydroxides, polyaniline etc. an early sign of the polarization might be observed due to the catalytic effect of the electrode material, and for that case the voltage window should be determined according to the onset of the water splitting reaction. In case of asymmetric supercapacitor, we could extend the voltage window beyond 1 V by using two dissimilar electrodes working in positive and negative potential range (discussed in chapter 4).

The CV curves provide information about the charge storage mechanism and amount of charge stored in the supercapacitors. A featureless rectangular profile of CV curve is representative of EDCL charge storage mechanism (Figure 1.3.a), on the other a rectangular

profile superimposed with oxidation/reduction peaks is the signature of pseudo–capacitive charge storage mechanism (Figure 1.3.b). In two–electrode configuration, charge storage happens at the electrode–electrolyte interface in both the electrodes. Individual electrode–electrolyte interface acts as a single parallel plate capacitor, where charges in the electrode act as one plate and solvated ions accumulated around its surface act as other plate (Figure 1.1.a). Thus, two–electrode supercapacitor configuration can be through of series combination of two capacitors developed at the electrode electrolyte interfaces in positive and negative electrodes. As per the rule of series combination of capacitors, overall capacity of a two–electrode cell is given by,

$$\frac{1}{C_{measured}} = \frac{1}{C_{positive}} + \frac{1}{C_{negative}} \quad 1.1$$

If both electrodes are of similar type (symmetric configuration) then, $C_{positive} = C_{negative} = C_{single}$, then the measured capacity, $C_{measured} = C_{single}/2$. Thus $C_{single} = 2C_{measured}$. Specific capacitance of the electrode material can be found by normalizing C_{single} value with respect to its mass (gravimetric/specific capacitance) or volume (volumetric capacitance). Thus, gravimetric/specific capacitance of the electrode material is given by,

$$C_s = \frac{2C_{measured}}{mass\ of\ a\ single\ electrode} = \frac{4C_{measured}}{mass\ of\ the\ both\ electrodes} \quad 1.2$$

In two–electrode configuration of a supercapacitor, the gravimetric/specific capacitance (C_s, F g^{-1}), the areal capacitance (C_{Area}, F cm^{-2}) and the volumetric capacitance (C_{Vol}, F cm^{-3}) of the single electrode are calculated from the integrated area of the CV curve using the following equations:

$$C_s = \frac{4}{mv\Delta V}\int_{V_i}^{V_f} idV \quad 1.3$$

$$C_{Area} = \frac{4}{Av\Delta V}\int_{V_i}^{V_f} idV \quad 1.4$$

$$C_{Vol} = \frac{4}{Vol \cdot v\Delta V}\int_{V_i}^{V_f} idV \quad 1.5$$

where i is the current density (A), V is the potential window (V) of the supercapacitor, v is the scan rate (mV s^{-1}), m is the total mass of the electrodes (g), A is the geometrical area of the electrode (cm^2) and Vol is the volume of the supercapacitor (cm^3).

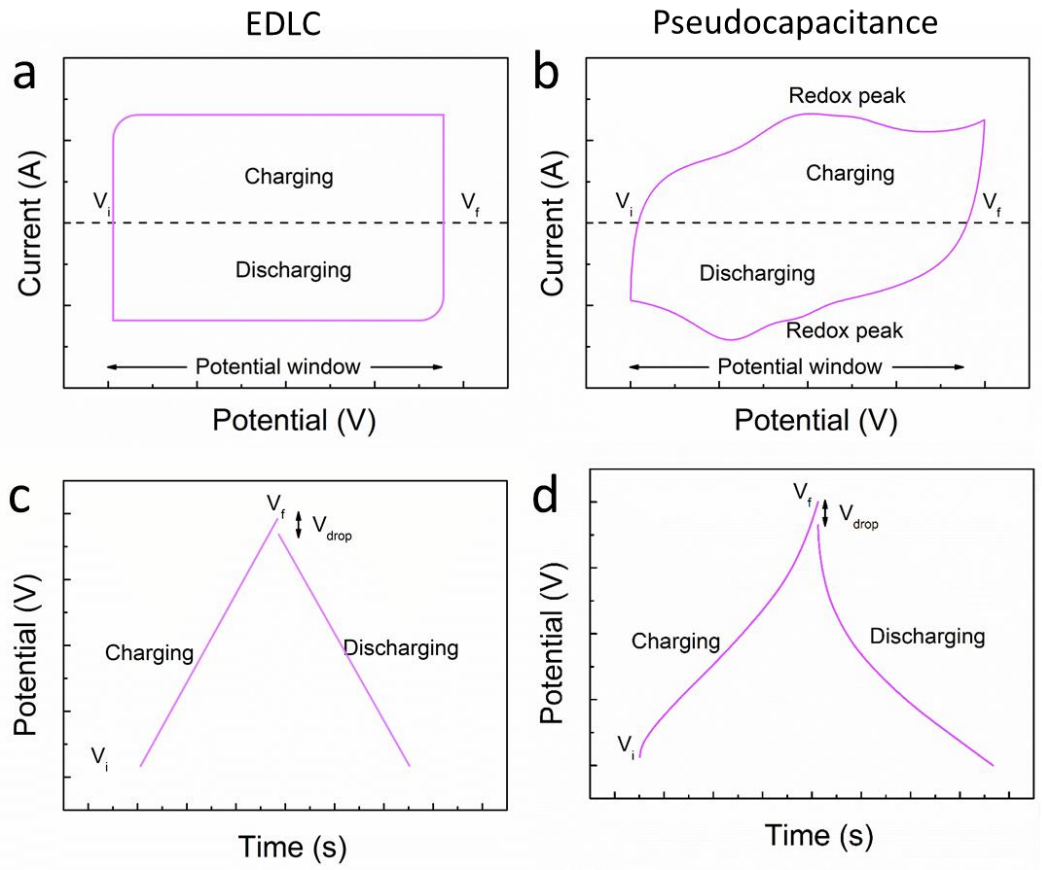

Figure 1.3. Comparison of charge–storage properties of EDLC and pseudocapacitance (a)–(b) cyclic voltammetry and (c)–(d) galvanostatic charge/discharge curves.

In three–electrode configuration since, only one electrode is involved instead of the two electrodes, the 4 factor in the above equations is to be replaced by 2 and m and Vol now represent the mass and volume of the working electrode respectively.

The specific and volumetric energy (Wh kg^{-1} and Wh l^{-1}) and power (W kg^{-1} and W l^{-1}) densities of a supercapacitor are calculated from the CV curves following the equations:

$$E_s = \frac{\Delta V}{3600 \cdot mv} \int_{V_i}^{V_f} idV \qquad 1.6$$

$$E_{Vol} = \frac{\Delta V}{3600 \cdot Vol \cdot v} \int_{V_i}^{V_f} idV \qquad 1.7$$

and

$$P_s = \frac{1}{m} \int_{V_i}^{V_f} idV \qquad 1.8$$

$$P_{Vol} = \frac{1}{Vol}\int_{V_i}^{V_f} idV \quad 1.9$$

1.4.2 Galvanostatic charge/discharge (GCD):

The GCD is another important characterization where the supercapacitor is charged up to maximum operating potential at a constant current and then discharged at the same current density. EDLC and pseudocapacitive charge storage mechanisms have distinctly different GCD, a purely linear decay of the current in the discharge profile is the characteristic of the former (Figure 1.3.c) whereas a fast linear decay of current followed by a non–linear slow decay is the characteristic of pseudocapacitors (Figure 1.3.d). At the start of discharge curve a voltage drop (V_{drop}) is commonly observed which is associated with resistive losses during discharge process (Figure 1.3.c–d).

In two–electrode configuration, the specific capacitance (C_s, F g^{-1}), the areal capacitance (C_{Area}, F cm^{-2}) and the volumetric capacitance (C_{Vol}, F cm^{-3}) of the single electrode of a supercapacitor are calculated from GCD using the following equations:

$$C_s = \frac{4I}{m\left(\frac{\Delta V}{\Delta t}\right)} \quad 1.10$$

$$C_{Area} = \frac{4I}{A\left(\frac{\Delta V}{\Delta t}\right)} \quad 1.11$$

$$C_{Vol} = \frac{4I}{Vol\left(\frac{\Delta V}{\Delta t}\right)} \quad 1.12$$

where I is the applied current (A) and Δt is the time of discharge (s).

Again in three–electrode configuration due to the presence of a single electrode, the 4 factor in the above equations is to be replaced by 2 and m and Vol now represent the mass and volume of the working electrode respectively.

The specific and volumetric energy (Wh kg^{-1} and Wh l^{-1}) and power (W kg^{-1} and W l^{-1}) densities of a supercapacitor are calculated from GCD following the equations:

$$E_s = \frac{1}{m}\int iVdt \quad 1.13$$

$$E_{Vol} = \frac{1}{Vol}\int iVdt \quad 1.14$$

and

$$P_s = \frac{E_s}{\Delta t} \quad 1.15$$

$$P_{Vol} = \frac{E_{Vol}}{\Delta t} \quad 1.16$$

1.4.3 Electrochemical impedance spectroscopy (EIS):

In addition to CV and GCD, EIS is another useful technique to characterize supercapacitor material. Typically, EIS data are collected by applying an AC signal of amplitude 10 mV in open–circuit potential within a frequency range of 1 mHz to 1 MHz. the EIS data can be expressed in Nyquist plot which is a plot between imaginary impedance (Z'') and real impedance (Z'). Besides, EIS data could also be represented in terms of Bode plot (phase angle vs frequency plot). Figure 1.4 represents a typical Nyquist plot where three separate regions are clearly observed. At low frequency region, the plot is quasi–parallel to Z'' axis representing a capacitive behaviour whereas at high frequency region a semi–circular nature is observed. This semi–circle represents two types of resistances namely, solution resistance obtained from the starting point of the semi–circle and charge transfer resistance, obtained by the width of the semi–circle. Apart from these, a 45° transition line is observed which connects the low frequency and high frequency regions. This transition line is called Warburg region which demonstrates the diffusion resistance of the electrode. A short Warburg region is therefore suitable for high performance electrode.

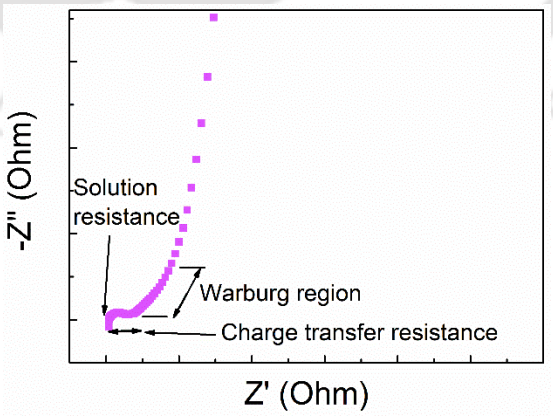

Figure 1.4. Typical Nyquist plot of EIS spectrum.

1.5 Graphene and graphene based hybrids for supercapacitor applications:

Since the discovery of graphene by Geim and co–workers, [26] it has gained tremendous interests in the field of supercapacitor application. As highlighted in the introduction section, graphene possesses excellent electrical conductivity and high specific surface area. High specific surface area of graphene allows large amount of charged ions to be adsorbed on its surface, thereby increasing the specific energy density. Due to this extraordinary conductivity, graphene permits fast movement of electrons through it during charge–discharge process with negligible resistive loss which enhances the rate performance of supercapacitor, and hence ensures high power density. Moreover, the excellent mechanical and chemical stabilities of graphene endow graphene based supercapacitor with long cycling stability. With these properties, theoretically graphene is assumed to exhibit a maximum specific capacitance of 550 F g^{-1} considering the whole surface area of graphene. [55] Although, this value is actually the Helmholtz capacitance of platinum in ionic electrolyte used for the comparison purpose. [56] For the true comparison of their specific capacitances, many facts need to be considered e.g. identical interfacial properties of graphene and platinum, no contribution from the quantum or space charge capacitance etc. [57]

Although pristine graphene can be exfoliated from graphite flake by scotch tape as discovered by Geim and Novoselov, but this process is not usable for energy storage applications which requires a mass scale production. The most common way to synthesize graphene for supercapacitor application is the controlled reduction of graphene oxide (GO) into reduced graphene oxide (RGO). Due to the presence of defective regions and residual functional groups in RGO it has some obvious differences with pristine graphene, but still RGO is commonly termed as graphene in scientific community. [58] GO is obtained via chemical oxidation and exfoliation of graphite powder (Hummers' method). [59] Among various reduction strategies, chemical reduction and thermal reduction of GO into RGO are the most useful ways mainly because of their large scalability. The pioneering work of Ruoff et al. showed the controlled chemical reduction of GO into RGO by heating a suspension of GO and hydrazine monohydrate at 100 °C for 24 h. The as–obtained graphene powder exhibited a high specific surface area (705 m^2 g^{-1}) and high gravimetric capacitance of 135 F g^{-1} in aqueous KOH electrolyte. [60] Ma et al. demonstrated that GO could be reduced into RGO by using hydrobromic acid (HBr) as the reducing agent. [61] The low level of reduction by HBr left many residual functional groups on RGO which not only increased the wettability of RGO but also took part in pseudocapacitance. As–obtained RGO exhibited a high gravimetric

capacitance of 348 F g^{-1} at a current density of 0.2 A g^{-1} in aqueous 1M H_2SO_4 electrolyte. Apart from chemical reduction, RGO could also be obtained by thermal reduction at elevated temperature. As a representative example, Rao and co–workers thermally exfoliated graphitic oxide into RGO at 1050 °C. [62] The obtained graphene was used as supercapacitor electrode and a specific capacitance of 117 F g^{-1} was obtained in aqueous H_2SO_4 electrolyte.

It is to be noted that, the major interest behind the application of graphene in energy applications is its large surface area. However, the high temperature treatment often leads to the irreversible aggregation or restacking of graphene sheets due to their strong interlayer π–π and van der Waals interactions which largely reduces the active surface area and thereby limits their performance especially at high scan rates or current densities. Moreover, in the aforementioned methods the graphene is obtained mainly as powder material which requires further processing to construct the electrode limiting their easy processability. In this regard preparation of porous graphene, assembly of graphene into 3D/2D macrostructures are very effective because in these structures not only the porosity of the electrode is maintained but their direct use as electrode material makes them advantageous over other synthesis strategies.

Kaner group demonstrated that, a 3D porous network structure of graphene could be obtained by direct laser writing GO film using a laser scribe DVD burner. [63] In this process, the photo–thermal reduction of GO reduced it to graphene and released gaseous species (CO, H_2O etc.) resulting in a restacking free porous structure. This process was used to prepare patterned porous graphene electrode, and as–developed graphene micro–supercapacitors exhibited a very high volumetric capacitance (3.05 F cm^{-3} at a volumetric current of 16.8 mA cm^{-3}) while retaining 60% of its initial capacitance at very high current density of 1.84×10^4 mA cm^{-3}. The main advantage of this technique was that no additional binders or additives were required to fabricate the electrode. Moreover, the porous graphene surface was fully accessible to the electrolyte which was responsible for the improved capacitance. Formation of three dimensional network by self–assembly is another attractive route to avoid face–to–face restacking of graphene. Shi et al. developed a 3D network of graphene in the form of hydrogel via hydrothermal self–assembly and reduction of GO. The prepared hydrogel was of highly conducting 5×10^{-3} S cm^{-1} and the water content of the hydrogel was measured to be 97.4%. [64] Importantly, the hydrogel was directly cut and assembled into supercapacitor without further electrode processing. The high conductivity and porous structure of hydrogel facilitated rapid charge transport within the electrode and as a result the hydrogel supercapacitor exhibited a high specific capacitance of 175 F g^{-1} at a scan rate of 10 mV s^{-1}.

Following the work of Shi et al., large number of publications resulted on 3D–hydrogel based supercapacitive energy storage and the focuses of all those publication were either to control the porous structure of hydrogel or tuning the electronic properties of graphene via hetero–atom doping or functionalization. [65-68] These modifications resulted in significant improvement in specific capacitance of the hydrogel. For example, nitrogen doped graphene hydrogel was found to possess nearly 2 times higher specific capacitance as compared to its un–doped counterpart. [69] Besides these 3D hydrogel structure, porous hydrogel in the form of film was reported by Li group which was developed by vacuum filtration of pre–reduced graphene dispersion. [70] This hydrogel film when was used as supercapacitor electrode showed high gravimetric capacitance of 215 F g^{-1} and exceptional rate capability up to a current density of 1080 A g^{-1}. These methodologies of hydrogel preparation developed so far require either thermal or electrical energy, which increases the processing cost. Further, ultra–large scalability is still remains a concern. Therefore, it was desired to develop graphene hydrogel at room temperature in a scalable way. In this regard, Maiti et al. developed a scalable sheet–like hydrogel of graphene via interfacial assembly and spontaneous reduction of GO over commercial zinc plate at ambient condition. [71] The as–formed hydrogel exhibited porous network structure and was used directly as supercapacitor electrode. The supercapacitor made of this graphene hydrogel sheet displayed an areal capacitance of 33.8 mF cm^{-2} at 1 mA cm^{-2} current density while maintaining a high rate performance of 78% at ultrahigh charge discharge rate of 100 mA cm^{-2}.

So far some of the pioneering works on purely graphene based supercapacitors have been discussed. However, in most of these cases specific capacitance of graphene is limited to less than 200 F g^{-1}, which is far below than the theoretically predicted value (550F/g). To increase the performance further, diverse nanomaterials were inserted in between the graphene sheets. Interestingly, the inserted nanomaterials not only restrict graphene restacking but it may also contribute to capacitance. In this direction, carbon nanotube (CNT) incorporation is very frequently employed as spacer between graphene sheets which shows significant improvement in capacitance as compared to compact graphene film without CNT. For example, Cheng et al. synthesized graphene and CNT composite film by vacuum filtration process. [72] The entangled CNTs in between graphene sheets reduced the internal resistance and also helped to mitigate agglomeration of graphene sheets. The as–obtained graphene/CNT composite film demonstrated a specific capacitance of 290.6 F g^{-1} and excellent stability in aqueous electrolyte.

Electro–active pseudocapacitive materials like metal oxides/hydroxides/sulfides, conducting polymers have also been incorporated within graphene structure. In these cases, guest pseudocapacitive nanomaterials not only act as spacer to limit the restacking but also significantly contribute to overall capacitance via their redox activity, thus synergistic enhancement of capacitance and rate performance can be achieved. Wu et al. developed hydrous RuO_2 stabilized over graphene sheets via sol–gel and mild annealing method. [73] The graphene sheets remained separated by the RuO_2 nanoparticles reducing the restacking problem. Thanks to high surface area and conducting properties of graphene and high pseudocapacitance of RuO_2, that the hybrid based supercapacitor exhibited a high specific capacitance of 570 F g^{-1} (with 38.3 wt% Ru loading) at 1 mV s^{-1}, improved rate performance and good cycling stability (97.9% retention after 1000 cycles). Similar to RuO_2, MnO_2 is another mostly studied metal oxide for high performance supercapacitor applications. The work of Yan et al. demonstrated that, the electrochemical performance of graphene–MnO_2 nanocomposite, prepared via microwave irradiation, was significantly improved as compared to bare graphene or MnO_2 particles (310 F g^{-1} at 2 mV s^{-1} with 78 wt% MnO_2 loading). [74] Moreover, the capacitance value was retained up to 74% at 500 mV s^{-1}. The enhanced performance was ascribed to the better interfacial electrical connectivity and exposed surface area of the electrode material. Apart from metal oxides, metal hydroxides are also utilized as high performance pseudocapacitive materials. For example, Chen et al. developed a 3D holey graphene and $Ni(OH)_2$ hybrid hydrogel via hydrothermal technique. [75] The $Ni(OH)_2$ nanoparticles were seen to be grown uniformly over the 3D porous framework of graphene. The as–developed hybrid exhibited a highest specific capacitance of 1250 F g^{-1}, good rate performance (50.1% at current 40 A g^{-1}) and good cyclic stability (> 95% after 1000 cycle). This excellent performance of the graphene–$Ni(OH)_2$ electrode originated from the pseudocapacitance of $Ni(OH)_2$ as well as the uniform porous architecture of the electrode which facilitated the ion accessibility and interfacial charge transport properties of the electrode.

Although the capacitive performance of metal oxides/hydroxides are enhanced when hybridized with graphene, the low conductivity of the oxides/hydroxides always remain a serious concern which can hinder their rate performance and long term cycling stability. To overcome the low conductivity of transition metal (TM) hydroxides, converting them into sulfides was shown to be a promising approach, as the TM–sulfides show metallic character. In this direction, Chen and co–workers hydrothermally treated a mixture of pre–synthesized

NiMn–layered double hydroxide (LDH) and GO with sulfur source ($Na_2S·9H_2O$), which ultimately resulted in graphene based hybrid with sulfides transformed from the corresponding LDH. [76] The sulfidation product exhibited an improved specific capacitance of 2077.5 F g^{-1} at a current density of 2 A g^{-1} than the NiMn–LDH (1612.5 F g^{-1}). The similar result was also obtained by Yang et al. where the specific capacitance of NiS/RGO (700 F g^{-1} at 1 A g^{-1}) was found to be higher than that of NiO/RGO. [77]

Conducting polymers such as polypyrrole (PPy), polyaniline (PANI) and poly–ethylenedioxythiophene (PEDOT) have studied extensively as supercapacitive materials owing to their high charge storage capacity and fast doping/de–doping properties. Although, low stability of conducting polymers is a practical concern, hybridizing conducting polymers with graphene could synergistically improve the charge storage and cycling stability of the nanohybrids. Chang and co–workers found that, PPy–RGO composite electrode prepared via electrochemical process showed a remarkable improvement in the specific capacitance than the bare PPy (from 108 F g^{-1} for PPy to 352 F g^{-1} for the hybrid). [78] Similarly, Cong et al. demonstrated that, not only the specific capacitance but the cycling stability of the PANI–graphene hybrid was enhanced drastically after hybridization. [79] Another work by Wu et al. showed that, graphene hydrogel can serve as excellent 3D platform for PANI nanowires growth over it directly via electro–polymerization, this simultaneously provided high areal and specific capacitances (8773 mF cm^{-2} and 783 F g^{-1}). [80] The excellent performance of this PANI–graphene hybrid was associated with the phase–separated structure of the electrode where the graphene hydrogel was uniformly covered by the PANI nanofibers. As a result, the PANI fibers were fully utilized in the charge storage process. Besides, graphene backbone can provide the stability to the hybrid structure giving rise to excellent performance with commercial mass loading. Still due to highly open porous structure of hydrogel, the volumetric energy density was low for this hybrid. To improve the volumetric performance of graphene–PANI hydrogel hybrid, an electrolyte assisted capillary compression method was proposed by Li et al. [81] They prepared PANI–graphene hydrogel electrode via in–situ polymerization of aniline inside graphene hydrogel film (prepared via vacuum filtration) and subsequently liquid assisted capillary compression of the electrode led to very compact and dense PANI–graphene electrode which exhibited a high volumetric capacitance of 572 F cm^{-3} at 5 A g^{-1} while maintaining an excellent rate performance (> 95% at 100 A g^{-1}). They also demonstrated that the interconnected porous architecture with well–retained nanostructure of PANI in the compact electrode remains the key parameters for high volumetric performance.

Apart from these important works, researchers have also found that doping of graphene can dramatically alter the surface chemistry and electronic properties of graphene such as improved surface wettability, increased electrical conductivity which can boost the supercapacitive performance of doped graphene. As an example, Dai and co–workers developed nitrogen (N) doped RGO hydrogel by facile hydrothermal treatment. [69] The specific capacitance of N–RGO hydrogel reached up to 390 F g^{-1} at 1 A g^{-1} while maintaining a rate performance of 61% at a high current density of 20 A g^{-1}. The specific capacitance value of N–doped graphene was 70% higher than the capacitance of bare RGO hydrogel (207 F g^{-1}). Fan et al. synthesized a hydrogel composite of N–doped holey graphene and PANI nanofiber by two–step hydrogel formation (hydrothermal treatment) and subsequent polymerization process. [82] The as–formed 3D N–doped graphene/PANI hydrogel composite was compressed by mechanical pressure and capillary shrinkage to form a free–standing compact film which exhibited a high volumetric capacitance of 1058 F cm^{-3} at a current density of 0.5 A g^{-1} with excellent rate performance (75% at 50 A g^{-1}) and good cycling stability (81.5% after 5000 cycles).

Interestingly, compared to single atomic doping, heteroatom (dual or multiple atomic) doping of graphene synergistically provide better structural and electrical properties to the graphene surface. As an example, a remarkably high capacitance of 566 F g^{-1} was obtained at 0.5 A g^{-1} for N and sulphur (S) co–doped graphene hydrogel by Wang group. [83] The capacitance value was way better than the capacitance of N–doped graphene (371 F g^{-1}) and S–doped graphene (282 F g^{-1}) prepared by the same condition. Similarly, in another study by Pan et al. a high specific capacitance of 350 F g^{-1} and a high volumetric capacitance of 234 F cm^{-3} were obtained for boron (B), phosphorus (P) and N ternary–doped holey RGO hydrogel with a commercial level mass loading (10.4 mg cm^{-2}). [84]

Very recently new class of nanomaterials e.g. metal organic frameworks (MOFs), MXenes are being hybridized with graphene and their energy storage properties are being studied. For example, a bi–metallic MOF (Ni/Co–MOF) and RGO composite was synthesized by one–pot refluxing method by Rahmanifar and co–workers. [85] The composite was used as supercapacitor electrode which delivered a very high specific capacitance of 860 F g^{-1} at a current density of 1 A g^{-1}. Banerjee et al. synthesized Ni–doped Ni–MOF/RGO nanocomposite via chemical synthesis route. [86] The redox activity of the MOF structure together with the reduced charge transfer resistance offered by the RGO sheets resulted in a large capacitance of 758 F g^{-1}. MXenes, sheet of carbides and carbo–nitrides of early transition metals having

general formula $M_{n+1}X_nT_x$ (M being the transition metals, X represents carbon and/or nitrogen and T_x symbolizes the surface terminal groups) are newly synthesized 2D nanomaterials possessing metallic conductivity and high pseudocapacitance. Thus, graphene based layered hybrid with MXene was explored with significant success not only to reduce the restacking but synergistically couple EDLC of both the materials and pseudocapacitance of the later. Gogotsi group developed a free standing film of MXene–RGO via a two–step electrostatic assembly of MXene and RGO and subsequent vacuum filtration process. [87] The aligned structure of MXene and RGO assembly prevented the restacking of both MXenes and RGO sheets as a result the hybrid delivered an ultra–high volumetric capacitance of 1040 F cm^{-3} at 2 mV s^{-1} with excellent rate performance (61% retention at a high scan rate of 1 V s^{-1}). Dutta and co–workers adopted a zinc plate assisted layer–by–layer self–assembly strategy at room–temperature to obtain a 2D hydrogel film of MXene–RGO hybrid. [88] The hybrid hydrogel displayed an excellent capacitance of 653.7 F g^{-1} at a scan rate of 2 mV s^{-1}. The electrolyte protected mechanical compression of the hydrogel led to a compressed hydrogel with well–maintained porous structure which displayed a remarkable volumetric capacitance (1522 F cm^{-3}).

1.6 Fundamentals of electrocatalytic oxygen evolution reaction (OER):

The electrochemical water splitting reaction is an important and facile method to generate oxygen as well as hydrogen. The overall water splitting reaction, given by the equation: $2H_2O \rightarrow 2H_2 + O_2$ consists of oxygen evolution reaction (OER, also known as water oxidation reaction) at the anode and hydrogen evolution reaction (HER) at the cathode of the electrolyzer cell. To split water and hence to generate this green fuel hydrogen, electrical energy input is required, thus water splitting gives an alternate electrochemical method to store this electrical energy directly in terms of fuel. The entire splitting reaction can be divided into two half reactions that happen at the cathode and anode respectively. The reaction mechanism is highly pH dependent, as a result, in different media the reaction follows different path. In acidic medium (pH 0), the corresponding cathodic/anodic equations are:

$$4H^+ + 4e^- \rightarrow 2H_2 \qquad E_c^o = 0 \text{ V}$$

$$2H_2O \rightarrow O_2 + 4H^+ + 4e^- \qquad E_a^o = 1.23 \text{ V}$$

where E_c^o and E_a^o are the respective equilibrium half–cell cathodic and anodic potentials at standard conditions (1 atm and 25 °C). In alkaline medium (pH 14), the reactions are:

$4H_2O + 4e^- \rightarrow 2H_2 + 4OH^-$ $E_c^o = -0.826$ V

$4OH^- \rightarrow O_2 + 2H_2O + 4e^-$ $E_a^o = 0.404$ V

In neutral media (pH 7), the reactions are as follows:

$4H_2O + 4e^- \rightarrow 2H_2 + 4OH^-$ $E_c^o = -0.413$ V

$2H_2O \rightarrow O_2 + 4H^+ + 4e^-$ $E_a^o = 0.817$ V

Therefore, at standard conditions a potential of 1.23 V is the thermodynamically requirement to split water. A full electrolyzer cell consists of anode and cathode, voltage difference between the two electrodes can be directly measured which is equals to the applied voltage to split the water. However, to know the mechanism of HER and OER, it is often required to know the exact potential of reactions occurring at each electrode with reference to a common pontifical which does not change during reaction. Depending on the stability of the electrolyte system used for water splitting, different reference electrodes are used, for example silver/silver chloride (Ag/AgCl) is commonly used in acidic electrolyte while a saturated calomel electrode (SCE, Hg/Hg_2Cl_2) is used for alkaline electrolyte. These reference electrodes do not directly take part in the water splitting reaction, but their redox couple always maintains a constant potential. Measured absolute value of potential for each half reaction will be different with respect to different reference electrode. To represent the electrochemical data with respect to unique reference point, the potentials are commonly referenced against reversible hydrogen electrode (RHE). Any measured value of potential with respect to Ag/AgCl or SCE are converted to present the result with respect to RHE, using standard formula: $E_{RHE} = E_{WP} + 0.059pH + E^0$, where E_{WP} is the working potential of the reference electrode (Ag/AgCl or SCE) and E^0 is the standard cell potential. For Ag/AgCl, $E^0 = 0.1976\ V$ and for SCE $E^0 = 0.242\ V$.

Evolution of oxygen is a multi–step process and requires the transfer of four electrons. As a result, OER process is kinetically sluggish and a large potential is required for the evolution of O_2 higher than the thermodynamically requirement. Therefore, for efficient OER process through electrochemical water splitting reaction, electrocatalysts with high activity and stability are highly desirable which could overcome the large energy barriers of OER process. Electrocatalysts play the most vital part in determining the performance and efficiency of OER process. There are several factors or parameters which we need to focus for the performance evaluation of an electrocatalyst.

1.6.1 Overpotential (η):

The most important factor to determine OER performance evaluation is the overpotential (η). Ideally, water splitting occurs when the applied potential equals the equilibrium potential. However, in reality the water splitting occurs at voltage higher than the equilibrium potential due to intrinsic energy barriers. According to Nernst equation, the applied potential for an electrocatalytic redox reaction is given by,

$$E = E^0 + \frac{RT}{nF}\ln\frac{C_0}{C_R} \quad 1.15$$

Where E^0 is the standard potential of the reaction, T is the absolute temperature, R is the universal gas constant, n is the number of electrons transferred, F is the Faraday constant and C_0 and C_R are respectively the oxidized and reduced reagents. The overpotential (η) is defined as,

$$\eta = E - E^{eq} \quad 1.16$$

where E^{eq} is the equilibrium potential. The overpotential to supply a current density 10 mA cm^{-2} current density is usually reported in the literature and a low overpotential denotes a superior electrocatalytic activity.

1.6.2 Tafel slope:

For practical applications, it is desired to get high current at low overpotential. The relationship between current (i) and overpotential (η) is expressed in terms of Butler–Volmer equation:

$$i = i_0\left[e^{\frac{\alpha_a \eta FE}{RT}} + e^{\frac{\alpha_c \eta FE}{RT}}\right] \quad 1.17$$

Where i_0 is the exchange current density and α_a and α_c are the respective coefficients for anode and cathode. At high anodic/cathodic overpotentials equation 1.17 can be approximated as Tafel equations,

$$i \approx i_0 e^{\frac{\alpha_a \eta FE}{RT}} \quad 1.18$$

and

$$i \approx i_0 e^{\frac{\alpha_c \eta FE}{RT}} \quad 1.19$$

To express the rate of increment of current density with overpotential, Tafel slope (b) is presented which is expressed as,

$$\eta = b \cdot \log(i/i_0) \quad 1.20$$

A lower value of Tafel slope is desired to get fast increment of current with overpotential.

1.6.3 Activity:

To determine the activity of a given electrocatalyst mass and specific activates should be evaluated. Since different catalyst loading of an electrode gives rise to different activity, mass normalized current density which is also known as "mass activity", remains an important parameter for the performance evaluation of a given catalyst. Besides, determination of electrochemical surface area (ECSA) of a catalyst is also very crucial to understand the intrinsic activity of a catalyst. ECSA further gives a direct indication of the number of exposed active sites accessible for OER reaction. In addition to ECSA, Brunauere–Emmette–Teller (BET) surface area provides the information about the mass specific surface area of a catalyst.

1.6.4 Stability:

The stability of an electrocatalyst over long period of time is one of the key criteria for practical application. Stability of a catalyst is generally determined by chronoamperometry or chronopotentiometry test where the change in current/potential is observed at a given fixed potential/current respectively for a long period of time.

1.7 Graphene and graphene based hybrids for oxygen evolution reaction (OER):

Although the use of graphene is very common in supercapacitor applications, its use in pristine form in electrocatalytic water splitting reaction is largely limited by the low chemical activity of the sp^2 bonded carbon atoms. Thus, graphene have been used in electrocatalytic processes either by activating its pristine surface via functionalization or heteroatom (N/S,O) doping or making hybrids with catalytic nanomaterials where its role is to act as high surface area conducting support. In the following sections state–of–the art progress in the use of graphene both as electrocatalysts as well as conductive backbone are presented.

The pioneering work of Yang and co–workers has shown that, the heteroatom doped carbon materials could be an efficient metal free electrocatalysts for OER process in alkaline medium. [89] For this, they synthesized N–doped graphene nanoribbons which showed a low overpotential of 360 mV for 10 mA cm^{-2} of current density with a very small Tafel slope (47 mV dec^{-1}) than the non–doped graphene. They showed that, the pyridinic N–doped sites in graphene can draw electrons from the adjacent carbon atoms which is favourable for the adsorption of OER intermediates like OH^- and OOH^- which remained the rate determining step

for OER in alkaline medium. Chai et al. developed nitrogen (N) and phosphorus (P) co–doped graphene framework via hydrothermal process. [90] The N/P–doped graphene exhibited a promising OER characteristic displaying an overpotential of 320 mV at a current density of 10 mA cm^{-2}. By correlating experimental observations with simulation study they showed that, oxidized P–dopant sites together with N sites stabilized graphitic N and thereby activated neighbouring C–sites for high OER activity. Tian et al. adopted in–situ N–doping during chemical vapour deposition (CVD) growth of graphene to develop N–doped graphene–CNT hybrid. [91] The as–formed hybrid demonstrated an improved catalytic activity toward OER process than the un–doped hybrid (~110 mV higher overpotential than N–doped catalyst) in alkaline medium. Tam et al. developed a B–doped graphene quantum dots decorated graphene hydrogel by facile hydrothermal treatment. [92] The as developed 3D all carbon catalysts exhibited a low overpotential of 370 mV at a current density of 10 mA cm^{-2} and a small Tafel slope of 70 mV dec^{-1}. They showed that the favourable ion adsorption capability of the BCO_2 bond of B–doped GQDs and the electrical conductivity provided by the graphene framework synergistically improved the electrocatalytic activity of the hybrid. Liu et al. exfoliated carbon cloth (CC) with argon plasma to fabricate edge defect rich oxygen functionalized graphene over CC. [93] The as–exfoliated oxygen functionalized graphene on CC exhibited an overpotential of 450 mV at 10 mA cm^{-2} of current density and stability for over 40000 s in alkaline medium. The improved catalytic activity of functionalized graphene was originated from the generation of more exposed edges due to exfoliation and electrical/chemical modulation due to oxygen functionalization.

Transition metals like Ni, Co, Fe, Mn have been studied extensively as an alternative electrocatalyst to precious IrO_2 and RuO_2 OER catalysts due to their high activity, earth abundance and low cost. However, bare transition metal catalysts show poor stability for long term usage under high overpotential in alkaline environment. Therefore, nanostructured conductive supports like the stabilization of these metals in CNTs, graphene sheets are frequently used to boost the electrocatalytic performance of the hybrids. In this regard, Cui et al. synthesized a series of catalysts composed of uniform Ni, Co, Fe and their alloys encapsulated by single graphene sheet by CVD growth. [94] The as–formed FeNi alloy and graphene composite showed lowest overpotential (at 10 mA cm^{-2}) of 280 mV, small Tafel slope of 70 mV and long term durability over 5000 CV cycles. The density functional theory (DFT) study revealed that the single layer graphene facilitated the transfer of electrons from the metal sites to the graphene sheets which regulated the electronic structure of graphene and

promoted the electrocatalytic OER process of the hybrid. Guan et al. developed a catalyst with mononuclear Mn dispersed over N–doped graphene via calcination in furnace. [95] The as–synthesized catalyst exhibited a minimum overpotential of 337 mV, a low Tafel slope of 55 mV dec^{-1} and long term durability up to 120 h. Through DFT study they concluded that the mononuclear Mn coordinated with the four N–atoms of the N–doped graphene to form metal–oxo species which promoted the adsorption of OER intermediates and triggered OER process.

Not only transition metal nanoparticles, but their oxides, sulfides, nitrides and hydroxides/oxo–hydroxides are also extensively used as OER electrocatalysts due to their low cost, tunable structure, high efficiency. Development of hybrid structure of graphene with these oxides/sulfides/nitrides/hydroxides/oxohydroxides not only enhances the electrical conductivity but also exposes the active surface area for high catalytic activity. For instance, Mao et al. constructed a highly active OER catalyst composed of crumpled graphene–cobalt oxide (Co_3O_4) nanohybrid. [96] The large surface area provided by the graphene structure and stable anchoring of oxide nanoparticles over graphene sheets promoted more exposed active sites which expedited OER reaction. The work of Dai group further confirmed that the OER activity of Co_3O_4 was enhanced drastically when composited with N–doped graphene. [97] They showed that the high OER activity of the hybrid catalyst arose from the strong synergistic coupling between Co_3O_4 and graphene sheets. Liu et al. developed a high performance OER catalyst composed of NiFe–bi–metallic sulphide ($NiFeS_2$) nanoparticles decorated over graphene via solvothermal treatment followed by sulfidation at 400 °C. [98] The as–formed hybrid catalyst required an overpotential of 320 mV to deliver 10 mA cm^{-2} of current density in alkaline medium and a small Tafel slope of 61 mV dec^{-1}. Similarly, Fan et al. fabricated NiFe–nitride (Ni_3FeN) nanoplates onto N–doped graphene by carrying out nitridation of NiFe–LDH/GO hybrid at 700 °C under NH_3 atmosphere. [99] Their study revealed that the ultrathin Ni_3FeN nanoplates over graphene surface provide intimate contact which facilitated rapid charge transfer process which resulted in an overpotential of 400 mV at 10 mA cm^{-2} current density. Moreover doping with Fe species provided stability of the catalyst even at very high temperature.

Transition metal based hydroxides particularly layered double hydroxides (LDHs) are considered to be one of the most promising OER electrocatalysts because of their high activity, tunable chemical structure, adjustable layered morphology, low cost etc. However, low conductivity of the hydroxides (~ 10^{-13}–10^{-17} S cm^{-1}) remains a practical concern. [100] As a result graphene has been used frequently as conductive backbone for these LDH materials. For

instance, Qiao group reported a 3D catalyst consisted of NiCo–LDH over N–doped graphene hydrogel which showed an onset potential of 350 mV and Tafel slope of 614 mV dec^{-1}. Shen et al. presented a liquid phase self–assembly of exfoliated NiFe–LDH and GO. [101] The subsequent reduction of GO formed NiFe–LDH/RGO hybrid which demonstrated an ultra–low overpotential of 273 mV at 30 mA cm^{-2} with a small Tafel slope of 49 mV dec^{-1}. The excellent OER activity of the hybrid was attributed to the unique array like structure of the hybrid having abundant active sites and the improved charge transfer efficiency due to the conductive graphene sheets. Ping and co–workers reported a novel 3D catalyst via electrostatic self–assembly of monolayer CoAl–LDH over a graphene framework. [102] The as–developed 3D catalyst exhibited a low overpotential of 252 mV at a current density of 10 mA cm^{-2} and a Tafel slope as small as 36 mV dec^{-1} surpassing the performance of commercial IrO_2 catalyst. They further revealed that the formation of uniform hybrid with porous structure facilitated rapid charge–transfer between graphene and LDH nanosheets which boosted the OER activity.

Recently, metal organic frameworks or MOFs in short, have emerged as a low cost alternative electrocatalysts for OER due to their unique properties like high surface area, tunable porosity and uniformly distributed metal centers. Nevertheless, the hybridization of MOFs with graphene could complement the poor electrical conductivity of MOFs ($<10^{-10}$ S cm^{-1}) [103] and enhances the charge transfer process for high OER activity. Jahan et al. fabricated a Cu–MOF and GO hybrid via hydrothermal treatment. [104] They proposed that the incorporation of GO in MOFs provided the stability and improved the OER activity of MOFs. Xie and co–workers developed a 3D Ni–MOF over graphene surface via freeze drying and ultrasonic treatment. [105] The 3D catalyst exhibited a high OER activity achieving an overpotential of 370 mV at 10 mA cm^{-2}. The high OER activity of the hybrid catalyst was ascribed to the porous 3D structure of the catalyst which provided the high surface area and the presence of conductive graphene surface which helped in promoting rapid mass and electron transfer during OER process. Cao et al. synthesized a novel OER electrocatalyst consisted of ultrathin Co–ZIF (zeolitic imidazolate framework) MOF nanosheets onto vertically aligned Co–hydroxide ($Co(OH)_2$) nanosheets over electrochemically exfoliated graphene foil. [106] The heterostructure possessed a strong electrochemical coupling and synergistic effect to achieve 10 mA cm^{-2} of current density at an affordable overpotential of 280 mV. Moreover, the Co–O species of Co–ZIF converted into Co–OOH during the OER process, which was also responsible for such excellent catalytic performance.

1.8 Existing challenges in the graphene based energy applications:

Although, the last decade has witnessed a tremendous growth in the use of graphene and graphene based hybrids in energy applications as discussed in the previous sections, a huge challenge is still present for the efficient and practical use of graphene in electrochemical energy generation/storage systems. The existing challenges are divided into two parts namely, challenges in supercapacitive energy storage and challenges in the field of OER. The following sections highlight these challenges in detail.

1.8.1 Challenges in supercapacitive energy storage

- *Bottleneck to simultaneously achieve high areal and gravimetric performances without sacrificing rate performance:*

Very frequently, high gravimetric performances were reported with very thin electrodes (with low areal mass loading < 2 mg cm^{-2}) made of graphene or its hybrids, and at a low charge–discharge rate. [70, 107-109] Both of the conditions are far from the requirements of practically usable supercapacitors. Slow charge–discharge rate means the sacrifice of signature characteristic of supercapacitor which separates itself from other energy storage technologies like battery. On the other hand, thin electrodes can ensure good electrolyte penetration and efficient accessibility of surfaces of active materials (graphene and/or nanomaterials in the hybrid), thus can display good gravimetric energy storage performance (capacitance per unit mass). But, to store much of energy per unit footprint of the device (areal energy density), thick electrode with high areal mass loading (> 5 mg cm^{-2}) is a practical need. Reported high gravimetric performances with thin electrodes are challenging to translate to thicker electrodes due to significant graphene restacking, lack of continuous ion channels, and hence poor surface accessibility by electrolyte ions. The seriousness of this challenge can be judged from the work of Hu et al, who showed that specific capacitance value decreases by one order of magnitude when areal loading increases from 72 µg cm^{-2} to 1.33 mg cm^{-2}. [110] In addition, increase of areal mass loading drastically reduces charge–discharge rate capability. Thus, for practical use it is very important to realize supercapacitors possessing not only high gravimetric capacitance but also high capacitance per unit area of the device (areal capacitance) without sacrificing the high rate capability, but still stands as a challenge to materialize.

- *Challenge to attain high volumetric performance at a high charge–discharge rate:*

Volumetric performance is an important metric to consider for the design of practical usable supercapacitor device. Although graphene based macropores electrodes can offer good electrochemically accessible surface area and hence good gravimetric energy and power densities, but the large pores will remain filled with electrolyte which increases the overall weight of the device. To avoid the increase of device weight arising from the electrolytes filled in large pores, the electrode must be compact but still displaying good capacitance. In other words, volumetric capacitance needs to be high. Unfortunately, in most of the reported cases, high volumetric performance was achieved by significantly sacrificing charge–discharge rate. How to attain excellent volumetric performance together with high charge–discharge rate is still remains a challenge.

- *Lack of simple, scalable and controlled processing of graphene based pseudocapacitive hybrid:*

Linking pseudocapacitive nanomaterials like conducting polymers with graphene can be expected to give high performance due to the synergistic effect of high conductivity of graphene and high pseudocapacitance of the polymers. However, conventional growth of polymers over isolated sheets of graphene, and the electrodes made out of it exhibit low performance possibly due to restacking. In this regard, graphene hydrogel based supercapacitive hybrids with conducting polymers have shown promising results however, such hydrogel hybrids are mostly produced via in–situ random nucleation and growth, thus there were less control in size and morphology of the nanomaterial. A simple, highly scalable processing is missing which can provide customize control in material characteristic.

1.8.2 Challenges in the field of OER

- *Requirement of large overpotential:*

Water splitting at a lower applied voltage is required for low cost hydrogen economy. However, need of large overpotential (> 300 mV) for OER reaction is still considered as prime challenge to limit the overall voltage requirement for splitting. Challenge to obtain suitable graphene based OER materials with customized shape and size, low overall surface area of the catalyst, and inefficient electron and mass transport pathway are the major performance limiting factors thus requiring high overpotentials.

- *Lack of facile, lost cost and scalable protocol for controlled graphene hybrid based OER catalyst:*

To enable commercial use of graphene based OER catalyst, not only performance needs to be optimized but these should also be produced in a large scale at low cost. MOFs based graphene hybrids are promising materials for OER, but lack of size and morphological tunability, ultimate scalability limits their performance and hence widespread use.

The current status in the field of energy storage demands immediate attention to overcome the aforementioned challenges. To do so, a coordinated strategy is required to address the bottlenecks in facile, low cost processibility, and to overcome the performance imitating factors. A suitable design of electrode structure with limited restacking of graphene and tuneable nanohybridization directly over the porous framework may be an adequate path in this direction. Binder free electrode design with retained good electrical conductivity, imparting 3D porosity for ions and mass transport, robust interface with hybridized nanomaterials are some of the key factors which need to be realized for possible success in this field. This motivates us take the following key objective to be implemented in this thesis which are expected to address the existing bottlenecks in the field of supercapacitive energy storage and OER catalysts.

1.9 Objectives of this thesis work:

Considering the existing challenges and the scope to overcome these issues, the following objectives have been taken in this thesis work:

- Development of facile and highly scalable interfacial co–assembly strategies for integrating graphene with pseudocapacitive nanomaterials like nanofibers of conducting polymers keeping a goal to achieve high volumetric and areal capacitance with high rate performance.
- Development of in–situ methodologies to realize graphene–hydrogel based pseudocapacitive polymeric hybrids with fine control over polymer growth to achieve high specific capacitance at large mass loading keeping the high rate performance.
- Molecular level understanding of hybridization process via molecular dynamic simulations studies.
- Development of simple, scalable and cost effective strategy to integrate graphene with MXene nanosheets in the form of hydrogel to realize high energy and power density supercapacitors.

- Exploring the possibility of compositional and morphology tuned growth MOF over graphene in a cost effective way with a final goal to activate OER catalysis at low overpotential.

- ***Discussion on the objectives*:**

The undertaken objectives are expected to overcome the existing challenges in the energy storage applications of graphene or graphene based hybrids. Firstly, the co–assembly synthesis process adopted in this work is facile, cost effective, arbitrarily scalable and could be applicable for the 3D hybridization of graphene hydrogel with vast number of nanomaterials e.g. conducting polymers, MXenes etc. mitigating the existing bottleneck of easy processability. Secondly, the fine structure tuning of conducting polymers, MOFs via facile and controlled hybridization with graphene hydrogel are expected to enhance both the supercapacitive and electrocatalytic performances originating from their uniform morphology, favourable charge transport kinetics and exposed catalytically active centers. Thirdly, such uniform and controlled nano–hybridization could give rise to high mass loading of the hybrid–hydrogel without any bulk aggregation. This uniform hybrid structure together with the porous framework of graphene hydrogel could promote the favourable charge and ion transfer process thereby overcoming the bottleneck of simultaneously achieving high specific and high areal performance with high rate capability. Finally, understanding the controlled hybridization process at molecular level would be beneficial for better adaptability of such strategies in practical applications.

1.10 Conclusion:

There is no doubt that graphene has brought a new era in the development of energy applications because of its extraordinary inherent properties. Nevertheless, a number of major issues are still need to be addressed for the commercialization of graphene based energy generation/storage devices. Therefore, while developing such devices we need to always keep focus on the following two key points:

Firstly, a cost effective and environmental friendly strategy should be developed to fabricate restacking free graphene and graphene based functional nanohybrids in large scale.

Secondly, the core understanding of ion transport, their interaction on the electrodes and catalytic effect over the electrocatalysts at the nanoscale level will drive us to design and configure better electrode materials.

In conclusion, more and more research efforts should be devoted in order to develop novel strategies and electrode design to address the current bottleneck associated with the graphene based energy generation/storage applications.

1.11 Organization of the thesis:

The entire thesis work has been divided into six different chapters starting with a brief introduction to the state–of–art technologies and challenges in energy storage devices and the rest of the chapters discuss the strategies to overcome these challenges. This thesis ends with concluding remarks and future prospects in the area of energy storage. A brief description of each chapter is presented below.

Chapter 1: Chapter 1 highlights a brief introduction to state–of–art energy storage and conversion technologies particularly focussing on supercapacitor and OER applications. Recent progress in graphene and graphene based hybrids toward the application of supercapacitor and OER process have also been presented. We have further elaborated the design principle of electrode architecture for commercial level applications. The motivation and objectives of the present work have been illustrated at the end of this chapter.

Chapter 2: In chapter 2 we present the development of highly scalable nanohybrids of 3D framework of porous graphene hydrogel and polyaniline (PANI) nanofibers (PGH) via co–assembly process at room temperature for customized performance supercapacitor electrode. The as obtained PGH with open porous structure and high mass loading exhibited excellent areal and volumetric capacitance while maintaining high charging–discharging rate capability Furthermore, the potential wearability of our hybrid hydrogel was demonstrated by directly integrating PGH with carbon cloths. The work presented in this chapter therefore highlights the strategy for developing graphene–PANI hybrids and the fundamental design principles of high areal loading supercapacitor electrodes for commercial applications.

Chapter 3: Chapter 3 presents the concept of graphene hydrogel–organic interfacial synthesis protocol toward the controlled development of ultrafine PANI nanostructure–graphene hybrid hydrogel (PANI–GH). Molecular dynamics study revealed that, slow diffusion of aniline monomer at the hydrogel organic interface and a strong attractive interaction of aniline and

graphene surface played the key role in controlling the polymerization rate and thereby the morphology of as grown PANI nanostructure. We also demonstrated an ultrafast assembly (5 min) process of GH at room temperature which is very unique in terms of time consumption and cost–effectiveness. This PANI–GH hydrogel when used as supercapacitor electrode exhibited an ultrahigh specific capacitance with superb rate performance even with a commercial scale mass loading. The high performance of PANI–GH electrode is attributed to the ultrafine growth of PANI nanostructure over the surface of graphene and the conducting open porous morphology of PANI–GH hybrid hydrogel which facilitates rapid ion transportation.

Chapter 4: Chapter 4 introduces graphene analogous functional 2D nanomaterial MXene ($Ti_3C_2T_x$) and the development a 3D hydrogel of MXene and graphene by zinc particle assisted gel–casting process completely at room temperature. An asymmetric capacitor developed with graphene–MXene as the negative electrode and a graphene–PANI hydrogel as the positive electrode displayed large operating potential window with ultra–high energy density and excellent rate performance. This work demonstrates a low cost facile synthesis strategy to develop 3D porous 2D–2D hybrid electrode for energy storage and other customized applications.

Chapter 5: In Chapter 5 we have introduced the development of morphology and crystal structure tuned MOF–graphene hybrid heterostructure via hydrogel–organic interfacial synthesis strategy at room temperature and used as highly efficient OER catalysts. Molecular dynamics study was performed to study the controlled diffusion of reactant species which leads to the controlled growth of MOFs within graphene framework. Moreover, the versatility of our synthesis protocol is demonstrated by developing graphene hybrids comprising of a range of transition metal based MOFs (e.g. ZIF67, ZIF8, HKUST1, NiCoFe–trimetallic MOF). The as developed rod–like NiCoFe–tri–metallic MOF–porous graphene hybrid exhibited state–of–art OER performance with a small overpotential and a low Tafel slope outperforming the catalytic activity of commercial RuO_2 electrocatalysts. This work paves a new direction toward the ambient condition synthesis of MOF–graphene hybrids and many more with a fine structure control over morphology, crystallinity and microstructure for versatile applications.

Chapter 6: Chapter 6 highlights the key findings of this work with concluding remarks. The future scope of the present thesis work has been presented at the end of this thesis.

References:

1. H. Lv, Y. V. Geletii, C. Zhao, J. W. Vickers, G. Zhu, Z. Luo, J. Song, T. Lian, D. G. Musaev and C. L. Hill, Polyoxometalate water oxidation catalysts and the production of green fuel, *Chem. Soc. Rev.*, 41 (2012), pp. 7572-7589.
2. G. Wu, A. Santandreu, W. Kellogg, S. Gupta, O. Ogoke, H. Zhang, H.-L. Wang and L. Dai, Carbon nanocomposite catalysts for oxygen reduction and evolution reactions: From nitrogen doping to transition-metal addition, *Nano Energy*, 29 (2016), pp. 83-110.
3. K. S. Balkhair and K. U. Rahman, Sustainable and economical small-scale and low-head hydropower generation: A promising alternative potential solution for energy generation at local and regional scale, *Applied Energy*, 188 (2017), pp. 378-391.
4. C. Budischak, D. Sewell, H. Thomson, L. Mach, D. E. Veron and W. Kempton, Cost-minimized combinations of wind power, solar power and electrochemical storage, powering the grid up to 99.9% of the time, *J. Power Sources*, 225 (2013), pp. 60-74.
5. T. R. Cook, D. K. Dogutan, S. Y. Reece, Y. Surendranath, T. S. Teets and D. G. Nocera, Solar Energy Supply and Storage for the Legacy and Nonlegacy Worlds, *Chem. Rev.*, 110 (2010), pp. 6474-6502.
6. J. A. Turner, Sustainable Hydrogen Production, *Science*, 305 (2004), pp. 972.
7. J. O. M. Bockris, The origin of ideas on a Hydrogen Economy and its solution to the decay of the environment, *Int. J. Hydrogen Energy*, 27 (2002), pp. 731-740.
8. S. Sharma and S. K. Ghoshal, Hydrogen the future transportation fuel: From production to applications, *Renewable and Sustainable Energy Reviews*, 43 (2015), pp. 1151-1158.
9. X. Chen, G. Liu, W. Zheng, W. Feng, W. Cao, W. Hu and P. Hu, Vertical 2D MoO2/MoSe2 Core–Shell Nanosheet Arrays as High-Performance Electrocatalysts for Hydrogen Evolution Reaction, *Adv. Funct. Mater.*, 26 (2016), pp. 8537-8544.
10. D.-H. Ha, B. Han, M. Risch, L. Giordano, K. P. C. Yao, P. Karayaylali and Y. Shao-Horn, Activity and stability of cobalt phosphides for hydrogen evolution upon water splitting, *Nano Energy*, 29 (2016), pp. 37-45.
11. M. I. Jamesh, Recent progress on earth abundant hydrogen evolution reaction and oxygen evolution reaction bifunctional electrocatalyst for overall water splitting in alkaline media, *J. Power Sources*, 333 (2016), pp. 213-236.
12. R. Li, D. Zhou, J. Luo, W. Xu, J. Li, S. Li, P. Cheng and D. Yuan, The urchin-like sphere arrays Co3O4 as a bifunctional catalyst for hydrogen evolution reaction and oxygen evolution reaction, *J. Power Sources*, 341 (2017), pp. 250-256.
13. H. Zhou, F. Yu, Y. Liu, J. Sun, Z. Zhu, R. He, J. Bao, W. A. Goddard, S. Chen and Z. Ren, Outstanding hydrogen evolution reaction catalyzed by porous nickel diselenide electrocatalysts, *Energy Environ. Sci.*, 10 (2017), pp. 1487-1492.
14. X. Zou and Y. Zhang, Noble metal-free hydrogen evolution catalysts for water splitting, *Chem. Soc. Rev.*, 44 (2015), pp. 5148-5180.
15. J. Suntivich, K. J. May, H. A. Gasteiger, J. B. Goodenough and Y. Shao-Horn, A Perovskite Oxide Optimized for Oxygen Evolution Catalysis from Molecular Orbital Principles, *Science*, 334 (2011), pp. 1383.
16. Q. Shi, C. Zhu, D. Du and Y. Lin, Robust noble metal-based electrocatalysts for oxygen evolution reaction, *Chem. Soc. Rev.*, 48 (2019), pp. 3181-3192.
17. W. Zhang and K. Zhou, Ultrathin Two-Dimensional Nanostructured Materials for Highly Efficient Water Oxidation, *Small*, 13 (2017), pp. 1700806.

18. J.-L. Shui, N. K. Karan, M. Balasubramanian, S.-Y. Li and D.-J. Liu, Fe/N/C Composite in Li–O2 Battery: Studies of Catalytic Structure and Activity toward Oxygen Evolution Reaction, *J. Am. Chem. Soc.*, 134 (2012), pp. 16654-16661.
19. J. Zhang, Z. Zhao, Z. Xia and L. Dai, A metal-free bifunctional electrocatalyst for oxygen reduction and oxygen evolution reactions, *Nat. Nanotechnol.*, 10 (2015), pp. 444-452.
20. D. Deng, K. S. Novoselov, Q. Fu, N. Zheng, Z. Tian and X. Bao, Catalysis with two-dimensional materials and their heterostructures, *Nat. Nanotechnol.*, 11 (2016), pp. 218-230.
21. B. Liu and K. Zhou, Recent progress on graphene-analogous 2D nanomaterials: Properties, modeling and applications, *Prog. Mater Sci.*, 100 (2019), pp. 99-169.
22. B. Mendoza-Sánchez and Y. Gogotsi, Synthesis of Two-Dimensional Materials for Capacitive Energy Storage, *Adv. Mater.*, 28 (2016), pp. 6104-6135.
23. P. Wang, T. Jia and B. Wang, A critical review: 1D/2D nanostructured self-supported electrodes for electrochemical water splitting, *J. Power Sources*, 474 (2020), pp. 228621.
24. X. Yu, S. Yun, J. S. Yeon, P. Bhattacharya, L. Wang, S. W. Lee, X. Hu and H. S. Park, Emergent Pseudocapacitance of 2D Nanomaterials, *Adv. Energy Mater.*, 8 (2018), pp. 1702930.
25. H. Zhang, M. Chhowalla and Z. Liu, 2D nanomaterials: graphene and transition metal dichalcogenides, *Chem. Soc. Rev.*, 47 (2018), pp. 3015-3017.
26. A. K. Geim and K. S. Novoselov, The rise of graphene, *Nat. Mater.*, 6 (2007), pp. 183-191.
27. K. S. Novoselov, V. I. Fal′ko, L. Colombo, P. R. Gellert, M. G. Schwab and K. Kim, A roadmap for graphene, *Nature*, 490 (2012), pp. 192-200.
28. D. A. C. Brownson, D. K. Kampouris and C. E. Banks, An overview of graphene in energy production and storage applications, *J. Power Sources*, 196 (2011), pp. 4873-4885.
29. M. F. El-Kady, Y. Shao and R. B. Kaner, Graphene for batteries, supercapacitors and beyond, *Nat. Rev. Mater.*, 1 (2016), pp. 16033.
30. J. Li, Z. Zhao, Y. Ma and Y. Qu, Graphene and Their Hybrid Electrocatalysts for Water Splitting, *ChemCatChem*, 9 (2017), pp. 1554-1568.
31. X. Li and L. Zhi, Graphene hybridization for energy storage applications, *Chem. Soc. Rev.*, 47 (2018), pp. 3189-3216.
32. J. Zhu, D. Yang, Z. Yin, Q. Yan and H. Zhang, Graphene and Graphene-Based Materials for Energy Storage Applications, *Small*, 10 (2014), pp. 3480-3498.
33. P. Sharma and T. S. Bhatti, A review on electrochemical double-layer capacitors, *Energy Convers. Manage.*, 51 (2010), pp. 2901-2912.
34. P. Simon and Y. Gogotsi, Materials for electrochemical capacitors, *Nat. Mater.*, 7 (2008), pp. 845-854.
35. X. Lang, A. Hirata, T. Fujita and M. Chen, Nanoporous metal/oxide hybrid electrodes for electrochemical supercapacitors, *Nat. Nanotechnol.*, 6 (2011), pp. 232-236.
36. C. Largeot, C. Portet, J. Chmiola, P.-L. Taberna, Y. Gogotsi and P. Simon, Relation between the Ion Size and Pore Size for an Electric Double-Layer Capacitor, *J. Am. Chem. Soc.*, 130 (2008), pp. 2730-2731.
37. G. Wang, L. Zhang and J. Zhang, A review of electrode materials for electrochemical supercapacitors, *Chem. Soc. Rev.*, 41 (2012), pp. 797-828.
38. J. R. Miller and P. Simon, Electrochemical Capacitors for Energy Management, *Science*, 321 (2008), pp. 651.

39. J. Libich, J. Máca, J. Vondrák, O. Čech and M. Sedlaříková, Supercapacitors: Properties and applications, *Journal of Energy Storage*, 17 (2018), pp. 224-227.
40. M. Salanne, B. Rotenberg, K. Naoi, K. Kaneko, P. L. Taberna, C. P. Grey, B. Dunn and P. Simon, Efficient storage mechanisms for building better supercapacitors, *Nat. Energy.*, 1 (2016), pp. 16070.
41. H. Helmholtz, Ueber einige Gesetze der Vertheilung elektrischer Ströme in körperlichen Leitern mit Anwendung auf die thierisch-elektrischen Versuche, *Annalen der Physik*, 165 (1853), pp. 211-233.
42. D. L. Chapman, LI. A contribution to the theory of electrocapillarity, *The London, Edinburgh, and Dublin Philosophical Magazine and Journal of Science*, 25 (1913), pp. 475-481.
43. M. Gouy, Sur la constitution de la charge électrique à la surface d'un électrolyte, *J. Phys. Theor. Appl.*, 9 (1910), pp. 457-468.
44. M. Winter and R. J. Brodd, What Are Batteries, Fuel Cells, and Supercapacitors?, *Chem. Rev.*, 104 (2004), pp. 4245-4270.
45. L. L. Zhang and X. S. Zhao, Carbon-based materials as supercapacitor electrodes, *Chem. Soc. Rev.*, 38 (2009), pp. 2520-2531.
46. B. E. Conway, V. Birss and J. Wojtowicz, The role and utilization of pseudocapacitance for energy storage by supercapacitors, *J. Power Sources*, 66 (1997), pp. 1-14.
47. H. Li, J. Wang, Q. Chu, Z. Wang, F. Zhang and S. Wang, Theoretical and experimental specific capacitance of polyaniline in sulfuric acid, *J. Power Sources*, 190 (2009), pp. 578-586.
48. C. Peng, D. Hu and G. Z. Chen, Theoretical specific capacitance based on charge storage mechanisms of conducting polymers: Comment on 'Vertically oriented arrays of polyaniline nanorods and their super electrochemical properties', *Chem. Commun.*, 47 (2011), pp. 4105-4107.
49. M. Toupin, T. Brousse and D. Bélanger, Charge Storage Mechanism of MnO2 Electrode Used in Aqueous Electrochemical Capacitor, *Chem. Mater.*, 16 (2004), pp. 3184-3190.
50. Y. Shao, M. F. El-Kady, J. Sun, Y. Li, Q. Zhang, M. Zhu, H. Wang, B. Dunn and R. B. Kaner, Design and Mechanisms of Asymmetric Supercapacitors, *Chem. Rev.*, 118 (2018), pp. 9233-9280.
51. V. Augustyn, J. Come, M. A. Lowe, J. W. Kim, P.-L. Taberna, S. H. Tolbert, H. D. Abruña, P. Simon and B. Dunn, High-rate electrochemical energy storage through Li+ intercalation pseudocapacitance, *Nat. Mater.*, 12 (2013), pp. 518-522.
52. L. Kong, C. Zhang, J. Wang, W. Qiao, L. Ling and D. Long, Free-Standing T-Nb2O5/Graphene Composite Papers with Ultrahigh Gravimetric/Volumetric Capacitance for Li-Ion Intercalation Pseudocapacitor, *ACS Nano*, 9 (2015), pp. 11200-11208.
53. V. Augustyn, P. Simon and B. Dunn, Pseudocapacitive oxide materials for high-rate electrochemical energy storage, *Energy Environ. Sci.*, 7 (2014), pp. 1597-1614.
54. M. D. Stoller and R. S. Ruoff, Best practice methods for determining an electrode material's performance for ultracapacitors, *Energy Environ. Sci.*, 3 (2010), pp. 1294-1301.
55. M. El-Kady, V. Strong, S. Dubin and R. Kaner, Laser Scribing of High-Performance and Flexible Graphene-Based Electrochemical Capacitors, *Science*, 335 (2012), pp. 1326-1330.
56. J. Xia, F. Chen, J. Li and N. Tao, Measurement of the quantum capacitance of graphene, *Nat. Nanotechnol.*, 4 (2009), pp. 505-509.

57. V. Deerattrakul, W. Hirunpinyopas, N. Pisitpipathsin, T. Saisopa, M. Sawangphruk, C. Nualchimplee and P. Iamprasertkun, The electrochemistry of size dependent graphene via liquid phase exfoliation: capacitance and ionic transport, *Phys. Chem. Chem. Phys.*, 23 (2021), pp. 11616-11623.
58. S. Pei and H.-M. Cheng, The reduction of graphene oxide, *Carbon*, 50 (2012), pp. 3210-3228.
59. W. S. Hummers and R. E. Offeman, Preparation of Graphitic Oxide, *J. Am. Chem. Soc.*, 80 (1958), pp. 1339-1339.
60. M. D. Stoller, S. Park, Y. Zhu, J. An and R. S. Ruoff, Graphene-Based Ultracapacitors, *Nano Lett.*, 8 (2008), pp. 3498-3502.
61. Y. Chen, X. Zhang, D. Zhang, P. Yu and Y. Ma, High performance supercapacitors based on reduced graphene oxide in aqueous and ionic liquid electrolytes, *Carbon*, 49 (2011), pp. 573-580.
62. S. R. C. Vivekchand, C. S. Rout, K. S. Subrahmanyam, A. Govindaraj and C. N. R. Rao, Graphene-based electrochemical supercapacitors, *J. Chem. Sci.*, 120 (2008), pp. 9-13.
63. M. F. El-Kady and R. B. Kaner, Scalable fabrication of high-power graphene micro-supercapacitors for flexible and on-chip energy storage, *Nat. commun.*, 4 (2013), pp. 1475.
64. Y. Xu, K. Sheng, C. Li and G. Shi, Self-Assembled Graphene Hydrogel via a One-Step Hydrothermal Process, *ACS Nano*, 4 (2010), pp. 4324-4330.
65. P. Chen, J.-J. Yang, S.-S. Li, Z. Wang, T.-Y. Xiao, Y.-H. Qian and S.-H. Yu, Hydrothermal synthesis of macroscopic nitrogen-doped graphene hydrogels for ultrafast supercapacitor, *Nano Energy*, 2 (2013), pp. 249-256.
66. W. S. V. Lee, M. Leng, M. Li, X. L. Huang and J. M. Xue, Sulphur-functionalized graphene towards high performance supercapacitor, *Nano Energy*, 12 (2015), pp. 250-257.
67. Y. Liao, Y. Huang, D. Shu, Y. Zhong, J. Hao, C. He, J. Zhong and X. Song, Three-dimensional nitrogen-doped graphene hydrogels prepared via hydrothermal synthesis as high-performance supercapacitor materials, *Electrochim. Acta*, 194 (2016), pp. 136-142.
68. Y. Xu, Z. Lin, X. Huang, Y. Wang, Y. Huang and X. Duan, Functionalized Graphene Hydrogel-Based High-Performance Supercapacitors, *Adv. Mater.*, 25 (2013), pp. 5779-5784.
69. S. Dai, Z. Liu, B. Zhao, J. Zeng, H. Hu, Q. Zhang, D. Chen, C. Qu, D. Dang and M. Liu, A high-performance supercapacitor electrode based on N-doped porous graphene, *J. Power Sources*, 387 (2018), pp. 43-48.
70. X. Yang, J. Zhu, L. Qiu and D. Li, Bioinspired Effective Prevention of Restacking in Multilayered Graphene Films: Towards the Next Generation of High-Performance Supercapacitors, *Adv. Mater.*, 23 (2011), pp. 2833-2838.
71. U. N. Maiti, J. Lim, K. E. Lee, W. J. Lee and S. O. Kim, Three-Dimensional Shape Engineered, Interfacial Gelation of Reduced Graphene Oxide for High Rate, Large Capacity Supercapacitors, *Adv. Mater.*, 26 (2014), pp. 615-619.
72. Q. Cheng, J. Tang, J. Ma, H. Zhang, N. Shinya and L.-C. Qin, Graphene and carbon nanotube composite electrodes for supercapacitors with ultra-high energy density, *Phys. Chem. Chem. Phys.*, 13 (2011), pp. 17615-17624.
73. Z.-S. Wu, D.-W. Wang, W. Ren, J. Zhao, G. Zhou, F. Li and H.-M. Cheng, Anchoring Hydrous RuO2 on Graphene Sheets for High-Performance Electrochemical Capacitors, *Adv. Funct. Mater.*, 20 (2010), pp. 3595-3602.

74. J. Yan, Z. Fan, T. Wei, W. Qian, M. Zhang and F. Wei, Fast and reversible surface redox reaction of graphene–MnO2 composites as supercapacitor electrodes, *Carbon*, 48 (2010), pp. 3825-3833.
75. S. Chen, J. Duan, Y. Tang and S. Zhang Qiao, Hybrid Hydrogels of Porous Graphene and Nickel Hydroxide as Advanced Supercapacitor Materials, *Chem. Eur. J.*, 19 (2013), pp. 7118-7124.
76. J. Chen, X. Wang, J. Wang and P. S. Lee, Sulfidation of NiMn-Layered Double Hydroxides/Graphene Oxide Composites toward Supercapacitor Electrodes with Enhanced Performance, *Adv. Energy Mater.*, 6 (2016), pp. 1501745.
77. J. Yang, X. Duan, W. Guo, D. Li, H. Zhang and W. Zheng, Electrochemical performances investigation of NiS/rGO composite as electrode material for supercapacitors, *Nano Energy*, 5 (2014), pp. 74-81.
78. H.-H. Chang, C.-K. Chang, Y.-C. Tsai and C.-S. Liao, Electrochemically synthesized graphene/polypyrrole composites and their use in supercapacitor, *Carbon*, 50 (2012), pp. 2331-2336.
79. H.-P. Cong, X.-C. Ren, P. Wang and S.-H. Yu, Flexible graphene–polyaniline composite paper for high-performance supercapacitor, *Energy Environ. Sci.*, 6 (2013), pp. 1185-1191.
80. J. Wu, Q. e. Zhang, A. a. Zhou, Z. Huang, H. Bai and L. Li, Phase-Separated Polyaniline/Graphene Composite Electrodes for High-Rate Electrochemical Supercapacitors, *Adv. Mater.*, 28 (2016), pp. 10211-10216.
81. Y. Wang, X. Yang, A. G. Pandolfo, J. Ding and D. Li, High-Rate and High-Volumetric Capacitance of Compact Graphene–Polyaniline Hydrogel Electrodes, *Adv. Energy Mater.*, 6 (2016), pp. 1600185.
82. Z. Fan, Z. Cheng, J. Feng, Z. Xie, Y. Liu and Y. Wang, Ultrahigh volumetric performance of a free-standing compact N-doped holey graphene/PANI slice for supercapacitors, *J. Mater. Chem. A*, 5 (2017), pp. 16689-16701.
83. T. Wang, L.-X. Wang, D.-L. Wu, W. Xia and D.-Z. Jia, Interaction between Nitrogen and Sulfur in Co-Doped Graphene and Synergetic Effect in Supercapacitor, *Sci. Rep.*, 5 (2015), pp. 9591.
84. Z. Pan, H. Zhi, Y. Qiu, J. Yang, L. Xing, Q. Zhang, X. Ding, X. Wang, G. Xu, H. Yuan, M. Chen, W. Li, Y. Yao, N. Motta, M. Liu and Y. Zhang, Achieving commercial-level mass loading in ternary-doped holey graphene hydrogel electrodes for ultrahigh energy density supercapacitors, *Nano Energy*, 46 (2018), pp. 266-276.
85. M. S. Rahmanifar, H. Hesari, A. Noori, M. Y. Masoomi, A. Morsali and M. F. Mousavi, A dual Ni/Co-MOF-reduced graphene oxide nanocomposite as a high performance supercapacitor electrode material, *Electrochim. Acta*, 275 (2018), pp. 76-86.
86. P. C. Banerjee, D. E. Lobo, R. Middag, W. K. Ng, M. E. Shaibani and M. Majumder, Electrochemical Capacitance of Ni-Doped Metal Organic Framework and Reduced Graphene Oxide Composites: More than the Sum of Its Parts, *ACS Appl. Mat. Interfaces*, 7 (2015), pp. 3655-3664.
87. J. Yan, C. E. Ren, K. Maleski, C. B. Hatter, B. Anasori, P. Urbankowski, A. Sarycheva and Y. Gogotsi, Flexible MXene/Graphene Films for Ultrafast Supercapacitors with Outstanding Volumetric Capacitance, *Adv. Funct. Mater.*, 27 (2017), pp. 1701264.
88. P. Dutta, A. Sikdar, A. Majumdar, M. Borah, N. Padma, S. Ghosh and U. N. Maiti, Graphene aided gelation of MXene with oxidation protected surface for supercapacitor electrodes with excellent gravimetric performance, *Carbon*, 169 (2020), pp. 225-234.
89. H. B. Yang, J. Miao, S.-F. Hung, J. Chen, H. B. Tao, X. Wang, L. Zhang, R. Chen, J. Gao, H. M. Chen, L. Dai and B. Liu, Identification of catalytic sites for oxygen

reduction and oxygen evolution in N-doped graphene materials: Development of highly efficient metal-free bifunctional electrocatalyst, *Sci. Adv.*, 2 (2016), pp. e1501122.

90. G.-L. Chai, K. Qiu, M. Qiao, M.-M. Titirici, C. Shang and Z. Guo, Active sites engineering leads to exceptional ORR and OER bifunctionality in P,N Co-doped graphene frameworks, *Energy Environ. Sci.*, 10 (2017), pp. 1186-1195.
91. G.-L. Tian, M.-Q. Zhao, D. Yu, X.-Y. Kong, J.-Q. Huang, Q. Zhang and F. Wei, Nitrogen-Doped Graphene/Carbon Nanotube Hybrids: In Situ Formation on Bifunctional Catalysts and Their Superior Electrocatalytic Activity for Oxygen Evolution/Reduction Reaction, *Small*, 10 (2014), pp. 2251-2259.
92. T. V. Tam, S. G. Kang, M. H. Kim, S. G. Lee, S. H. Hur, J. S. Chung and W. M. Choi, Novel Graphene Hydrogel/B-Doped Graphene Quantum Dots Composites as Trifunctional Electrocatalysts for Zn−Air Batteries and Overall Water Splitting, *Adv. Energy Mater.*, 9 (2019), pp. 1900945.
93. Z. Liu, Z. Zhao, Y. Wang, S. Dou, D. Yan, D. Liu, Z. Xia and S. Wang, In Situ Exfoliated, Edge-Rich, Oxygen-Functionalized Graphene from Carbon Fibers for Oxygen Electrocatalysis, *Adv. Mater.*, 29 (2017), pp. 1606207.
94. X. Cui, P. Ren, D. Deng, J. Deng and X. Bao, Single layer graphene encapsulating non-precious metals as high-performance electrocatalysts for water oxidation, *Energy Environ. Sci.*, 9 (2016), pp. 123-129.
95. J. Guan, Z. Duan, F. Zhang, S. D. Kelly, R. Si, M. Dupuis, Q. Huang, J. Q. Chen, C. Tang and C. Li, Water oxidation on a mononuclear manganese heterogeneous catalyst, *Nat. Catal.*, 1 (2018), pp. 870-877.
96. S. Mao, Z. Wen, T. Huang, Y. Hou and J. Chen, High-performance bi-functional electrocatalysts of 3D crumpled graphene–cobalt oxide nanohybrids for oxygen reduction and evolution reactions, *Energy Environ. Sci.*, 7 (2014), pp. 609-616.
97. Y. Liang, Y. Li, H. Wang, J. Zhou, J. Wang, T. Regier and H. Dai, Co3O4 nanocrystals on graphene as a synergistic catalyst for oxygen reduction reaction, *Nat. Mater.*, 10 (2011), pp. 780-786.
98. C. Liu, H. Ma, M. Yuan, Z. Yu, J. Li, K. Shi, Z. Liang, Y. Yang, T. Zhu, G. Sun, H. Li and S. Ma, (NiFe)S2 nanoparticles grown on graphene as an efficient electrocatalyst for oxygen evolution reaction, *Electrochim. Acta*, 286 (2018), pp. 195-204.
99. Y. Fan, S. Ida, A. Staykov, T. Akbay, H. Hagiwara, J. Matsuda, K. Kaneko and T. Ishihara, Ni-Fe Nitride Nanoplates on Nitrogen-Doped Graphene as a Synergistic Catalyst for Reversible Oxygen Evolution Reaction and Rechargeable Zn-Air Battery, *Small*, 13 (2017), pp. 1700099.
100. L. Wu, L. Yu, X. Xiao, F. Zhang, S. Song, S. Chen and Z. Ren, Recent Advances in Self-Supported Layered Double Hydroxides for Oxygen Evolution Reaction, *Research*, 2020 (2020), pp. 3976278.
101. J. Shen, P. Zhang, R. Xie, L. Chen, M. Li, J. Li, B. Ji, Z. Hu, J. Li, L. Song, Y. Wu and X. Zhao, Controlled Self-Assembled NiFe Layered Double Hydroxides/Reduced Graphene Oxide Nanohybrids Based on the Solid-Phase Exfoliation Strategy as an Excellent Electrocatalyst for the Oxygen Evolution Reaction, *ACS Appl. Mat. Interfaces*, 11 (2019), pp. 13545-13556.
102. J. Ping, Y. Wang, Q. Lu, B. Chen, J. Chen, Y. Huang, Q. Ma, C. Tan, J. Yang, X. Cao, Z. Wang, J. Wu, Y. Ying and H. Zhang, Self-Assembly of Single-Layer CoAl-Layered Double Hydroxide Nanosheets on 3D Graphene Network Used as Highly Efficient Electrocatalyst for Oxygen Evolution Reaction, *Adv. Mater.*, 28 (2016), pp. 7640-7645.
103. L. Sun, M. G. Campbell and M. Dincă, Electrically Conductive Porous Metal–Organic Frameworks, *Angew. Chem. Int. Ed.*, 55 (2016), pp. 3566-3579.

104. M. Jahan, Z. Liu and K. P. Loh, A Graphene Oxide and Copper-Centered Metal Organic Framework Composite as a Tri-Functional Catalyst for HER, OER, and ORR, *Adv. Funct. Mater.*, 23 (2013), pp. 5363-5372.
105. A. Xie, J. Du, F. Tao, Y. Tao, Z. Xiong, S. Luo, X. Li and C. Yao, Three-dimensional graphene surface-mounted nickel-based metal organic framework for oxygen evolution reaction, *Electrochim. Acta*, 305 (2019), pp. 338-348.
106. J. Cao, C. Lei, J. Yang, X. Cheng, Z. Li, B. Yang, X. Zhang, L. Lei, Y. Hou and K. Ostrikov, An ultrathin cobalt-based zeolitic imidazolate framework nanosheet array with a strong synergistic effect towards the efficient oxygen evolution reaction, *J. Mater. Chem. A*, 6 (2018), pp. 18877-18883.
107. S. Giri, D. Ghosh and C. K. Das, Growth of Vertically Aligned Tunable Polyaniline on Graphene/ZrO2 Nanocomposites for Supercapacitor Energy-Storage Application, *Adv. Funct. Mater.*, 24 (2014), pp. 1312-1324.
108. Y. Liu, Y. Ma, S. Guang, H. Xu and X. Su, Facile fabrication of three-dimensional highly ordered structural polyaniline–graphene bulk hybrid materials for high performance supercapacitor electrodes, *J. Mater. Chem. A*, 2 (2014), pp. 813-823.
109. H. Wang, H. S. Casalongue, Y. Liang and H. Dai, Ni(OH)2 Nanoplates Grown on Graphene as Advanced Electrochemical Pseudocapacitor Materials, *J. Am. Chem. Soc.*, 132 (2010), pp. 7472-7477.
110. L. Hu, J. W. Choi, Y. Yang, S. Jeong, F. La Mantia, L.-F. Cui and Y. Cui, Highly conductive paper for energy-storage devices, *Proceedings of the National Academy of Sciences*, 106 (2009), pp. 21490.

Chapter 2

Scalable Fabrication of Graphene Polyaniline Hybrid Hydrogel for Customized Performance Supercapacitors

Chapter 2

Scalable Fabrication of Graphene Polyaniline Hybrid Hydrogel for Customized Performance Supercapacitors

Achieving high volumetric, areal energy densities with potential wearability are the primary requirements for an electrochemical supercapacitors to be used in portable/wearable devices. In this chapter, synthesis and electrochemical performance of a highly scalable graphene hydrogel hybridized with polyaniline (PANI) nanowires are presented. As developed hydrogel hybrids (PGH) exhibited a high areal capacitance of 853 mF cm^{-2} which is easily increasable up to 2.2 F cm^{-2} by customizing electrode architecture. Further, the compressed gel hybrids obtained via controlling the hydration level (< 35 wt%) results in excellent volumetric capacitance of 560 F cm^{-3}, while still retaining high areal and rate performances. Moreover, by directly integrating PGH with a carbon cloth, a wearable device was fabricated which exhibited excellent performance metrics. The high supercapacitive performance of our PGH hybrids is attributed to the porous graphene framework which provides continuous electron conduction pathways and facilitates ion transportation for the effective utilization of PANI nanowires.

2.1 Introduction:

The rapidly increasing demand for portable devices over the past few years has called the development of low cost, high performance compact energy storage devices. Graphene based supercapacitors whose charge storage mechanism is based on the electrical double layer capacitance (EDLC), remain at the front runners in this field due to their high gravimetric power (normalized by mass of the electrode) densities. [1-5] The main criteria for a practically meaningful portable device are that the electrode must be compact and should possess a high areal mass loading (> 5 mg cm^{-2}) so that the electrode could simultaneously achieve high areal and volumetric performance within the limited foot–print of the portable device. Unfortunately, graphene based supercapacitors so far, achieved high gravimetric performances with a very low level of areal mass loading (< 1 mg cm^{-2}) and/or loosely stacked graphene sheets, which usually favours rapid charge transportation kinetics and thereby results in high gravimetric charge storage properties. However, the high electrochemical performance shown by graphene supercapacitors with low mass loading often failed to maintain when the electrode mass loading is identically increased owing to the moderate electron transportation and increased ion diffusion resistance in these high mass loaded thick electrodes. Moreover, the compactness of

graphene electrode not only leads to the blockage of ion channels but also irreversible restacking or agglomeration of graphene sheets. These effects lead to the addition of "dead mass" to the electrode owing to the inaccessibility of active material by the electrolyte ions. This adverse effect is more prominent at large current densities where rapid charge and ion transportation is crucial for maintaining a good rate performance.

In this regard, development of graphene hydrogels hybridized with various pseudocapacitive materials has gained much interests, [6-9] where the graphene framework provides a conducting network with continuous ion channel pathways to ensure high rate performance. Moreover, the individual EDLC and faradaic contributions in the hybrids are synergistically coupled to improve the energy densities of the device. Nevertheless, the graphene hydrogel based hybrid pseudocapacitors are limited by following practical concerns: (i) easy processability: the existing gelation and hybridization strategies are energy and time consuming and often limited by large scalability [4, 5] and (ii) the macropores of the hydrogel are flooded with electrolytes and therefore are not suitable for compact electrodes. [10]

In this chapter, we present the development of highly scalable PANI nanowire and graphene hydrogel hybrid via a spontaneous co–assembly strategy at ambient combination. A facile electrolyte (1 M H_2SO_4) protected mechanical compression of the hybrid electrodes leads to the highly compact electrode with preserved ion channels. A supercapacitor device with a large areal mass loading up to 15 mg cm^{-2} were achieved via multi–stacking of hydrogel hybrid electrodes which exhibited a high areal capacitance of 2.2 F cm^{-2} at a current density of 1 mA cm^{-2} and stable rate performances. On the other hand, a high volumetric capacitance of 560 F cm^{-3} and excellent rate performance were obtained with electrolyte protected compressed hybrid hydrogels. Moreover, the versatility of as developed hybridization strategy was demonstrated by constructing a wearable device by directly developing PANI–gel hybrid over a carbon cloth.

2.2 Experimental section:

2.2.1 Preparation of graphene oxide (GO) dispersion:

GO was synthesized according to Hummers' method with slight modifications. [11] In brief, 1.5 g of graphite powder (sigma) was added into 70 mL concentrated sulfuric acid (H_2SO_4) and the resultant mixture was cooled to 0℃. Subsequently, 4.5 g of potassium permanganate ($KMnO_4$) powder was added to the mixture very slowly under stirring while maintaining the temperature of the system below 20℃. After adding $KMnO_4$, the system was put in a water

bath of temperature 35℃. After stirring for 3 hours at 35℃ a thick paste was formed. Subsequently, the hot water bath was replaced by a room temperature water bath and a total of 400 mL water was added very cautiously (to avoid any vigorous exothermic reaction). This process turned the green coloured material into a dark brown dispersion. The reaction was stopped by adding 5–10 mL of 30% hydrogen peroxide (H_2O_2) solution, which turned the colour of the solution to bright yellow. The resultant dispersion was then washed repeatedly, first with 10% hydrochloric acid (HCl) solution and then with deionized (DI) water via centrifugation. The resulting brown dispersion was further diluted by adding more DI water, sonicated for 1 hour for the exfoliation of graphite oxide into graphene oxide (GO) and dialysed for 1 week in order to remove acid and other impurities. The as–obtained GO dispersion was stored in a cool and dark place for further usage.

2.2.2 Synthesis of PANI nanowire dispersion:

Uniform PANI nanowires were synthesized by oil–in–water interfacial polymerization method. [12] In this interfacial polymerization strategy, ammonium persulfate (APS) (0.8 mmol) dissolved in 10 mL 1M HCl aqueous solution was placed on the top of organic phase contained 3.2 mmol aniline dissolved in 10 mL of chloroform. After an overnight reaction the as formed PANI nanowires at the interface were collected and thoroughly washed several times with ethanol and water. A stock solution is prepared via dispersing nanowires in water with a concentration of 12 mg mL^{-1} for further use.

2.2.3 Preparation of PGH by co–assembly:

PGH gels were prepared via spontaneous interfacial co–assembly of GO and PANI nanowires over zinc plate, and subsequent reduction of GO to form reduced graphene oxide (rGO) based hydrogel network. [13] Before assembly, a homogeneous mixed suspension of GO and PANI was prepared by mixing aqueous solution of GO and appropriate volume of PANI stock solution, followed by sonication for 10 min (Table 2.1). Subsequently a polished zinc foil was immersed into the GO–PANI suspension for the co–assembly and the simultaneous reduction of GO into PGH film. After a gelation of 3 hours, a freestanding PGH film was obtained by etching away zinc foil using 8 M KOH solution. The hydrogel was then washed several times with water to remove KOH. Different weight ratio of GO and PANI were synthesized by taking different concentration and volume of PANI and GO as tabulated below. In all the samples the concentration of GO was fixed to 3 mg mL^{-1}. For comparison pure GH was prepared following the same protocol using a GO solution of 3 mg mL^{-1}.

Table 2.1. Synthesis condition for different samples

Sample name	GO amount	PANI amount
GH	40 mL, 3 mg mL^{-1}	–
$PGH_{1:3}$	30 mL, 4 mg mL^{-1}	10 mL, 4 mg mL^{-1}
$PGH_{1:1}$	30 mL, 4 mg mL^{-1}	10 mL, 12 mg mL^{-1}
$PGH_{3:2}$	10 mL, 12 mg mL^{-1}	30 mL, 6 mg mL^{-1}

2.2.4 Material characterization:

The morphological and structural properties of the samples were characterized by FESEM (Zeiss, Sigma 300), FETEM (Jeol), X–ray diffractometer (Rigaku), Fourier transform infra–red spectrometer (FTIR, Perkin Elmer BX) and Raman spectroscopy (Horiba, LabRam HR).

2.2.5 Electrochemical characterizations:

The electrochemical performance of all the PGH samples were measured in a two electrode cell. To assemble the supercapacitor cell two freestanding PGH hydrogels (area 1 × 1 cm^2) are sandwiched between two Pt foils. A commercial separator (Celgurd 3400) soaked in 1 M H_2SO_4 (as electrolyte) was used as separator. The choice of current collector is based on the criteria that it must have high conductivity, low contact resistance and excellent stability in electrolyte. The noble metal based foils e.g. Pt foil, Au foil etc. are the best choices for current collectors in acidic electrolyte solution considering their low corrosion and low contact resistance. Therefore, in our work we have used Pt foil as a current collector. For the solid state assembly, PVA/H_2SO_4 hydrogel was used as electrolyte and separator. The gel electrolyte was prepared by adding 2 g PVA and 2 g H_2SO_4 in 20 mL water and heating the same at 85 ℃ under constant stirring until a clear solution is formed. Two $PGH_{3:2}$@CC strips (area 3 × 1.5 cm^2) were uniformly coated with the gel electrolyte and dried overnight before assembled into a solid state supercapacitor. For the measurement of volumetric capacitance, $PGH_{3:2}$ films were pressed with pressures 25 MPa and 100 MPa using a hydraulic press. Before pressing the $PGH_{3:2}$ films were saturated with 1 M H_2SO_4. Thickness of the pressed $PGH_{3:2}$ gels measured from FESEM images were found to be 39 µm (for P_a = 25 MPa) and 13 µm (for P_a = 100 MPa). All the electrochemical tests were performed in PARSTAT 3000A–DX (Princeton Applied Research) electrochemical workstation. The cyclic voltammetry (CV) measurements were done at scan rates ranging from 5 mV s^{-1} to 50 mV s^{-1} under a potential window of 0 V to 0.8 V. cyclic charge–discharge (CC) tests were carried out at current densities from 1 mA cm^{-2} to

30 mA cm^{-2} in a potential range of 0 V to 0.8 V. The impedance analysis was done at a potential of amplitude 10 mV in the frequency range of 0.01 Hz to 100 kHz.

2.3 Results and discussions:

The graphene PANI hydrogel hybrid (PGH) was developed via a simple, ambient temperature interfacial gelation and co–assembly process [13] (Experimental section). Briefly, a zinc foil was directly dipped into a premixed graphene oxide (GO) and PANI nanowire aqueous dispersion. The spontaneous layer–by–layer co–assembly of GO and PANI nanowires over the zinc foil and the simultaneous reduction of GO into reduced GO (RGO) results in the formation of graphene–PANI hydrogel–hybrid as shown schematically in Figure 2.1.a. To measure the water content of the hybrid hydrogel, an aerogel was made by dehydrating the same hydrogel and their weights were compared. The water content of the hydrogel was found to be 96% of its weight. The excellent processability of the hybridization strategy was realized by developing a hydrogel hybrid with a dimension of ~ 30 cm × 12 cm (Figure 2.1.b).

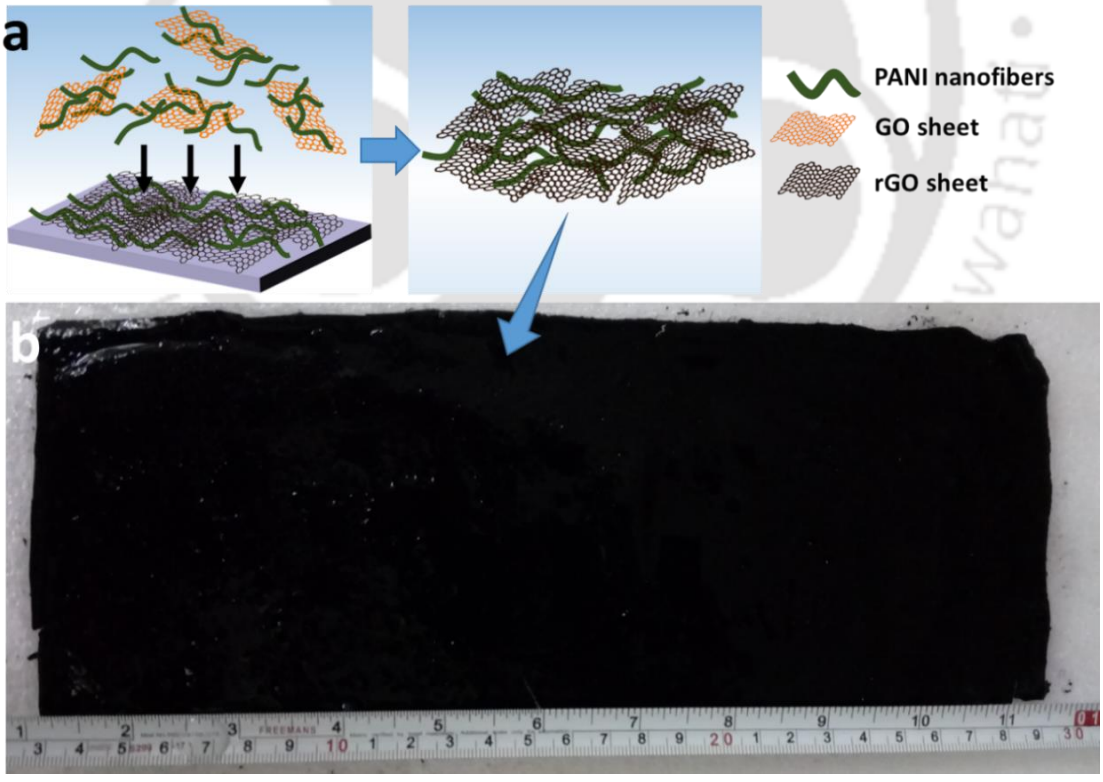

Figure 2.1. (a) Schematic illustration of synthesis of PGH by co–assembly process; (b) a large hydrogel of PGH (~30 cm × 12 cm).

Further, the PANI content of the hybrids was tuned by simply varying its content in the premixed dispersion. The as obtained samples with PANI:GO weight ratios 3:2, 1:1 and 1:3 are denoted as $PGH_{3:2}$, $PGH_{1:1}$ and $PGH_{1:3}$ respectively. For comparison, bare graphene hydrogel (GH) without PANI nanowires was also developed following the same procedure. The thickness of the PGHs increased significantly with increasing PANI loading (Figure 2.2) indicating incorporation of PANI nanowires in graphene framework.

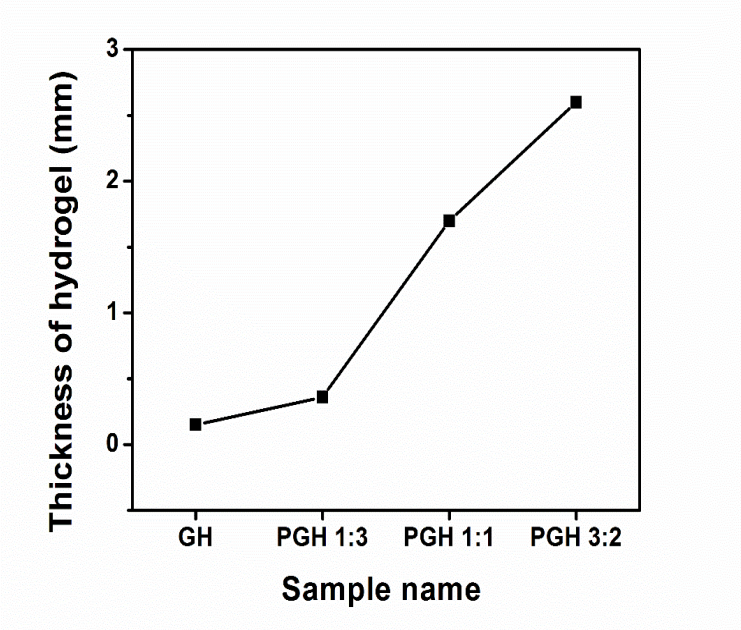

Figure 2.2. Variation of the thickness of the hydrogel with different PGH hybrids (corresponding to different PANI loading).

2.3.1 Structural analyses:

The structural features of the as developed PGH hybrids were characterised with X–ray diffraction (XRD), Raman spectroscopy and Fourier transformed infrared spectroscopy (FTIR). First the XRD pattern of GO shows a strong peak at $2\theta = 10°$ which after reduction and forming GH, exhibits a broad peak at ~ 25° (Figure 2.3) corresponding to the (002) crystal plane of graphite. [5] This indicates a successful reduction of GO into RGO in GH framework. The XRD pattern of PANI nanowire exhibits three broad peaks at 15.8°, 20.4° and 25.3° corresponding to the (011), (020) and (200) planes of emeraldine phase of PANI nanostructure. [14] Interestingly, PGH hybrid does not exhibit any characteristic peak of PANI (Figure 2.3) which is expected because of the presence of low crystalline form of emeraldine phase of PANI. [15]

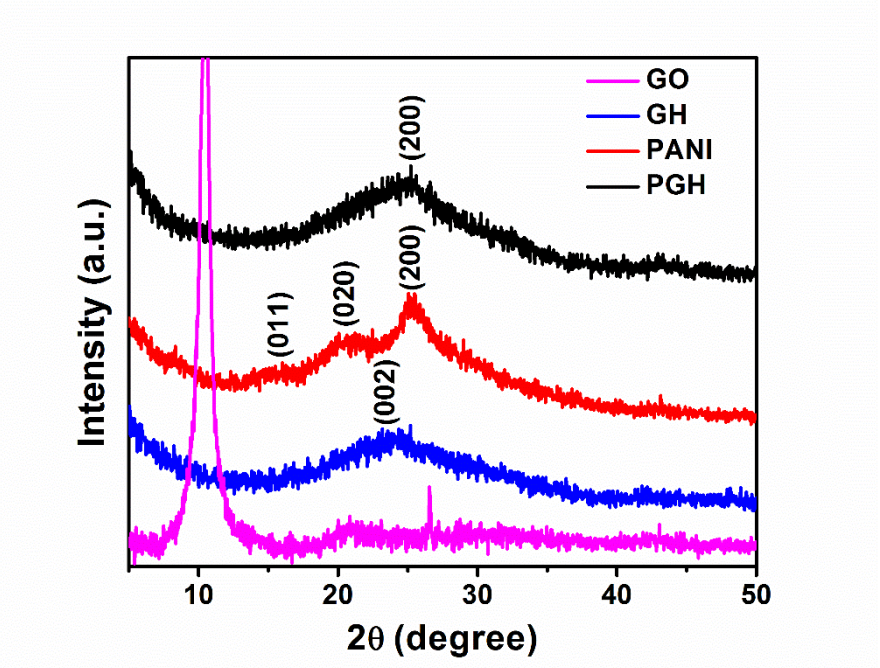

Figure 2.3. XRD patterns corresponding to the samples GO, GH, PANI and PGH.

The Raman spectrum of PANI nanowires (Figure 2.4.a) shows various broad peaks at 1329 cm^{-1}, 1427cm^{-1} and 1592 cm^{-1} corresponding to the C–N^{+} stretching of semiquinoid radical, C=N stretching and the C=C stretching of benzenoid ring respectively. [16, 17] The Raman spectrum of PGH consists of characteristic G band at 1583 cm^{-1} and D band at 1322 cm^{-1} (Figure 2.4.a) which are respectively assign to the in–plane C=C stretching mode and the presence of defects in graphene. A comparison of Raman spectra of GO and PGH further reveals that, the ratio of D and G band intensities (I_D/I_G) increases from 1.15 for GO to 1.56 in RGO of PGH which is attributed to the increased number of sp^2 domains after the reduction. [18, 19] Once again the PGH does not contain any characteristic Raman peaks of PANI (Figure 2.4.a) which is attribute to the presence of high intensity D and G peaks of graphene which superimpose over PANI peaks.

To actually confirm the formation of graphene PANI hybrids in PGH, FTIR spectroscopy studies were carried out (Figure 2.4.b). It is observed from figure that GO possesses peaks at 3400 cm^{-1} and 1722 cm^{-1} corresponding to the O–H and C=O bonds of –COOH group, while the peaks at 1624 cm^{-1} and 1426–1104 cm^{-1} correspond to the vibrations of C–O in C–OH/C–O–C functionalities of GO sheets. [20, 21] After reduction, GH possesses significantly diminished peaks, revealing removal of functional groups of GO upon reduction. A small peak around 1590 cm^{-1} in the FTIR spectrum of GH represent the C=C bonding

graphene. The FTIR spectrum of PGH hybrid contains several peaks at 1578 cm^{-1}, 1489 cm^{-1}, 1307 cm^{-1}, 1150 cm^{-1} which are assigned to the C=C vibration of quinoid ring, C=C stretching of benzene ring, C–N stretching and C–H bending of quinoid ring respectively suggesting the presence of emeraldine phase of PANI and thereby successful formation of hybrid structure of PANI and graphene.

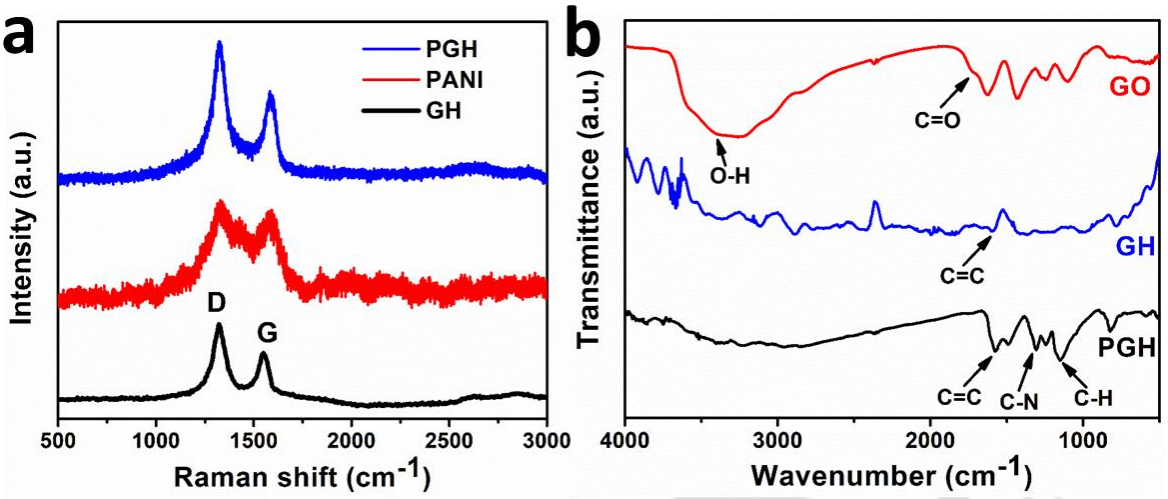

Figure 2.4. Structural characterization: (a) Raman spectra of PGH, PANI and GH; (b) FTIR spectra of GO, GH and PGH.

2.3.2 Morphological study:

The morphological characterization of as synthesized samples, field emission scanning electron microscope (FESEM) and field emission transmission electron microscope (FETEM) were used. The cross–sectional FESEM image of freeze dried GH (Figure 2.5.a) exhibits an open porous architecture where graphene sheets are interconnected to form a network structure. The FESEM image of PANI nanowires reveal that PANI has an average diameter of 50 nm with their lengths varying within the range of 100 nm–500 nm (Figure 2.5.b). Interestingly in the hybrid structure, PGH not only displays porous morphology like GH but the PANI nanowires remain uniformly wrapped within the graphene sheets (Figure 2.5.c). FETEM image further confirms the uniform distribution and wrapping of PANI nanowires (Figure 2.5.d). Such uniform distribution with intimate contact of graphene and PANI is beneficial for improved electron and ion transfer. The PGH hybrid consisting of conducting RGO sheets and PANI nanowires having uniform porous framework structure is ideal for high performance supercapacitor electrodes.

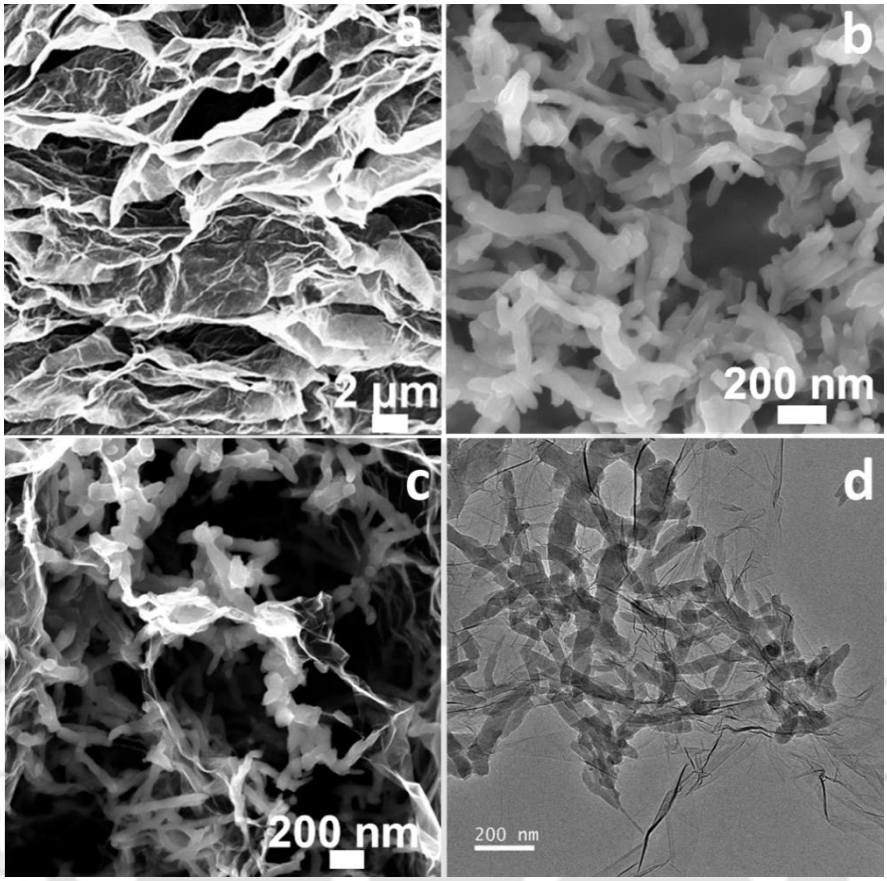

Figure 2.5. (a) Cross–sectional FESEM image of GH; (b) FESEM image of PANI nanofibers; (c) cross–sectional FESEM image and (d) FETEM image of PGH hybrid.

2.3.3 Electrochemical performances:

To study the charge storage performance of the GH and PGH hybrids electrochemical characterizations were performed by directly assembling two pieces of hydrogels in symmetric two–electrode configuration (Details in experimental section). The charge storage behaviour of various samples was first analysed by cyclic voltammetry (CV) profiles (Figure 2.6). The CV curves of bare GH exhibit a quasi–rectangular profiles (Figure 2.6.a) which demonstrate that the charge storage mechanism is predominantly of EDLC type. [3, 13] The CV profiles of as developed PGH hybrids (Figure 2.6.b) with varying PANI content exhibit superposition of redox peaks with rectangular profiles. A couple of prominent redox peaks within the potential range of 0.2–0.6 V in the CV profiles of PGH hybrids is attributed to the reversible redox

transition of leukoemeraldine and emeraldine phases of PANI nanostructure. [10] A comparison of the CV profiles of GH and other PGH samples reveal that (Figure 2.6.b), the area under the CV curve of GH is significantly increased after hybridization with PANI nanowires, suggesting an enhancement in the charge storage characteristics in the hybrid samples compared to the bare GH. The CV profiles of $PGH_{3:2}$ sample at higher scan rates (5 mV s^{-1} to 50 mV s^{-1}) do not exhibit any peak shift or distortions of the profile indicating a fast and reversible redox reaction (Figure 2.7.a). The peak current densities from CV profiles are further found to be increased linearly with the scan rates, implying a good rate performance of the electrode material (Figure 2.7.b).

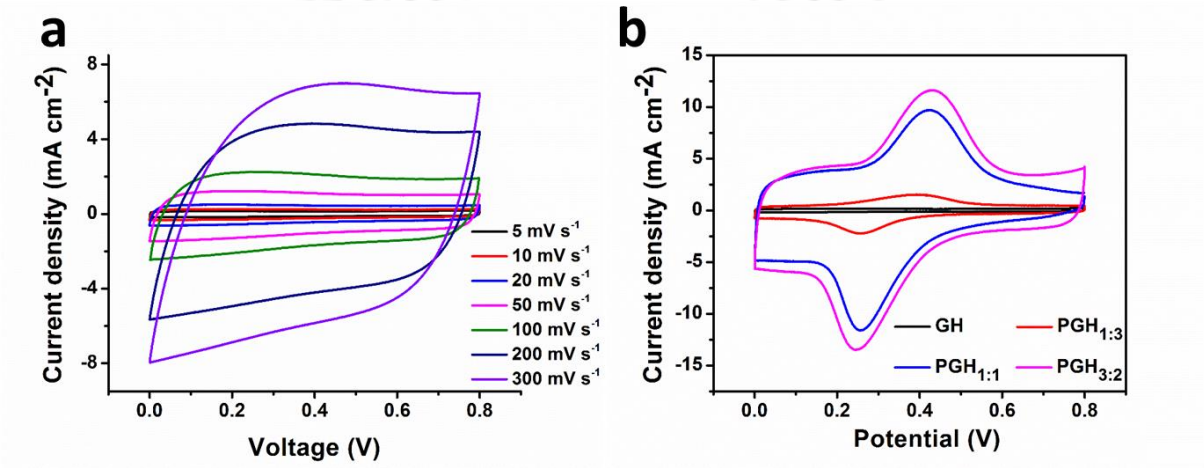

Figure 2.6. Electrochemical characterization: (a) Cyclic voltammetry (CV) curves of GH at different scan rates; (b) comparison of CV profiles of GH and various PGH hybrids at a scan rate of 5 mV s^{-1}.

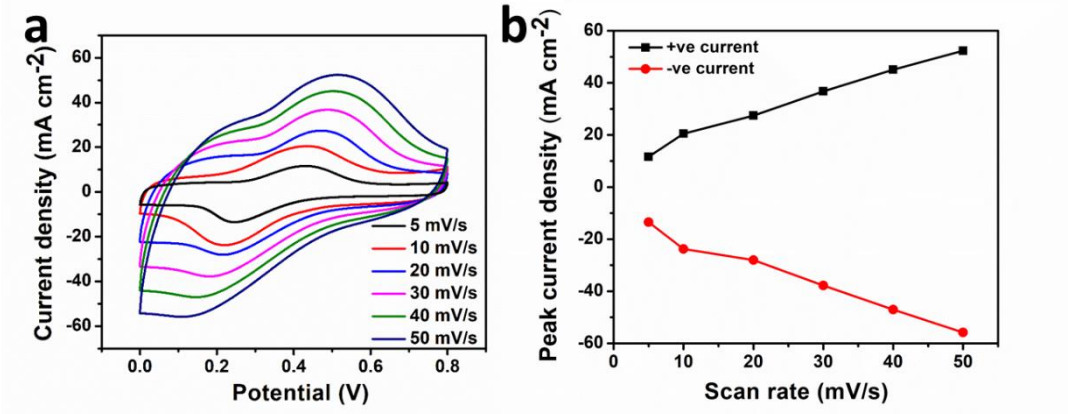

Figure 2.7. Electrochemical performances of $PGH_{3:2}$: (a) CV curves at different scan rates and (b) variation of peak current densities with scan rate.

The charge storage behaviour of the samples were further analysed by galvanostatic charge–discharge profiles (GCD). The GCD profiles of GH (Figure 2.8.a) show a symmetric quasi–triangular shape, further confirming the EDLC behaviour of carbon based materials. A significant deviation from the triangular GCD profile of GH is observed for PGH samples (Figure 2.8.b) which is attributed to the faradaic reaction of PANI nanowires. The areal

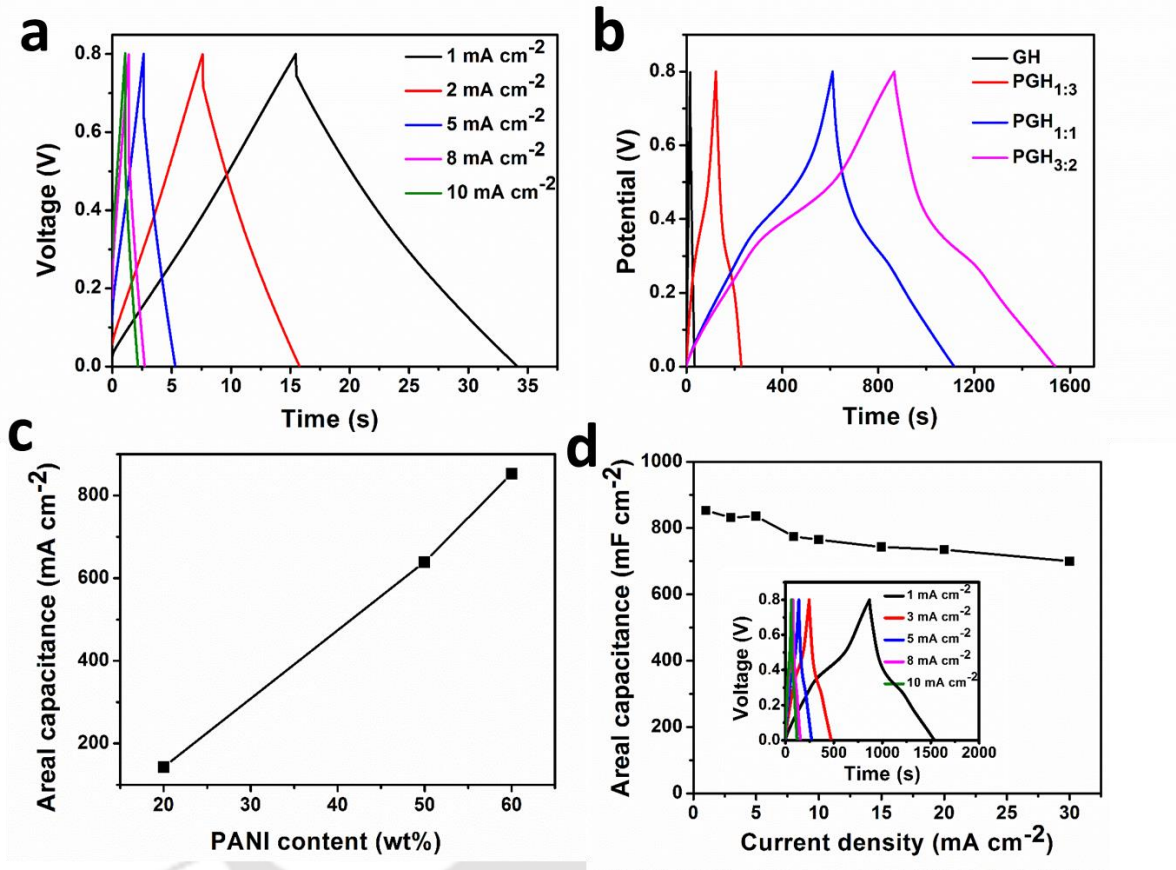

Figure 2.8. Electrochemical characterization: (a) galvanostatic charge–discharge (GCD) profile of GH at different scan rates; (b) comparison of GCD profiles for GH and other PGH hybrids at 1 mA cm^{-2}; (c) variation of areal capacitance of $PGH_{3:2}$ with scan rates (inset shows the GCD profiels of $PGH_{3:2}$ at different scan rates) and (d) areal capacitance as a function of PANI loading of the PGH hybrids.

capacitance of the samples was calculated from the GCD curves (Figure 2.8.b). A large areal capacitance of 853 mF cm^{-2} at a current density of 1 mA cm^{-2} was obtained for $PGH_{3:2}$ (with highest PANI loading of 60 wt%) and the areal capacitance was found to increase linearly with the increasing PANI loading (Figure 2.8.c). More importantly, the $PGH_{3:2}$ still retains the high areal capacitance up to 82% when the charge–discharge rate was increased from 1 mA cm^{-2} to

30 mA cm^{-2} (Figure 2.8.d) demonstrating its excellent rate performance. In contrast, bare GH shows a capacitance of only 25 mF cm^{-2} at the current density of 1 mA cm^{-2}. This result suggest that, the high performance of the PGH hybrid is mainly dominated by the pseudocapacitance of PANI nanowires. In addition, $PGH_{3:2}$ shows a long term stability retaining > 95% after 5000 continuous charge–discharge cycles at a large current density of 10 mA cm^{-2} (Figure 2.9.a). Furthermore, the Coulombic efficiency (defined by the ratio of discharging time to the charging time of a supercapacitor at a constant current) of $PGH_{3:2}$ was found to increase with the current densities and stabilize at 98% representing excellent reversibility of the redox reaction offered by PANI nanostructures (Figure 2.9.b).

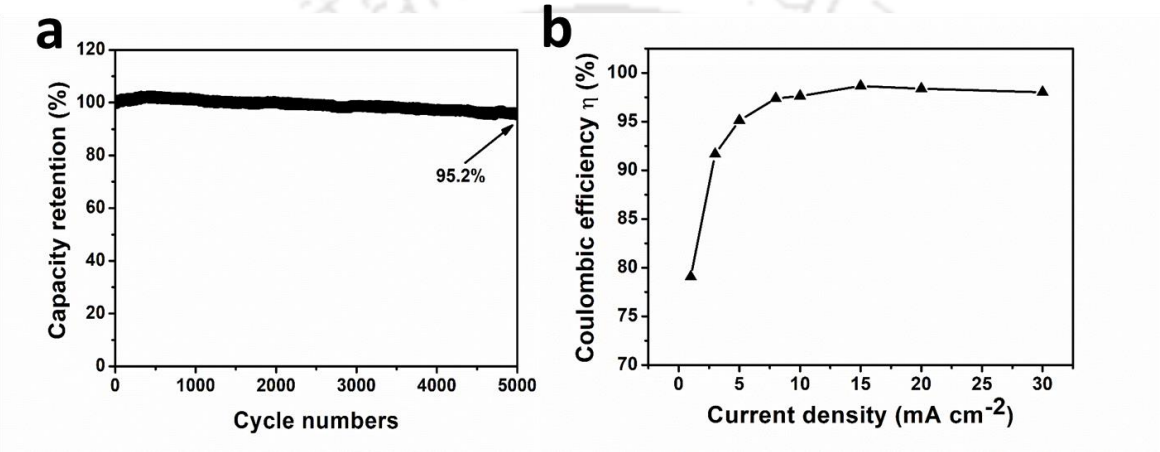

Figure 2.9. (a) Cycling stability of $PGH_{3:2}$ at a current density of 20 mA cm^{-2} and (b) Coulombic efficiency of $PGH_{3:2}$ at various current densities.

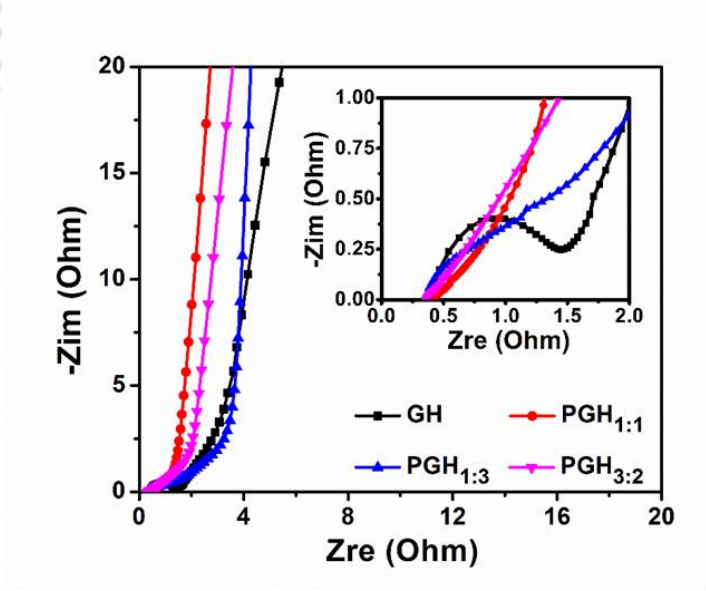

Figure 2.10. Nyquist plot of GH and various other PGH hybrids. The inset shows the zoomed view of the high frequency region.

To understand the origin of high charge storage properties of the hybrid samples, electrochemical impedance spectroscopy (EIS) analysis was studied. The Nyquist plot (plot of imaginary impedance vs real impedance) (Figure 2.10) reveals that at low frequencies all the samples exhibit quasi–vertical lines parallel to the imaginary impedance axis representing capacitive behaviour. While at high frequencies a slight deviation of the vertical lines (45° line) are associated with the very low diffusion resistance. The low diffusion resistant observed for PGH samples can be attributed to the fast electrolyte ion transportation through the porous structure of the hydrogel framework. Further the equivalent series resistances (ESR) and the charge transfer resistances (R_{ct}) of the PGH samples as estimated from the Nyquist plots, are found to be very low (Table 2.2) (inset of Figure 2.10), indicating the low electrical and ionic resistances of the hydrogel hybrids. [16, 20]

Table 2.2. Comparison of various resistances of samples calculated from Nyquist plots.

Samples	R_{sol} (Ω)	R_{ct} (Ω)	R_{ESR} (Ω)
GH	0.40	1.1	1.5
$PGH_{3:2}$	0.36	–	0.36
$PGH_{1:1}$	0.43	–	0.43
$PGH_{1:3}$	0.36	0.639	1

After successfully preparing PGH electrode with high areal capacitance at a mass loading of 5.1 mg cm^{-2} ($PGH_{3:2}$), we examined whether we could linearly increase the areal capacitance by directly increasing the mass loading of the electrode without deteriorating the high rate performance. To realize this we first increase the areal loading of $PGH_{3:2}$ in steps through multiple stacking of hydrogel hybrids and directly use it as electrode material. In this way electrode loading up to 15.3 mg cm^{-2} was achieved by stacking three hydrogel hybrids. Interestingly, CV profiles of stacked electrodes (Figure 2.11.a) do not show any noticeable deformation. The areal capacitances of these stacked electrodes were measured from the GCD curves (Figure 2.11.b) and it was found that the areal capacitances have a near linear relationship with the increasing mass loading (Figure 2.11.c). The highest areal capacitance value was obtained with a mass loading of 15.3 mg cm^{-2} and at a current density of 1 mA cm^{-2} it was found to be as high as 2.2 F cm^{-2}. Moreover, all these stacked electrodes exhibit excellent rate performances at high charge–discharge current densities as observed from the

inset of Figure 2.11.c. Interestingly, a slight increment of the ESR value from 0.36 Ω to 0.95 Ω was noticed in the Nyquist plot (Figure 2.11.d) when the mass loading was increased by threefold (15.3 mg cm^{-2}).

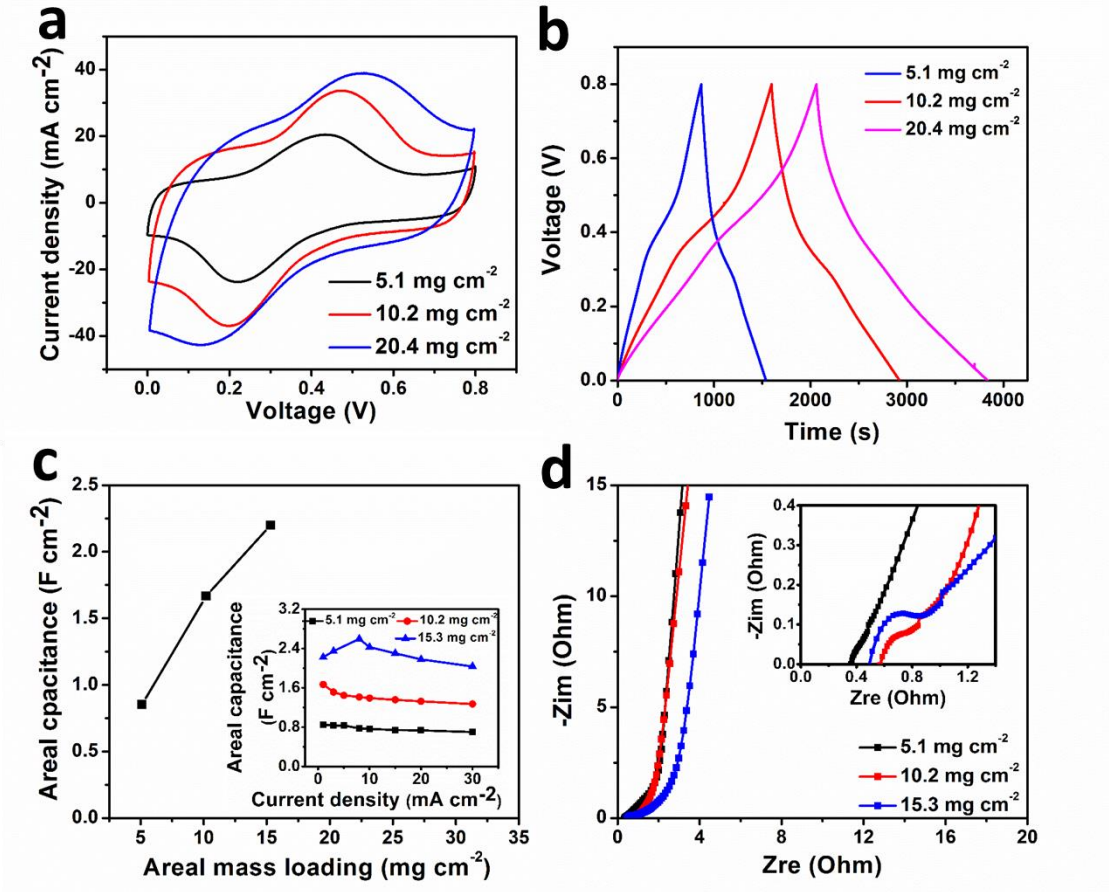

Figure 2.11. Electrochemical characterization of high mass–loaded PGH electrodes: (a) CV profiles, (b) GCD curves, (c) variation of areal capacitance (the inset shows the areal capacitance as a function of discharge current density) and (d) Nyquist plot of PGH electrode with varying areal loading of the electrode (the inset shows the magnified view of the high frequency region).

The excellent areal capacitance values with high rate performances are associated with the high conductivity and the low ionic resistance of the stacked hybrid electrodes. The low electrical resistances of the PGH hybrids are originating from the presence of highly conductive graphene backbone and its additive/ binder free continuous interconnected network structure which promotes rapid electron transfer. Moreover, the direct contact of graphene with PANI nanowires facilitates interfacial charge transfer process. The continuous interconnected conducting graphene framework also ensures continuous electron transfer pathways even in

the multi–stacked electrode. On the other hand, the low ionic resistances of PGH hybrids result from the facile electrolyte ion diffusion process within the bulk of the electrode materials due to the open porous structure of the electrode. This process further favours effective utilization of pseudocapacitive PANI nanowires by the electrolyte ions and thereby forms a good electrolyte/electrode interface. [21] More importantly, porous structure of the electrodes further allow facile ion diffusion through the junction of the stacked electrode. As a result of the synergistic effect of conducting and porous architecture, the PGH electrodes exhibit remarkable areal charge storage properties.

Besides high areal capacitance, achieving high volumetric capacitance is also very important for portable miniaturized electronics. To achieve high volumetric performance with $PGH_{3:2}$ hybrid, the hydrogel was first saturated with electrolyte (1 M H_2SO_4) and then subjected to simple mechanical compression. As a result, the hydrogel gets compressed with a controlled level of hydration. Two different pressures of 2.5 MPa (P1) and 10 MPa (P2) were applied and the compressed samples with a water content of 46 wt% and 33 wt% were named as $PGH_{3:2}$–P1 and $PGH_{3:2}$–P2 respectively. To establish the importance of keeping the hydrogel structure in achieving high volumetric performance, a vacuum dried aerogel sample was prepared and its charge storage behaviour was compared. The cross–sectional FESEM images of all the compressed samples ($PGH_{3:2}$–P1, $PGH_{3:2}$–P2 and dry aerogel) exhibit very compact structure in comparison to the original hybrid (Figure 2.12.a–c). The thickness of the $PGH_{3:2}$–P1 and $PGH_{3:2}$–P2 were measured from the cross–sectional FESEM images and they are found to be 39 micron and 13 micron respectively (2.6 mm thickness before compression).

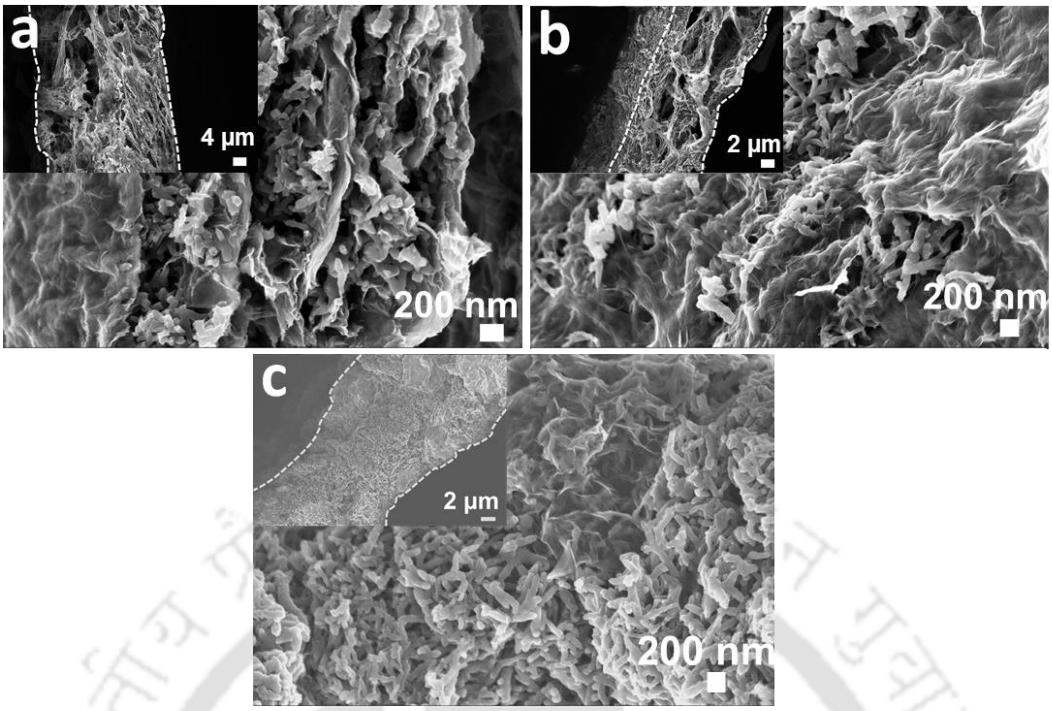

Figure 2.12. High magnification cross–sectional FESEM images of (a) $PGH_{3:2}$–P1, (b) $PGH_{3:2}$–P2 and (c) dried PGH gel (insets show corresponding low magnification FESEM images).

A comparison of CV profiles (Figure 2.13.a) readily shows that, the CV profiles of compressed samples exhibit prominent redox peaks due to the faradaic reaction of PANI nanowires whereas, the CV profile is found to be distorted in case of dried hybrid. The CV results therefore clearly indicate that, in dried hybrid aerogel the redox activity of PANI is limited by the inaccessibility of electrolyte ions owing to the constricted dry channels whereas, the electrolyte protected hydrated nano–channels present in the $PGH_{3:2}$–P1 and $PGH_{3:2}$–P2 are highly effective to maintain a good charge storage behaviour. The volumetric capacitances of various samples were calculated from GCD curves (Figure 2.13.b) and was found that $PGH_{3:2}$–P2 possessed the highest capacitance of 560 F cm^{-3} at a current density of 1 mA cm^{-2}. The importance of hydrated nano–channels in the compressed hybrids is further reflected from their rate performances at high current densities (Figure 2.13.c). It is observed that, compressed samples maintain an excellent rate performance even at large current densities (up to 20 mA cm^{-2}) with a capacity retention of 75% and 81.3% for $PGH_{3:2}$–P1 and $PGH_{3:2}$–P2 respectively. In contrast, the capacitance of dried hybrid aerogel rapidly fades with increasing current densities (only 17 % retention at 20 mA cm^{-2}).

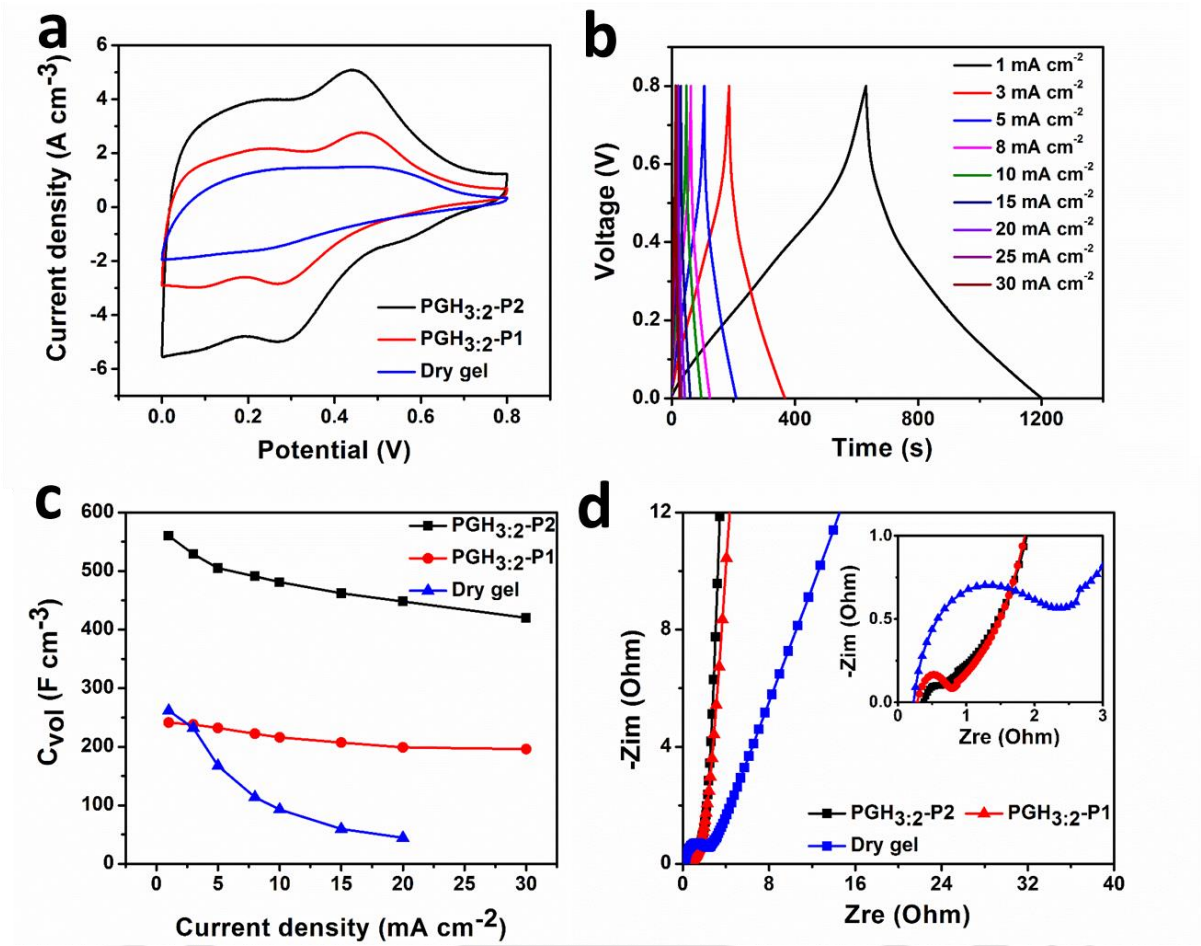

Figure 2.13. Volumetric electrochemical characterization: (a) comparison of CV profiles of $PGH_{3:2}$–P1, $PGH_{3:2}$–P2 and dried PGH gel; (b) GCD curves of $PGH_{3:2}$–P2 at different current densities; (c) variation of volumetric capacitance with current densities and (d) comparison of Nyquist plots of $PGH_{3:2}$–P1, $PGH_{3:2}$–P2 and dried PGH gel. The inset of (d) shows the magnified view of the high frequency region.

The mass transport kinetics of the electrode was further examined by the EIS analysis. The quasi–vertical lines shown by the compressed hydrogel hybrids in the low frequency regime of the Nyquist plot (Figure 2.13.d) suggest good capacitive behaviour. Further, at high frequency region, the plots show a small semi–circle and a short 45° transition line indicating low diffusion resistance. In comparison, a significantly increased diffusion resistance is observed for dried aerogel as is evident from the slanting line in the Nyquist plot. without any water content. These results imply that, the preserved hydration level in the compressed samples can effectively maintain the nano–channels in the material sufficient for the electrolyte ions to diffuse. On the other hand, constricted dry pores of the dried aerogel limits the ion

Table 2.3. Comparison of electrochemical performances of various PANI–graphene/carbon based supercapacitors

Electrode material	**Preparation method**	**Mass loading (mg cm^{-2})**	**Configuration**	**Areal capacitance (mF cm^{-2})**	**Volumetric capacitance (F cm^{-3})**	**Ref**
PANI on rGO paper	Electro–polymerization	5.8	Three electrode, 1 M H_2SO_4	1404, 2 mV s^{-1}	135, 2 mV s^{-1}	[8]
PANI@OGH film	Chemical polymerization	1.06	Two electrode, 1 M H_2SO_4	562, 10.6 mA cm^{-2}	–	[22]
PANI@ Carboxyl–functionalized GO	Chemical polymerization	3	Three electrode, 1 M H_2SO_4	1575, 0.9 mA cm^{-2}	–	[23]
3D porous graphene/ PANI	Inkjet printing	0.22	Three electrode, 1 M H_2SO_4	190.6, 0.5 mA cm^{-2}	–	[24]
3D PANI@ pillared graphene sheets	in situ polymerization	3	Two electrode, 0.5 M H_2SO_4	1520, 3 mA cm^{-2}	122, 3 mA cm^{-2}	[25]
rGO foam/PANI	in situ polymerization	0.65	Two electrode, 1 M H_2SO_4	513.5, 0.65 mA cm^{-2}	205.4, 0.65 mA cm^{-2}	[26]
PANI/ graphene hydrogel	Chemical polymerization	*0.714	Two electrode, 0.4 M hydroquinone in 1 M H_2SO_4	414.5, 0.29 mA cm^{-2}	592.96, 0.29 mA cm^{-2}	[27]
PANI nanofiber/graphene foam	Electro–deposition	3	Three electrode, 1 M H_2SO_4	4300, 1.4 mA cm^{-2}	86, 1.4 mA cm^{-2}	[28]
Graphene-PANI Compact Films	layer–by–layer vacuum filtration	–	Two electrode, 1 M H_2SO_4	368, 10 mV s^{-1}	736, 10 mV s^{-1}	[29]
PANI/CCG	in situ polymerization	0.97	Two electrode, 1 M H_2SO_4	*436.5, 4.85 mA cm^{-2}	572, 4.85 mA cm^{-2}	[10]
N–doped holey graphene/PANI slice	Chemical polymerization	*0.725	Three electrode, 1 M H_2SO_4	*529, 0.36 mA cm^{-2}	1058, 0.36 mA cm^{-2}	[30]
PANI/N–doped CNT	Electro–deposition	0.416	Three electrode, 1 M H_2SO_4	151, 1.56 mA cm^{-2}	216.6, 1.56 mA cm^{-2}	[31]

PANI@graphene nanoribbon	Chemical polymerization	3.5	Three electrode, 1 M H_2SO_4	*1190, 0.875 mA cm^{-2}	–	[32]
PANI/SWCNT	Chemical polymerization	0.78	Three electrode, 1 M H_2SO_4	330, 0.2 mA cm^{-2}	40.5, 0.2 mA cm^{-2}	[33]
PANI–rGO hydrogel ($PGH_{3:2}$)	**Co–assembly gelation**	**5.1**	**Two electrode, 1 M H_2SO_4**	**842, 1 mA cm^{-2}**	**560, 1 mA cm^{-2}**	**This work**

[a] calculated based on the data provided in the report.

diffusion in the electrode which significantly increase the diffusion resistance as observed in the Nyquist plot. The excellent performance of the compressed hydrogel hybrids is further reflected from the Ragone plot (the relationship between energy and power density) (Figure 2.14). Although supercapacitors are known for their high power densities rather than delivering high energy density, interestingly, $PGH_{3:2}$–P2 delivered a maximum volumetric energy density of 49 Wh L^{-1} at a high power density of 60 kW L^{-1}. Further, the maximum power density of 68 kW L^{-1} was obtained with a still high energy density of 39 Wh L^{-1}. In contrast, the power and energy densities of dried aerogel decays pretty quickly with increasing current density. The areal and volumetric capacitances of $PGH_{3:2}$ hybrid is compared with the other reported values of PANI/graphene based supercapacitors in Table 2.3.

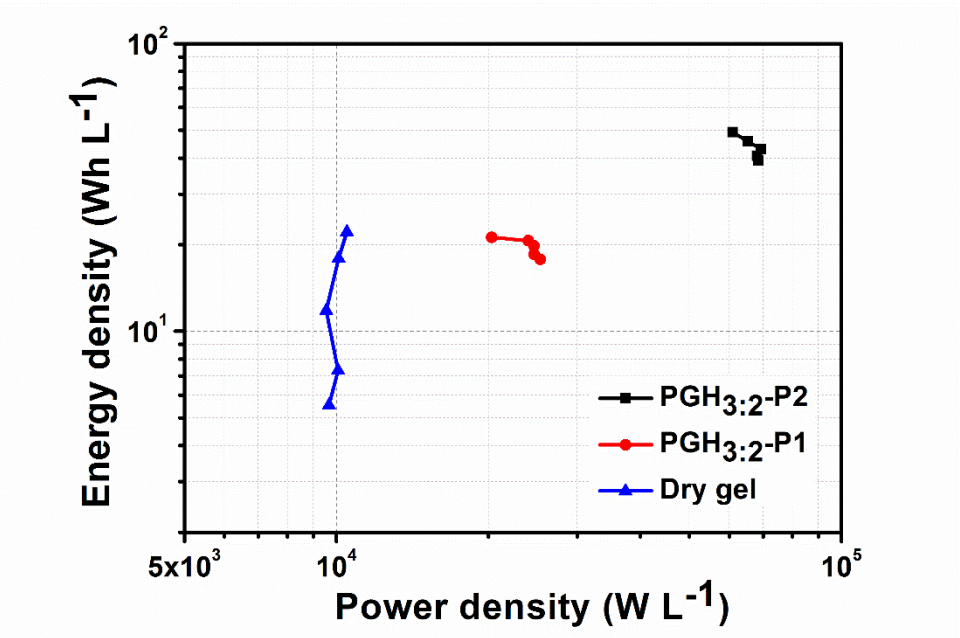

Figure 2.14. Ragone plot of $PGH_{3:2}$–P1, $PGH_{3:2}$–P2 and dried PGH gel

To potential versatility of as developed hydrogel hybrids were further demonstrated by directly assembling $PGH_{3:2}$ over a conducting carbon cloth ($PGH_{3:2}$@CC). (details in experimental section) the as developed $PGH_{3:2}$@CC are directly assembled into a solid state supercapacitor device (PVA/H_2SO_4) was used as both solid state electrolyte and separator) and can be sewed with garments to realize all–solid–state wearable supercapacitor device (Figure 2.15.a). The wearable all–solid–state device exhibited a good areal capacitance of 289 mF cm^{-2} at 1 mA cm^{-2}. One of the basic criteria of a wearable supercapacitor is its flexibility. To test the performance of $PGH_{3:2}$@CC under flexible condition, CV tests were performed. The CV curves show that there is a slight change in the shape of the profile when the supercapacitor device was bended completely (only 0.08 % decrement in total area of CV at 180° bending) (Figure 2.15.b). Moreover, the continuous cyclic bending test (at a bending angel of 180°) of the supercapacitor device was performed for 5000 cycles (Figure 2.15.c) and the corresponding capacitance was measured after each bending cycle. Interestingly, after an initial fluctuation for a few cycles (inset of Figure 2.15.c), no significant alteration in the capacitance value was observed indicating the flexible nature of the device and its potential to be operated under wearable conditions. Besides, $PGH_{3:2}$@CC demonstrated an excellent cycling stability (97.8%) for over 2500 continuous charge–discharge cycles at 5 mA cm^{-2} (Figure 2.15.d).

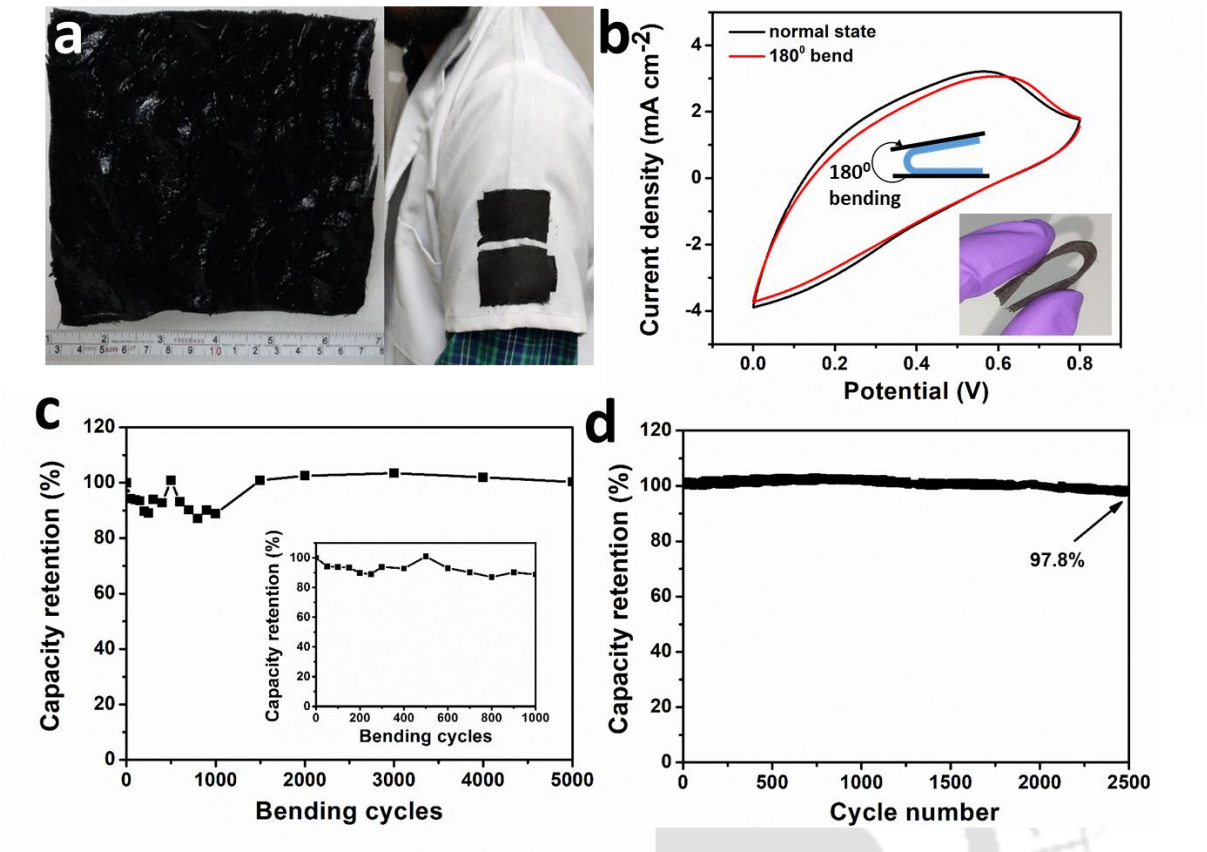

Figure 2.15. Wearable application of PGH: (a) large scale synthesis of flexible $PGH_{3:2}$@CC electrode and integration of a solid state device with garments; (b) CV profiles of $PGH_{3:2}$@CC under normal and 180° bending state; (c) cyclic bending test of $PGH_{3:2}$@CC at a current density of 1 mA cm^{-2} (the inset shows the first 1000 cycles) and (d) cycling stability of $PGH_{3:2}$@CC at 5 mA cm^{-2}.

For practical application of solid state device, often higher output voltage (>1 V) is required. To increase the voltage window of the supercapacitor, the devices were connected in series. A maximum operating voltage window of 3.2 V (compared to only 0.8 V for a single device) was achieved by connecting four devices in series. The increase of voltage window with increase in cell number (solid state device) in series connection is evident from the CV and GCD curves (Figure 2.16.a–b). Interestingly, the benefit of the interconnected conducting structure of the hybrid is also obvious for the case of solid–sate $PGH_{3:2}$@CC device which is indicated by a small potential drop of 114 mV at the beginning of the discharge curve of four cell pack (Figure 2.16.b) demonstrating a low internal resistance of the device.

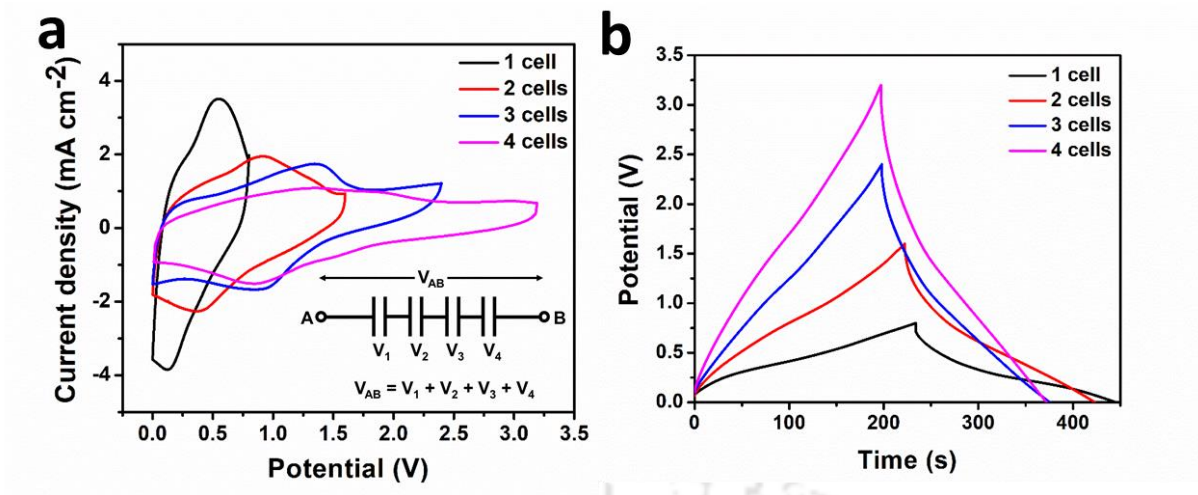

Figure 2.16. Device application of $PGH_{3:2}$@CC: (a) CV profiles at 10 mV s^{-1} and (b) CC curves at 1 mA cm^{-2} with the increase in solid–state $PGH_{3:2}$@CC capacitors connected in series.

2.4 Conclusion:

A highly scalable, facile and room temperature protocol for the development of hydrogel hybrids of graphene and polyaniline (PANI) is presented in this chapter. The hydration level of porous hydrogel structure is found to be the key point to achieve high faradic activity of the PANI nanowires in thick and high mass loaded electrodes. and its high pseudocapacitive performance remains preserved in the mechanically compressed dense yet hydrated structure. Hydration avoids the complete collapse of continuously connected pore structure via graphene restacking, which ensures fast faradic charge storage offered by pseudocapacitor component (PANI) of the hydrogel–hybrid. The protocol presented here can straightforwardly be adopted to engineer high areal or volumetric energy density superapacitors to satisfy customized requirements and also can be used in wearable applications. Simplicity of the approach, ultimate scalability and versatility together with high electrochemical activity, excellent rate capability and long cyclic life can qualify this protocol for the next generation energy storage.

References:

1. Y. Zhu, S. Murali, M. D. Stoller, K. J. Ganesh, W. Cai, P. J. Ferreira, A. Pirkle, R. M. Wallace, K. A. Cychosz, M. Thommes, D. Su, E. A. Stach and R. S. Ruoff, Carbon-Based Supercapacitors Produced by Activation of Graphene, *Science*, 332 (2011), pp. 1537.
2. M. F. El-Kady, Y. Shao and R. B. Kaner, Graphene for batteries, supercapacitors and beyond, *Nat. Rev. Mater.*, 1 (2016), pp. 16033.
3. M. F. El-Kady, V. Strong, S. Dubin and R. B. Kaner, Laser Scribing of High-Performance and Flexible Graphene-Based Electrochemical Capacitors, *Science*, 335 (2012), pp. 1326.
4. X. Yang, C. Cheng, Y. Wang, L. Qiu and D. Li, Liquid-Mediated Dense Integration of Graphene Materials for Compact Capacitive Energy Storage, *Science*, 341 (2013), pp. 534.
5. Y. Xu, K. Sheng, C. Li and G. Shi, Self-Assembled Graphene Hydrogel via a One-Step Hydrothermal Process, *ACS Nano*, 4 (2010), pp. 4324-4330.
6. D. Zhang, X. Zhang, Y. Chen, P. Yu, C. Wang and Y. Ma, Enhanced capacitance and rate capability of graphene/polypyrrole composite as electrode material for supercapacitors, *J. Power Sources*, 196 (2011), pp. 5990-5996.
7. G. Yu, L. Hu, N. Liu, H. Wang, M. Vosgueritchian, Y. Yang, Y. Cui and Z. Bao, Enhancing the Supercapacitor Performance of Graphene/MnO2 Nanostructured Electrodes by Conductive Wrapping, *Nano Lett.*, 11 (2011), pp. 4438-4442.
8. D.-W. Wang, F. Li, J. Zhao, W. Ren, Z.-G. Chen, J. Tan, Z.-S. Wu, I. Gentle, G. Q. Lu and H.-M. Cheng, Fabrication of Graphene/Polyaniline Composite Paper via In Situ Anodic Electropolymerization for High-Performance Flexible Electrode, *ACS Nano*, 3 (2009), pp. 1745-1752.
9. X. Yu, B. Lu and Z. Xu, Super Long-Life Supercapacitors Based on the Construction of Nanohoneycomb-Like Strongly Coupled CoMoO4–3D Graphene Hybrid Electrodes, *Adv. Mater.*, 26 (2014), pp. 1044-1051.
10. Y. Wang, X. Yang, A. G. Pandolfo, J. Ding and D. Li, High-Rate and High-Volumetric Capacitance of Compact Graphene–Polyaniline Hydrogel Electrodes, 6 (2016), pp. 1600185.
11. W. S. Hummers and R. E. Offeman, Preparation of Graphitic Oxide, *J. Am. Chem. Soc.*, 80 (1958), pp. 1339-1339.
12. J. Huang and R. B. Kaner, A General Chemical Route to Polyaniline Nanofibers, *J. Am. Chem. Soc.*, 126 (2004), pp. 851-855.
13. U. N. Maiti, J. Lim, K. E. Lee, W. J. Lee and S. O. Kim, Three-Dimensional Shape Engineered, Interfacial Gelation of Reduced Graphene Oxide for High Rate, Large Capacity Supercapacitors, *Adv. Mater.*, 26 (2014), pp. 615-619.
14. J. Yan, T. Wei, B. Shao, Z. Fan, W. Qian, M. Zhang and F. Wei, Preparation of a graphene nanosheet/polyaniline composite with high specific capacitance, *Carbon*, 48 (2010), pp. 487-493.
15. J. P. Pouget, M. E. Jozefowicz, A. J. Epstein, X. Tang and A. G. MacDiarmid, X-ray structure of polyaniline, *Macromolecules*, 24 (1991), pp. 779-789.
16. H.-P. Cong, X.-C. Ren, P. Wang and S.-H. Yu, Flexible graphene–polyaniline composite paper for high-performance supercapacitor, *Energy Environ. Sci.*, 6 (2013), pp. 1185-1191.

17. Z. Tong, Y. Yang, J. Wang, J. Zhao, B.-L. Su and Y. Li, Layered polyaniline/graphene film from sandwich-structured polyaniline/graphene/polyaniline nanosheets for high-performance pseudosupercapacitors, *J. Mater. Chem. A*, 2 (2014), pp. 4642-4651.
18. S. Stankovich, D. A. Dikin, R. D. Piner, K. A. Kohlhaas, A. Kleinhammes, Y. Jia, Y. Wu, S. T. Nguyen and R. S. Ruoff, Synthesis of graphene-based nanosheets via chemical reduction of exfoliated graphite oxide, *Carbon*, 45 (2007), pp. 1558-1565.
19. H. Wang, J. T. Robinson, X. Li and H. Dai, Solvothermal Reduction of Chemically Exfoliated Graphene Sheets, *J. Am. Chem. Soc.*, 131 (2009), pp. 9910-9911.
20. H. Fan, N. Zhao, H. Wang, J. Xu and F. Pan, 3D conductive network-based free-standing PANI–RGO–MWNTs hybrid film for high-performance flexible supercapacitor, *J. Mater. Chem. A*, 2 (2014), pp. 12340-12347.
21. S. Wang, L. Ma, M. Gan, S. Fu, W. Dai, T. Zhou, X. Sun, H. Wang and H. Wang, Free-standing 3D graphene/polyaniline composite film electrodes for high-performance supercapacitors, *J. Power Sources*, 299 (2015), pp. 347-355.
22. Y. Wang, X. Yang, L. Qiu and D. Li, Revisiting the capacitance of polyaniline by using graphene hydrogel films as a substrate: the importance of nano-architecturing, *Energy Environ. Sci.*, 6 (2013), pp. 477-481.
23. Y. Liu, R. Deng, Z. Wang and H. Liu, Carboxyl-functionalized graphene oxide–polyaniline composite as a promising supercapacitor material, *Journal of Materials Chemistry*, 22 (2012), pp. 13619-13624.
24. K. Chi, Z. Zhang, J. Xi, Y. Huang, F. Xiao, S. Wang and Y. Liu, Freestanding Graphene Paper Supported Three-Dimensional Porous Graphene–Polyaniline Nanocomposite Synthesized by Inkjet Printing and in Flexible All-Solid-State Supercapacitor, *ACS Appl. Mat. Interfaces*, 6 (2014), pp. 16312-16319.
25. P. Sekar, B. Anothumakkool and S. Kurungot, 3D Polyaniline Porous Layer Anchored Pillared Graphene Sheets: Enhanced Interface Joined with High Conductivity for Better Charge Storage Applications, *ACS Applied Materials & Interfaces*, 7 (2015), pp. 7661-7669.
26. P. Yu, X. Zhao, Z. Huang, Y. Li and Q. Zhang, Free-standing three-dimensional graphene and polyaniline nanowire arrays hybrid foams for high-performance flexible and lightweight supercapacitors, *J. Mater. Chem. A*, 2 (2014), pp. 14413-14420.
27. M. Moussa, Z. Zhao, M. F. El-Kady, H. Liu, A. Michelmore, N. Kawashima, P. Majewski and J. Ma, Free-standing composite hydrogel films for superior volumetric capacitance, *Journal of Materials Chemistry A*, 3 (2015), pp. 15668-15674.
28. J. Pedrós, A. Boscá, J. Martínez, S. Ruiz-Gómez, L. Pérez, V. Barranco and F. Calle, Polyaniline nanofiber sponge filled graphene foam as high gravimetric and volumetric capacitance electrode, *Journal of Power Sources*, 317 (2016), pp. 35-42.
29. Z.-S. Wu, K. Parvez, S. Li, S. Yang, Z. Liu, S. Liu, X. Feng and K. Müllen, Alternating Stacked Graphene-Conducting Polymer Compact Films with Ultrahigh Areal and Volumetric Capacitances for High-Energy Micro-Supercapacitors, *Advanced Materials*, 27 (2015), pp. 4054-4061.
30. Z. Fan, Z. Cheng, J. Feng, Z. Xie, Y. Liu and Y. Wang, Ultrahigh volumetric performance of a free-standing compact N-doped holey graphene/PANI slice for supercapacitors, *Journal of Materials Chemistry A*, 5 (2017), pp. 16689-16701.
31. R. Malik, L. Zhang, C. McConnell, M. Schott, Y.-Y. Hsieh, R. Noga, N. T. Alvarez and V. Shanov, Three-dimensional, free-standing polyaniline/carbon nanotube composite-based electrode for high-performance supercapacitors, *Carbon*, 116 (2017), pp. 579-590.

32. L. Li, A.-R. O. Raji, H. Fei, Y. Yang, E. L. G. Samuel and J. M. Tour, Nanocomposite of Polyaniline Nanorods Grown on Graphene Nanoribbons for Highly Capacitive Pseudocapacitors, *ACS Appl. Mat. Interfaces*, 5 (2013), pp. 6622-6627.
33. D. Ge, L. Yang, L. Fan, C. Zhang, X. Xiao, Y. Gogotsi and S. Yang, Foldable supercapacitors from triple networks of macroporous cellulose fibers, single-walled carbon nanotubes and polyaniline nanoribbons, *Nano Energy*, 11 (2015), pp. 568-578.

Chapter 3

Diffusion Limited Surface Polymerization over Graphene-hydrogel framework for High Area and Mass Specific Energy Storage

Chapter 3

Diffusion Limited Surface Polymerization over Graphene–hydrogel framework for High Area and Mass Specific Energy Storage

Engineering nanomaterials via diffusion controlled mechanism although is very common for biological process, realizing the basic mechanism behind this for the fine structure tuning of nanomaterials in practical laboratory process is still lacking. In this chapter, we demonstrate the development of an ultrafast self–assembled graphene hydrogel and its usage as a hydrated confined reactor (like biological system) for the diffusion controlled growth of ultrafine conducting polyaniline (PANI) nanostructures over the graphene surface (PANI–GH) via hydrogel–organic interfacial reaction. The hydrogel–organic interface restricts the diffusion rate of monomers and the subsequent confined polymerization within the porous compartments of hydrogel structure leads to the significant control over the polymerization process. In addition, molecular dynamics study reveals a strong attractive interaction between monomer and graphene surface which plays a significant role in controlling the nucleation and tuning the morphology of PANI nanostructures. The as synthesized PANI–GH with high areal mass loading of 8.8 mg cm^{-2} demonstrates an excellent specific capacitance of 503 F g^{-1} and long term cycling stability. Moreover, PANI–GH exhibits an excellent rate performance of 88.6% at a large current density of 30 A g^{-1}.

3.1 Introduction:

The previous chapter demonstrates a very simple co–assembly strategy to obtain a graphene hydrogel–polyaniline nanohybrid and has been successfully applied for high mass loaded supercapacitor electrodes. Nevertheless, such co–assembly hybridization strategy does not allow much tuning over the morphology or structure of the hybridized nanomaterials, although we could expect enhanced electrochemical activity originated from the controlled hybridization process. [1–4]

Bio–mineralization is a phenomenon where inorganic materials self–assembled into complex composites having exquisite physicochemical properties via controlled diffusion and restricted mineralization within the porous hydrated matrix of biological systems. [5, 6] Nevertheless, the real challenge lies in understanding and mimicking such delicate natural process in practical laboratory synthesis process to tune the structure of nanomaterials for

functional applications. [6, 7] In this chapter, we demonstrate the diffusion controlled interfacial surface polymerization process for the development of ultrafine polyaniline (PANI) nanostructures within a porous graphene hydrogel structure mimicking the bio–mineralization mechanism. Graphene hydrogel (GH) being a hydrated porous structure, closely resembles to biological systems and could be effectively modeled to grow structure tuned nanomaterials.

We have first developed GH by adopting a unique minute–scale fast assembly and reduction of graphene oxide (GO) at room temperature, and then used this hydrogel as a medium to realize the concept of diffusion controlled nano–hybridization process. In this process, the fine control over the diffusion of monomer reactant (aniline) within the graphene hydrogel is achieved following an aqueous–organic interfacial polymerization process. In this bi–phasic (aqueous–organic) reaction, the role of the hydrogel is first, to function as an interface to delicately control the diffusion of monomer from the organic to the aqueous phase (confined within hydrogel) and second, to provide porous compartments for the constrained polymerization of aniline leading to the development of PANI–graphene hydrogel hybrid (PANI–GH). The molecular dynamics (MD) study shows that the diffusion coefficient of aniline monomer in the bulk interfacial reaction (without hydrogel) is remarkably lowered in case of hydrogel–organic interfacial reaction. MD study further reveals the presence of strong van der Waals and electrostatic interactions of monomer molecules and as formed oligomers with the basal plane of graphene sheets. The slow diffusion process along with the observed molecular interactions significantly restrain the nucleation and subsequent polymerization process resulting into morphology tuned uniform nano–hybridization.

The functional application of PANI–GH hybrid is demonstrated by utilizing PANI–GH as a binder free electrode for high performance supercapacitor device which exhibits a remarkably high specific capacitance of 503 F g^{-1} at a current density of 5 A g^{-1} and long term cycling stability (95.8% retention after 3000 charge–discharge cycles). In addition, the hybrid electrode exhibits an excellent rate performance (retaining 88.6% at a large current density of 30 A g^{-1}). Importantly, the high supercapacitive performance of the PANI–GH hybrid is obtained with a high areal mass loading of the electrode (8.8 mg cm^{-2}). Achieving such a high performance at practical level of mass loading is very important from commercial application perspective because in general energy storage performance degrades with increasing mass loading owing to the increased ion diffusion resistance. [8–11] The exhibited high performance metric of PANI–GH electrode is attributed to the synergistic effect of the pseudocapacitive

contribution of the ultrafine PANI nanostructure and the porous conducting framework of graphene hydrogel.

3.2 Experimental section:

3.2.1 Preparation of graphene hydrogel (GH):

The GH was prepared through an ammonia assisted electroless reduction and ultrafast assembly of graphene oxide. [12, 13] Namely, graphene oxide aqueous dispersion (4 mg mL^{-1}, 5 mL), prepared via procedure as described in chapter 2, [14] was first mixed with 5 mL of ammonium hydroxide solution ($NH_3.H_2O$, 30 wt%). Then a pre–cleaned zinc foil (Zn) of dimension 60 mm × 70 mm × 0.25 mm was immersed directly into the above solution for simultaneous reduction and gelation process. The gelation time was varied from 1 to 10 min. Subsequently, the developed GH along with the zinc plate was washed with water and kept in water for 1 h. Finally, the hydrogel film of GH was obtained by etching Zn in 8 M KOH solution and washing repeatedly with water.

3.2.2 Development of PANI–GH hybrids:

The as prepared GH (with gelation time of 5 min.) was first saturated with ammonium persulfate ($(NH_4)_2S_2O_8$, APS) solution in 1 M HCl for 1 day. Different concentrations of APS solution in 10 mL of 1 M HCl were used namely, 0.16 mmol, 8 mmol and 16 mmol. Subsequently, GH saturated with APS was immersed in a solution containing 3.2 mmol aniline dissolved in 10 mL chloroform and kept further for 1 day at ambient condition for the interfacial polymerization and hybridization process. After the formation of hybrid, the gel was taken out of the chloroform solution and washed thoroughly with ethanol and water. The as developed hybrids with increasing APS concentrations are named as PANI–GH1, PANI–GH2 and PANI–GH3. The mass loadings of the as formed hybrids were found to be 3 mg cm^{-2} (PANI–GH1), 7.8 mg cm^{-2} (PANI–GH2) and 8.8 mg cm^{-2} (PANI–GH3). For comparison, PANI–GH hybrids have also been prepared purely in aqueous phase (APANI–GH). Namely, GH was first saturated with 16 mmol APS solution in 10 mL 1 M HCl for 1 day. Next the GH with APS was put into a solution containing 3.2 mmol aniline in 10 mL water for 1 day. Finally, the APANI–GH hybrid was washed thoroughly with water. Additionally, bulk PANI nanowires were also synthesized via previously reported traditional aqueous–organic interfacial reaction. (19)

3.2.3 Material characterizations:

The morphology of the samples was characterized by field emission scanning electron microscope (FESEM, Zeiss, Sigma 300) and field emission transmission electron microscope (FETEM, JEOL–2100F). The thickness of the GH samples was measured from the cross–sectional FESEM images of freeze dried samples by measuring the width at five different positions and averaging them. The scanning transmission electron microscope (STEM) elemental mapping was performed using Oxford STEM analyzer attached with FETEM. The crystal structure of the samples was studied by X–ray diffractometer (XRD, Rigaku) in powder XRD mode with Cu–Kα radiation (λ = 0.15418 nm). Raman studies were performed on a laser micro Raman spectrometer (Horiba, LabRam HR). The ionic state and the elemental analysis of GH sample was conducted using ESCALAB Xi+ (Thermo Fisher) X–ray photo electron spectroscopy (XPS) instrument.

3.2.4 Theoretical study:

All the required structures (aniline, emeraldine tetramer and GH) were constructed using Avogadro and VMD. [15, 16] In the structure of graphene, epoxy (C–O–C) and hydroxyl (–OH) functional groups were located on the basal plane of the graphene sheets whereas the carboxyl functional groups (–COOH) were located on the edges only. [17] The chemical composition of reduced graphene oxide (rGO) was taken as $C_{30}O_1(OH)_1(COOH)_{0.5}$. The modelling of water molecules was done by TIP3P water model [18] and the bond lengths of O–H were constrained following SETTLE algorithm. [19] Molecular dynamics (MD) simulations were studied using Nanoscale Molecular Dynamics (NAMD) [20] with all–atom optimized potentials for liquid simulations (OPLS–AA) force field parameters (time step– 1 fs). [21] Two types of interactions were studied, namely, van der Waals interaction which was computed through Lennard–Jones potential with a cut–off distance of 12 Å and a long–range electrostatic interaction calculated by Particle mesh Ewald (PME) method. [22] After the equilibration, the production runs were performed for 20 ns with NVE ensemble at ambient temperature. Before initiating simulations, energy minimization was conducted followed by equilibrating the system for 1 ns at ambient temperature and 1 atm pressure using NPT ensemble. Modified Nosé–Hoover method was used to control the pressure (the values of barostat oscillation time and damping factor were kept at 0.3 ps). Temperature was controlled using Langevin dynamics (damping factor– 5 ps^{-1}). While equilibrating, all the atoms except water, were constrained to their initial positions (force constraint– 1.0 kcal/mol $Å^2$). During the simulation run, top and bottom layers of GH were constrained so that the boundary of GH could

be defined accurately. While all the other graphene sheets and the molecules were allowed to interact freely. The diffusion coefficient is calculated using Einstein's diffusion equation:

$$D = \frac{1}{2d} \lim_{t \to \infty} \frac{\langle [\vec{r}(t_0 + t) - \vec{r}(t_0)]^2 \rangle}{t}$$

where D is the self diffusion coefficient, d is the dimensionality of the system and $\vec{r}(t)$ is the position of the concerned particle at time t.

3.2.5 Electrochemical characterization:

The supercapacitive performance of GH and PANI–GH hybrids were tested in a symmetric cell configuration with 1 M H_2SO_4 as electrolyte. The details of the cell assembly is given in the experimental section of chapter 1. The cyclic voltammetry (CV) tests were performed in a potential window of 0 to 0.8 V at different scan rates ranging from 5 mV s^{-1} to 300 mV s^{-1}. The constant current charge–discharge (GCD) tests were carried out under the same potential window (0 to 0.8 V) at current densities ranging from 2 A g^{-1} to 30 A g^{-1}. The electrochemical impedance spectroscopy (EIS) was carried within a frequency range of 0.01 Hz to 100 kHz at a fixed potential of 10 mV. The specific capacitance (C_s) was calculated from GCD curves using the equation 1.10. The specific energy density (U) and power density (P) of PANI–GH electrodes were calculated from the equations 1.13 and 1.15 respectively. The real (C') and imaginary (C") parts of complex capacitances were calculated from the equations given below:

$$C' = -Z"/(2\pi f|Z|^2)$$

$$C" = -Z'/(2\pi f|Z|^2)$$

where Z", Z' and $|Z|$ are the imaginary, real and absolute impedance as calculated from EIS. f is the frequency (Hz).

3.3 Results and discussions:

For the fine structure controlled hybridization of graphene–polyaniline hydrogel, graphene hydrogel was first prepared via a facile ultrafast room temperature gelation strategy followed by its use as a medium for the interfacial polymerization process. The ultrafast growth of GH was realized by carefully modifying previously reported zinc plate assisted gelation strategy of graphene oxide (GO) into GH. [12, 13] In this process the application of ammonia solution in GO dispersion leads to the formation of zinc–ammino complex ($Zn(NH_3)_4^{2+}$) via reaction with zinc ions of zinc plate. The in–situ formed zinc–ammino complex being positively charged ions strongly attract negatively charged GO sheets which results in the fast assembly of GO

sheets over the zinc plate (schematic illustration in Figure 3.1). The simultaneous charge transfer form metallic zinc to GO surface leads to the reduction of GO and formation of graphene hydrogel (GH). The thickness of the as formed hydrogel was found to increase with the gelation time (1, 2, 5 and 10 min) (insets of Figure 3.2a–d). Such a gelation strategy is not only unique form its facile processability but it is highly scalable which is very important for its practical usage. [23–27] Since, thick hydrogel might offer hindered diffusion, GH with 5 min. of gelation time was used for electrochemical study and hybridization process considering its moderate thickness. Therefore, we mention GH developed in 5 min of gelation simply as GH unless otherwise mentioned.

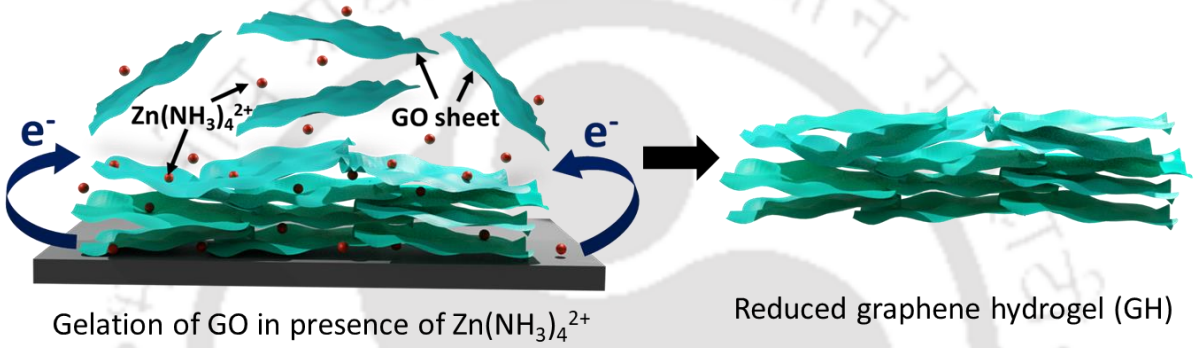

Figure 3.1. Schematic illustration of the preparation of GH via ammonia assisted gelation process.

3.3.1 Morphological study of GH:

The morphology of the as developed GH was studied by field emission scanning electron microscope (FESEM). The highly interconnected hierarchical porous structure of the GH was observed from the cross–sectional FESEM images (Figure 3.2c). The pore dimension was seen to be varying from a few nanometres to several micrometres and the pore walls were constructed by the thin layers of crumpled graphene sheets. Besides these smaller pores, big macro voids were also detected from the low magnification FESEM images (insets of Figure 3.2a–d). Further, all the hydrogel samples, irrespective of gelation time, show similar porous morphology with different cross–sectional width (Figure 3.2a–d).

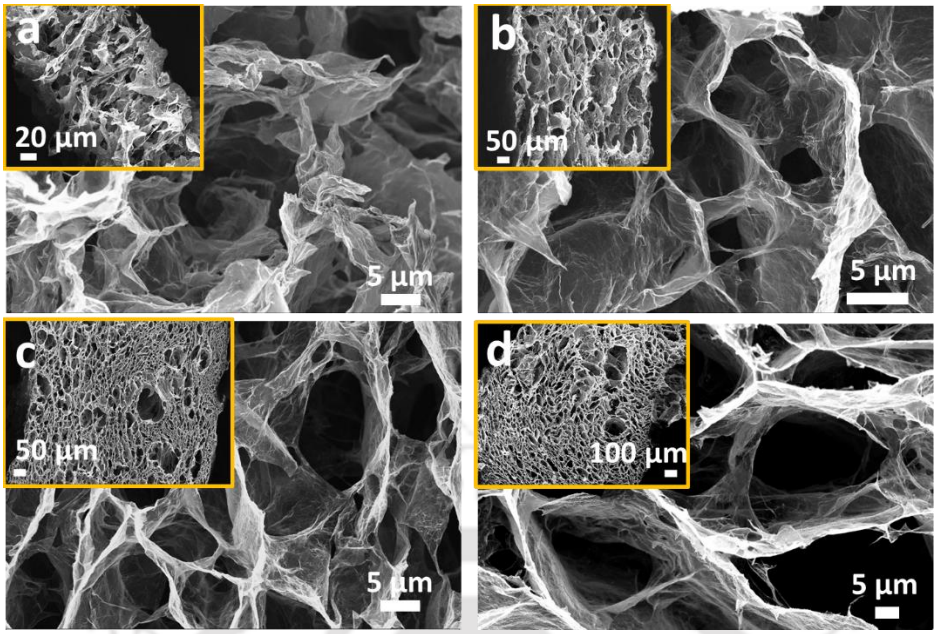

Figure 3.2. Cross–sectional FESEM images of GH with gelation time: (a) 1 min, (b) 2 min, (c) 5 min, (d) 10 min. Insets show the corresponding low magnification images.

3.3.2 Structural analyses of GH:

The crystal structure and compositional analyses of GH were examined by powder X–ray diffraction (XRD) and Raman spectroscopy. XRD pattern of GO suggests the presence of a sharp peak at 2θ = 9.4° (with a d–spacing of 9.4 Å) which corresponds to the (001) crystal plane (Figure 3.3.a). After the reduction process, the observed sharp peak of GO completely disappeared and a broad peak appeared at around 2θ of 24.2° (with a d–spacing of 3.6 Å) which

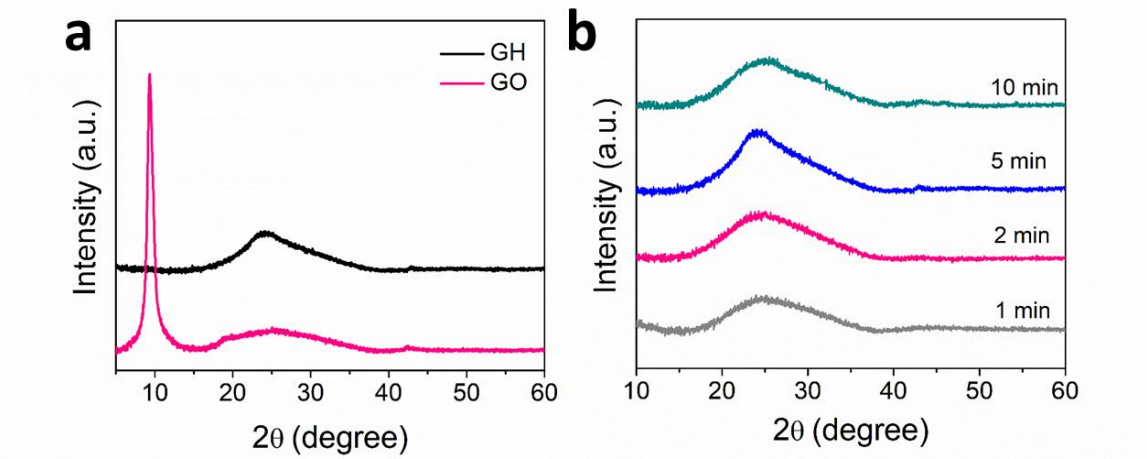

Figure 3.3. Structural characterizations of GH: XRD pattern of (a) GH and GO and (b) GH with different gelation time.

is attributed to the graphitic (002) plane. This suggests the significant removal of the oxygen containing functional groups upon the reduction of GO into graphitic structure. [27] Furthermore, all the GH samples exhibited similar XRD pattern revealing successful reduction of GO irrespective of the gelation time (Figure 3.3.b).

In the Raman spectra of GH (Figure 3.4a–c), two peaks at 1583 cm^{-1} and 1322 cm^{-1} corresponding to the characteristic D and G peaks were observed. These D and G peaks are originated respectively from the presence of defects in the graphitic structure and the in–plane stretching mode of C=C bonds. Moreover, the D–peak to G–peak intensity ratio (I_D/I_G) were found to be increased from 1 for GO to 1.84 for GH (Figure 3.4a), which indicates the successful reduction process of GO. [28–31]

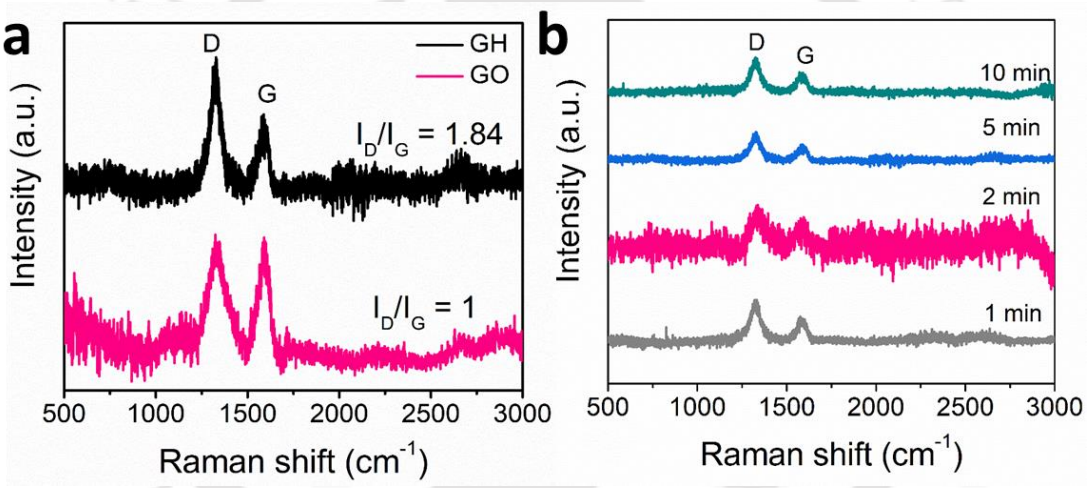

Figure 3.4. Structural characterizations of GH: Raman spectra of (c) GH and GO and (d) GH with different gelation time.

The chemical structure of GH was studied by X–ray photoelectron spectroscopy (XPS). First, the XPS survey spectrum of GH confirms the existence of C and O species in GH (inset of Figure 3.5). The high resolution C1s XPS spectrum was then deconvoluted to obtain three major peaks which were associated with the C–C/C=C (284.6 eV), C–O (286.9 eV) and O–C=O (288.5 eV) bonding respectively (Figure 3.5). [12, 32] The highly diminished intensity of O–C=O bond further confirms the removal of oxygen functionalities and the reduction of GO.

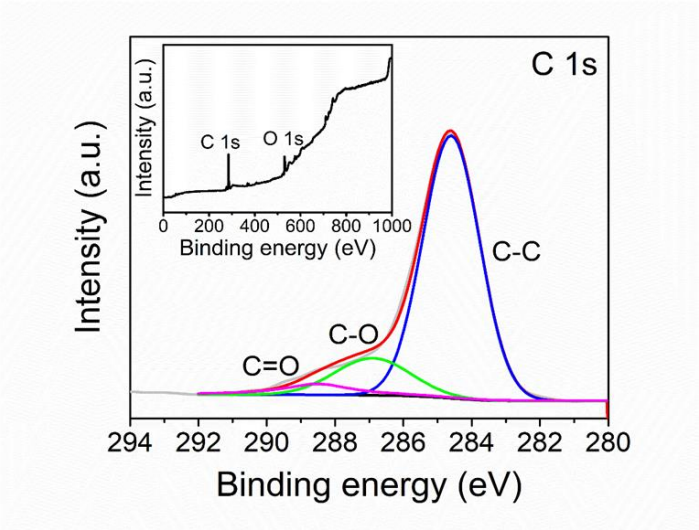

Figure 3.5. High resolution XPS spectrum of C1s. The inset shows survey spectrum of GH.

3.3.3 The concept of hydrogel–organic interfacial polymerization process through theoretical study:

The porous hydrated framework of GH closely resembles to the biological systems possessing similar porous hydrated matrix. The graphene sheets of GH serve the similar purpose of biological membranes in bio–mineralization process through which the restricted diffusion of solutes from the outside of GH into its porous structure occurs. Inspired by this natural phenomenon, it is expected that the slow reaction rate mediated by the controlled diffusion of reactant molecules could have a significant effect on the nucleation and subsequent growth of the nanomaterials; [33, 34] which might lead to the tuned physicochemical properties of the as grown nanomaterials. In this study, a unique hydrogel–organic bi–phasic reaction system has been adopted to simultaneously realize the hybridization and tuning the morphology of PANI nanostructure (schematic in Figure 3.6). This hydrogel–organic system differs from the conventional bulk aqueous–organic interfacial reaction system by the presence of graphene hydrogel which serves as the confined aqueous medium. As a result, instead of bulk growth of the nanomaterials in case of bulk aqueous–organic interfacial reaction, the porous graphene hydrogel in hydrogel–organic system has a direct effect in controlling the diffusion of molecule from outside organic phase into the hydrogel–confined aqueous phase, and the subsequent growth of nanomaterials.

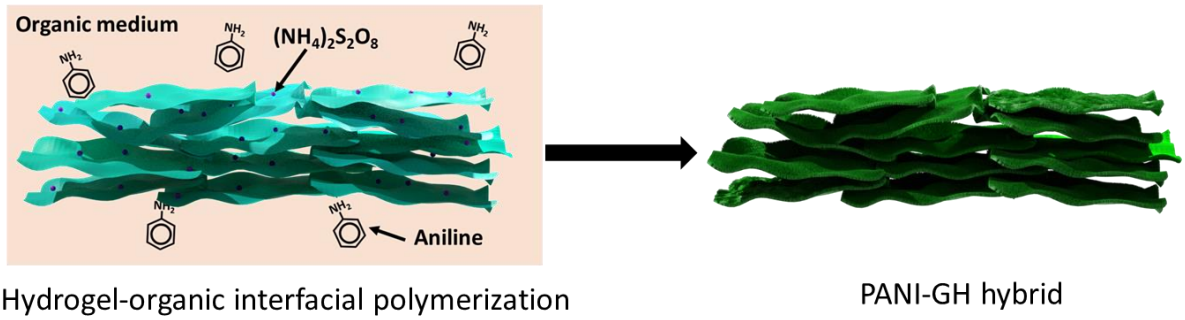

Figure 3.6. Schematic illustration of the synthesis process of PANI–GH hybrid via hydrogel–organic interfacial reaction.

To better understand the diffusion kinetics of monomer molecules and the active role of hydrogel in the hybridization process, molecular dynamics (MD) simulation study was performed. Three different reaction systems namely, hydrogel–organic interfacial, bulk aqueous–organic interfacial and bulk aqueous phase reaction systems have been considered for the study of the polymerization process of aniline into emeraldine phase of PANI. Figure 3.7.a–b visually demonstrate the two–step diffusion process of different aniline molecules: first, through the interface of hydrogel–organic system and second, the subsequent intra–hydrogel diffusion as revealed via MD simulation study. The diffusion coefficient of aniline monomer at hydrogel–organic interface was calculated to be 9.64×10^{-7} cm^2 s^{-1} which was 1.7 times lower than the corresponding diffusion coefficient at the bulk aqueous–organic interface (16.12×10^{-7} cm^2 s^{-1}) (Figure 3.7.c). As expected, the diffusion coefficient of aniline monomer was found to be maximum in the bulk aqueous phase reaction system (253.86×10^{-7} cm^2 s^{-1}) (Figure 3.7.d). In addition, the graphene sheets of GH further offer strong electrostatic and van der Waals interaction toward the aniline monomer as revealed from the simulation results (Figure 3.8).

The above simulation results clearly indicate that, the graphene surface plays a significant role in restricting the bulk diffusion of aniline monomers. Such restricted diffusion process leads to the slow and continuous feeding of the monomers through the hydrogel–organic interface into the confined aqueous phase within the hydrogel where aniline gets oxidized by the APS molecules. Once the monomers start to get oxidized into emeraldine oligomers (we have studied for the case of tetramers) within the GH, it exhibited strong affinity toward the basal planes of graphene sheets via electrostatic and van der Waals interactions Figure 3.9.a–b and this kind of interaction promotes the uniform hybridization of the PANI nanostructure with the GH. This controlled polymerization due to the slow diffusion of

monomers and their interaction with the graphene surface significantly reduce the size of as grown PANI nanostructure and results in uniform nano–hybridization.

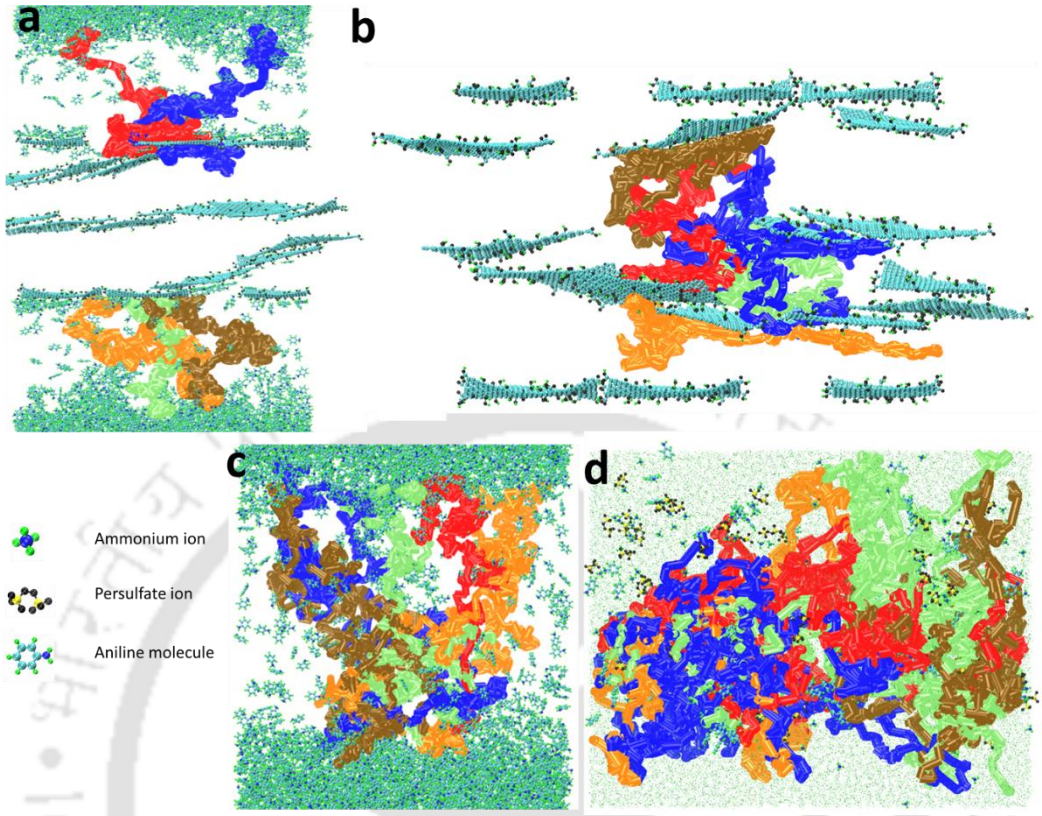

Figure 3.7. MD simulation study: representative trajectories of aniline molecules (a) at the hydrogel−organic interface, (b) inside the graphene hydrogel, (c) at bulk aqueous–organic interface (without hydrogel) and (d) in sole aqueous phase reaction. Five different trajectories in each case are represented with different colors.

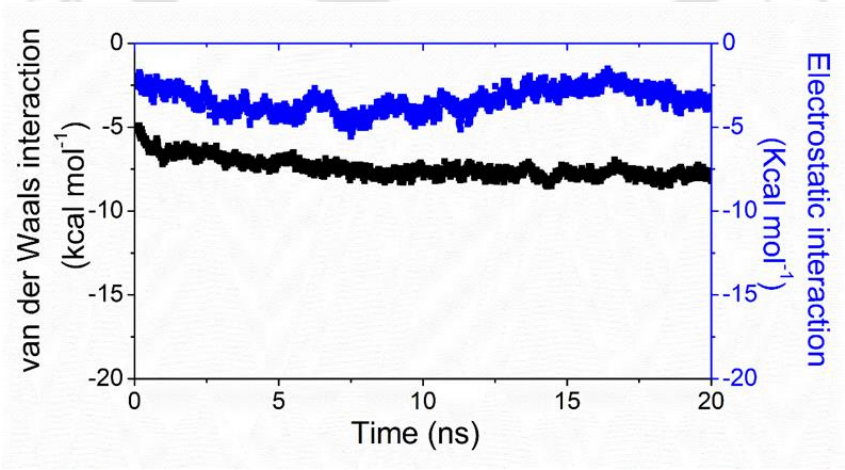

Figure 3.8. MD simulation results: van der Waals and electrostatic interactions of aniline and graphene.

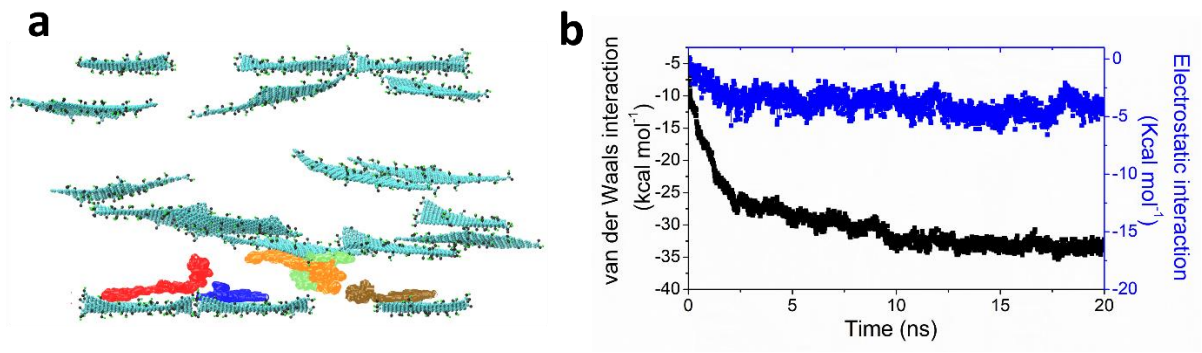

Figure 3.9. MD simulation results: (a) Representative trajectories of emeraldine tetramers (PANI) inside the graphene hydrogel. Five different trajectories are represented with different colors; (b) van der Waals and electrostatic interactions of emeraldine and graphene.

3.3.4 Morphological study of PANI–GH hybrids:

The high and low magnification FESEM images of PANI–GH hybrids provide a clear indication of the morphology tuned nanostructuring of PANI and its uniform nanohybridization with the GH. Figure 3.10.a–c reveal that, PANI nanostructures have a wrinkled morphology with a vertical protrusion and having lengths in the range of 20–50 nm.

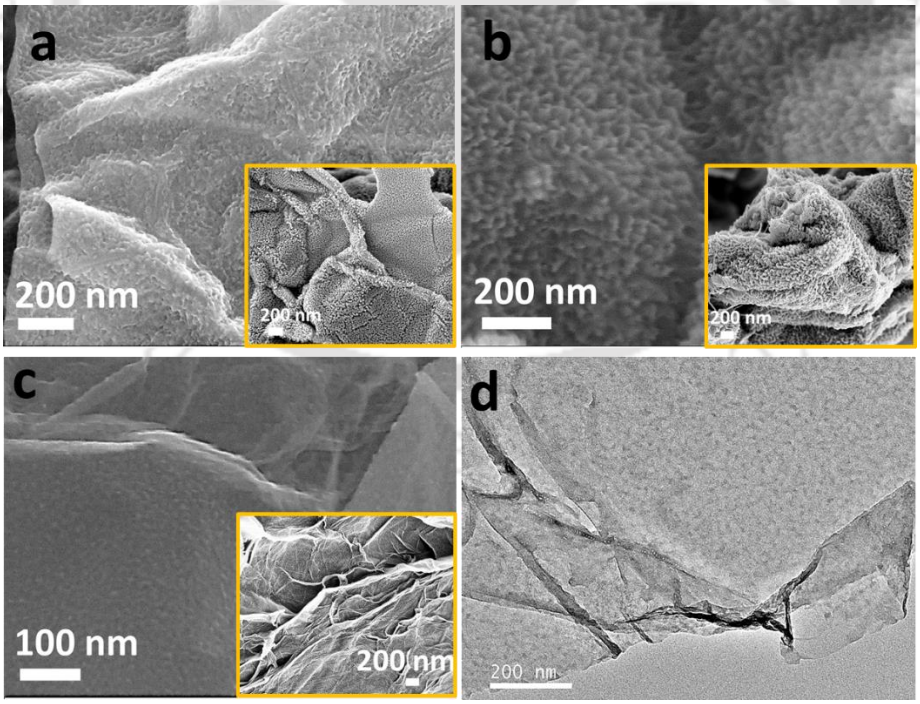

Figure 3.10. Morphology of PANI−GH hybrids: FESEM images of (a) PANI−GH3, (b) PANI−GH2 and (c) PANI−GH1. The insets show the corresponding low magnification images. (d) FETEM image of PANI−GH3.

These PANI nanostructures are distributed uniformly and densely over the graphene surface. This observation was further supported by the field emission transmission electron microscope (FETEM) image (Figure 3.10.d). It is further observed that, PANI developed via different hybridization conditions possess different nano–morphology (Figure 3.10.a–c). Since, the aniline concentration in all the hybridization process remained fixed, the difference in PANI morphology could be associated with the variation in oxidizer (APS) concentrations that remained confined within GH leading to the different rate of polymerization and therefore size variation in the PANI structure. Figure reveals that, PANI has the smallest size for the case of PANI–GH1 (prepared with the lowest concentration of APS) and the PANI becomes bigger in size and more denser growth is observed as the concentration of APS increases (in case of PANI–GH2 and PANI–GH3) owing to the increased reaction rate. As opposed to the uniform nano–hybridization, a non–uniform bulk growth of PANI fibers (sizes up to 1 μm) are seen to grow over the graphene surface (APANI–GH) (Figure 3.11) in case of sole water phase reaction. This observation is in complete agreement with the results obtained in MD simulations.

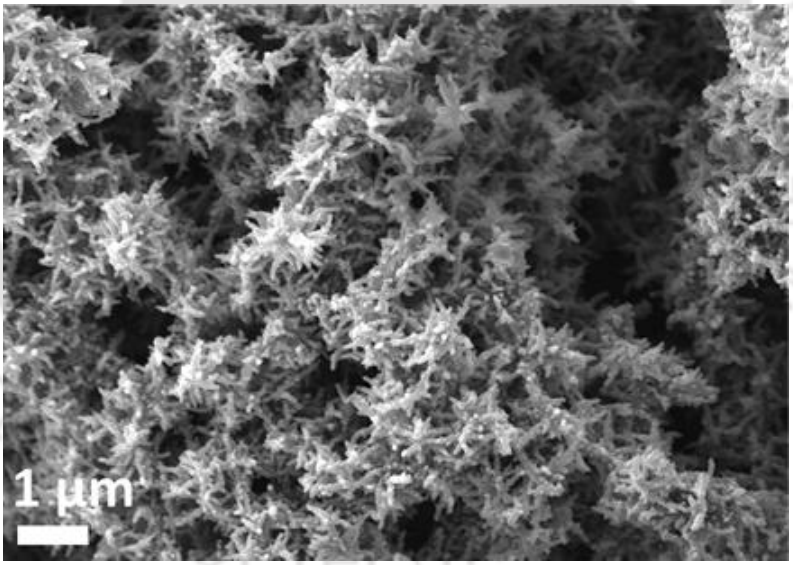

Figure 3.11. FESEM image of APANI–GH hybrid prepared in aqueous phase reaction.

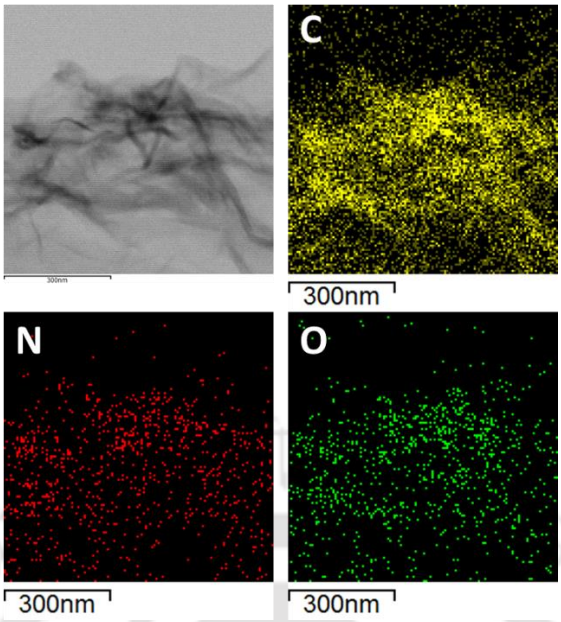

Figure 3.12. STEM elemental mapping of PANI–GH3 showing distribution of different elements (C, N and O).

3.3.5 Structural characterization of PANI–GH hybrids:

The structural and compositional analysis of PANI–GH hybrids were carried out through the scanning transmission electron microscope (STEM) mapping, XRD pattern and Raman spectroscopy results. The STEM elemental mapping result reveals the uniform distribution of the constituents of PANI that is C, N and O species over the graphene surface (Figure 3.12). The crystal structure of PANI was further analyzed by XRD results. The XRD patterns of PANI–GH3 and PANI–GH2 (Figure 3.13.a) show the presence of three diffraction peaks at 2θ of 14.9°, 20.7° and 25.3° which are associated with the (011), (020) and (200) crystallographic planes of the emeraldine phase of PANI–nanostructure. [35, 36] However, the diffraction peaks are not prominent in case of PANI–GH1 due to the very low PANI loading in the hybrid (Figure 3.13.a). The successful growth of PANI was further confirmed from the Raman spectra (Figure 3.13.b) by analysing various chemical bonding present in the hybrid structure. The various peaks at 1327 cm^{-1}, 1436 cm^{-1} and 1581 cm^{-1} in the Raman spectra of the hybrids (Figure 3.13.b) are ascribed to the C–N^{+} stretching mode of semiquinone radical, C=N stretching vibrations and the C=C stretching mode of the quinonoid ring of PANI respectively indicating the existence of PANI nanostructure in the PANI–GH hybrid. [35, 37]

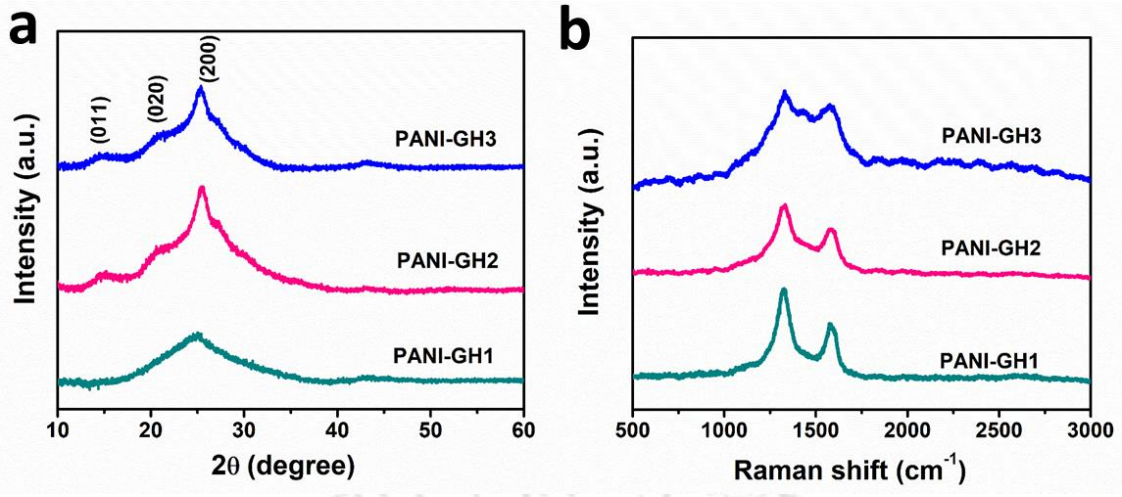

Figure 3.13. Structural characterization of PANI–GH: (a) XRD pattern and (b) Raman spectra of different PANI–GH hybrids.

3.3.6 Electrochemical characterizations:

PANI–GH hybrid having highly porous morphology with uniform PANI nanostructure is ideal for high performance supercapacitor electrode. The electrochemical performance and charge storage behavior of as developed samples were characterized in a symmetric two–electrode configuration. The hydrogel samples were cut and directly assembled into supercapacitor device without using any additives or binders. The cyclic voltammetry (CV) profiles of bare GH at scan rates 5–300 mV s^{-1} reveal quasi–rectangular curves (Figure 3.14), indicating nearly ideal electrolytic double layer type capacitance (EDLC) behavior.

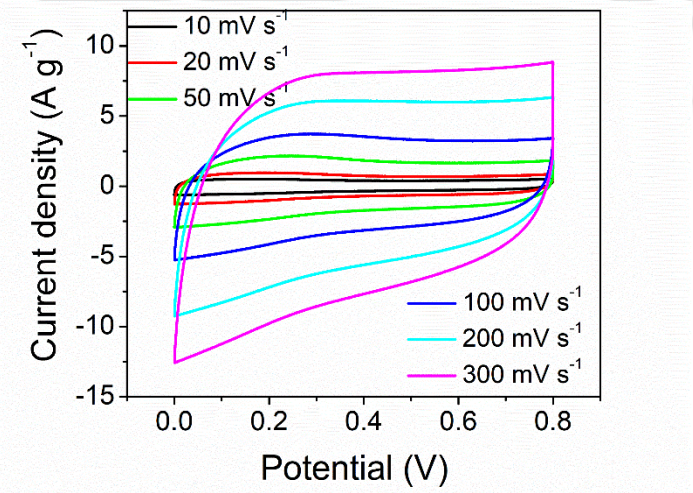

Figure 3.14. Electrochemical characterization of GH: Cyclic voltammetry (CV) curves of GH at different scan rates (5–300 mV s^{-1}).

Figure 3.15.a shows the CV profiles of the PANI–GH hybrids at a scan rate of 5 mV s^{-1} which exhibit a couple of redox peaks (within the potential range 0.2–0.5 V) superimposed over a rectangular CV background. These redox peaks are ascribed to the redox transition between leukoemeraldine and emeraldine states of PANI, indicating the pseudocapacitive property of PANI nanostructure. [38] Besides, the CV profiles largely maintain their shapes even at high scan rates (up to 300 mV s^{-1}) without significant peak distortion suggesting a fast and reversible faradaic redox reaction occurring at the electrodes (Figure 3.15.b–d).

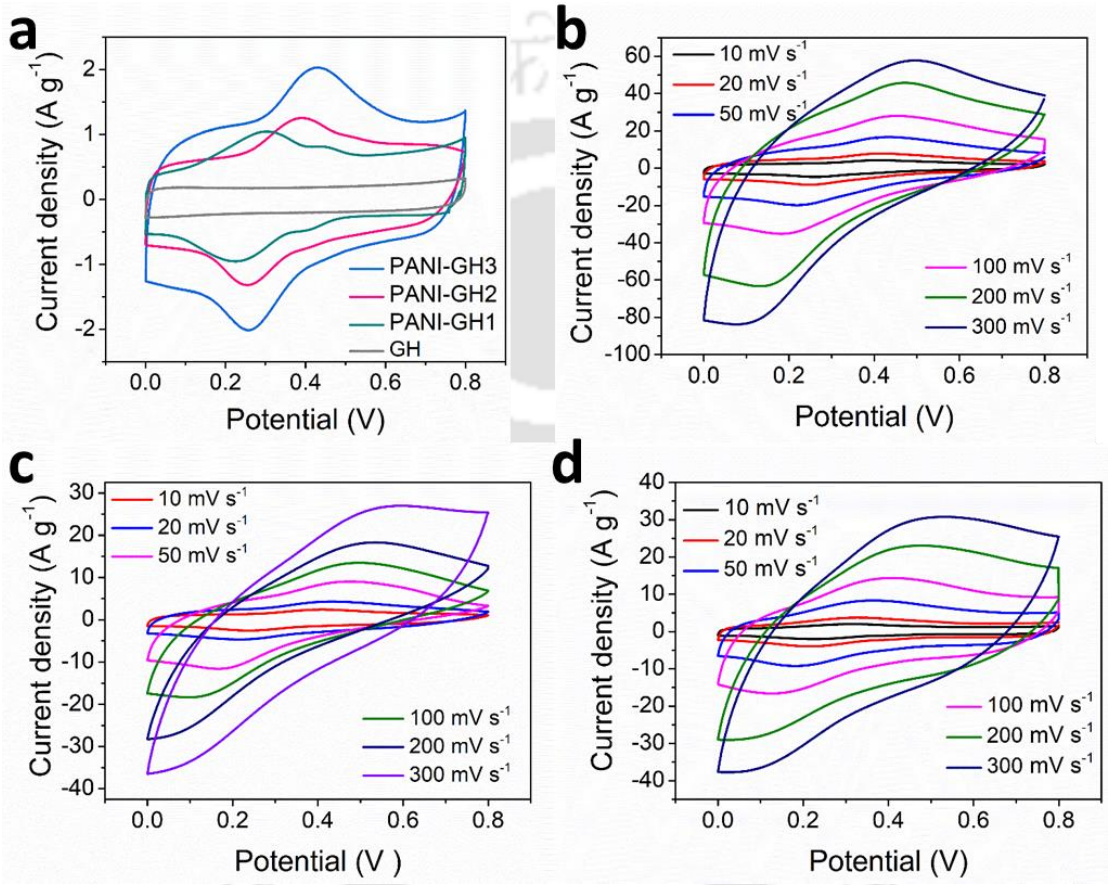

Figure 3.15. Electrochemical characterizations: (a) Comparison of cyclic voltammetry (CV) profiles of GH and different PANI–GH hybrids at 5 mV s^{-1}; CV profiles at different scan rates for (b) PANI–GH3, (c) PANI–GH2 and (d) PANI–GH1.

The galvanostatic charge–discharge (GCD) profiles at a current density of 5 A g^{-1} (Figure 3.16.a) shows that, all the PANI–GH samples possesses two potential stages from 0.8–0.4 V and from 0.4–0 V in comparison to a quasi–triangular GCD profile of GH. The first potential stage in the GCD of PANI–GH hybrids is due to the EDLC behavior while the second stage with a much slower discharge rate is attributed to the combination effect of EDLC and

pseudocapacitive properties of PANI–GH hybrid. Nevertheless, all the GCD profiles of PANI–GH samples (Figure 3.16.b–d) are symmetric in nature illustrating the high reversibility of the faradaic process. The specific capacitances (C_s) of various samples were calculated from the GCD curves (Figure 3.16.a–d). It was found that, the bare GH had a C_s of 60 F g^{-1} at 5 A g^{-1} which attained a value of 38 F g^{-1} at a high current density of 30 A g^{-1} (Figure 3.17). A comparison of C_s values of PANI–GH hybrids reveals that, C_s is the highest for the PANI–GH3 electrode exhibiting a remarkably high C_s of 503 F g^{-1} at a current density of 5 A g^{-1} followed by the hybrids PANI–GH2 (343 F g^{-1}) and PANI–GH1 (227 F g^{-1}) at the same current density (Figure 3.17).

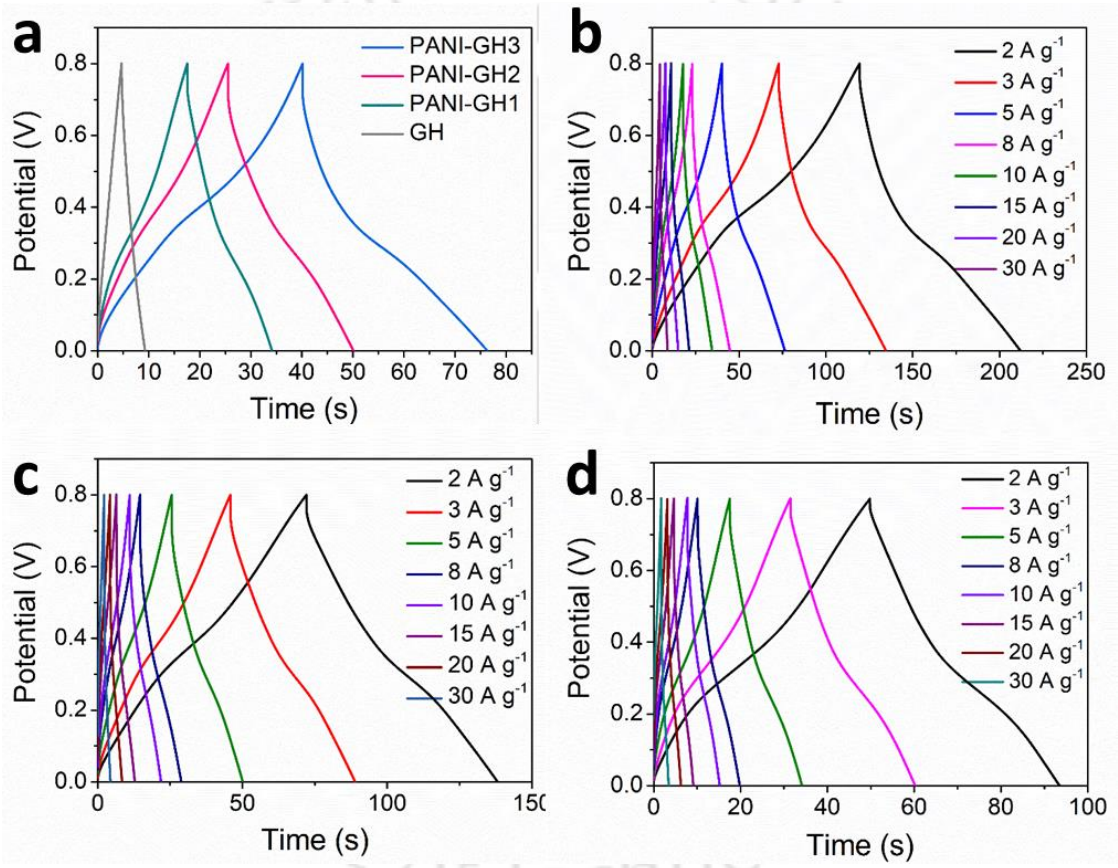

Figure 3.16. Electrochemical characterizations: (a) Comparison of galvanostatic charge–discharge (GCD) profiles of GH and different PANI–GH hybrids at 5 A g^{-1}; GCD profiles at different current densities for (b) PANI–GH3, (c) PANI–GH2 and (d) PANI–GH1.

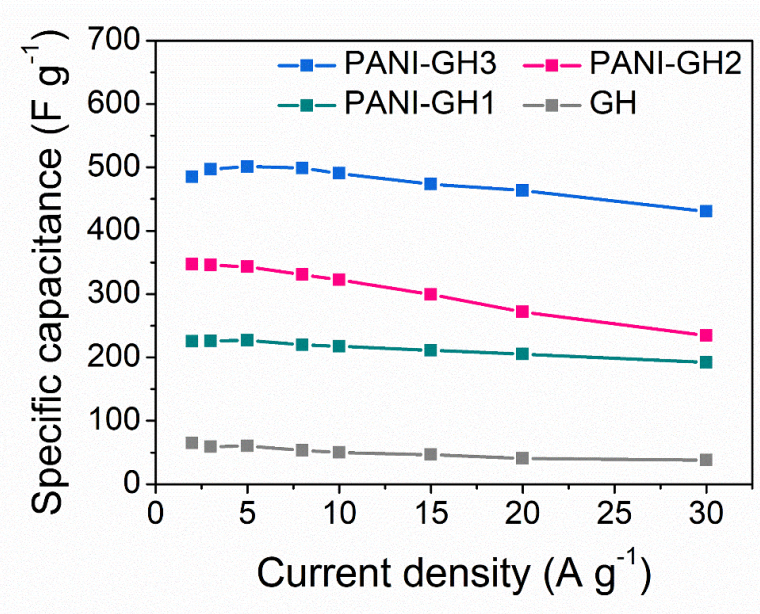

Figure 3.17. Comparison of specific capacitances vs current densities for GH and different PANI–GH hybrids.

The observed difference in the capacitance values of GH and PANI–GH samples indicate that the capacitance of the PANI–GH hybrids are predominantly due to the pseudocapacitive contribution of PANI nanostructure. Such high C_s values of PANI–GH samples are associated with the synergistic contribution of the uniform conformal growth of PANI nanostructure within the porous conducting hydrogel framework. This kind of uniform conformal growth with ultrafine nanostructure leads to the effectively high loading of PANI over the graphene and the high PANI loading is expected to result in high electrochemical performance. As a result, the difference in PANI loading for different PANI–GH hybrids leads to the variation in C_s values as calculated from GCD profiles. PANI–GH3 containing the highest PANI loading (83% with respect to the weight of the hydrogel) thus exhibited the highest value of capacitance followed by the other hybrids with decreasing PANI loading e.g. PANI–GH2 (with 80.7% PANI loading) and PANI–GH1 (with 50% PANI loading).

It is to be mentioned that, in most of the reports the high specific capacitances were obtained based on the three–electrode configuration. [39–41] Such three–electrode set up although is a good technique for the electrochemical characterization of a single electrode but in real device applications (based on two–electrode setup) those characterizations only lead to the overestimation of the capacitance value. [42] Furthermore, the PANI based supercapacitors reported thus far are often rely on a very low level of electrode mass loading (from microgram

to less than 3 mg) (Table 3.1). The performance of these electrodes generally fades away with increasing areal mass loading owing to the increased ion diffusion resistance. Although for the real device applications a high mass loading of the electrode is required to achieve high energy storage within the limited foot–print of the device. [42] In case of PANI–GH3 hybrid, the high specific capacitance was obtained in a real device two–electrode configuration with a commercial level of electrode loading (8.8 mg cm^{-2}). More importantly, the excellent capacitance exhibited by PANI–GH3 is highly maintained even at large current densities up to 30 A g^{-1} retaining more than 88.6% of its initial capacitance at 2 A g^{-1} (Figure 3.17). This remarkably high rate performance was also exhibited by other hybrid samples (PANI–GH2 and PANI–GH1) as shown in Figure 3.17.

Such excellent capacitive performance at a practical electrode mass loading is highly promising for commercial device applications. Unlike the bulk growth of PANI fibers within the graphene framework which could limit the ion diffusion channels; [39, 43–45] the restricted conformal growth of ultrafine PANI nanostructure over the hydrogel surface maintain the intrinsic porosity of the framework structure. The well preserved porosity of the hybrids promotes rapid ion diffusion and thereby maintain a high rate performance. The high performance metric of PANI–GH hybrid is further indicated by its excellent cycling stability. The PANI–GH3 could maintain a capacity retention of 95.8% after 3000 charge–discharge cycles at a high current density of 5 A g^{-1} (Figure 3.18). The performance of PANI–GH3 with other reported PANI based supercapacitor is presented in Table 3.1.

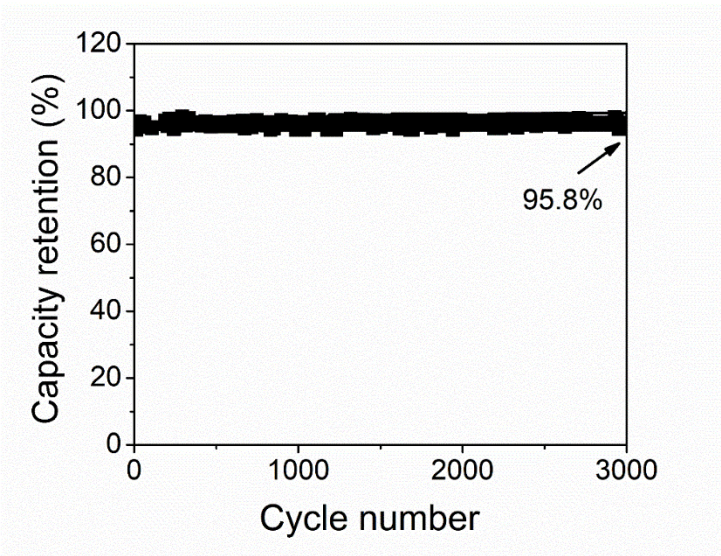

Figure 3.18. Long term cycling stability test of PANI–GH3 at a current density of 5 A g^{-1}.

Table 3.1. Performance comparison of other reported PANI–graphene based supercapacitors.

Electrode material	**Mass loading (mg cm^{-2})**	**Current density/ Scan rate**	**Specific capacitance (F g^{-1})**	**Rate capability**	**Reference**
PANI–N–doped graphene hydrogel	3	1 A g^{-1}	610	57.3% at 20 A g^{-1}	[39]
PANI NWA @ exfoliated graphite	5.89	1 A g^{-1}	607	72.4% at 10 A g^{-1}	[46]
PANI NWA /ordered bimodal mesoporous carbon	8	0.1 A g^{-1}	517	71.2% at 5 A g^{-1}	[10]
rGO wrapped PANI NFs	2.1	1 A g^{-1}	921	76% at 5 A g^{-1}	[47]
PANI–rGO petal	2.2	1 A g^{-1}	626	72% at 4 A g^{-1}	[48]
PANI wrapped grapheme sheet	2	1 A g^{-1}	578	72.7% at 10 A g^{-1}	[49]
PANI–GO	2	0.5 A g^{-1}	780	66% at 50 A g^{-1}	[50]
PANI NFs over functionalized rGO	0.91	1 A g^{-1}	692	53.5% at 40 A g^{-1}	[51]
RGO–F/PANI	0.65	1 A g^{-1}	790	75.7% at 10 A g^{-1}	[52]
PANI/B–doped graphene	6	1 mV s^{-1}	406	57% at 40 mV s^{-1}	[8]
PANI–CNT	2.6	0.5 A g^{-1}	385	66% at 10 A g^{-1}	[53]
N–doped G/PANI	2	0.5 A g^{-1}	620	76% at 20 A g^{-1}	[54]
G–PANI–PA	1	10 mV s^{-1}	652	65% at 10 A g^{-1}	[55]
PANI–porous carbon	0.08	1 A g^{-1}	512	71% at 20 A g^{-1}	[56]
PANI–rGO composite	1.8	0.8 A g^{-1}	423	81% at 26.5 A g^{-1}	[57]
sulfonated triazine functional graphene/PANI	0.01	1 A g^{-1}	1225	50.5% at 15 A g^{-1}	[58]
PANI nanoparticle/ graphene	0.013	0.1 A g^{-1}	257	56.42 % at 1 A g^{-1}	[59]

Hollow graphene/ PANI/graphene	0.14	0.5 A g^{-1}	682.75	31.8% at 20 A g^{-1}	[60]
Layered PANI/ graphene film	1.42	0.5 A g^{-1}	384	50% at 10 A g^{-1}	[35]
PANI@ Graphene /ZrO_2	0.01	0.3 A g^{-1}	1178.6	57% at 2 A g^{-1}	[61]
PANI–GH3	**8.8**	**5 A g^{-1}**	**503**	**88.6% at 30 A g^{-1}**	**This work**

The practical device applications of high performing PANI–GH electrodes could be understood from the Ragone plot which presents the relationship between specific energy and power densities for the real device full cell configuration (Figure 3.19). It was found that, PANI–GH3 electrode exhibited the maximum energy density of 29.85 Wh kg^{-1} with a corresponding high power density of 1.16 kW kg^{-1}. The maximum power density obtained by PANI–GH3 electrode was 19.5 kW kg^{-1} at a high energy density of 23.6 Wh kg^{-1}, illustrating its potential to be used in commercial applications.

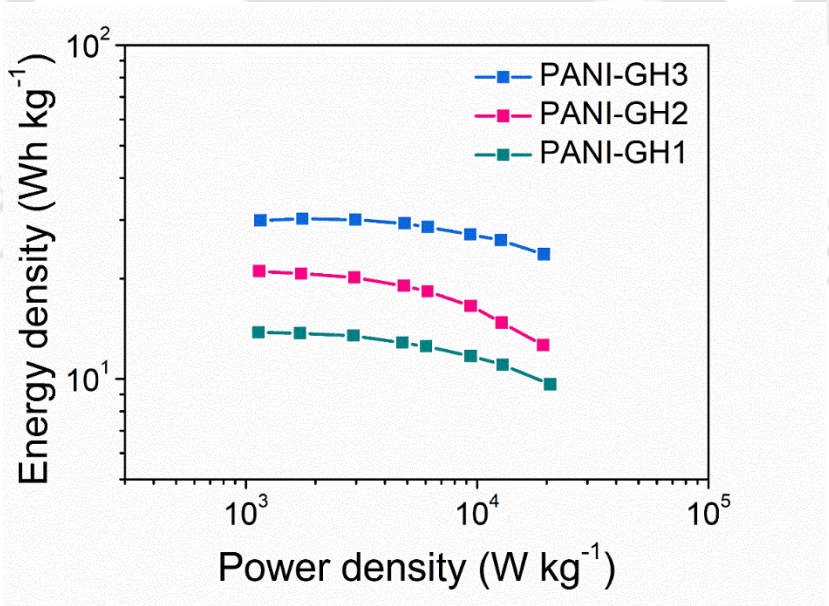

Figure 3.19. Ragone plots of different PANI–GH hybrids.

To further investigate the high capacitive performance of PANI–GH hybrid electrodes, electrochemical impedance spectroscopy (EIS) was studied. The Nyquist plots (within the frequency range of 100 kHz–10 mHz) of the GH and various hybrid samples exhibited quasi–

vertical lines parallel to imaginary Z axis in the low frequency range (Figure 3.20), suggesting capacitive behavior. However, in the high frequency region, the presence of a small semicircle with a short 45° transition line (Warburg region) from the semicircle to the quasi–vertical line (inset of Figure 3.20) demonstrate a low charge transfer and the ion diffusion resistances respectively of the hybrid material.

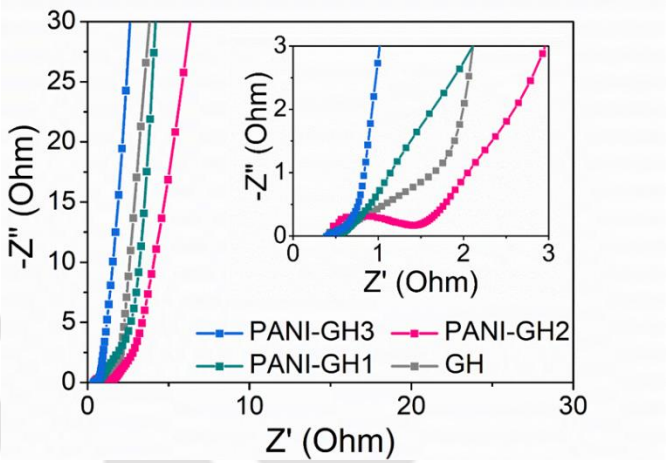

Figure 3.20. Electrochemical impedance spectra: Nyquist plots of GH and different PANI–GH hybrids.

To inspect this fast mass transport kinetics, we further studied the frequency dependent complex capacitances and the Bode plot (Figure 3.21.a–d). From the real (C') and imaginary (C'') part of complex capacitance vs frequency (f) plots (Figure 3.21.a–c), the value of relaxation time (τ_0) i.e. the time required to discharge the full energy of a capacitor with efficiency greater than 50%, was calculated from the peak frequency of C''. It was observed that, the PANI–GH hybrids showed a very low value of τ_0. The lowest τ_0 value of 0.25 s was obtained for PANI–GH3 (Figure 3.21.a). This result was further verified from the Bode plot (Figure 3.21.d) where a shifting from the resistive to the capacitive behavior was noticed at a phase angle of –45° which correspond to the knee frequency (f_0). The relaxation time constant could be calculated from f_0 and the value was found to be 0.2 s for PANI–GH3 sample. The obtained value of time constant is consistent with the value of τ_0 obtained above. The excellent frequency response of the PANI–GH hybrids stems from the unique porous and uniform nano–morphology of the hybrids which promotes fast mass transport kinetics.

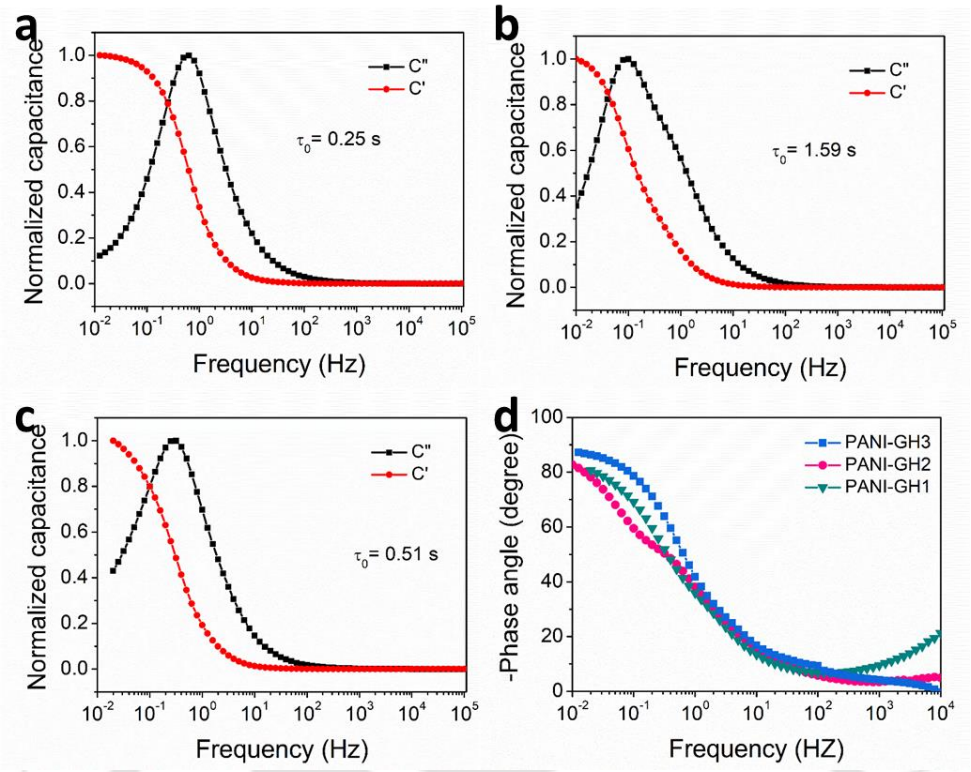

Figure 3.21. Complex capacitance (real and imaginary parts) vs frequency plot of (a) PANI−GH3, (b) PANI−GH2, and (c) PANI−GH1. (d) Bode plot of various PANI−GH hybrids.

A further comparison of the electrochemical performance of PANI–GH hybrid with APANI–GH hybrid (prepared solely in aqueous phase reaction) showed that, the shape of the CV profiles (Figure 3.22.a) changes sharply with the increase of scan rates which is attributed to the increased ion diffusion resistance owing to the agglomeration of PANI fibers within graphene hydrogel. Evidently, APANI–GH exhibited a very low specific capacitance of 142.7 F g^{-1} and poor rate performance with a capacity retention of only 57.6% at 10 A g^{-1} (Figure 3.22.b–c). Moreover, a large charge transfer resistance of ~ 9 Ω was obtained from the EIS spectrum of APANI–GH (Figure 3.22.d).

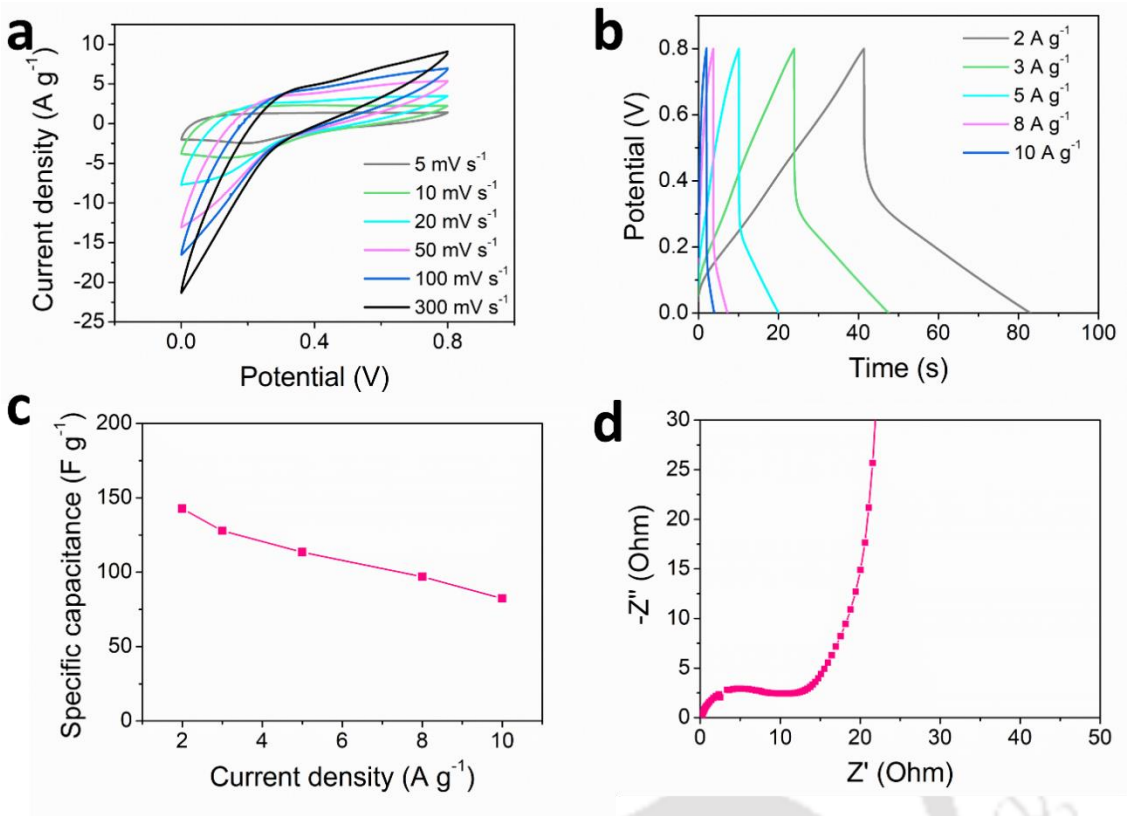

Figure 3.22. Electrochemical characterization of APANI–GH: (a) CV profiles at different scan rates, (b) CC curves at different current densities, (d) Specific capacitance vs current densities and (d) EIS spectrum of APANI–GH.

From the above results the excellent supercapacitive performance of the PANI–GH hybrid electrodes can be associated with a number of factors. Firstly, the uniform and dense nanostructure of PANI over the graphene surface resulted in a high redox–active mass loading of the electrode which gave rise to high specific pseudocapacitance even at practical level of mass loading. Secondly, the direct connection of ultrafine PANI nanostructure with the graphene surface without any bulk aggregation maintained a good electrical connection. Besides, the nanometre sized ultrafine morphology of PANI facilitates rapid interfacial charge transfer process by minimizing electron transport pathways. Finally, the hybridization of PANI with GH did not affect the porous network of hydrogel structure due to the direct vertical growth of PANI over graphene surface which remains one of the key advantages of this unique hybridization strategy. The open porous hybrid framework without any bulk aggregation of redox active PANI facilitates the fast electrolyte ion diffusion kinetics leading to the excellent capacitive performance at very high current densities.

3.4 Conclusions:

In conclusion, we have adopted a bio–mimicking unique strategy of hydrogel–organic interfacial reaction to develop ultrafine PANI–graphene hybrid hydrogel. A minute–scale ultrafast assembly process gives rise to porous graphene hydrogel which serves as an ideal medium for the development of fine structure tuned PANI nanostructures via controlled diffusion and restricted polymerization process. The MD simulation results provide the insights of the diffusion process in hydrogel–organic system and the presence of multiple attractive interactions of monomers (aniline) and as grown oligomers (emeraldine phase) with the graphene surface. As developed PANI–GH hybrid electrode with a high mass loading of 8.8 mg cm^{-2} exhibited remarkably high specific capacitance of 503 F g^{-1}, excellent rate performance (88.6% retention at 30 A g^{-1}) and long lasting cycling stability (with 95.8% retention after 3000 cycles). This exceptional performance of the PANI–GH hybrid was ascribed to the synergistic effect of the pseudocapacitive contribution of the PANI nanostructures and the favourable ion and charge transfer kinetics of the electrode due to the porous and conducting framework of the hybrid structure. Therefore, PANI–GH hybrid with a practical level of mass loading and excellent charge storage properties are very promising for real device applications.

References:

1. L.–Y. Chen, J.–Q. Xu, H. Choi, H. Konishi, S. Jin and X.–C. Li, Rapid control of phase growth by nanoparticles, *Nat. commun.*, 5 (2014), pp. 3879.
2. H. Hu, L. Wu, Y. Tan, Q. Zhong, M. Chen, Y. Qiu, D. Yang, B. Sun, Q. Zhang and Y. Yin, Interfacial Synthesis of Highly Stable CsPbX3/Oxide Janus Nanoparticles, *J. Am. Chem. Soc.*, 140 (2018), pp. 406–412.
3. B. Kowalczyk, K. J. M. Bishop, I. Lagzi, D. Wang, Y. Wei, S. Han and B. A. Grzybowski, Charged nanoparticles as supramolecular surfactants for controlling the growth and stability of microcrystals, *Nat. Mater.*, 11 (2012), pp. 227–232.
4. I. S. Smolkova, N. E. Kazantseva, V. Babayan, J. Vilcakova, N. Pizurova and P. Saha, The Role of Diffusion–Controlled Growth in the Formation of Uniform Iron Oxide Nanoparticles with a Link to Magnetic Hyperthermia, *Cryst. Growth Des.*, 17 (2017), pp. 2323–2332.
5. L. A. Estroff, Introduction: Biomineralization, *Chem. Rev.*, 108 (2008), pp. 4329–4331.
6. F. C. Meldrum and H. Cölfen, Controlling Mineral Morphologies and Structures in Biological and Synthetic Systems, *Chem. Rev.*, 108 (2008), pp. 4332–4432.
7. A. Garai, W. Shepherd, J. Huo and D. Bradshaw, Biomineral–inspired growth of metal–organic frameworks in gelatin hydrogel matrices, *J. Mater. Chem. B*, 1 (2013), pp. 3678–3684.
8. Q. Hao, X. Xia, W. Lei, W. Wang and J. Qiu, Facile synthesis of sandwich–like polyaniline/boron–doped graphene nano hybrid for supercapacitors, *Carbon*, 81 (2015), pp. 552–563.
9. H. Sun, L. Mei, J. Liang, Z. Zhao, C. Lee, H. Fei, M. Ding, J. Lau, M. Li, C. Wang, X. Xu, G. Hao, B. Papandrea, I. Shakir, B. Dunn, Y. Huang and X. Duan, Three–dimensional holey–graphene/niobia composite architectures for ultrahigh–rate energy storage, *Science*, 356 (2017), pp. 599.
10. Y. Yan, Q. Cheng, Z. Zhu, V. Pavlinek, P. Saha and C. Li, Controlled synthesis of hierarchical polyaniline nanowires/ordered bimodal mesoporous carbon nanocomposites with high surface area for supercapacitor electrodes, *J. Power Sources*, 240 (2013), pp. 544–550.
11. M. Yu, Y. Ma, J. Liu and S. Li, Polyaniline nanocone arrays synthesized on three–dimensional graphene network by electrodeposition for supercapacitor electrodes, *Carbon*, 87 (2015), pp. 98–105.
12. U. N. Maiti, J. Lim, K. E. Lee, W. J. Lee and S. O. Kim, Three–Dimensional Shape Engineered, Interfacial Gelation of Reduced Graphene Oxide for High Rate, Large Capacity Supercapacitors, *Adv. Mater.*, 26 (2014), pp. 615–619.
13. X. Wang, F. Wan, L. Zhang, Z. Zhao, Z. Niu and J. Chen, Large–Area Reduced Graphene Oxide Composite Films for Flexible Asymmetric Sandwich and Microsized Supercapacitors, *Adv. Funct. Mater.*, 28 (2018), pp. 1707247.
14. A. Sikdar, A. Majumdar, P. Dutta, M. Borah, S. O. Kim and U. N. Maiti, Ultra–large area graphene hybrid hydrogel for customized performance supercapacitors: High volumetric, areal energy density and potential wearability, *Electrochim. Acta*, 332 (2020), pp. 135492.
15. M. D. Hanwell, D. E. Curtis, D. C. Lonie, T. Vandermeersch, E. Zurek and G. R. Hutchison, Avogadro: an advanced semantic chemical editor, visualization, and analysis platform, *J. Cheminformatics*, 4 (2012), pp. 17.
16. W. Humphrey, A. Dalke and K. Schulten, VMD: Visual molecular dynamics, *J. Mol. Graph.*, 14 (1996), pp. 33–38.

17. H. Tang, D. Liu, Y. Zhao, X. Yang, J. Lu and F. Cui, Molecular Dynamics Study of the Aggregation Process of Graphene Oxide in Water, *J. Phys. Chem. C*, 119 (2015), pp. 26712–26718.
18. W. L. Jorgensen, J. Chandrasekhar, J. D. Madura, R. W. Impey and M. L. Klein, Comparison of simple potential functions for simulating liquid water, *J. Chem. Phys.*, 79 (1983), pp. 926–935.
19. S. Miyamoto and P. A. Kollman, Settle: An analytical version of the SHAKE and RATTLE algorithm for rigid water models, *J. Comput. Chem.*, 13 (1992), pp. 952–962.
20. J. C. Phillips, R. Braun, W. Wang, J. Gumbart, E. Tajkhorshid, E. Villa, C. Chipot, R. D. Skeel, L. Kalé and K. Schulten, Scalable molecular dynamics with NAMD, *J. Comput. Chem.*, 26 (2005), pp. 1781–1802.
21. W. L. Jorgensen, D. S. Maxwell and J. Tirado–Rives, Development and Testing of the OPLS All–Atom Force Field on Conformational Energetics and Properties of Organic Liquids, *J. Am. Chem. Soc.*, 118 (1996), pp. 11225–11236.
22. U. Essmann, L. Perera, M. L. Berkowitz, T. Darden, H. Lee and L. G. Pedersen, A smooth particle mesh Ewald method, *J. Chem. Phys.*, 103 (1995), pp. 8577–8593.
23. V. Chabot, D. Higgins, A. Yu, X. Xiao, Z. Chen and J. Zhang, A review of graphene and graphene oxide sponge: material synthesis and applications to energy and the environment, *Energy & Environmental Science*, 7 (2014), pp. 1564–1596.
24. O. C. Compton, Z. An, K. W. Putz, B. J. Hong, B. G. Hauser, L. Catherine Brinson and S. T. Nguyen, Additive–free hydrogelation of graphene oxide by ultrasonication, *Carbon*, 50 (2012), pp. 3399–3406.
25. Y. Xu, Z. Lin, X. Huang, Y. Wang, Y. Huang and X. Duan, Functionalized Graphene Hydrogel–Based High–Performance Supercapacitors, *Adv. Mater.*, 25 (2013), pp. 5779–5784.
26. Y. Xu, G. Shi and X. Duan, Self–Assembled Three–Dimensional Graphene Macrostructures: Synthesis and Applications in Supercapacitors, *Acc. Chem. Res.*, 48 (2015), pp. 1666–1675.
27. X. Yang, L. Qiu, C. Cheng, Y. Wu, Z.–F. Ma and D. Li, Ordered Gelation of Chemically Converted Graphene for Next–Generation Electroconductive Hydrogel Films, *Angew. Chem. Int. Ed.*, 50 (2011), pp. 7325–7328.
28. K. Krishnamoorthy, M. Veerapandian, R. Mohan and S.–J. Kim, Investigation of Raman and photoluminescence studies of reduced graphene oxide sheets, *Appl. Phys. A*, 106 (2012), pp. 501–506.
29. S. Stankovich, D. A. Dikin, R. D. Piner, K. A. Kohlhaas, A. Kleinhammes, Y. Jia, Y. Wu, S. T. Nguyen and R. S. Ruoff, Synthesis of graphene–based nanosheets via chemical reduction of exfoliated graphite oxide, *Carbon*, 45 (2007), pp. 1558–1565.
30. H. Wang, J. T. Robinson, X. Li and H. Dai, Solvothermal Reduction of Chemically Exfoliated Graphene Sheets, *J. Am. Chem. Soc.*, 131 (2009), pp. 9910–9911.
31. Y. Xu, K. Sheng, C. Li and G. Shi, Self–Assembled Graphene Hydrogel via a One–Step Hydrothermal Process, *ACS Nano*, 4 (2010), pp. 4324–4330.
32. R. Al–Gaashani, A. Najjar, Y. Zakaria, S. Mansour and M. A. Atieh, XPS and structural studies of high quality graphene oxide and reduced graphene oxide prepared by different chemical oxidation methods, *Ceram. Int.*, 45 (2019), pp. 14439–14448.
33. N. G. Bastús, J. Comenge and V. Puntes, Kinetically Controlled Seeded Growth Synthesis of Citrate–Stabilized Gold Nanoparticles of up to 200 nm: Size Focusing versus Ostwald Ripening, *Langmuir*, 27 (2011), pp. 11098–11105.

34. J. Wu, X. Chen, J. Fan, Y. Guo and W. Fang, Control of Reduction Kinetics to Form Palladium Nanocubes Enables Tunable Concavity, *Chem. Mater.*, 32 (2020), pp. 4591–4599.
35. Z. Tong, Y. Yang, J. Wang, J. Zhao, B.–L. Su and Y. Li, Layered polyaniline/graphene film from sandwich–structured polyaniline/graphene/polyaniline nanosheets for high–performance pseudosupercapacitors, *J. Mater. Chem. A*, 2 (2014), pp. 4642–4651.
36. J. Yan, T. Wei, B. Shao, Z. Fan, W. Qian, M. Zhang and F. Wei, Preparation of a graphene nanosheet/polyaniline composite with high specific capacitance, *Carbon*, 48 (2010), pp. 487–493.
37. H.–P. Cong, X.–C. Ren, P. Wang and S.–H. Yu, Flexible graphene–polyaniline composite paper for high–performance supercapacitor, *Energy & Environmental Science*, 6 (2013), pp. 1185–1191.
38. Y. Wang, X. Yang, A. G. Pandolfo, J. Ding and D. Li, High–Rate and High–Volumetric Capacitance of Compact Graphene–Polyaniline Hydrogel Electrodes, *Advanced Energy Materials*, 6 (2016), pp. 1600185.
39. J. Luo, W. Zhong, Y. Zou, C. Xiong and W. Yang, Preparation of morphology–controllable polyaniline and polyaniline/graphene hydrogels for high performance binder–free supercapacitor electrodes, *J. Power Sources*, 319 (2016), pp. 73–81.
40. J. Wu, Q. e. Zhang, J. Wang, X. Huang and H. Bai, A self–assembly route to porous polyaniline/reduced graphene oxide composite materials with molecular–level uniformity for high–performance supercapacitors, *Energy & Environmental Science*, 11 (2018), pp. 1280–1286.
41. K. Zhang, L. L. Zhang, X. S. Zhao and J. Wu, Graphene/Polyaniline Nanofiber Composites as Supercapacitor Electrodes, *Chem. Mater.*, 22 (2010), pp. 1392–1401.
42. M. D. Stoller and R. S. Ruoff, Best practice methods for determining an electrode material's performance for ultracapacitors, *Energy & Environmental Science*, 3 (2010), pp. 1294–1301.
43. J. Zhang, J. Wang, J. Yang, Y. Wang and M. B. Chan–Park, Three–Dimensional Macroporous Graphene Foam Filled with Mesoporous Polyaniline Network for High Areal Capacitance, *ACS Sustain. Chem. Eng.*, 2 (2014), pp. 2291–2296.
44. Q. Wu, Y. Xu, Z. Yao, A. Liu and G. Shi, Supercapacitors Based on Flexible Graphene/Polyaniline Nanofiber Composite Films, *ACS Nano*, 4 (2010), pp. 1963–1970.
45. H. Qiu, X. Han, F. Qiu and J. Yang, Facile route to covalently–jointed graphene/polyaniline composite and it's enhanced electrochemical performances for supercapacitors, *Appl. Surf. Sci.*, 376 (2016), pp. 261–268.
46. Y.–J. Ye, Z.–H. Huang, Y. Song, J.–W. Geng, X.–X. Xu and X.–X. Liu, Electrochemical Growth of Polyaniline Nanowire Arrays on Graphene Sheets in Partially Exfoliated Graphite Foil for High–Performance Supercapacitive Materials, *Electrochim. Acta*, 240 (2017), pp. 72–79.
47. N. Hu, L. Zhang, C. Yang, J. Zhao, Z. Yang, H. Wei, H. Liao, Z. Feng, A. Fisher, Y. Zhang and Z. J. Xu, Three–dimensional skeleton networks of graphene wrapped polyaniline nanofibers: an excellent structure for high–performance flexible solid–state supercapacitors, *Sci. Rep.*, 6 (2016), pp. 19777.
48. C.–M. Chang, Z.–H. Hu, T.–Y. Lee, Y.–A. Huang, W.–F. Ji, W.–R. Liu, J.–M. Yeh and Y. Wei, Biotemplated hierarchical polyaniline composite electrodes with high performance for flexible supercapacitors, *J. Mater. Chem. A*, 4 (2016), pp. 9133–9145.

49. J. Li, D. Xiao, Y. Ren, H. Liu, Z. Chen and J. Xiao, Bridging of adjacent graphene/polyaniline layers with polyaniline nanofibers for supercapacitor electrode materials, *Electrochim. Acta*, 300 (2019), pp. 193–201.
50. Q. Zhou, T. Wei, J. Yue, L. Sheng and Z. Fan, Polyaniline nanofibers confined into graphene oxide architecture for high–performance supercapacitors, *Electrochim. Acta*, 291 (2018), pp. 234–241.
51. K. Jin, W. Zhang, Y. Wang, X. Guo, Z. Chen, L. Li, Y. Zhang, Z. Wang, J. Chen, L. Sun and T. Zhang, In–situ hybridization of polyaniline nanofibers on functionalized reduced graphene oxide films for high–performance supercapacitor, *Electrochim. Acta*, 285 (2018), pp. 221–229.
52. P. Yu, X. Zhao, Z. Huang, Y. Li and Q. Zhang, Free–standing three–dimensional graphene and polyaniline nanowire arrays hybrid foams for high–performance flexible and lightweight supercapacitors, *J. Mater. Chem. A*, 2 (2014), pp. 14413–14420.
53. S. K. Simotwo, C. DelRe and V. Kalra, Supercapacitor Electrodes Based on High–Purity Electrospun Polyaniline and Polyaniline–Carbon Nanotube Nanofibers, *ACS Appl. Mat. Interfaces*, 8 (2016), pp. 21261–21269.
54. M. Ge, H. Hao, Q. Lv, J. Wu and W. Li, Hierarchical nanocomposite that coupled nitrogen–doped graphene with aligned PANI cores arrays for high–performance supercapacitor, *Electrochim. Acta*, 330 (2020), pp. 135236.
55. P. Sekar, B. Anothumakkool and S. Kurungot, 3D Polyaniline Porous Layer Anchored Pillared Graphene Sheets: Enhanced Interface Joined with High Conductivity for Better Charge Storage Applications, *ACS Appl. Mat. Interfaces*, 7 (2015), pp. 7661–7669.
56. W. Zhang, X. Jin, H. Chai, G. Diao and Y. Piao, 3D Hybrids of Interconnected Porous Carbon Nanosheets/Vertically Aligned Polyaniline Nanowires for High–Performance Supercapacitors, *Advanced Materials Interfaces*, 5 (2018), pp. 1800106.
57. Z. Wang, Q. e. Zhang, S. Long, Y. Luo, P. Yu, Z. Tan, J. Bai, B. Qu, Y. Yang, J. Shi, H. Zhou, Z.–Y. Xiao, W. Hong and H. Bai, Three–Dimensional Printing of Polyaniline/Reduced Graphene Oxide Composite for High–Performance Planar Supercapacitor, *ACS Appl. Mat. Interfaces*, 10 (2018), pp. 10437–10444.
58. Y. Liu, Y. Ma, S. Guang, H. Xu and X. Su, Facile fabrication of three–dimensional highly ordered structural polyaniline–graphene bulk hybrid materials for high performance supercapacitor electrodes, *J. Mater. Chem. A*, 2 (2014), pp. 813–823.
59. Z.–F. Li, H. Zhang, Q. Liu, L. Sun, L. Stanciu and J. Xie, Fabrication of High–Surface–Area Graphene/Polyaniline Nanocomposites and Their Application in Supercapacitors, *ACS Appl. Mat. Interfaces*, 5 (2013), pp. 2685–2691.
60. X. Liu, N. Wen, X. Wang and Y. Zheng, A High–Performance Hierarchical Graphene@Polyaniline@Graphene Sandwich Containing Hollow Structures for Supercapacitor Electrodes, *ACS Sustain. Chem. Eng.*, 3 (2015), pp. 475–482.
61. S. Giri, D. Ghosh and C. K. Das, Growth of Vertically Aligned Tunable Polyaniline on Graphene/ZrO2 Nanocomposites for Supercapacitor Energy–Storage Application, *Adv. Funct. Mater.*, 24 (2014), pp. 1312–1324.

Chapter 4

Large Scale Ambient Casting of Graphene-MXene-3D Hydrogel for High Energy Density Asymmetric Supercapacitor

Chapter 4

Large Scale Ambient Casting of Graphene–MXene 3D Hydrogel for High Energy Density Asymmetric Supercapacitor

The assembly of 2D sheets of MXene into 3D macroscopic structure has gained intriguing research interests due to their versatile functionality but is largely restricted by the intrinsic properties of MXenes e.g. small flake size, hydrophilic nature, rigidity of MXene sheets and tendency to oxidize particularly at elevated temperature. In this chapter, we present a facile room temperature casting based self–assembly of MXene and reduced graphene oxide (RGO) 3D hydrogel hybrid. The highly porous and conducting RGO–MXene hydrogel hybrid (MGH) possesses a low level of oxidation as revealed from the X–ray photoelectron spectroscopy (XPS) study. The MGH with 20 wt% graphene content has been directly used as a high performing supercapacitor electrode exhibiting a specific capacitance of 357.1 F g^{-1} at a scan rate of 10 mV s^{-1}. Furthermore, an asymmetric supercapacitor device has been fabricated with MGH as the negative electrode and a polyaniline–RGO hydrogel hybrid (PGH) as the positive electrode providing a maximum energy density of 30.3 Wh kg^{-1} at an ultrahigh power density of 1.13 kW Kg^{-1}.

4.1 Introduction:

MXenes are a new class of 2D materials having been represented by $M_{n+1}X_nT_x$, M being the transition metals, X represents carbon and/or nitrogen and T_x symbolizes the surface terminal groups. [1] Due to their unique physical and chemical properties such as excellent electrical conductivity (~10000 S cm^{-1}), redox active hydrophilic surface, and high mechanical stability. [2] [3] MXenes have shown promising potential for the applications in energy storage, [4] [5] EMI shielding, [6] [7] catalysis, [8] gas sensing [9] etc. Nonetheless, their versatile applications are largely impaired by the restacking of 2D MXene sheets owing to their high surface energy and interlayer van der Waals interactions.

As highlighted in chapter 1, the assembly of 2D materials into 3D macroscopic structure is one of the viable routes to restrain the restacking issue. [10] [11] Although such assemblies have been easily achieved for graphene, the direct assembly of MXene sheets are largely restricted by their small flake size, hydrophilic character, rigidity of MXene sheets and high tendency to get oxidized particularly at elevated temperature. So far, 3D assembly of MXene

has been realized via chemical cross–linking with polymer or cellulose fibers and graphene assisted gelation strategies. [12–15] However, most of these synthesis protocols are relied on the heat involved steps which not only increase the cost of the process but more importantly raise the chance of oxidation of MXenes. [16] Furthermore, the non–conducting polymeric linkers tend to inhibit the overall conductivity of the MXenes. Therefore, a new assembly strategy of MXenes should be developed to address these challenges.

In this chapter, we demonstrate a room temperature metal particle (zinc) assisted assembly of MXene–reduced graphene oxide (MGH) 3D hybrid hydrogel. The zinc particles in this process simultaneously assemble and reduce the GO sheets into RGO via continuous electron transfer from zinc to GO sheets. Importantly, this assembly process possesses excellent processability which has been shown by casting the hydrogel over arbitrary templates resulting in customised shaped 3D hydrogel. Moreover, XPS study reveals that the room temperature mild gelation strategy largely limits the high degree oxidation of MXene sheets. The as developed MGH having a conducting porous framework structure has been utilized a high performing supercapacitor electrode which exhibits an excellent specific capacitance of 357.1 F g^{-1} at 10 mV s^{-1} with good rate performance. To increase the energy density of a device we need large the operating voltage window, since energy density varies as the square of the voltage window. To increase the voltage window we have fabricated an asymmetric supercapacitor device by utilizing MGH as the negative electrode and a PANI–RGO hybrid 3D hydrogel (PGH) as the positive electrode. The PGH was obtained by hybridizing GH with uniform PANI nanocones via previously demonstrated hydrogel–organic interfacial reaction. The as fabricated all–pseudocapacitance asymmetric supercapacitor device (MGH//PGH) provided a very high energy density of 30.3 Wh kg^{-1} corresponding to a power density of 1.13 kW kg^{-1}. This work demonstrates a facile and cost effective strategy to develop 3D MXene–hybrid assembly for high performance energy storage devices.

4.2 Experimental section:

4.2.1 Synthesis of few layer MXene ($Ti_3C_2T_x$) aqueous dispersion:

The synthesis of few layer MXene aqueous dispersion was prepared by etching Ti_3AlC_2 powder in LiF/HCl mixture as reported elsewhere. [17] Briefly, 1 g LiF powder was first dissolved in 20 mL 9 M HCl. Subsequently, 1 g Ti_3AlC_2 powder was added slowly to the LiF/HCl mixture under continuous stirring and kept at 35 °C for 24 hours. The obtained clay like material was washed repeatedly with deionized water by centrifuging at 3500 rpm for 5 min until the pH

becomes ~7. The material was re–dispersed in water, ultrasonicated for 1 hour under continuous aRGOn bubbling and centrifuged again at 3500 rpm for 1 hour to obtain few layer MXene ($Ti_3C_2T_x$) aqueous dispersion.

4.2.2 Fabrication of MXene/RGO hybrid hydrogel (MGH):

Aqueous dispersion of GO was first prepared following modified hummers method as described in our previous report. [18] A typical fabrication of MGH4:1 with 80% MXene is as follows: aqueous dispersion of MXene (6 mL, 20 mg mL^{-1}) and GO (2.14 mL, 14 mg mL^{-1}) were first mixed and diluted by adding 6.86 mL of deionized water. Then, 37.5 mg of Zn powder (Zn powder/GO = 1.25:1, w/w) was added to the above MXene/GO mixture and shaken it for a few seconds by hand before keeping it for 12 hours at room temperature. The as developed MGH was reacted with 10% HCl solution to etch Zn powder. Finally the hydrogel was washed with deionized water to remove HCl and residual Zn ions. Hybrid hydrogels with different weight ratios of MXene and GO were prepared by varying the MXene and GO content keeping the total concentration of MXene and GO in the dispersion fixed at 10 mg mL^{-1}. The MXene content in MGH was varied with wt% of 80, 70, 60 and 50 and named as MGH4:1, MGH7:3, MGH3:2 and MGH1:1 respectively. For comparison pure RGO hydrogel (GH) was prepared under the same experimental procedure and condition of MGH4:1 except adding MXene.

4.2.3 Development of PANI/RGO hybrids (PGH):

As developed GH was hybridized with PANI by interfacial polymerization technique. [19] For the development of PGH hybrids with varying PANI content, GH was first saturated with ammonium persulfate (8 mmol, 16 mmol and 24 mmol) dissolved in 10 mL 1M HCl for 1 day at ambient condition. The interfacial polymerization process was carried out by keeping GH saturated with different amount of ammonium persulfate in a solution containing 3.2 mmol of aniline dissolved in 10 mL chloroform for 1 day at room temperature. The as developed PGH hybrid hydrogel was washed with ethanol, deionized water repeatedly and kept in water for further use. Depending upon the ammonium persulfate concentrations, the PGH hybrids were named as PGH1, PGH2 and PGH3 respectively.

4.2.4 Characterizations:

The morphology of the obtained samples was observed using Zeiss Sigma 300 field emission scanning electron microscope (FESEM) and JEOL–2100F field emission transmission electron

microscope (FETEM, accelerating voltage–200 kV). The X–ray diffraction (XRD) data was collected in powder mode with Cu–Kα radiation (wavelength of 0.15418 nm) on Rigaku (SmartLab, 5 kW) X–ray diffractometer. Raman spectra were recorded on a Horiba (LabRam HR) laser micro Raman spectrometer using a laser source of 514 nm. The chemical composition of MGH was analysed by ESCALAB Xi+ (Thermo Fisher) X–ray photo electron spectroscopy (XPS) instrument.

4.2.5 Electrochemical measurement:

The electrochemical performance of the samples was tested at room temperature in a plastic Swagelok cell using a PARSTAT 3000A–DX (Princeton Applied Research) electrochemical workstation. 3 M H_2SO_4 was used as electrolyte. The three–electrode tests were performed by directly using free standing MGH or PGH hydrogels on glassy carbon as working electrode, Ag/AgCl (in 1 M KCl) as reference electrode and activated carbon (YP 50) as counter electrode. The cyclic voltammetry (CV) and galvanostatic charge–discharge (GCD) tests for MGH were conducted within a potential window of –0.6–0.2 V vs Ag/AgAgCl whereas for PGH a potential window of 0–0.8 V was used. The electrochemical impedance spectroscopy (EIS) tests were carried out in a frequency range of 10 mHz to 100 kHz at a fixed potential of amplitude of 10 mV.. In asymmetric device, MGH4:1 and PGH3 were used as negative and positive electrodes respectively.

The specific capacitance (C_s) of various samples was calculated from CV curves using the equation 1.3.

To construct the asymmetric device, the masses of the positive (PGH3) and negative (MGH4:1) electrodes were balanced according to the following equation:

$$\frac{m_+}{m_-} = \frac{C_- \times \Delta E_-}{C_+ \times \Delta E_+}$$

Where ΔE_+ and ΔE_- are the potential window for the positive and negative electrodes respectively as obtained from three–electrode measurements. The gravimetric energy and power density of the asymmetric device were evaluated from GCD curves using the equations 1.13 and 1.15.

4.3 Results and discussions:

Figure 4.1 illustrates the synthesis process of RGO–MXene hydrogel (MGH). Uniform Ti_3C_2 MXene dispersion was first obtained by etching Al from the titanium aluminium carbide

(Ti_3AlC_2) MAX phase. For the gelation process, a certain amount of zinc powder was mixed with a dispersion containing aqueous solutions of MXene (80 wt%) and GO. The mechanism of gelation process is similar to the previously developed PGH hybrid as discussed in chapter 2. In short, when zinc particles are added to the mixed dispersion there is a continuous electron transfer from metallic zinc to the GO sheets owing to the higher reduction potential of zinc (−0.76 V for Zn/Zn^{2+}) as compared to GO (−0.6 V for RGO/GO). Consequently, Zn^{2+} ions are also formed simultaneously which attract negatively charged sheets of GO and MXene which resulted in the 3D assembly of MXene and RGO. [20] The water content of the hydrogel was measured to be 95% of its own weight. The zinc particles embedded within the hydrogel were removed by etching them with 10% HCl solution followed by washing with water. The as obtained MGH with 80% MXene content was named as MGH4:1. To compare the electrochemical performance, MGH hybrids with different MXene content namely, MGH7:3 (70% MXene), MGH3:2 (60% MXene), MGH1:1 (50% MXene), GH (0% MXene) were also synthesized by the same protocol. The excellent processability of this gelation protocol was demonstrated by adopting a template–casting based approach in which GO and MXene mixed with zinc powered was casted into desired shape resulting in a porous conducting hybrid hydrogel (Figure 4.2). Moreover, the gelation process is highly scalable which is established by developing a large sized hybrid hydrogel with a dimension of 6 cm × 4 cm (Figure 4.2).

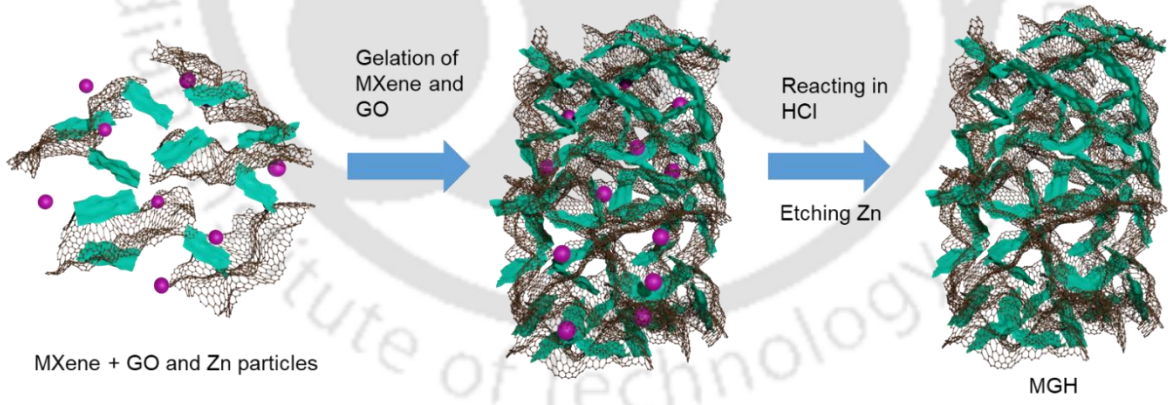

Figure 4.1. Schematic illustration of the gelation process of MGH hybrid.

Figure 4.2. Template assisted gel casting of MGH hybrid for desired shape. The scale bar is 1 cm.

4.3.1 Morphological study of MGH:

FESEM image showed that MGH4:1 hybrid possessed an interconnected 3D porous structure where the dimension of the pores varies in the range 1–5 µm. The pore walls of the hydrogel were constructed by the thin sheets of RGO and MXene. Although it is very hard to distinguish MXene and RGO sheets from the FESEM image. FETEM image further showed that the RGO sheets contain numerous nanosheets of MXenes. Such an interconnected porous structure is beneficial for the prevention of the restacking of MXene and RGO sheets.

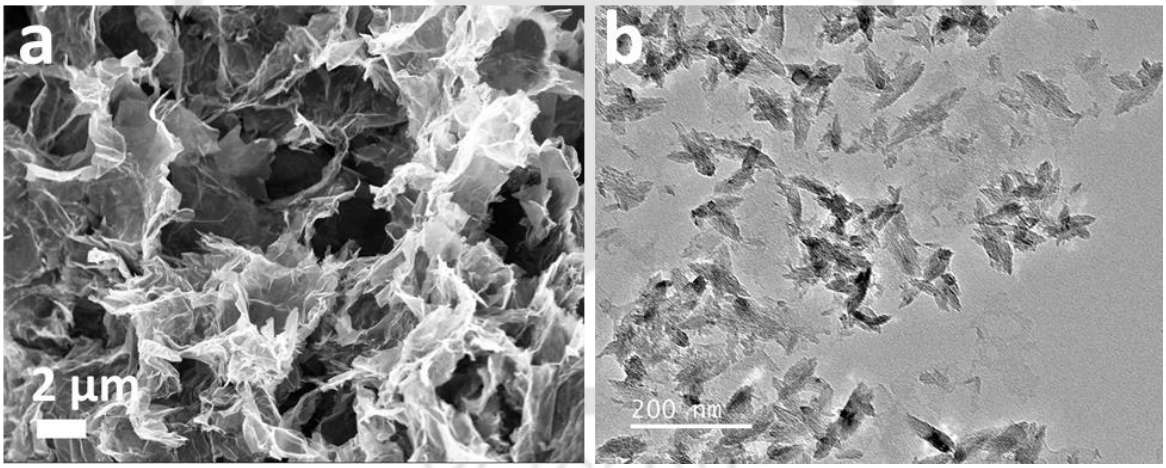

Figure 4.3. Morphology of MGH: (a) FESEM and (b) FETEM images of MGH hybrid.

4.3.2 Structural analysis of MGH hybrid:

The successful etching and delamination of Ti_3AlC_2 into Ti_3C_2 MXene was confirmed from the XRD study. It was seen that, the XRD pattern of Ti_3AlC_2 (Figure 4.4) contains several sharp peaks owing to the crystalline state of Ti_3AlC_2. [21] However, after the etching process, only the peak corresponding to the (002) plane remained although broadened and shifted to lower 2θ (from 9.5° Ti_3AlC_2 in to 7.8° in MXene) values, while the other peaks got so much

broadened that they were very hard to detect (Figure 4.4). The shifting of the peaks to lower 2θ values indicates increase of interlayer spacing in the MXene sample suggesting successful delamination of MAX layers. [20] In the XRD pattern of MGH4:1 hybrid (Figure 4.4), we again observed the presence of only (002) peak at 2θ of 6.1° indicating the well preserved structure of MXene in the MGH4:1 hybrid. Once again the (002) peak was seen to be broadened and shifted to the lower 2θ value as compared to the pure MXene. [22, 23] This result indicate that, the 2D sheets of MXenes and RGO were well separated in the MGH4:1 hybrid suggesting the prevention of restacking of 2D sheets in the 3D structure. Nevertheless, no peak was detected corresponding to the RGO structure which was attributed to the presence of very low wt% of RGO in MGH4:1.

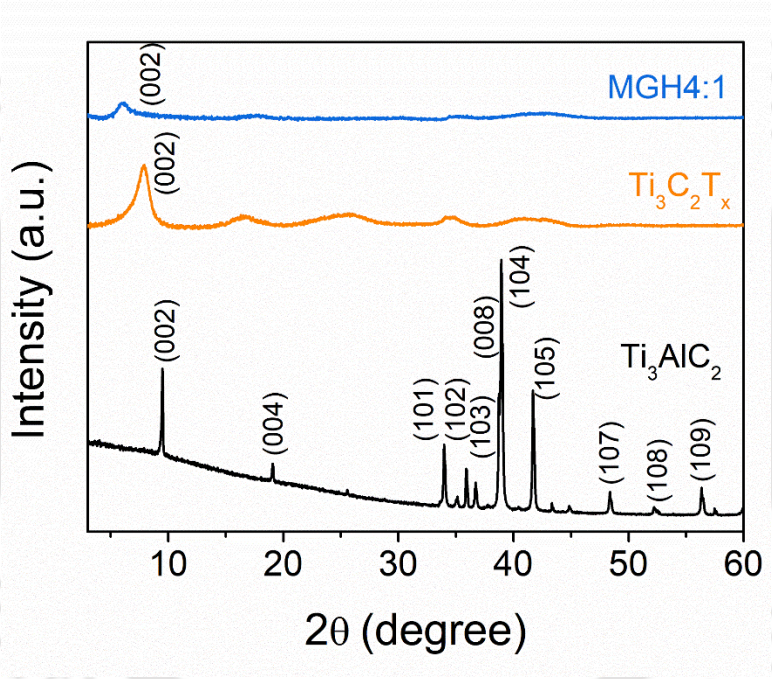

Figure 4.4. Structural characterization: comparison of XRD patterns of MGH, MXene ($Ti_2C_2T_x$) and Ti_3AlC_2.

Raman spectroscopy studies were further performed to confirm the successful formation of the MXene and RGO hybrid in MGH4:1. The Raman spectrum of MGH (Figure 4.5) exhibited characteristics D and G peaks of RGO at 1350 and 1590 cm^{-1} corresponding to the presence of defects in the graphitic structure and the in–plane stretching mode of C=C bonds. In addition, five more peaks were also detected in the range 150–750 cm^{-1} (Figure 4.5), which are associated with the out–of–plane vibrations (A_{1g} mode) of Ti and C atoms (198.4

and 721 cm^{-1}) and in–plane vibrations (E_{2g}) of Ti, C and surface terminations (282, 392, 603 cm^{-1}). [24] Theses Raman peaks altogether reveals a well–preserved hybrid structure of MXene and RGO in MGH4:1 hydrogel.

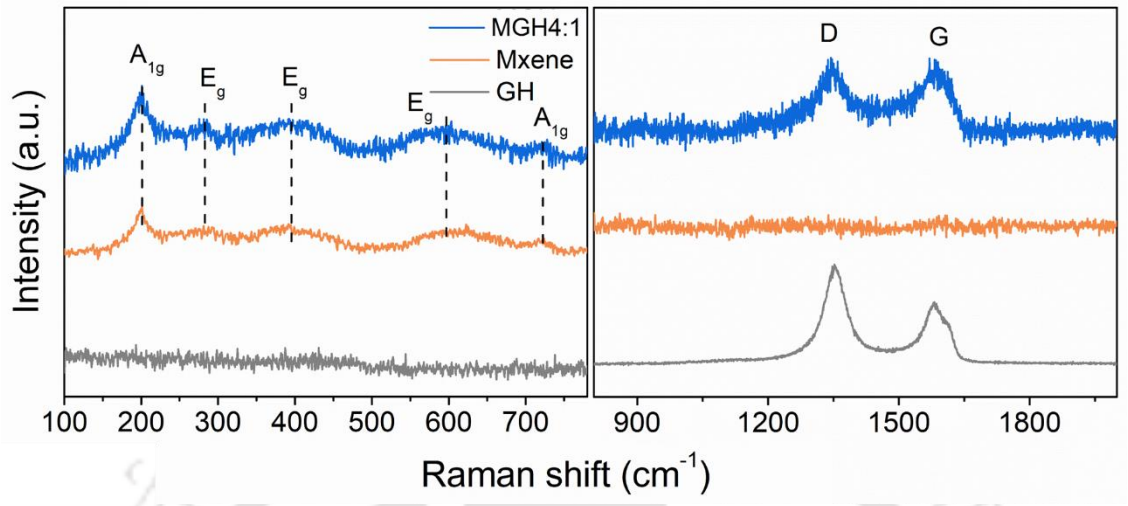

Figure 4.5. Structural characterization: comparison of Raman spectra of MGH, MXene ($Ti_2C_2T_x$) and pure GH.

The XPS characterizations revealed the electronic structure of MXene and MGH4:1 hybrid. First, the survey spectra revealed the presence of the constituents of MXene i.e. Ti, C, O and F in both MXene and MGH4:1 hybrid (Figure 4.6.a). Next, the high resolution C1s XPS spectra of pure MXene and MGH4:1 were deconvoluted into five components (Figure 4.6.b) associated with the C–Ti (282.2 eV), Ti–C–O (283.2 eV), C–C (284.8 eV), C–O (286.2 eV) and O=C–O (287.6 eV) bonds. [29] Importantly, the atomic% of C–C (from 43.1% to 60.1%) and C–O (from 6.1% to 12.4%) were found to increase in MGH4:1 (Figure 4.6.b), in comparison to MXene suggesting successful incorporation of MXene and RGO sheets in the hybrid structure. Furthermore, the high resolution Ti 2p spectra of MXene and MGH4:1 (Figure 4.6.c) were fitted with five doublets (Ti 2p3/2–Ti 2p1/2) of which four doublets were associated with Ti (I, II or III) (455 and 461.2 eV), Ti^{2+} (I, II or III) (455.8 and 461.5 eV), Ti^{3+} (I, II or III) (457.1 and 462.8 eV), Ti^{4+} (458.9 and 464.5 eV) of TiO_2 whereas the fifth doublet at 460.2 and 466.2 eV was ascribed to the C–Ti–F_x (III) ionic states of Ti of MXene. [25] The numbers I, II and III as appeared above denote the respective moieties e.g. $Ti_3C_2O_x$, $Ti_3C_2(OH)_x$ and $Ti_3C_2F_x$ present in MXene. Very importantly, the peak intensity related to the TiO_2 of MXene

was not found to increase after the gelation process, suggesting the possible inhibition of the oxidation of MXene sheets in MGH4:1.

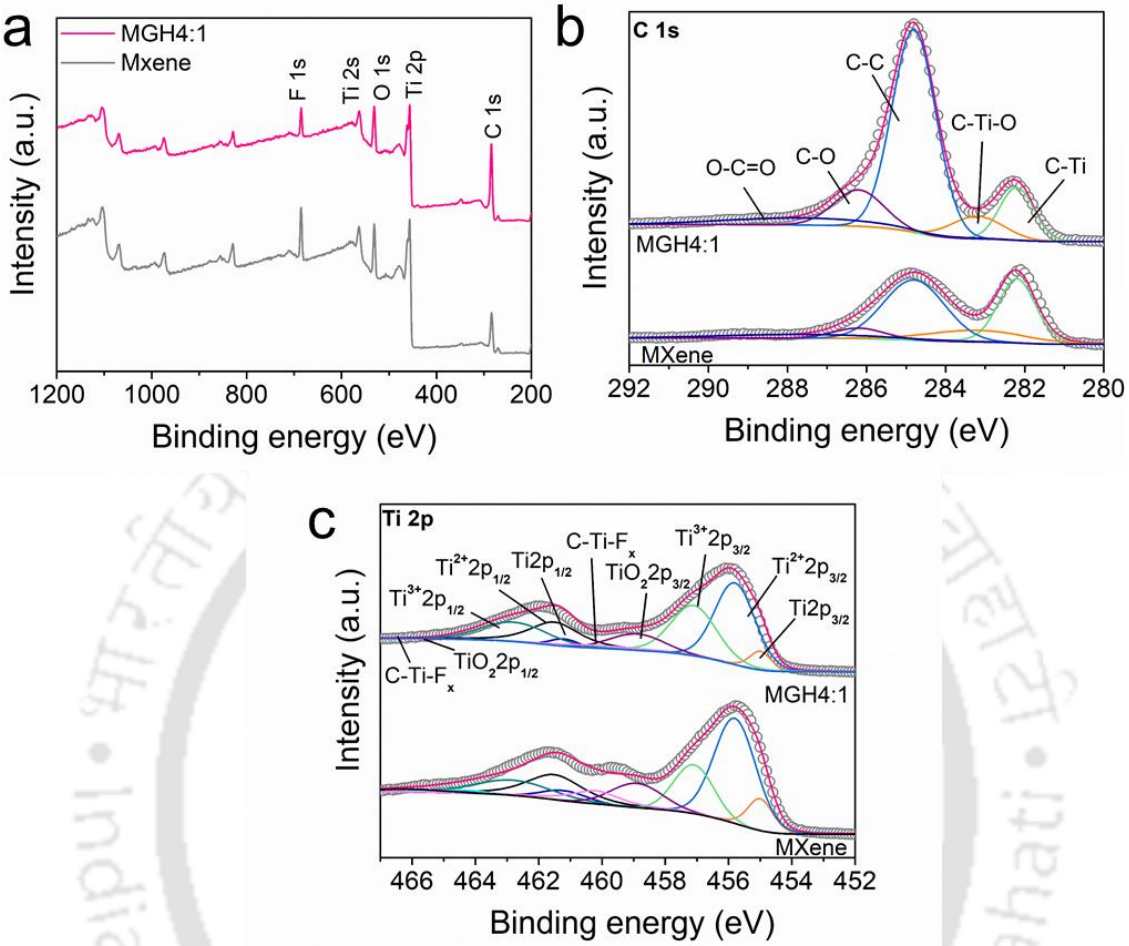

Figure 4.6. (a) XPS survey spectra of MGH4:1 and MXene; High resolution (b) C 1s and (b) Ti 2p spectra of MGH4:1 and MXene.

4.3.3 Development of graphene–polyaniline (PGH) hybrid:

To demonstrate the versatile applicability of casted hydrogel, it has been used as hydrated confined reactor for controlled in–situ growth of ultrafine conducting polymer polyaniline (PANI) over bare GH framework at ambient condition. Here we have adopted the previously demonstrated (Chapter 3) hydrogel–organic bi–phasic polymerization to grow PANI over GH. FESEM image of PGH (Figure 4.7.a) showed that ultrafine nanocones (length ~ 50 nm) of PANI was uniformly and densely developed over the surface of GH without any bulk aggregation. The ultrafine nanocone morphology is very different as compared to the growth of PANI via regular aqueous–organic interfacial process which results in much larger

nanowire (up to several microns) morphology as discussed in chapter 3. This growth pattern highlights the important role of GH in controlled nano–hybridization. Moreover, PGH exhibited porous structure (inset of Figure 4.7.a) very similar to MGH owing to the conformal growth of PANI over 3D framework without bulk growth within the pores. The uniform development of PANI nanocones is also evident from the FETEM image (Figure 4.7.b). To identify the crystal structure of PANI, XRD pattern of PGH was analysed. Figure 4.8 shows that, the XRD pattern of PGH exhibits characteristic diffraction peaks at 2θ of 14.7°, 20.5° and 25.4° corresponding to the (011), (020) and (200) crystallographic planes confirming the formation of emeraldine phase of PANI nanostructure. [26]

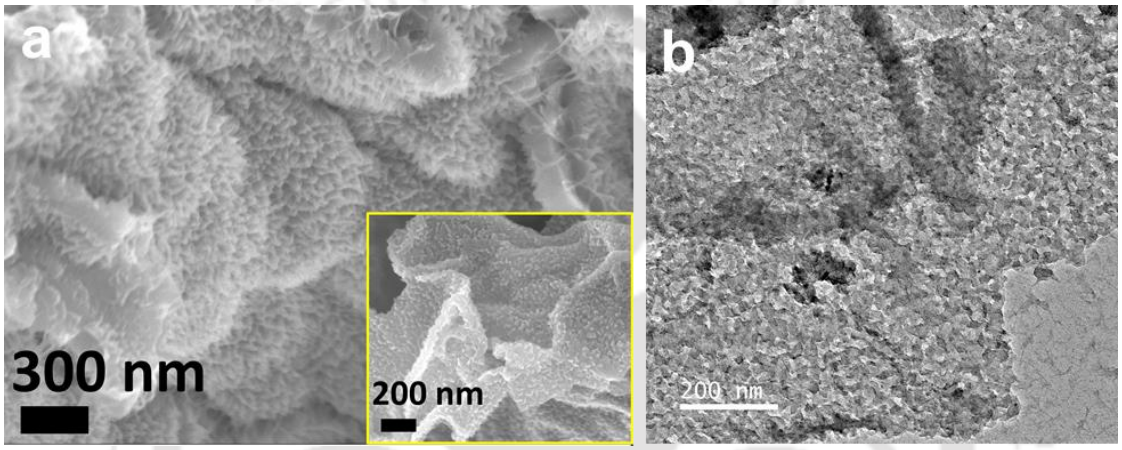

Figure 4.7. Morphology of PGH: (a) FESEM and (b) FETEM images of PGH. The inset of (a) shows corresponding low magnification FESEM image.

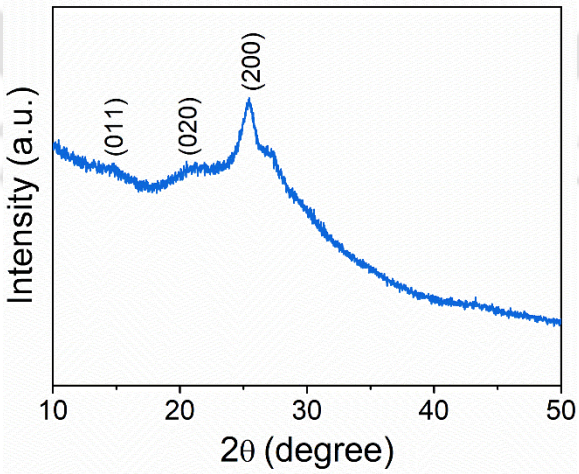

Figure 4.8. XRD pattern of PGH.

4.3.4 Electrochemical characterizations:

The 3D MGH4:1 hybrid having highly conducting porous morphology is ideal for supercapacitor electrode. To test the performance of the hybrid electrode, electrochemical characterizations were performed in three–electrode configuration. The cyclic voltammetry (CV) profile of MGH hybrids (Figure 4.9) with different MXene content at a scan rate of 10 mV s^{-1} exhibited a pair of distinct redox peaks within the potential range of –0.5 V to 0.1 V vs Ag/AgCl indicating the pseudocapacitive nature of MGH electrodes which was attributed to the surface redox activity of MXene sheets. [27] The specific capacitance obtained from the CV profiles at 10 mV s^{-1} (Figure 4.9) showed that the capacitance value was highest for MGH4:1 (357.1 F g^{-1}) with MXene content 80 wt% and the capacitance value decreased with the decreasing MXene content (indicated by the decreased area of CV profiles) (Figure 4.9). This result suggests that the capacitive contribution of MXene electrodes was mainly dominated by the pseudocapacitance of MXene.

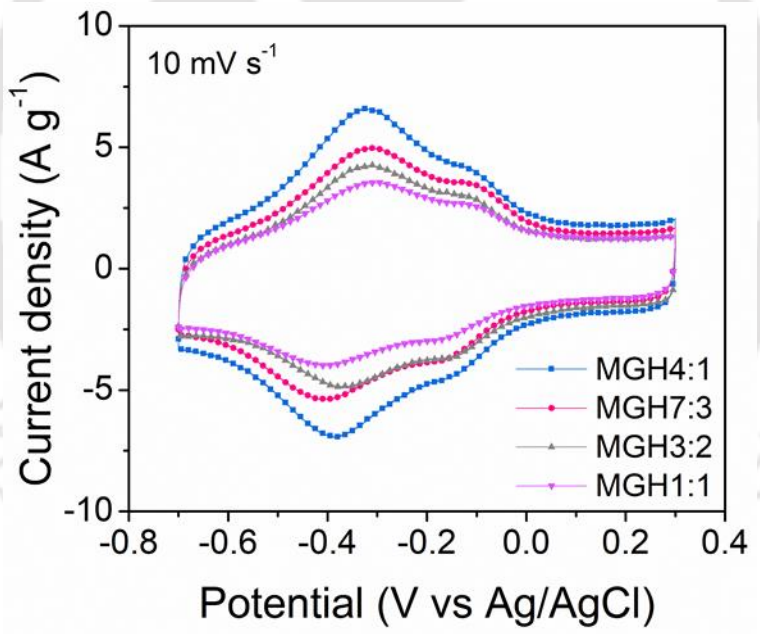

Figure 4.9. Electrochemical characterization: cyclic voltammetry curves of MGH hybrids with varying MXene content at 10 mV s^{-1}

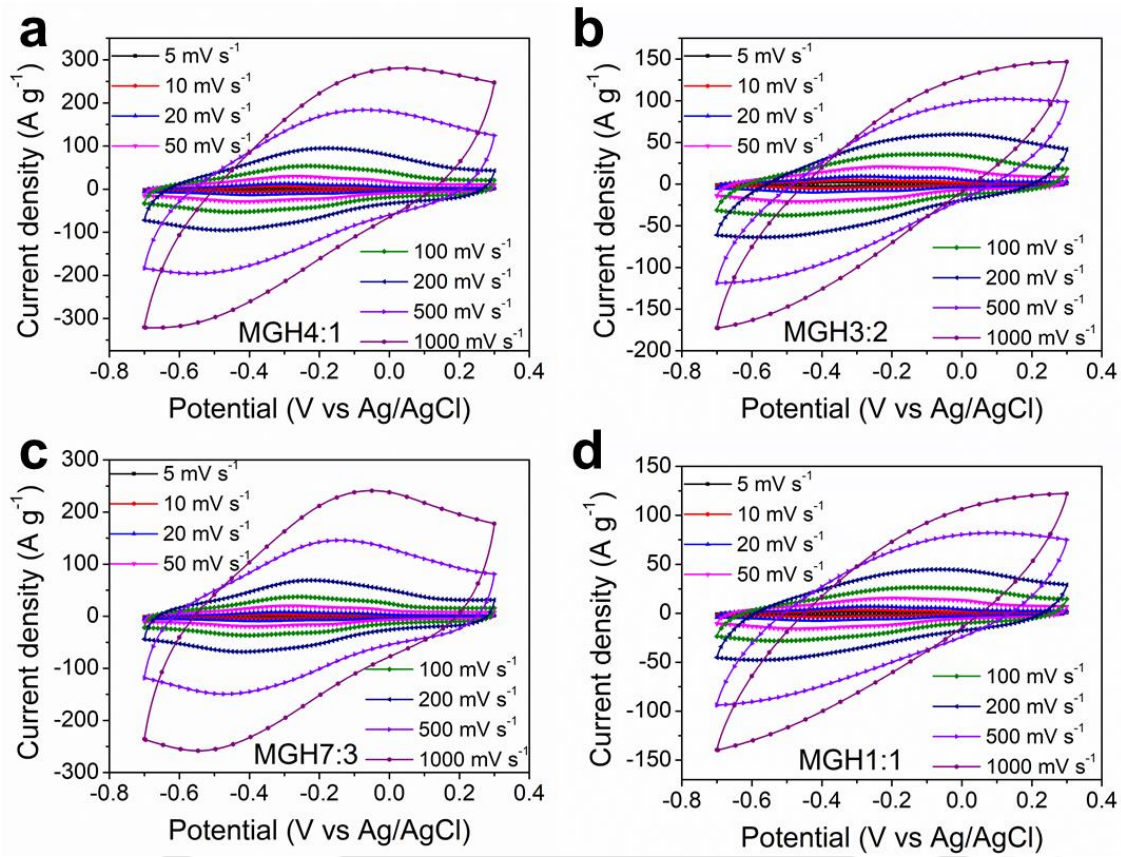

Figure 4.10. Electrochemical characterization: cyclic voltammetry curves at scan rates 5–1000 mV s^{-1} of (a) MGH4:1; (b) MGH3:2; (c) MGH7:3 and (d) MGH1:1.

It was observed that, the shape of the CV profiles were largely maintained for all the MGH hybrids (Figure 4.10.a–d) demonstrating the excellent rate capability of the hybrid samples (Figure 4.11). For instance, MGH4:1 exhibited a superb capacity retention up to 88% at 100 mV s^{-1} and 40% even at a very high scan rate of 1 V s^{-1} (Figure 4.11). Figure 4.12.a–d exhibit the galvanostatic charge–discharge (GCD) profiles of MGH electrodes The GCD curve of all the MGH hybrids showed a non–linear profiles (Figure 4.12.a–d) without any obvious plateau further confirming the pseudocapacitive nature of MGH electrodes. The symmetric nature of GCD curves reveals the excellent reversibility of MGH electrodes.

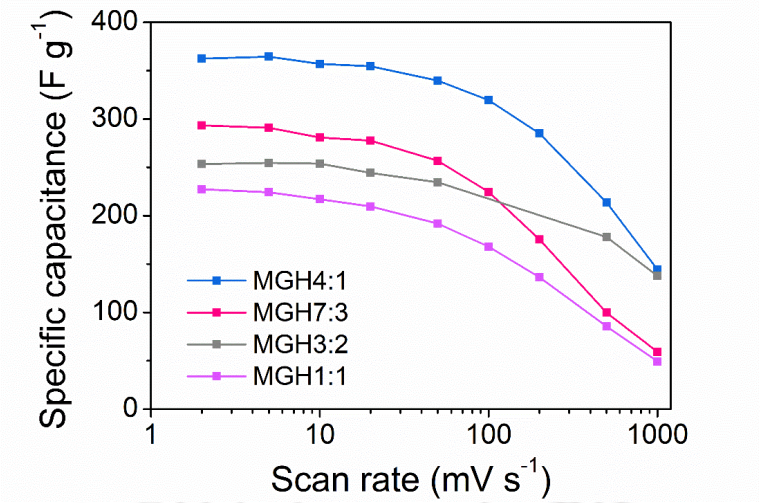

Figure 4.11. Comparison of specific capacitance vs scan rates of different MGH hybrids.

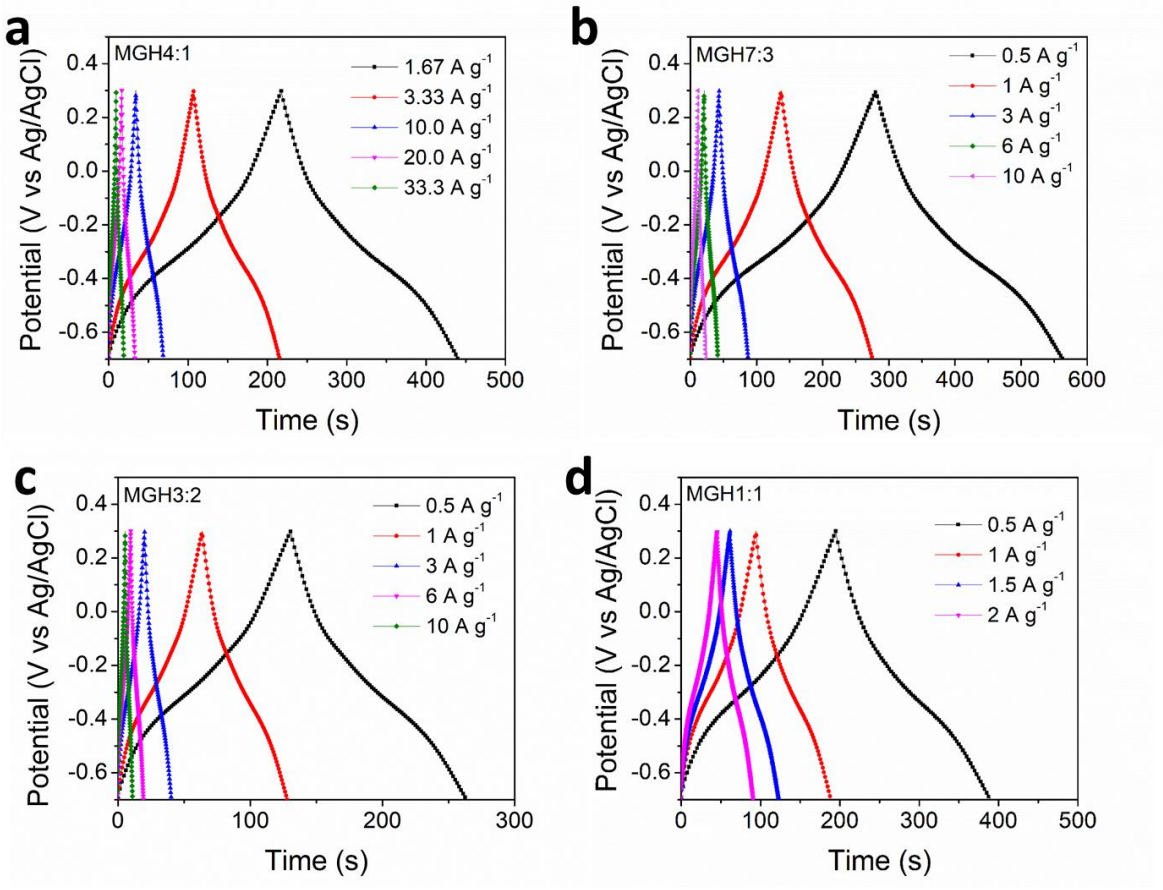

Figure 4.12. Electrochemical characterization: galvanostatic charge–discharge profiles at different current densities for (a) MGH4:1; (b) MGH3:2; (c) MGH7:3 and (d) MGH1:1.

In order to understand the charge–storage mechanism of MGH electrodes electrochemical impedance spectroscopy (EIS) study was performed. It can be observed from the Nyquist plot (Figure 4.13) that, MGHs with different MXene content exhibit quasi–vertical lines in the low frequency regime indicating good capacitive behaviour. In the high frequency region, the absence of semi–circular portion demonstrated a very low series and charge transfer resistances (inset of Figure 4.13). The low value of impedance is a direct evidence of high conductivity of the MGH electrodes. Moreover, the highly interconnected hydrogel structure of MGH electrodes maintains excellent electrical connections throughout the electrode structure and thereby can promote the facile electron transfer process.

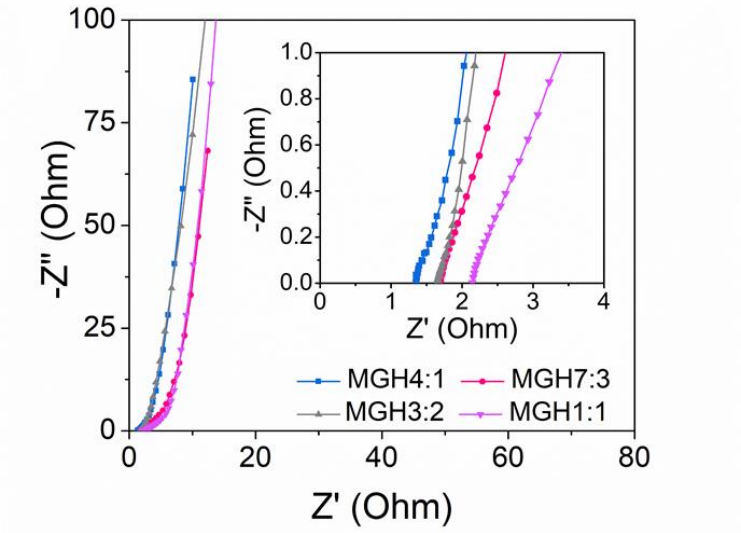

Figure 4.13. Electrochemical impedance spectroscopy: Nyquist plot of different MGH hybrids. The inset shows magnified view of the high frequency region.

The excellent performance of MGH electrode was further reflected by the long term stability of MGH (Figure 4.14) decaying to only 95.6% over 10000 cycles of continuous charge–discharge at a high current density of 10 A g^{-1}.

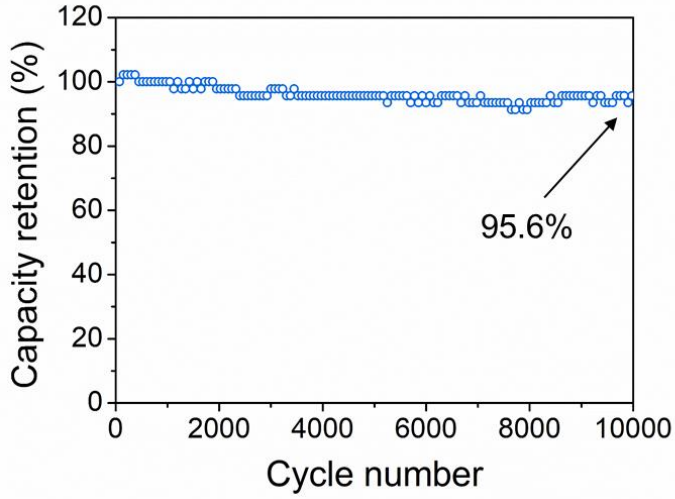

Figure 4.14. Stability test of MGH4:1 at a current density of 10 A g^{-1}.

MXene and polyaniline are both pseudo capacitive materials and they complement each other. MXene can be used as negative electrode due to its negative potential window (–0.8–0.2 V vs Ag/AgCl) whereas polyaniline can be used as positive electrode on behalf of its positive potential window (0–0.8 V vs Ag/AgCl). Thus, it can be possible to design an all pseudocapacitance based asymmetric device having much higher operating potential window. This asymmetric device therefore can essentially increase the energy density of the device due to the increased voltage window. Thus it is expected that MGH and PGH can be good choice as negative and positive electrode due to their suitable composition and binder free continuous conducting porous structure.

Before designing asymmetric supercapacitor, the performance of PGH hybrids was tested in three–electrode configuration. Figure 4.15 shows the comparison of CV profiles of PGH at a scan rate of 10 mV s^{-1}. The CV profiles of all the PGH hybrids at scan rates 2–1000 mV s^{-1} (Figure 4.16.a–c) exhibited a pair of redox peaks which is due to the redox transition of leukoemeraldine and emeraldine states of PANI. The pseudocapacitive behaviour of PGH hybrids was also evident from the non–linear characteristics of the GCD curves as shown in Figure 4.17.a–c. The highest specific capacitance was obtained for PGH3 electrode with a value of 469.2 F g^{-1} at a scan rate of 10 mV s^{-1} (Figure 4.18).

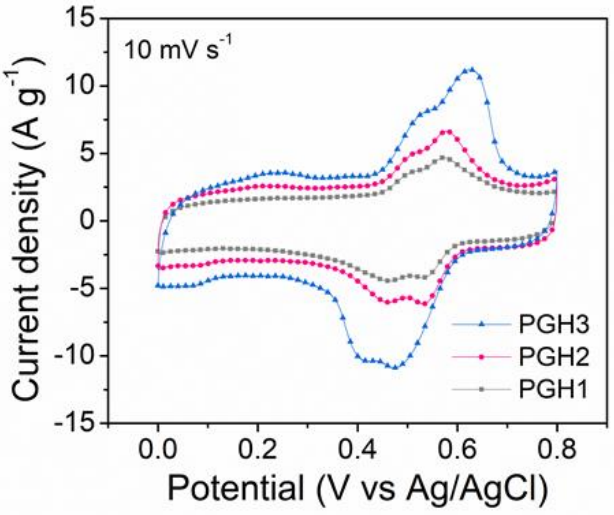

Figure 4.15. Electrochemical characterization of PGH: comparison of CV profiles of PGH1, PGH2 and PGH3 at a scan rate of 10 mV s^{-1}.

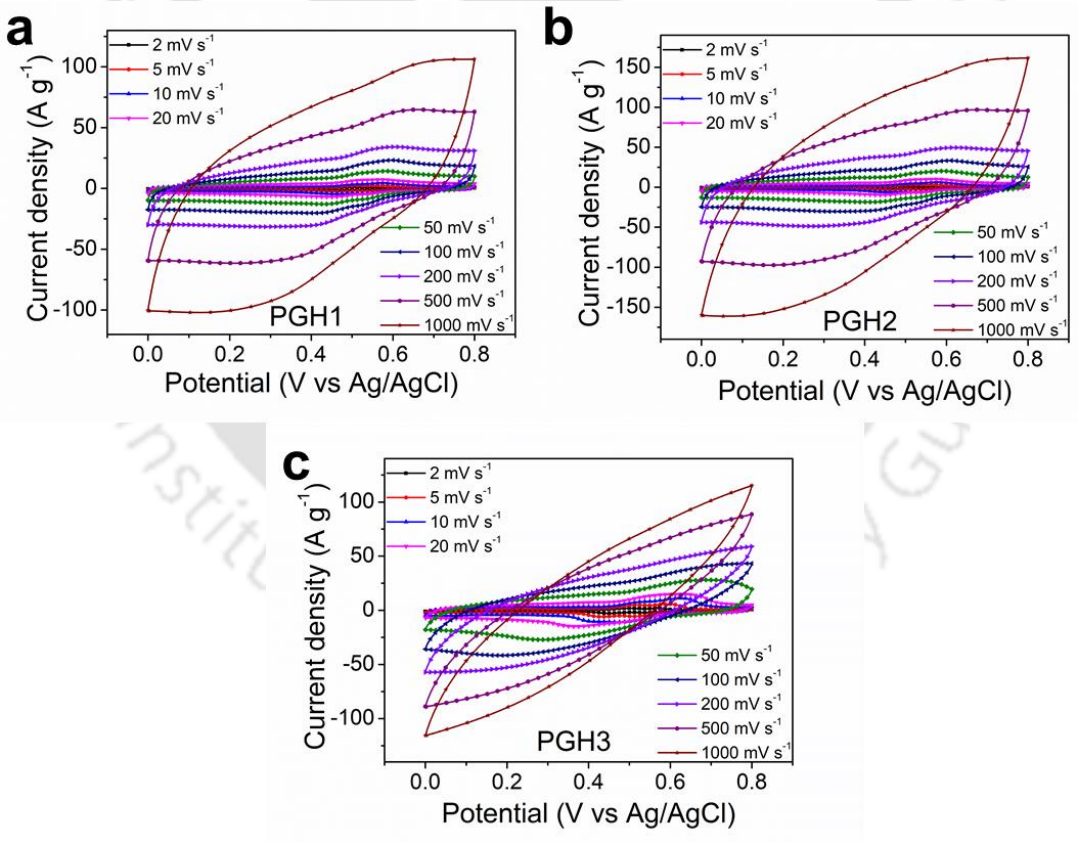

Figure 4.16. Electrochemical characterization of PGH: CV profiles at different scan rates (2–1000 mV s^{-1}) for (a) PGH1, (b) PGH2 and (c) PGH3.

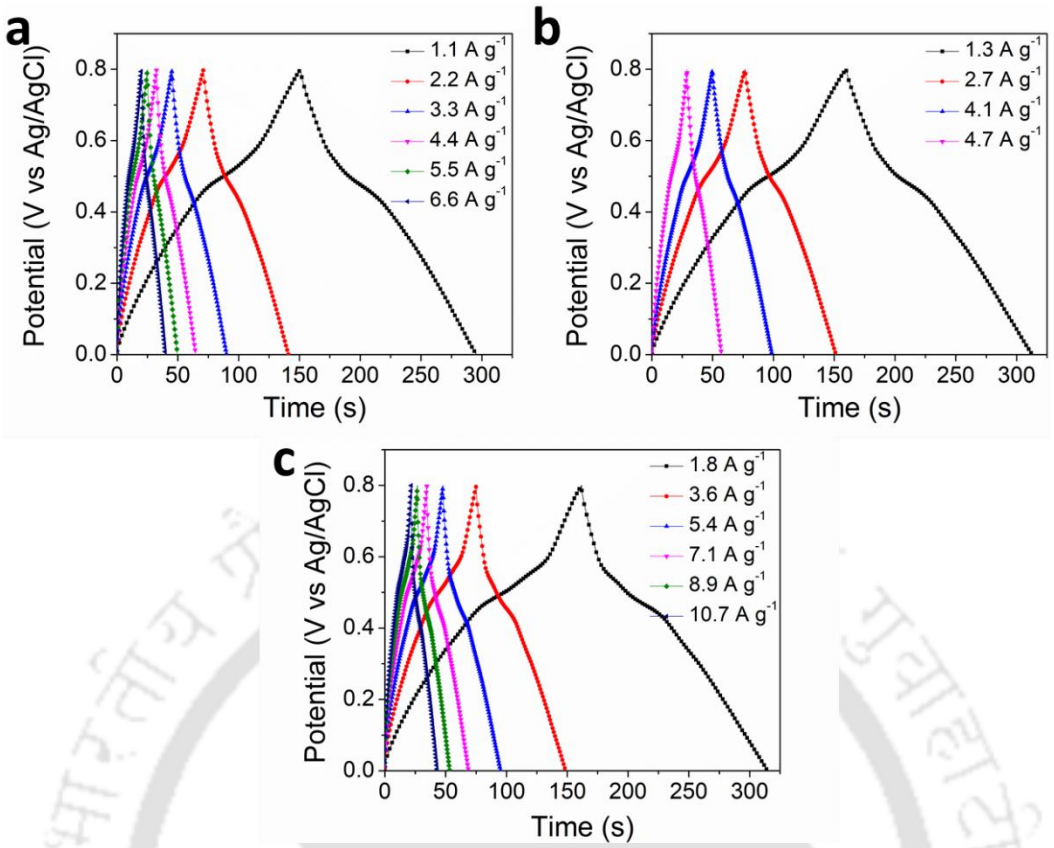

Figure 4.17. Electrochemical characterization of PGH: GCD profiles at different current densities for (a) PGH1, (b) PGH2 and (c) PGH3.

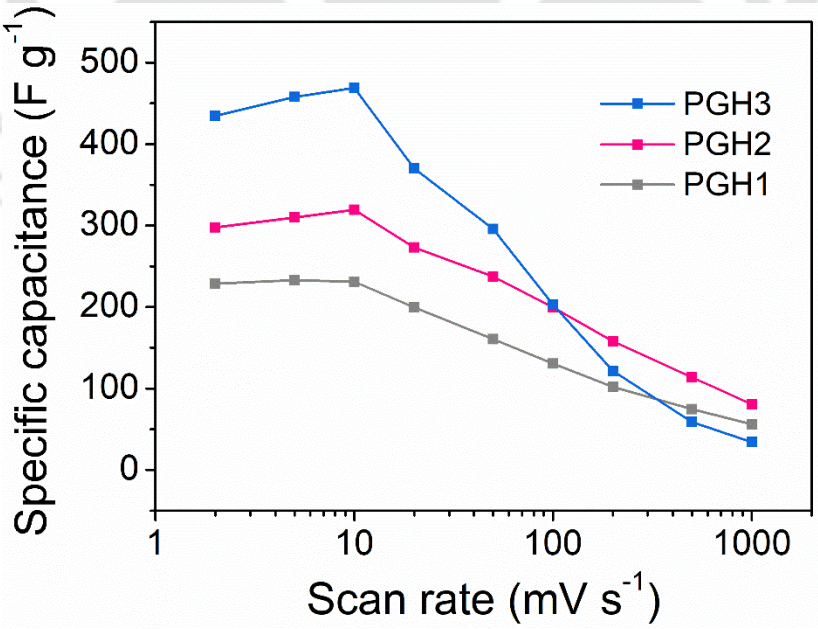

Figure 4.18. Comparison of specific capacitances of PGH hybrids at different scan rates.

The excellent charge–storage characteristics of PGH was further reflected by EIS spectra. It is seen from Figure 4.19 that, all the PGH hybrids exhibit very low series (< 4 Ohm) and negligible charge transfer resistances at high frequency region whereas PGH hybrids show a good capacitive response at the low frequency regime. Moreover PGH exhibited a minimum 45° transition line indicating very low Warburg impedance. The excellent electrochemical performance of PGH electrode can be associated with various factors: (1) the uniform development of PANI nanocones over the GH provided a good electrical connection with GH and PANI. (2) The nanometer sized vertically oriented PANI maintained the porous morphology of the hydrogel which facilitated high electrolyte ion diffusion process. As a result the unique porous morphology with excellent mass transport properties of PGH and the presence of conducting RGO and pseudocapacitive PANI nanocones synergistically enhanced the electrochemical performance of PGH electrode.

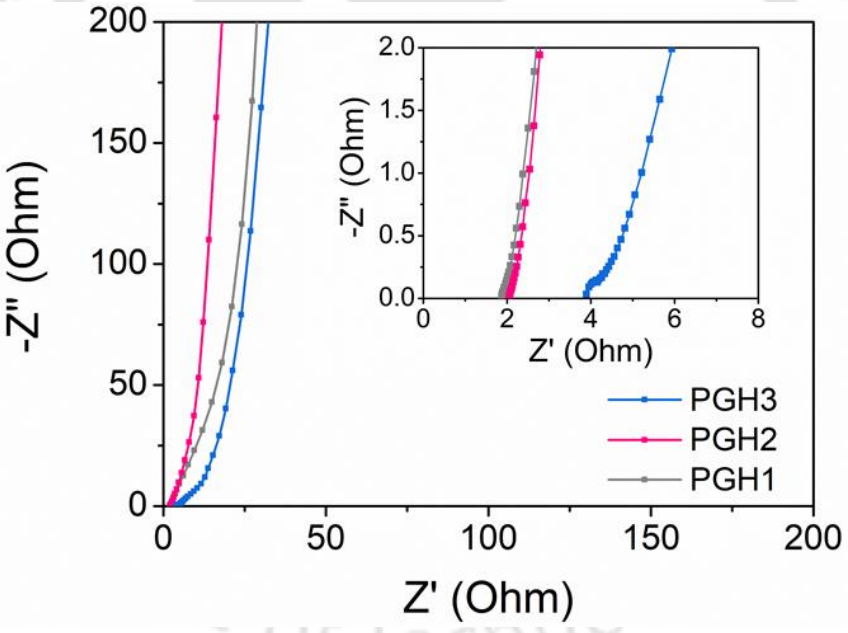

Figure 4.19. EIS spectra of PGH hybrids. The inset shows corresponding magnified view of high frequency region.

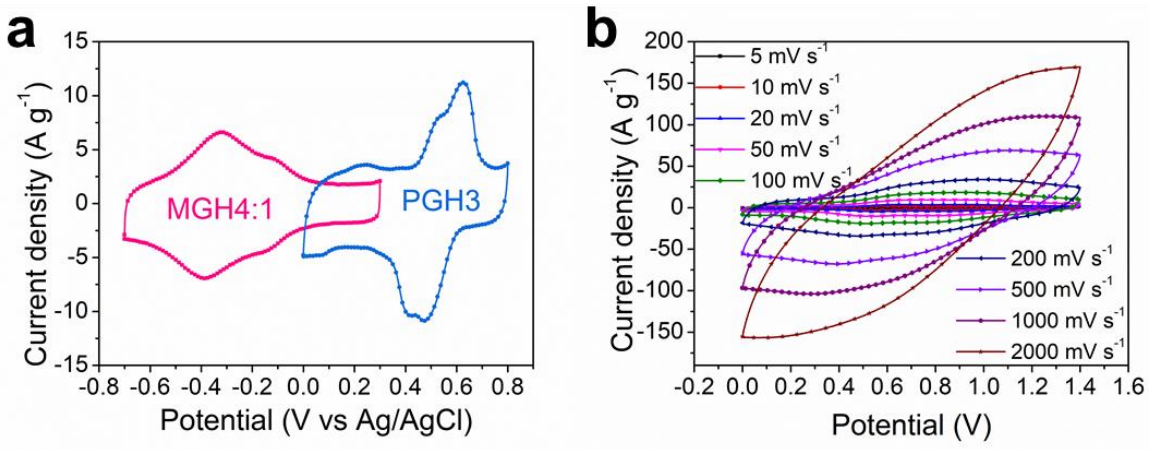

Figure 4.20. Electrochemical characterization of asymmetric device: (a) CV curves of MGH4:1 negative electrode and PGH3 positive electrode at a scan rate of 10 mV s^{-1}; (b) CV curves of MGH4:1//PGH3 asymmetric device at various scan rates.

To demonstrate the practical applicability of as developed hybrid hydrogels an all pseudocapacitive asymmetric supercapacitor device has been fabricated with MGH4:1 as the negative electrode and PGH as the positive electrode. The respective potential window of positive and negative electrodes was first determined using a three–electrode configuration. Figure 4.20.a shows the CV curves of negative electrode MGH4:1 (–0.8–0.2 V vs Ag/AgCl) and positive electrode PGH3 (0–0.8 V vs Ag/AgCl) at a scan rate of 10 mV s^{-1}. Both MGH4:1 and PGH3 exhibited distinct redox peaks in their respective potential window. To enhance the specific capacitance and potential window the mass ratio of PGH3 and MGH4:1 electrodes was set to 0.95 to balance the charge in the two electrodes. The CV profiles of as developed MGH4:1//PGH3 asymmetric device (two–electrode configuration) at scan rates 5–2000 mV s^{-1} exhibited a pair of prominent and reversible redox peaks in the potential window of 0.5–1 V vs Ag/AgCl (Figure 4.20.b). The redox peak could be observed even at high scan rates indicating a fast and reversible faradaic process. The gravimetric capacitance based on the total mass of both the electrodes for MGH4:1//PGH3 was found to be 137.5 F g^{-1} at a scan rate of 10 mV s^{-1} and the value was largely maintained over a high scan rates up to 2000 mV s^{-1} (87% capacity retention at 100 mV s^{-1} and 24.5% retention at 2000 mV s^{-1}) (Figure 4.21.a). Figure 4.21.b shows the non–linear GCD curves at different current densities further confirming the pseudocapacitive nature of the asymmetric device.

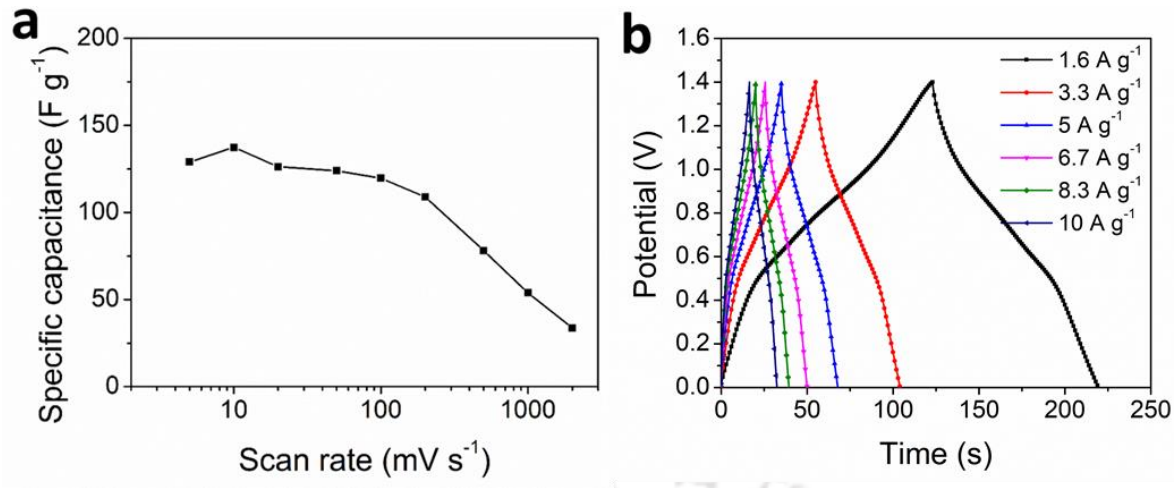

Figure 4.21. Electrochemical characterization of asymmetric device: (a) specific capacitance as a function of scan rates and (b) GCD profiles at different current densities of MGH4:1//PGH3 asymmetric device.

The gravimetric energy and power densities of the asymmetric device were calculated from the GCD curves (Figure 4.21.b). The Ragone plot (Figure 4.22) showed that, the maximum energy density was found to be 30.3 Wh kg^{-1} corresponding to an ultra–high power density of 1.13 kW kg^{-1}. The maximum power density obtained was 6.6 kW kg^{-1} with a nominal decrement in the energy density (29.1 Wh kg^{-1}). The high performance of MGH4:1//PGH3 asymmetric device is attribute to the high voltage window of the device due to the well matched pseudocapacitance of positive and negative electrodes together with the conducting porous structure of both MGH4:1 and PGH3 electrodes. These results indicate the potential of MGH4:1//PGH3 asymmetric device to be used for practical applications. Table 4.1 directly compares the charge storage properties of MGH4:1 and MGH4:1//PGH3 asymmetric device with previously reported MXene based supercapacitor devices.

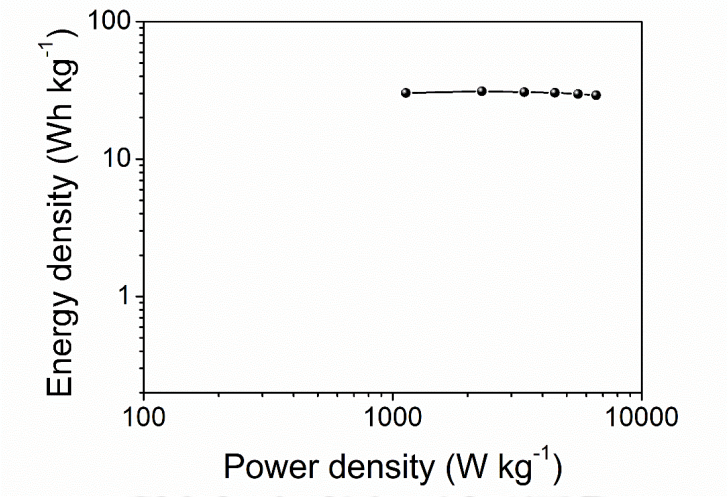

Figure 4.22. Ragone plot of MGH4:1//PGH3 asymmetric device.

Table 4.1. Performance comparison of MGH4:1 and MGH4:1//PGH3 asymmetric device with previously reported MXene based supercapacitor devices

Electrode material	Cell configuration*	Electrolyte	Scan rate	Gravimetric Capacitance ($F\ g^{-1}$)	References
Mxene (Ti_3C_2)	2E	1 M Li_2SO_4	2 $mV\ s^{-1}$	191.5	[28]
Mxene–rHGO	3E	3M H2SO4	2 $mV\ s^{-1}$	438	[23]
MXene MXene/rGO	3E	3M H_2SO_4	2 $mV\ s^{-1}$	335.4	[22]
MXene/rGO	3E	6M KOH	1 $A\ g^{-1}$	405	[29]
d– Ti_3C_2	3E	1M H2SO4	2	325	[30]
MXene hydrogel	3E	3M H_2SO_4	2	272	[31]
Nanoporous MXene film	3E	3M H_2SO_4	0.5 $A\ g^{-1}$	346	[32]
Mxene hydrogel	3E	3M H_2SO_4	2 $mV\ s^{-1}$	380	[33]
RGO–MXene hydrogel	2E	3M H_2SO_4	2 $mV\ s^{-1}$	384.2	[20]
MGH4:1	**3E**	**3M H_2SO_4**	**10 $mV\ s^{-1}$**	**357.1**	**This work**

*2E represents two–electrode and 3E represents three–electrode configuration

Asymmetric electrodes	Cell voltage (V)	Energy density (Wh kg^{-1})	Corresponding Power density (W kg^{-1})	References
rGO// $Ti_3C_2T_x$	1.1	8	50	[34]
Ni–S/1d–Ti_3C_2//d–Ti_3C_2	2	20	500	[35]
wavy–$Ti_3C_2T_x$//rGO/CNT/PANI	1.45	28.6	590	[36]
VN/PC//$Ti_3C_2T_x$	1.8	12.81	985.8	[37]
Ti_3C_2//Ti_3C_2/CuS	1.5	15.4	750.2	[38]
MGH4:1//PGH3	**1.4**	**30.3**	**1130**	**This work**

4.4 Conclusions:

In summary, a facile ambient condition protocol has been developed to assemble graphene–MXene hybrid hydrogel (MGH) having 3D porous network structure. The excellent processability of gelation technique has been demonstrated by casting hydrogel in arbitrary shapes. Benefitted by 3D porous structure with continuous ion transporting channel as developed MGH hydrogel based supercapacitor electrode exhibited high energy storage performance (357.1 F g^{-1} at a scan rate of 10 mV s^{-1}) with excellent rate capability (40% at 1000 mV s^{-1}). To widen the operating potential window and hence to increase the energy density asymmetric supercapacitor was developed by using MGH as negating electrode and the hybrid of polyaniline–graphene hydrogel (PGH) as positive electrode. PGH having uniform polyaniline nanocones over graphene–MXene surface was developed via interfacial controlled polymerization strategy using the hydrogel as confined reactor. As developed all–pseudocapacitive asymmetric device MGH //PGH showed a very high energy (30.3 Wh kg^{-1}) and power densities (6.6 kW kg^{-1}), which are comparable to the best results. This work paves a way toward the design and fabrication of graphene–MXene based 3D structure with hydrogel–shape tunability for high performance supercapacitor devices and other customized applications.

Reference:

1. Y. Gogotsi and B. Anasori, The Rise of MXenes, *ACS Nano*, 13 (2019), pp. 8491–8494.
2. M. Naguib, V. N. Mochalin, M. W. Barsoum and Y. Gogotsi, 25th Anniversary Article: MXenes: A New Family of Two–Dimensional Materials, *Adv. Mater.*, 26 (2014), pp. 992–1005.
3. A. Lipatov, H. Lu, M. Alhabeb, B. Anasori, A. Gruverman, Y. Gogotsi and A. Sinitskii, Elastic properties of 2D Ti₃C₂T_{x} MXene monolayers and bilayers, *Sci. Adv.*, 4 (2018), pp. eaat0491.
4. B. Anasori, M. R. Lukatskaya and Y. Gogotsi, 2D metal carbides and nitrides (MXenes) for energy storage, *Nat. Rev. Mater.*, 2 (2017), pp. 16098.
5. D. Xiong, X. Li, Z. Bai and S. Lu, Recent Advances in Layered Ti3C2Tx MXene for Electrochemical Energy Storage, *Small*, 14 (2018), pp. 1703419.
6. F. Shahzad, M. Alhabeb, C. B. Hatter, B. Anasori, S. Man Hong, C. M. Koo and Y. Gogotsi, Electromagnetic interference shielding with 2D transition metal carbides (MXenes), *Science*, 353 (2016), pp. 1137.
7. J. Liu, H.–B. Zhang, R. Sun, Y. Liu, Z. Liu, A. Zhou and Z.–Z. Yu, Hydrophobic, Flexible, and Lightweight MXene Foams for High–Performance Electromagnetic–Interference Shielding, *Adv. Mater.*, 29 (2017), pp. 1702367.
8. J. Ran, G. Gao, F.–T. Li, T.–Y. Ma, A. Du and S.–Z. Qiao, Ti3C2 MXene co–catalyst on metal sulfide photo–absorbers for enhanced visible–light photocatalytic hydrogen production, *Nat. commun.*, 8 (2017), pp. 13907.
9. E. Lee, A. VahidMohammadi, B. C. Prorok, Y. S. Yoon, M. Beidaghi and D.–J. Kim, Room Temperature Gas Sensing of Two–Dimensional Titanium Carbide (MXene), *ACS Appl. Mat. Interfaces*, 9 (2017), pp. 37184–37190.
10. Z. Wu, T. Shang, Y. Deng, Y. Tao and Q.–H. Yang, The Assembly of MXenes from 2D to 3D, 7 (2020), pp. 1903077.
11. Y. Deng, T. Shang, Z. Wu, Y. Tao, C. Luo, J. Liang, D. Han, R. Lyu, C. Qi, W. Lv, F. Kang and Q.–H. Yang, Fast Gelation of Ti3C2Tx MXene Initiated by Metal Ions, 31 (2019), pp. 1902432.
12. Y. Ma, Y. Yue, H. Zhang, F. Cheng, W. Zhao, J. Rao, S. Luo, J. Wang, X. Jiang, Z. Liu, N. Liu and Y. Gao, 3D Synergistical MXene/Reduced Graphene Oxide Aerogel for a Piezoresistive Sensor, *ACS Nano*, 12 (2018), pp. 3209–3216.
13. Y. Jiang, X. Xie, Y. Chen, Y. Liu, R. Yang and G. Sui, Hierarchically structured cellulose aerogels with interconnected MXene networks and their enhanced microwave absorption properties, *J. Mater. Chem. C*, 6 (2018), pp. 8679–8687.
14. J. Liu, H.–B. Zhang, X. Xie, R. Yang, Z. Liu, Y. Liu and Z.–Z. Yu, Multifunctional, Superelastic, and Lightweight MXene/Polyimide Aerogels, *Small*, 14 (2018), pp. 1802479.
15. J. Song, X. Guo, J. Zhang, Y. Chen, C. Zhang, L. Luo, F. Wang and G. Wang, Rational design of free–standing 3D porous MXene/rGO hybrid aerogels as polysulfide reservoirs for high–energy lithium–sulfur batteries, *J. Mater. Chem. A*, 7 (2019), pp. 6507–6513.
16. C. J. Zhang, S. Pinilla, N. McEvoy, C. P. Cullen, B. Anasori, E. Long, S.–H. Park, A. Seral–Ascaso, A. Shmeliov, D. Krishnan, C. Morant, X. Liu, G. S. Duesberg, Y. Gogotsi and V. Nicolosi, Oxidation Stability of Colloidal Two–Dimensional Titanium Carbides (MXenes), *Chem. Mater.*, 29 (2017), pp. 4848–4856.

17. M. Ghidiu, M. R. Lukatskaya, M.–Q. Zhao, Y. Gogotsi and M. W. Barsoum, Conductive two–dimensional titanium carbide 'clay' with high volumetric capacitance, *Nature*, 516 (2014), pp. 78–81.
18. A. Sikdar, A. Majumdar, P. Dutta, M. Borah, S. O. Kim and U. N. Maiti, Ultra–large area graphene hybrid hydrogel for customized performance supercapacitors: High volumetric, areal energy density and potential wearability, *Electrochim. Acta*, 332 (2020), pp. 135492.
19. J. Huang and R. B. Kaner, A General Chemical Route to Polyaniline Nanofibers, *J. Am. Chem. Soc.*, 126 (2004), pp. 851–855.
20. P. Dutta, A. Sikdar, A. Majumdar, M. Borah, N. Padma, S. Ghosh and U. N. Maiti, Graphene aided gelation of MXene with oxidation protected surface for supercapacitor electrodes with excellent gravimetric performance, *Carbon*, 169 (2020), pp. 225–234.
21. X. Zhao, M. Liu, Y. Chen, B. Hou, N. Zhang, B. Chen, N. Yang, K. Chen, J. Li and L. An, Fabrication of layered Ti3C2 with an accordion–like structure as a potential cathode material for high performance lithium–sulfur batteries, *J. Mater. Chem. A*, 3 (2015), pp. 7870–7876.
22. J. Yan, C. E. Ren, K. Maleski, C. B. Hatter, B. Anasori, P. Urbankowski, A. Sarycheva and Y. Gogotsi, Flexible MXene/Graphene Films for Ultrafast Supercapacitors with Outstanding Volumetric Capacitance, *Adv. Funct. Mater.*, 27 (2017), pp. 1701264.
23. Z. Fan, Y. Wang, Z. Xie, D. Wang, Y. Yuan, H. Kang, B. Su, Z. Cheng and Y. Liu, Modified MXene/Holey Graphene Films for Advanced Supercapacitor Electrodes with Superior Energy Storage, *Advanced Science*, 5 (2018), pp. 1800750.
24. M. Hu, Z. Li, T. Hu, S. Zhu, C. Zhang and X. Wang, High–Capacitance Mechanism for Ti3C2Tx MXene by in Situ Electrochemical Raman Spectroscopy Investigation, *ACS Nano*, 10 (2016), pp. 11344–11350.
25. J. Halim, K. M. Cook, M. Naguib, P. Eklund, Y. Gogotsi, J. Rosen and M. W. Barsoum, X–ray photoelectron spectroscopy of select multi–layered transition metal carbides (MXenes), *Appl. Surf. Sci.*, 362 (2016), pp. 406–417.
26. J. Yan, T. Wei, B. Shao, Z. Fan, W. Qian, M. Zhang and F. Wei, Preparation of a graphene nanosheet/polyaniline composite with high specific capacitance, *Carbon*, 48 (2010), pp. 487–493.
27. C. Zhan, M. Naguib, M. Lukatskaya, P. R. C. Kent, Y. Gogotsi and D.–e. Jiang, Understanding the MXene Pseudocapacitance, *The Journal of Physical Chemistry Letters*, 9 (2018), pp. 1223–1228.
28. C. Yang, Y. Tang, Y. Tian, Y. Luo, Y. He, X. Yin and W. Que, Achieving of Flexible, Free–Standing, Ultracompact Delaminated Titanium Carbide Films for High Volumetric Performance and Heat–Resistant Symmetric Supercapacitors, *Adv. Funct. Mater.*, 28 (2018), pp. 1705487.
29. S. Xu, G. Wei, J. Li, W. Han and Y. Gogotsi, Flexible MXene–graphene electrodes with high volumetric capacitance for integrated co–cathode energy conversion/storage devices, *J. Mater. Chem. A*, 5 (2017), pp. 17442–17451.
30. Y. Dall'Agnese, M. R. Lukatskaya, K. M. Cook, P.–L. Taberna, Y. Gogotsi and P. Simon, High capacitance of surface–modified 2D titanium carbide in acidic electrolyte, *Electrochem. Commun.*, 48 (2014), pp. 118–122.
31. Y. Deng, T. Shang, Z. Wu, Y. Tao, C. Luo, J. Liang, D. Han, R. Lyu, C. Qi, W. Lv, F. Kang and Q.–H. Yang, Fast Gelation of Ti3C2Tx MXene Initiated by Metal Ions, *Adv. Mater.*, 31 (2019), pp. 1902432.

32. Z. Fan, Y. Wang, Z. Xie, X. Xu, Y. Yuan, Z. Cheng and Y. Liu, A nanoporous MXene film enables flexible supercapacitors with high energy storage, *Nanoscale*, 10 (2018), pp. 9642–9652.
33. M. R. Lukatskaya, S. Kota, Z. Lin, M.–Q. Zhao, N. Shpigel, M. D. Levi, J. Halim, P.–L. Taberna, M. W. Barsoum, P. Simon and Y. Gogotsi, Ultra–high–rate pseudocapacitive energy storage in two–dimensional transition metal carbides, *Nature Energy*, 2 (2017), pp. 17105.
34. A. M. Navarro–Suárez, K. L. Van Aken, T. Mathis, T. Makaryan, J. Yan, J. Carretero–González, T. Rojo and Y. Gogotsi, Development of asymmetric supercapacitors with titanium carbide–reduced graphene oxide couples as electrodes, *Electrochim. Acta*, 259 (2018), pp. 752–761.
35. Y. Luo, C. Yang, Y. Tian, Y. Tang, X. Yin and W. Que, A long cycle life asymmetric supercapacitor based on advanced nickel–sulfide/titanium carbide (MXene) nanohybrid and MXene electrodes, *J. Power Sources*, 450 (2020), pp. 227694.
36. K. Li, X. Wang, X. Wang, M. Liang, V. Nicolosi, Y. Xu and Y. Gogotsi, All–pseudocapacitive asymmetric MXene–carbon–conducting polymer supercapacitors, *Nano Energy*, 75 (2020), pp. 104971.
37. S. Venkateshalu and A. N. Grace, Ti3C2Tx MXene and Vanadium nitride/Porous carbon as electrodes for asymmetric supercapacitors, *Electrochim. Acta*, 341 (2020), pp. 136035.
38. Z. Pan, F. Cao, X. Hu and X. Ji, A facile method for synthesizing CuS decorated Ti3C2 MXene with enhanced performance for asymmetric supercapacitors, *J. Mater. Chem. A*, 7 (2019), pp. 8984–8992.

Chapter 5

A General Morphological Tuning and Hybridization of MOF with Grpahene Hydrogel for Highly Active OER Electrocatalysts

Chapter 5

A General Morphological Tuning and Hybridization of MOF with Grpahene Hydrogel for Highly Active OER Electrocatalysts

Exposing the active sites of metal organic frameworks (MOFs) through morphology and fine structure tuning is an effective strategy to enhance the electrocatalytic performances of MOFs. In this chapter, we have extended the concept of hydrogel–organic interfacial reaction to develop controlled MOF nanocrystals directly over graphene hydrogel framework. Molecular dynamics (MD) simulation results show that the controlled diffusion process of organic ligand molecules in this hydrogel–organic interfacial system together with their interactions with the graphene surface are very crucial to develop tunable MOF–graphene heterostructure. The obtained porous aerogel of tri–metallic MOFs–graphene hydrogel hybrids exhibit state–of–the art performance toward alkaline oxygen evolution reaction (OER) with a low overpotential of 255 mV at a current density 10 mA cm^{-2} a small Tafel slope of 44.3 mV dec^{-1}. Furthermore, the hydrogel–organic interfacial reaction has been generalized to develop versatile transition metal based graphene–MOFs heterostructures with tunable structural features which have usage in diverse application fields.

5.1 Introduction:

In the previous chapters we have discussed the development of graphene based diverse nanohybrids namely graphene–PANI hybrid, graphene–MXene hybrid through facile large scale synthesis strategies. We have also successfully applied these nanohybrids as a binder free high performance supercapacitor electrodes. Beside this supercapacitor devices another aspect of energy applications is generation of clean fuel like hydrogen. As discussed in chapter 1, electrocatalytic water splitting reaction is one of the green and facile way to generate hydrogen. However, the kinetically sluggish oxygen evolution reaction (OER) occurring at the other electrode of the overall water splitting reaction remains the practical concern for the efficient production of hydrogen. Therefore, a low cost and highly active OER electrocatalyst needs to be developed to address the current bottlenecks of clean energy generation.

Metal organic frameworks or MOFs in short, are formed by coordinating metal nodes with organic ligands. Due to their unique porous and tunable structural features, MOFs have huge application prospects in myriads of fields. [1-6] In particular, transition metal based

MOFs with high surface area, tunable porosity, and uniformly distributed atomic centers have gained increasing attentions in the area of electrocatalytic oxygen evolution reaction (OER). Nevertheless, the activity of pristine MOF based electrocatalysts are highly limited by their intrinsically low conductivity, lack of exposed catalytic sites and low operational stability. To overcome these issues following strategies have been adopted: (1) hybridizing MOFs with conducting substrates like graphene, [7-9] and (2) tuning the intrinsic structure of MOFs to increase exposed sites. [10-13] In particular, structure tuned MOFs such as bi/tri–metallic MOFs in the form of foam or 2D sheet like structure recently have shown to possess promising OER activity originating from their synergistic co–metal centre coupling and active site enhancement through their planar/porous architecture. [10, 14-16] Despite such progress, the electro–catalytic MOF research encounter the following major challenges: (i) intrinsic structure control (size, shape, and chemical composition) limitation of MOFs for high electrocatalytic activity, (ii) limited electrolyte accessibility and catalytic activity of previous MOF–graphene composites due to the π–π interactions driven stacking issues, (iii) ultimate scalability, and low cost processing e.g. common techniques to synthesize nanostructured MOFs are hydrothermal process, complex refluxing etc. [17-20] which not only increase the power consumption but also limit the large scale processability. In order to realize practical MOF–based electro–catalytic technology, alternative synthetic protocol of MOF based system needs to develop to resolve the aforementioned limitations.

In this chapter we demonstrate the concept of graphene hydrogel–organic bi–phasic reaction strategy for the tunable growth of versatile MOFs graphene porous framework. Aqueous–organic interfacial reaction is one of the most common strategies to synthesize nanomaterials. [21-23] By further adopting graphene hydrogel–organic interfacial reaction where the confined water of the hydrogel served as the aqueous phase, we have successfully synthesized morphology tuned ultrafine polyaniline nanostructures within graphene framework as discussed in chapter 2. In this chapter, we have generalized the strategy of hydrogel–organic interfacial reaction to develop morphology and crystal structure tuned MOF nanoparticles within porous graphene framework at room temperature. The significant control over the morphology results from the slow and continuous diffusion of ligand molecules from the outer organic phase into the hydrogel structure. The structural tunability of the as grown MOFs in conjugation with the high conductivity and open porous structure of the graphene framework result in a high electrocatalytic activity. As an example, we have demonstrated the electrocatalytic OER activity of rod–like nickel–cobalt–iron tri–metallic MOF–porous

graphene hybrid which exhibited a remarkably low overpotential of 255 mV to achieve a current density of 10 mA cm^{-2} and a small Tafel slope of 44.3 mV dec^{-1} outperforming the performance of commercial RuO_2 catalyst. We have demonstrated the importance of hydrogel–organic interfacial strategy as a generalized and versatile platform to develop diverse graphene based functional nanohybrids beyond MOFs.

5.2 Experimental section:

5.2.1 Preparation of porous graphene hydrogel (PG):

The PG was prepared following a modified electroless reduction of graphene oxide. [24, 25] Briefly, an aqueous dispersion of 4 mg/mL graphene oxide solution (20 mL) was first mixed with an equal volume (1:1 V/V) of NH_4OH. Then a polished zinc plate (Zn) was put directly into the graphene oxide–NH_4OH solution for 5 min. Subsequently, film of PG developed over Zn was washed thoroughly with water and the PG was detached from Zn surface by reacting it with 8 M KOH solution. Finally the PG was washed with water to remove KOH and kept in water for further use.

5.2.2 General synthetic strategy for various nanomaterial–PG hybrids:

The as formed PG was hybridized with different nanomaterials via gel–organic interfacial self–assembly method. In all the following reactions the embedded water of PG was first saturated with respective aqueous phase for 24 hours. Subsequently PG saturated with aqueous phase was immersed in organic solution of respective reactants to start the interfacial reaction for another 24 hours. Finally the PG nanohybrids were taken out of the organic phase and washed with ethanol, water repeatedly to remove any impurities. Following this protocol we have developed various PG based hybrids e.g. MOF–PG ($_{AOG}$Cu(BTC)–PG, $_{AOG}$ZIF67–PG, $_{AOG}$ZIF8–PG, $_{AOG}$TM–PG[S], $_{AOG}$TM–PG[R]) and metal nanoparticles–PG ($_{AOG}$Pt–PG).

- ***Detailed synthesis of various MOF–PG nanohybrids:***

For the interfacial synthesis of $_{AOG}$ZIF67–PG, the aqueous phase was prepared by $Co(NO_3)_2.6H_2O$ (0.137 M) dissolved in DI water and the corresponding organic solution was prepared by dissolving 2–mIm (0.61 M) in $CHCl_3$. In case of $_{AOG}$ZIF8–PG, the aqueous solution was made by $Zn(NO_3)_2.6H_2O$ (0.098 M) dissolved in D.I water and the organic phase was prepared by 2–mIm (0.394 M) dissolved in $CHCl_3$. In case of $_{AOG}$Cu(BTC)–PG, aqueous phase contained $Cu(COOCH_3)_2.H_2O$ (0.36 M) in DI water while BTC (0.08 M) dissolved in 1–octanol served as the organic phase. For the synthesis of tri–metallic $_{AOG}$TM–PG[R] hybrids,

the aqueous phase was prepared by dissolving $Ni(CH_3COO)_2.4H_2O$ (0.123 M), $Co(CH_3COO)_2.4H_2O$ (0.061 M) and $Fe(NO_3)_3.9H_2O$ (0.015 M) in D.I water. The corresponding organic phase was prepared by first dissolving BDC (0.2 M) in a mixed solvent of 1–octanol and DMSO (3:2 v/v). For, the synthesis of $_{AOG}$TM–PG[S], all the reactant concentrations remained same as in the case of $_{AOG}$TM–PG[R], except instead of $Fe(NO_3)_3.9H_2O$, $Fe(CH_3COO)_2$ (0.015 M) was used. The reaction conditions stated above are the primary conditions to synthesize MOF–PG hybrids via hydrogel–organic interfacial reaction. In order to study the effect of concentration of reactants on the morphology of the samples two other concentrations of reactants were taken as tabulated below.

Table 5.1: Concentration variation of various MOF–PG hybrids.

Material	Other concentrations 1	Other concentrations 2
$_{AOG}$ZIF67–PG	$Co(NO_3)_2.6H_2O$ – 0.0685 M 2–mIm – 0.305 M	$Co(NO_3)_2.6H_2O$ – 0.274 M 2–mIm – 1.22 M
$_{AOG}$ZIF8–PG	$Zn(NO_3)_2.6H_2O$ – 0.049 M 2–mIm – 0.197 M	$Zn(NO_3)_2.6H_2O$ – 0.196 M 2–mIm – 0.788 M
$_{AOG}$Cu(BTC)–PG	$Cu(COOCH_3)_2.H_2O$ – 0.09 M BTC – 0.02 M	$Cu(COOCH_3)_2.H_2O$ – 0.18 M BTC – 0.04 M
$_{AOG}$TM–PG[R]	$Ni(CH_3COO)_2.4H_2O$ – 0.062 M $Co(CH_3COO)_2.4H_2O$ – 0.031 M $Fe(NO_3)_3.9H_2O$ – 0.0075 M BDC– 0.1 M	$Ni(CH_3COO)_2.4H_2O$– 0.248 M $Co(CH_3COO)_2.4H_2O$ – 0.124 M $Fe(NO_3)_3.9H_2O$– 0.03 M BDC– 0.4 M
$_{AOG}$TM–PG[S]	$Ni(CH_3COO)_2.4H_2O$ – 0.062 M $Co(CH_3COO)_2.4H_2O$– 0.031 M $Fe(CH_3COO)_2$ – 0.0075 M BDC – 0.1 M	$Ni(CH_3COO)_2.4H_2O$– 0.248 M $Co(CH_3COO)_2.4H_2O$ – 0.124 M $Fe(CH_3COO)_2$ – 0.03 M BDC – 0.4 M

Depending upon the reactant concentrations we named our samples where necessary, as $_{AOG}$MOF–PG_{High}, $_{AOG}$MOF–PG_{Med} and $_{AOG}$MOF–PG_{Low} for highest, moderate and low concentrations of reactants.

- ***Synthesis of noble metal (Pt)–PG nanohybrids:***

For the diffusion controlled interfacial synthesis of $_{AOG}$Pt–PG hybrid, the aqueous phase was constructed by $NaBH_4$ (0.042 M) dissolved in D.I water and the corresponding organic phase consisted of H_2PtCl_6 (0.0029 M) dispersed in chloroform.

5.2.3 Controlled bulk phase interfacial synthesis of MOF nanoparticles without PG:

In a typical bulk phase interfacial synthesis of MOFs ($_{AO}$Cu(BTC), $_{AO}$ZIF67, $_{AO}$ZIF8 and $_{AO}$TM[R]), the concentration of reactants remained the same as described above, except without saturating PG with aqueous phase, the aqueous solutions of the respective metal precursors were slowly put directly over the top of the corresponding organic phases. After a reaction of 24 hours, the MOFs synthesized at the interface were collected and centrifuged repeatedly with ethanol and water in order to remove any unreacted reactants. Finally the MOFs were dried in vacuum for 24 hrs.

5.2.4 Bulk water phase synthesis of MOFs:

For the bulk water phase synthesis of $_{A}$Cu(BTC), $_{A}$ZIF67 and $_{A}$ZIF8 and $_{A}$TM[R] MOFs the metal and ligand concentrations remained the same as in the case of interfacial method (section 1.3.1) except the ligands were dispersed in D.I water. Only in case of $_{A}$Cu(BTC) and $_{A}$TM[R], due to poor solubility of BTC/BDC in water, it was dissolved in DMSO with the same concentration as previously stated.

5.2.5 Controlled water phase synthesis of MOF–PG hybrids:

For the aqueous phase synthesis of $_{AG}$Cu(BTC)–PG, $_{AG}$ZIF67–PG and $_{AG}$ZIF8–PG, the PG was first saturated with respective aqueous phase with the same metal ion concentration as mentioned in the case of interfacial reaction (section 1.3.1). Next the gel containing metal ions were put in the aqueous solution of respective ligand molecules. Except in the case of $_{AG}$Cu(BTC)–PG, due to poor solubility of BTC in water, the PG containing copper solution was put in a solution of BTC dissolved in DMSO.

5.2.6 Material characterization:

The morphology of the as synthesized materials were characterized with Zeiss Sigma 300 FESEM. A JEOL 2100F FETEM operated at 200 kV was used to study the morphology, lattice fringes and elemental mapping (STEM). The crystal structure of various samples were examined in powder XRD mode using Rigaku X–ray diffractometer. The energy dispersive X–

ray spectroscopic (EDAX) analysis was performed using Ametek EDAX module attached to FESEM. For ionic state and the elemental analysis, XPS was carried out in ESCALAB Xi+ (Thermo Fisher) instrument. N_2 sorption isotherms were recorded by using Quantachrome Quadrasorb evo surface area (Brunauer–Emmett–Teller, BET) analyser at 77K. Before the sorption analysis, the degassing of the samples were carried out at 100°C under high vacuum for 12 h.

5.2.7 Electrochemical measurements:

All the electrochemical measurements were performed at room temperature in a standard three–electrode cell configuration with as synthesized MOF–PG hybrid deposited over nickel foam as the working electrode, a platinum wire (CHI) as counter electrode and a saturated calomel electrode (SCE) (CHI 150) as reference electrode. A PARSTAT 3000A–DX potentiostat controlled by Versa Studio software was used for the electrochemical characterizations. For the preparation of working electrode, 3 mg of freeze dried MOF–PG hybrid or RuO_2 catalyst was dispersed in 3 mL absolute ethanol by sonication. After forming a uniform suspension, 40 µL of 5 wt% Nafion was added to it and the suspension was further sonicated for 20 min. to form a homogeneous ink. Subsequently the as prepared catalyst ink was drop casted over a pre–cleaned Ni–foam and dried overnight. The final loading of the catalyst was kept fixed at 0.64 mg cm^{-2} for all the samples. The linear sweep voltammetry (LSV) curves were taken in a nitrogen saturated 1 M KOH electrolyte at a scan rate of 5 mV s^{-1} and were corrected with 100% iR drop compensation. All the potentials used in this work were referenced against reversible hydrogen electrode (RHE) according to the formula: $E_{RHE} = E_{SCE} + 0.059\,pH + 0.242$. The measured current was normalized with geometrical area of the working electrode (1 cm^{-2}). The OER overpotential (η) was calculated following the formula: $\eta = E_{RHE} - 1.23\,V$. The impedance curves were obtained at the overpotential of 288 mV vs RHE within a frequency range of 0.1 Hz to 10^6 Hz with an AC amplitude of 10 mV.

5.2.8 Calculation of various performance metrics:

- ***Calculation of mass activity:***

The mass activity of the catalysts were calculated by normalizing current density (J) at an overpotential of 300 mV by the catalyst mass loading (m) of the electrode:

Mass activity $= {}^{J}/_{m}$

- ***Calculation of double layer specific capacitance (C_{dl}) and estimation of electrochemically active surface area (ECSA):***

The double layer capacitance was measured from the cyclic voltammetry (CV) curves obtained within a voltage window of 1.25–1.35 V vs RHE (non–Faradaic region) at scan rates of 10–70 mV s^{-1}. The C_{dl} value was obtained from the half of the slope of the $J_a - J_c$ vs v plot; where, J_a and J_c are the anodic and cathodic currents respectively at potential 1.3 V vs RHE and v is the scan rate. The ECSA was estimated to be proportional to the evaluated C_{dl}.

5.2.9 Computational methods:

First the structure of all the components (PG, 2–mIm, $Co(NO_3)_2.6H_2O$ and ZIF67) were constructed using Avogadro and VMD. [26, 27] The chemical composition of PG used in this study was $C_{30}O_1(OH)_1(COOH)_{0.5}$ where the epoxy and hydroxyl functional groups were located on the basal plane of the graphene nanosheet and the carboxyl functional groups were located on the edges. [28] In this work we have used an identical simulation system as given in details in the experimental section of chapter 3.

5.3 Results and discussions:

In this work graphene hydrogel has been successfully used as a reaction medium to design MOF nanostructures through a two–stage controlled diffusion of ligand molecules employing the previous graphene hydrogel–organic bi–phasic reaction strategy. The systematic study of the reaction process and various characterization of the as developed samples are presented in the following sections.

5.3.10 Structural and morphological analyses of PG:

The porous graphene hydrogel was first prepared through simultaneous assembly and reduction of GO over zinc plate. [24, 25] The reduction of GO was examined by X–ray diffraction (XRD) and Raman spectroscopy results. The XRD pattern of PG (Figure 5.1) suggests that, the peak at 2θ of 9.4° due to the (001) plane of GO is significantly diminished after the reduction and the emergence of a broad peak at 2θ = 24.1° (with a d–spacing of 3.7 Å) indicates the graphitic (002) plane. [29]

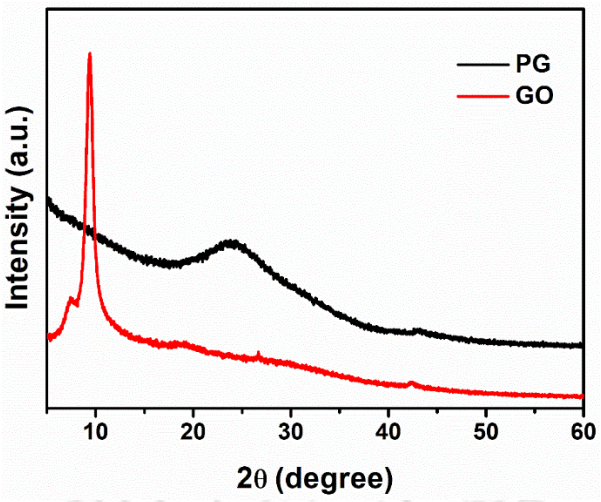

Figure 5.1. Structural characterization of PG: XRD pattern of PG and GO.

The reduction of GO into PG was further investigated from the Raman spectra. Both GO and PG exhibited characteristic D and G peaks in the Raman spectra (Figure 5.2) which correspond to the defects in the graphitic structure and the in–plane C=C stretching mode respectively. Moreover, the calculated intensity ratio of D and G peaks (I_D/I_G) was found to increase from 1.44 for GO to 1.78 for PG suggesting possible increment in the number of sp2 bonded carbon atoms and a decrement of sp2 domain size upon the removal of oxygen functionalities further confirming the reduction of GO. [30]

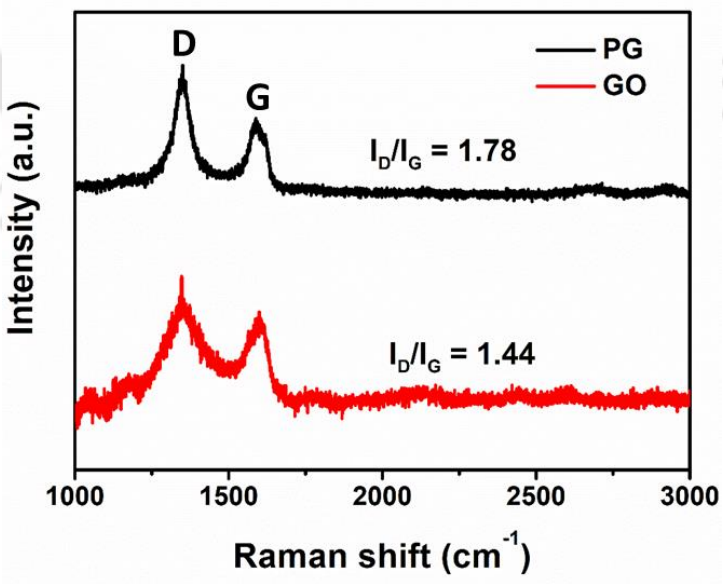

Figure 5.2. Structural characterization of PG: Raman spectra of PG and GO.

The field–emission electron microscope (FESEM) image of the PG shows an open porous architecture with the pore walls consisting of a few layers of wrinkled graphene sheets (Figure 5.3). The water containing pores of the PG can be exploited to realize the hydrogel–organic interfacial reaction to grow MOF nanostructures as discussed in the following sections.

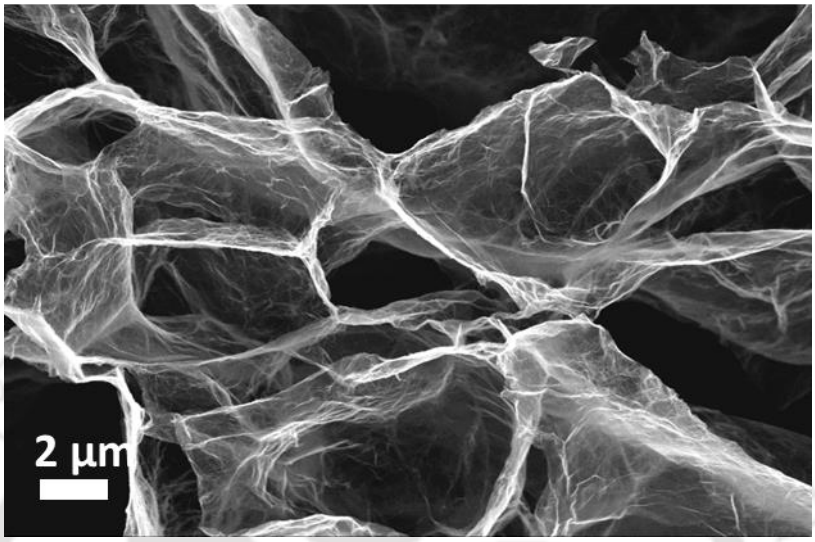

Figure 5.3. Morphology of PG: Cross–sectional FESEM image of PG.

5.3.11 Adaptation of the graphene hydrogel–organic interfacial reaction to develop tunable MOF–graphene nanohybrids:

As discussed in chapter 3, the graphene hydrogel–organic bi–phasic system for the growth of MOF–graphene nanohybrids can be realized by first saturating the graphene hydrogel with metal ions and then by placing the hydrogel in the organic phase containing the corresponding ligand molecules. In this bi–phasic system, the linker molecules diffuse from the outer organic phase into the aqueous phase confined within the hydrogel where the coordination of metal atoms with the organic ligands results in the formation of MOF nanostructures (Figure 5.4). It is to be noted that, by using chelating agent the growth of nanostructures are commonly controlled via slow and continuous release of reactants in the reaction environment. [31-33] However, in case of hydrogel–organic reaction the growth of MOF is effectively controlled through similar slow and continuous release of ligand molecules which was achieved by a controlled two–step diffusion of ligands namely, diffusion at the hydrogel–organic interface and the diffusion within the hydrogel itself.

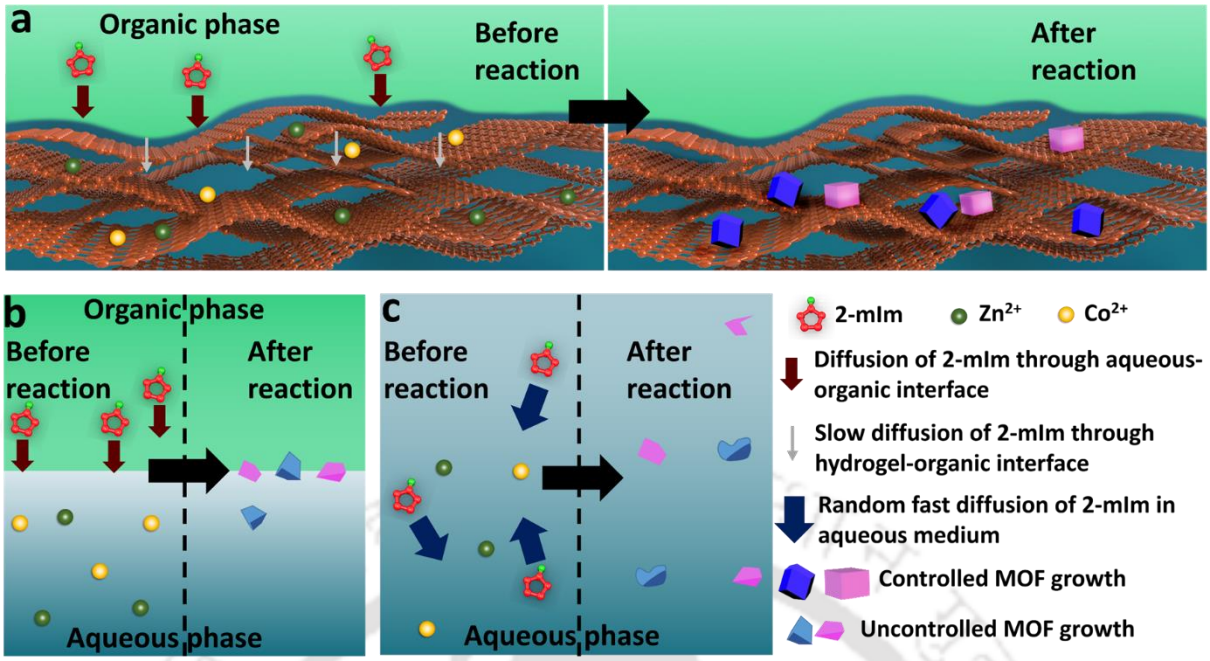

Figure 5.4. Schematic illustrations of different reaction systems showing the diffusion of 2–mIm for the shape tunable growth of MOFs: (a) graphene hydrogel–organic system for the controlled growth of MOF–PG hybrids; (b) bulk interfacial reaction and (c) bulk aqueous phase reaction demonstrating uncontrolled growth of MOFs.

To understand this controlled diffusion process we have performed MD simulation study for the growth of a representative cobalt based MOF (ZIF67) containing 2–methyl imidazole (2–mIm) as organic ligand. The simulation result showed that diffusion coefficient of 2–mIm at the hydrogel–organic interface and within the hydrogel were 3.5×10^{-6} cm^2 sec^{-1} and 1.997×10^{-6} cm^2 sec^{-1} respectively (Figure 5.5.a–b). In contrast, the diffusion coefficient of 2–mIm in the homogeneous medium was found to be 2.2×10^{-5} cm^2 sec^{-1} (Figure 5.6). Evidently, the diffusion process of 2–mIm ligand was significantly controlled due to the presence of graphene framework. Simulation results further revealed that 2–mIm and in–growing MOFs showed van der Waals and electrostatic interactions with the basal plane of graphene (Figure 5.7.a–b). This interaction effect synergistically coupled with the slow diffusion of ligand molecules ultimately resulted in an effective control over the rate of the nucleation process and thereby tune the morphology and crystal structure of the as grown MOF nanostructure.

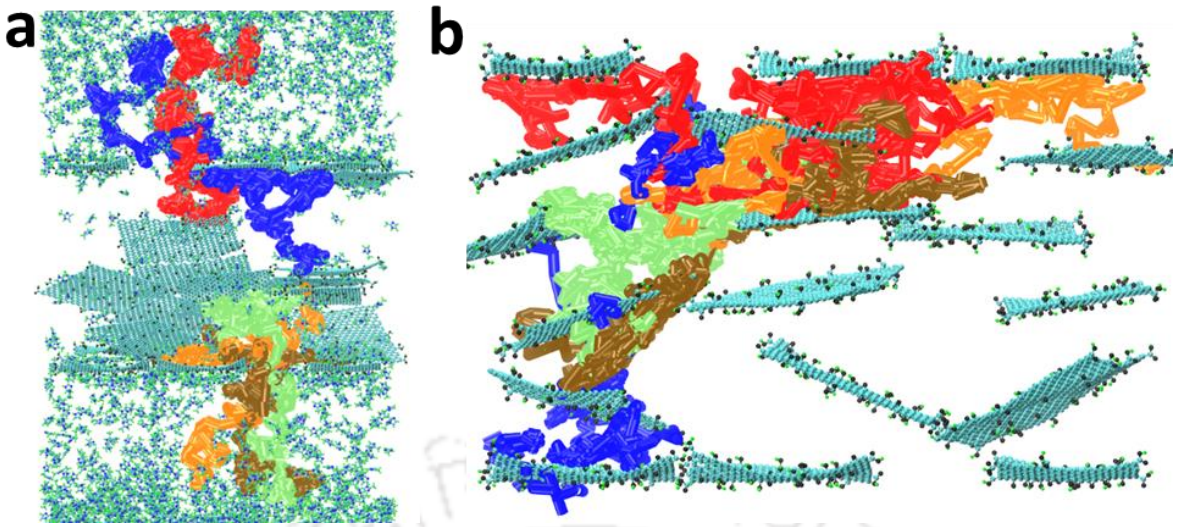

Figure 5.5. MD simulation results: representative trajectory of the 2–mIm molecules (a) at the graphene hydrogel–organic interface; (b) inside the graphene layers.

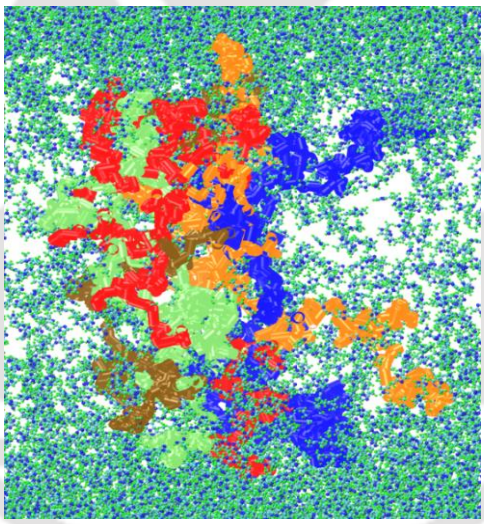

Figure 5.6. MD simulation results: representative trajectory of the 2–mIm molecules at the bulk aqueous–organic interface.

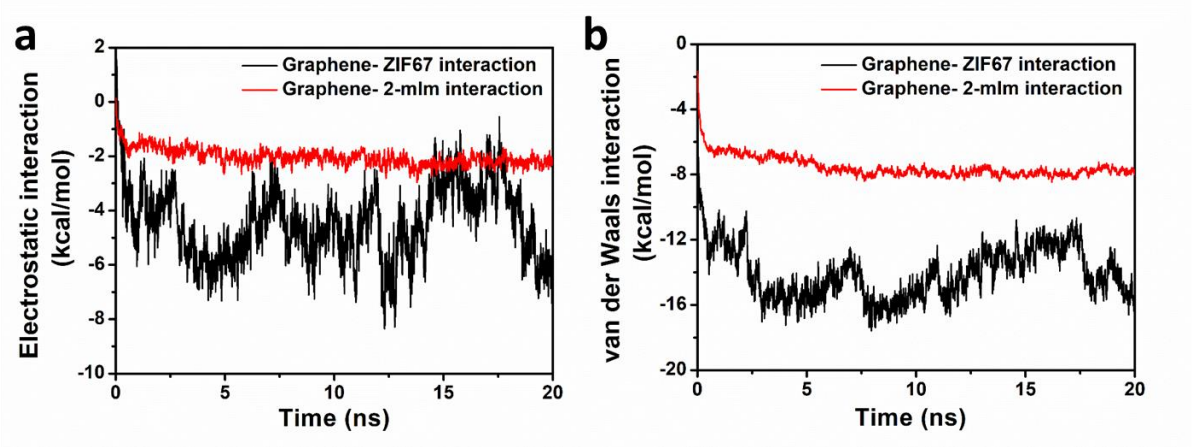

Figure 5.7. MD simulation results: (a) electrostatic and (b) van der Waals interactions of 2–mIm and ZIF67 with graphene surface.

A diverse morphology tuned MOF nanostructures possessing transition metal nodes (e.g. copper, cobalt, zinc, nickel, iron) and corresponding organic ligands (e.g. 1,3,5–benzene–tricarboxylic acid (BTC), 2–methyl imidazole (2–mIm), 1,4–benzene–dicarboxylic acid (BDC)), hybridized with porous graphene framework (MOF–PG) has been developed following this unique synthesis strategy. The corresponding hybrids are called $_{AOG}$Cu(BTC)–PG, $_{AOG}$ZIF67–PG, $_{AOG}$ZIF8–PG, tri–metallic (Ni, Co, Fe) MOFs–graphene hybrid ($_{AOG}$TM–PG) where the prefix 'AOG' indicates graphene hydrogel–organic–aqueous interfacial reaction).

5.3.12 Morphological and structural analyses of MOF–graphene hybrids:

Field emission scanning electron microscope (FESEM) and field emission transmission electron microscope (FETEM) images of MOF–PG hybrids provide a clear evidence of morphology tuning of MOF nanostructures whereas the X–ray diffraction (XRD) patterns of the hybrids revealed the crystal structures of the as developed MOFs. For example, uniform nanowire structure can be observed for the Cu(BTC) MOFs in the hybrid $_{AOG}$Cu(BTC)–PG from FESEM and FETEM images (Figure 5.8.a–b). The length of these nanowires remained in the range of a few microns whereas their diameter varied in the range of 50–200 nm as shown in the figure (Figure 5.8.a–b). Further its XRD pattern (Figure 5.9.a) revealed that as grown Cu(BTC) MOFs possessed monoclinic crystal structure having $P\ 2_{1/c}$ space group symmetry (Figure 5.9.b and Table 5.2) which matched with the crystal structure of Cu(BTC)·3H_2O MOF reported previously. [34] Moreover, the parallel lattice planes observed in the high resolution TEM (HRTEM) image (Figure 5.10.a) as well as the symmetric spots in the selected area

electron diffraction (SAED) pattern (Figure 5.10.b) imply the single crystalline nature of Cu(BTC) MOF. The inter–planer spacing was calculated from the HRTEM image and it was found to be 0.34 nm which was associated with the (200) crystallographic planes (Figure 5.10.a). To the best of our knowledge, such a non–typical nanowire structure of Cu(BTC) MOF grown via facile template free method has not been realized so far.

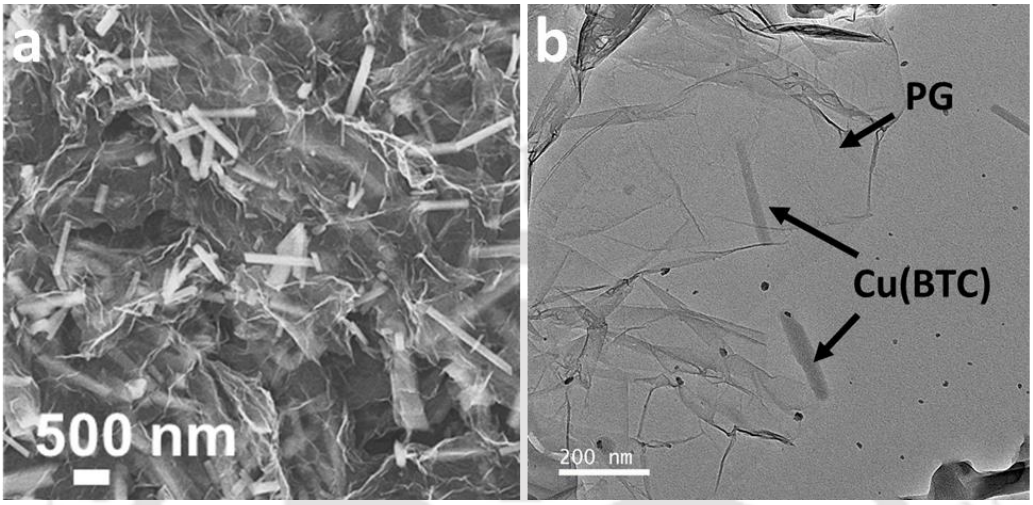

Figure 5.8. Morphological characterization of $_{AOG}$Cu(BTC)–PG: (a) FESEM and (b) FETEM images of $_{AOG}$Cu(BTC)–PG.

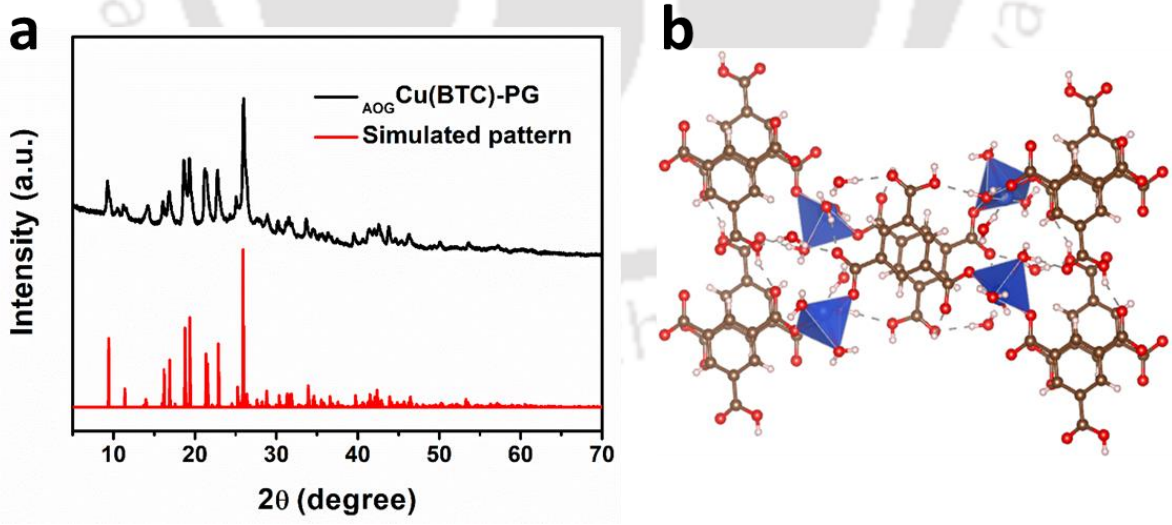

Figure 5.9. Structural characterization of $_{AOG}$Cu(BTC)–PG: (a) XRD pattern and (b) an unit cell of Cu(BTC) MOF of $_{AOG}$Cu(BTC)–PG hybrid.

Table 5.2. Summary of structure determinations of Cu(BTC) of $_{AOG}$Cu(BTC)–PG hybrid.

Material	Cu(BTC)
Crystal system	Monoclinic
Space group	P $2_{1/c}$
Lattice parameters	
a (Å)	6.87780
b (Å)	18.82060
c (Å)	8.53840
α (˚)	90
β (˚)	92.4710
γ (˚)	90
Volume (Å^3)	1104.2197

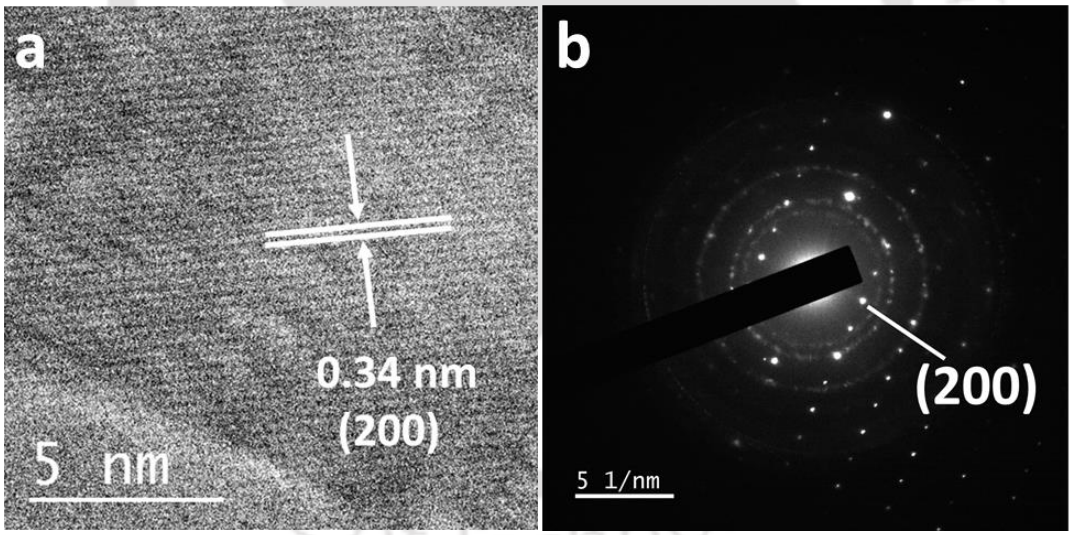

Figure 5.10. (a) HRTEM image and (b) SAED pattern of $_{AOG}$Cu(BTC)–PG hybrid.

For the case of $_{AOG}$ZIF67–PG and $_{AOG}$ZIF8–PG hybrids, both the MOFs ZIF67 (Co based MOF) and ZIF8 (Zn based MOF) possessed a typical cubic morphology with respective sizes in the range of 200–300 nm and 500 nm as observed from FESEM and FETEM images (Figure 5.11.a–d). Moreover, both of these MOFs crystalized into usual cubic structures (JCPDS #00–062–1030) as revealed from the XRD patterns (Figure 5.12) and their

polycrystalline nature was observed from the circular rings in the corresponding SAED patterns (insets of Figure 5.11.c–d).

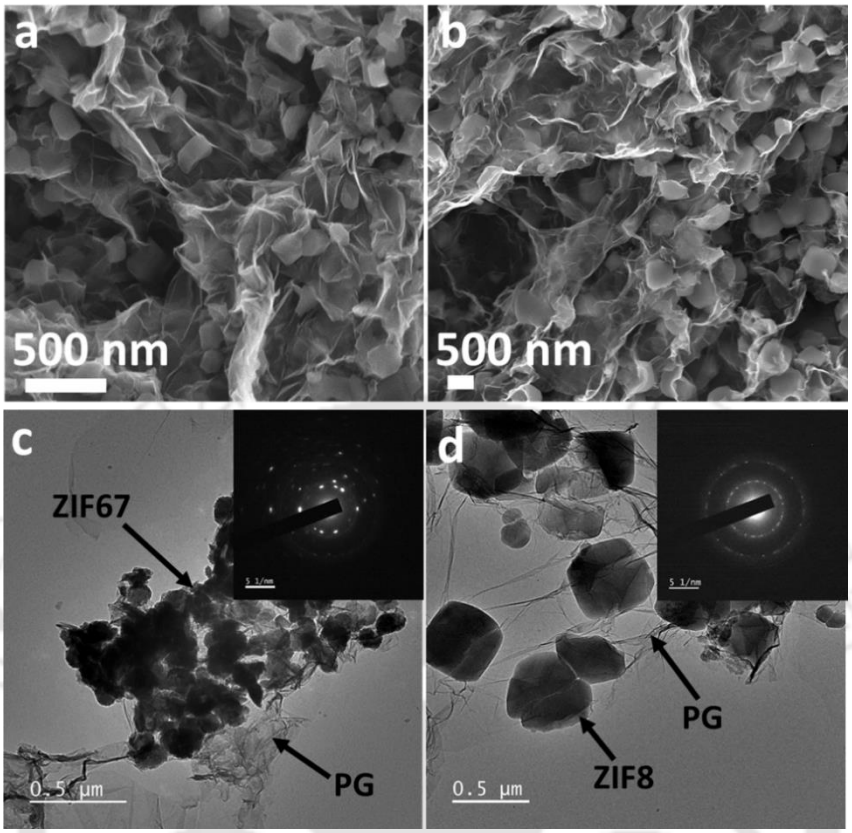

Figure 5.11. Morphological characterization of ZIF–MOF–PG hybrids: FESEM images of (a) $_{AOG}$ZIF67–PG and (b) $_{AOG}$ZIF8–PG; FETEM images of (c) $_{AOG}$ZIF67–PG and (d) $_{AOG}$ZIF8–PG.

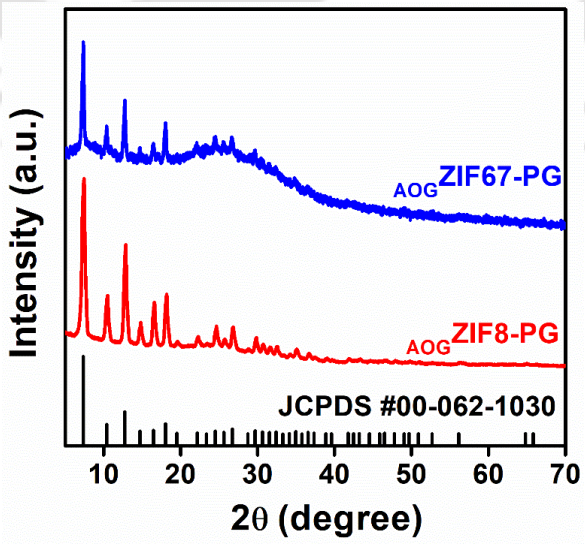

Figure 5.12. Structural characterization of ZIF–MOF–PG hybrids: XRD patterns of $_{AOG}$ZIF67–PG and $_{AOG}$ZIF8–PG

Apart from the conventional mono–metallic MOFs, a more complex tri–metallic (Ni, Co, Fe) MOFs with BDC ligand were hybridized following the same protocol. Here two types of tri–metallic MOF–PG hybrids were developed namely, one with the iron nitrate precursor (corresponding hybrid was denoted as $_{AOG}$TM–PG[R]), and another with the iron acetate precursor (corresponding hybrid was denoted as $_{AOG}$TM–PG[S]). Interestingly, the FESEM and FETEM images revealed that, $_{AOG}$TM–PG[R] hybrid had a rod–like morphology (with a length in the range of 400–600 nm and average width of ~250 nm) (Figure 5.13.a and Figure 5.14.a), whereas the hybrid $_{AOG}$TM–PG[S] possessed a sheet like structure (with sheet size ~ 300 nm to several micron) (Figure 5.13.b and Figure 5.14.b).

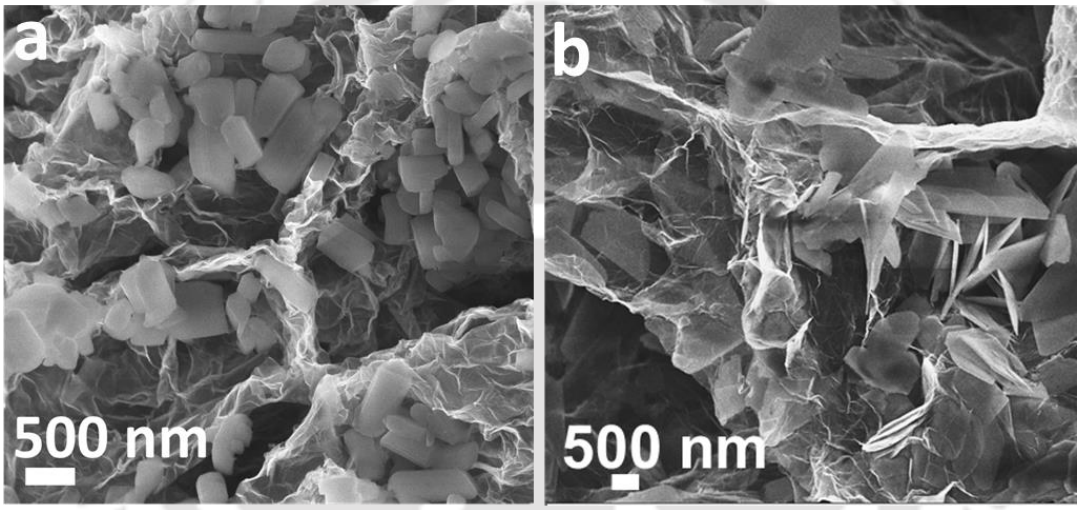

Figure 5.13. Morphological characterizations of TM–MOF–PG hybrids: FESEM images of (a) $_{AOG}$TM–PG[R] and (b) $_{AOG}$TM–PG[S].

Furthermore, it was found that both the MOFs in the $_{AOG}$TM–PG[R] and $_{AOG}$TM–PG[S] hybrids possessed triclinic crystal structure with *P 1* space group symmetry despite of using iron sources with varying oxidation states (+3/+2) as confirmed from their XRD patterns and simulated crystal structure (Figure 5.15.a–b; lattice parameters are given in Table 5.3). Moreover, the as grown tri–metallic MOFs had polycrystalline structure as evident from the SAED patterns (insets of Figure 5.14.a–b). Furthermore, the iron centers in both the MOFs possessed Fe^{3+} state as observed from the high resolution Fe 2p XPS data (Figure 5.16.a–d), suggesting possible oxidation of Fe^{2+} into Fe^{3+} before its co–ordination with the BDC ligand for MOF formation. [15, 20, 35]

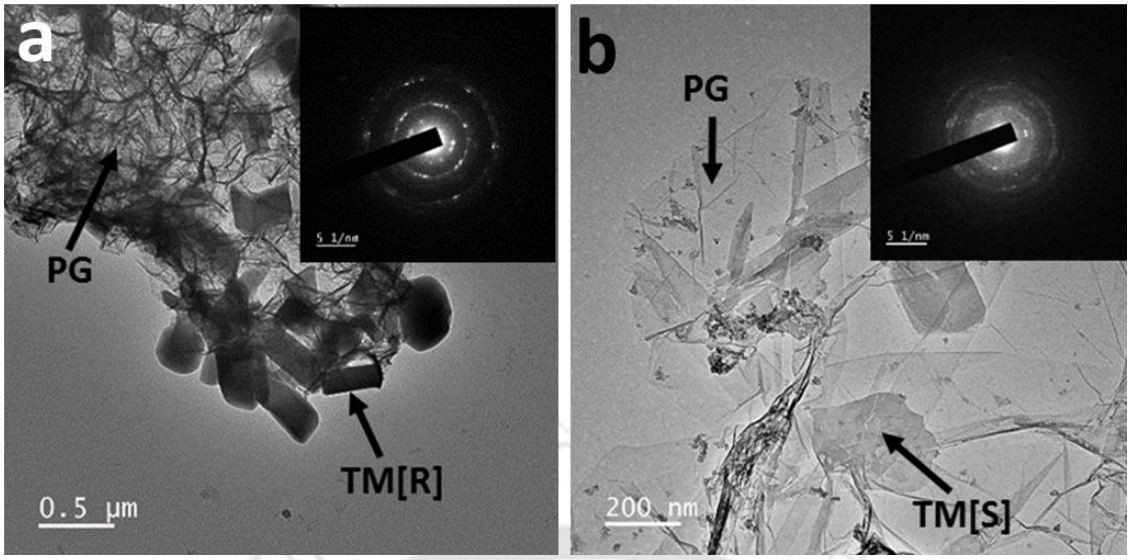

Figure 5.14. Morphological characterizations of TM–MOF–PG hybrids: FETEM images of (a) $_{AOG}$TM–PG[R] and (b) $_{AOG}$TM–PG[S]. The insets show corresponding SAED patterns.

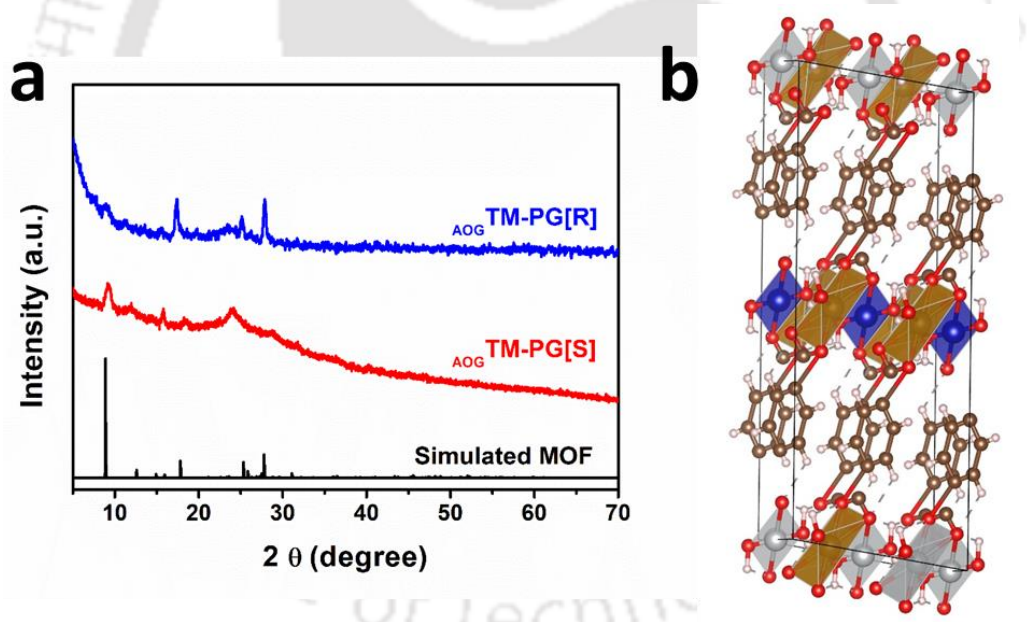

Figure 5.15. Structural characterizations of TM–MOF–PG hybrids: (a) XRD patterns of $_{AOG}$TM–PG[R] and $_{AOG}$TM–PG[S]; (b) an unit cell of TM–MOF crystal in $_{AOG}$TM–PG hybrid.

Table 5.3. Summary of structure determinations of TM of $_{AOG}$TM–PG hybrid.

Material	TM
Crystal system	Triclinic
Space group	P 1
Lattice parameters	
a (Å)	7.74407
b (Å)	7.80632
c (Å)	20.2100
α (˚)	90.5044
β (˚)	80.5890
γ (˚)	115.5600
Volume (Å^3)	1084.7233

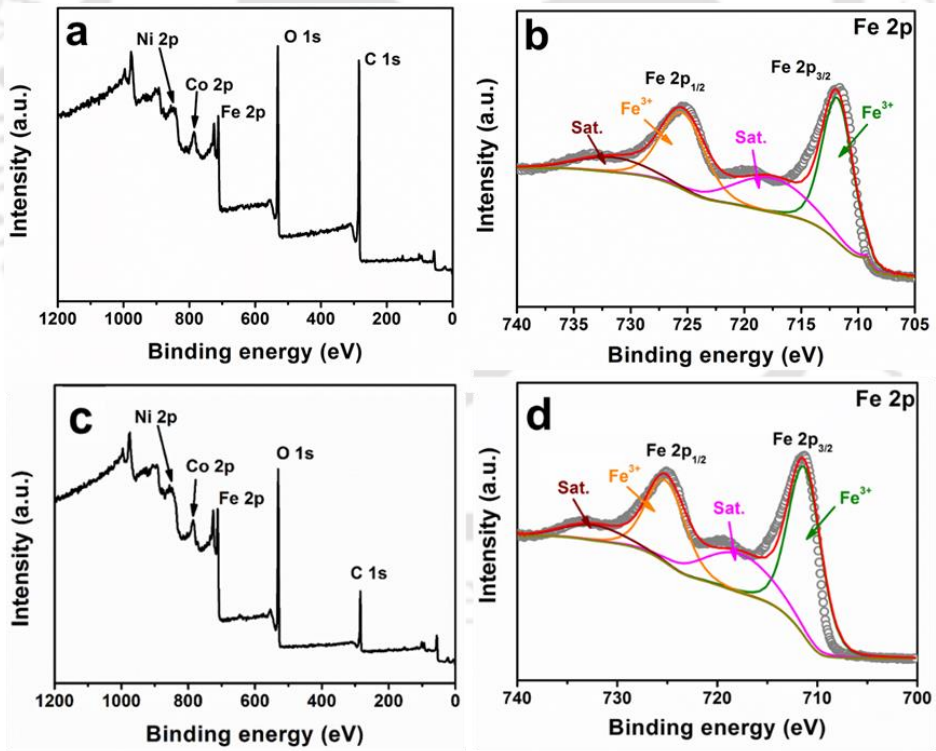

Figure 5.16. (a) XPS survey spectrum and (b) high resolution Fe 2p XPS spectrum of $_{AOG}$TM–PG[R]; (c) XPS survey spectrum and (d) high resolution Fe 2p XPS spectrum of $_{AOG}$TM–PG[S].

We further propose that the nanowire morphology of Cu(BTC) and the rod–like structure of TM–MOFs in $_{AOG}$Cu(BTC)–PG and $_{AOG}$TM–PG[R] respectively are associated with the preferential nucleation and subsequent oriented growth of the nuclei within the graphene framework. The preferential nucleation is related to the strong electrostatic and $\pi - \pi$ interactions of the benzene rings of BTC/BDC ligands with the basal plane of graphene as observed in MD simulation study, [36, 37] while the controlled and slow diffusion of BTC/BDC ligands into the hydrogel medium leads to the subsequent oriented growth of the nuclei. In contrast, the sheet like morphology of the MOF in $_{AOG}$TM–PG[S] hybrid can be ascribed to the capping effect of acetate ions used in as the precursors, [38] these acetate ions can preferentially absorb onto the top surface of the in–growing nanocrystals and thereby limit their longitudinal growth which ultimately results in nanosheets structure.

To further support the proposed growth mechanism, evolution of MOF structures was examined for different hydrogel–organic reaction times (e.g. 0.5h, 4h and 24h). The FESEM images revealed that there is a continuous evolution of the morphology of the as grown MOF nanostructures with increasing reaction time. The evolution of nanowire structure is clearly evident for the case of Cu(BTC), where after a reaction time of 0.5 h, nanorods of Cu(BTC) of sizes 50–200 nm was formed (Figure 5.17.c). These nanorods further grew into nanowires shape of sizes 1–2 μm (Figure 5.17.d) and finally into a few microns (Figure 5.8.a) after a hydrogel–organic reaction for 4 h and 24 respectively. For the case of tri–metallic MOFs in both the hybrids no particle growth was observed at the initial stage (after 0.5 h) of the reaction (Figure 5.17.e and g). However, rod–like (Figure 5.17.f) and very small protruding sheet–like (Figure 5.17.h) morphologies were observed for tri–metallic MOFs in the hybrids $_{AOG}$TM–PG[R] and $_{AOG}$TM–PG [S] respectively after 4 h of reaction. After 24 h the smaller protruding sheets in the hybrid $_{AOG}$TM–PG [S] were seen to further grow into bigger sheets (up to several microns) (Figure 5.13.a–b). These time dependent growth of the morphology of MOFs in hydrogel–organic reaction clearly indicates the preferential nucleation and their subsequent oriented growth into different MOF structures.

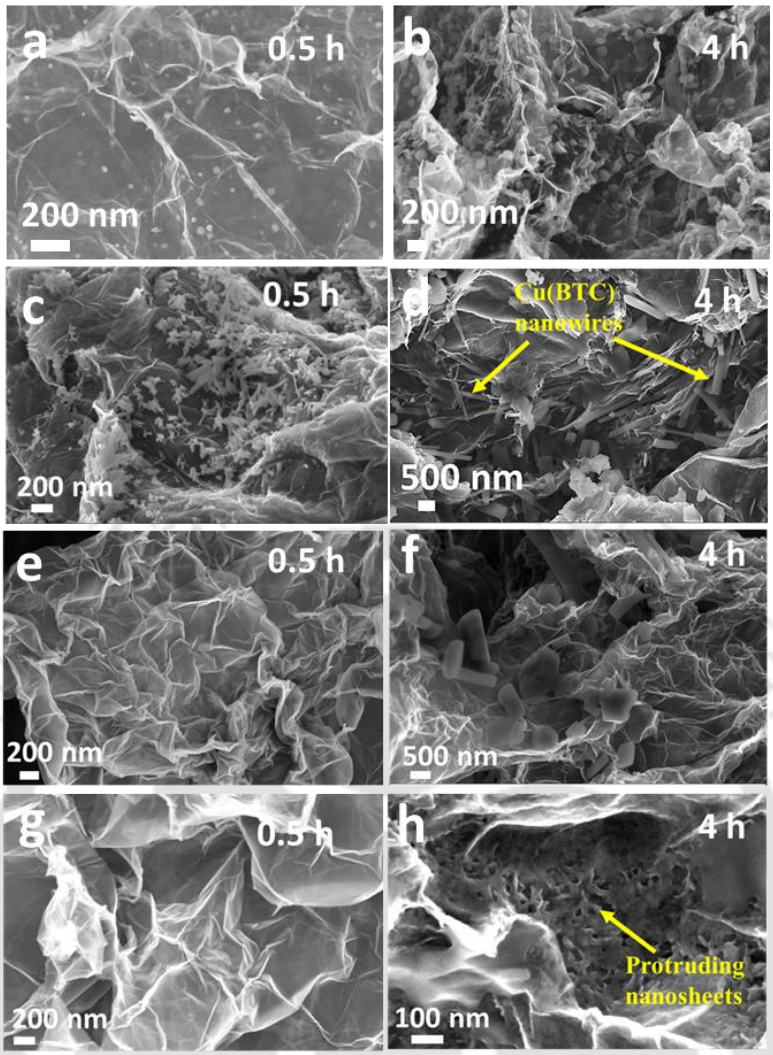

Figure 5.17. Time dependent FESEM study for gel–organic interfacial reaction time 0.5 h and 4h: (a)–(b) $_{AOG}$ZIF67–PG, (c)–(d) $_{AOG}$Cu(BTC)–PG, (e)–(f) $_{AOG}$TM–PG[R] and (g)–(h) $_{AOG}$TM–PG[S].

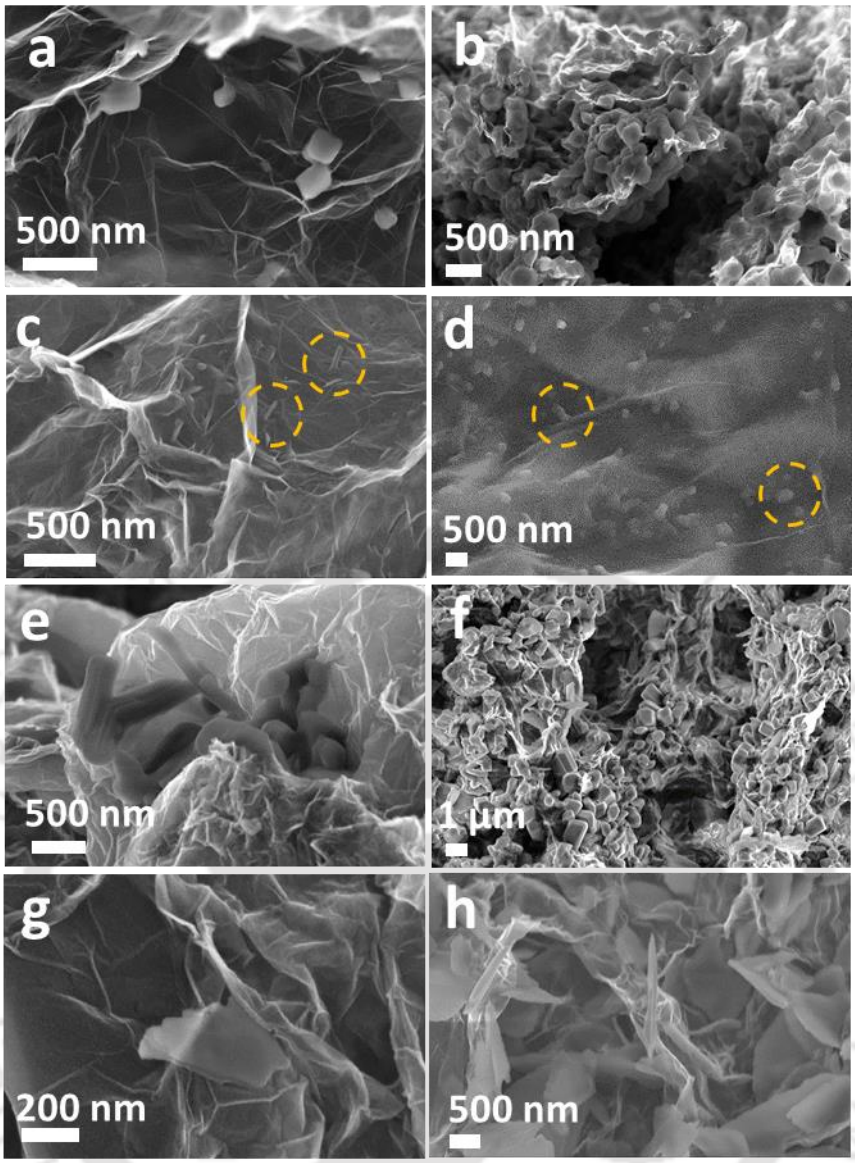

Figure 5.18. FESEM images of MOFs prepared at different concentrations of reactants: (a)–(b) $_{AOG}$ZIF67–PG, (c)–(d) $_{AOG}$Cu(BTC)–PG, (e)–(f) $_{AOG}$TM–PG[R] and (g)–(h) $_{AOG}$TM–PG[S].

Not only the reaction time but the morphologies of the MOFs were found to be highly dependent on the concentration of the reactant species. FESEM images reveal that the MOF sizes remain the smallest for very low concentration of reactants whereas the MOF sizes increase when high reactant concentrations were used (Figure 5.18.a–h). At very high concentration of reactants, agglomerated structures can be observed in some cases ($_{AOG}$ZIF67–PG, $_{AOG}$TM–PG[R]) (Figure 5.18.b and f). Nevertheless, XRD data suggests that the crystal structures of these MOFs remain mostly unaffected by the change in reactant concentrations

(Figure 5.19.a–d). The above results suggest that, to develop MOFs with uniform morphology and homogeneous distribution within porous graphene framework we require to have a reaction condition with the high reactant concentration for $_{AOG}$Cu(BTC) and medium concentrations for $_{AOG}$ZIFs, $_{AOG}$TMs with 24 hours of reaction time (for all cases).

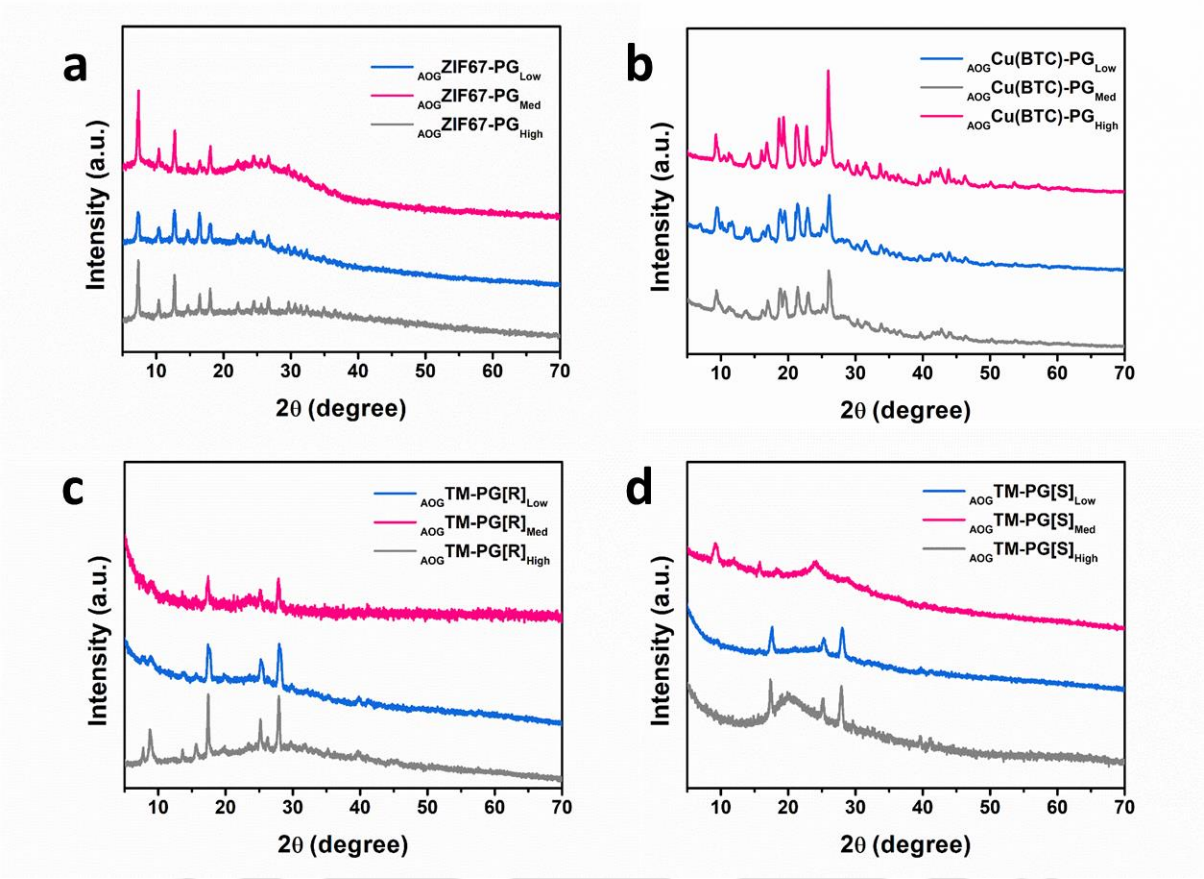

Figure 5.19. XRD patterns of MOFs prepared at different concentrations of reactants: (a) $_{AOG}$ZIF67–PG, (b) $_{AOG}$Cu(BTC)–PG, (c) $_{AOG}$TM–PG[R] and (d) $_{AOG}$TM–PG[S].

5.3.13 Role of graphene hydrogel and organic phase in controlling MOF nanostructure:

We have further investigated the role of graphene hydrogel in this bi–phasic reaction in tuning MOF nanostructure, by conducting controlled experiments for the growth of MOFs in purely bulk aqueous–organic bi–phasic reaction system without the presence of graphene hydrogel (related MOFs are denoted as $_{AO}$MOF). On the other hand, the role of organic interface in controlling the MOF structure could be understood by conducting experiments in sole aqueous phase reaction in both presence (corresponding hybrids were denoted as $_{AG}$MOF–PG) and absence of PG (the MOFs were called $_{A}$MOF). As expected, MOFs grown in bulk phase

reactions without the presence of graphene hydrogel either exhibited non–uniform bulk sheet–like mixed morphology (for the cases of $_{AO}$Cu(BTC), $_{A}$Cu(BTC) and $_{A}$ZIF8) (Figure 5.20.a–b and f), or irregular structures (for the cases of $_{AO}$ZIF67/8, $_{AO}$TM[R], $_{A}$ZIF67, $_{A}$TM[R]) (Figure 5.20.c–d, e and g–h).

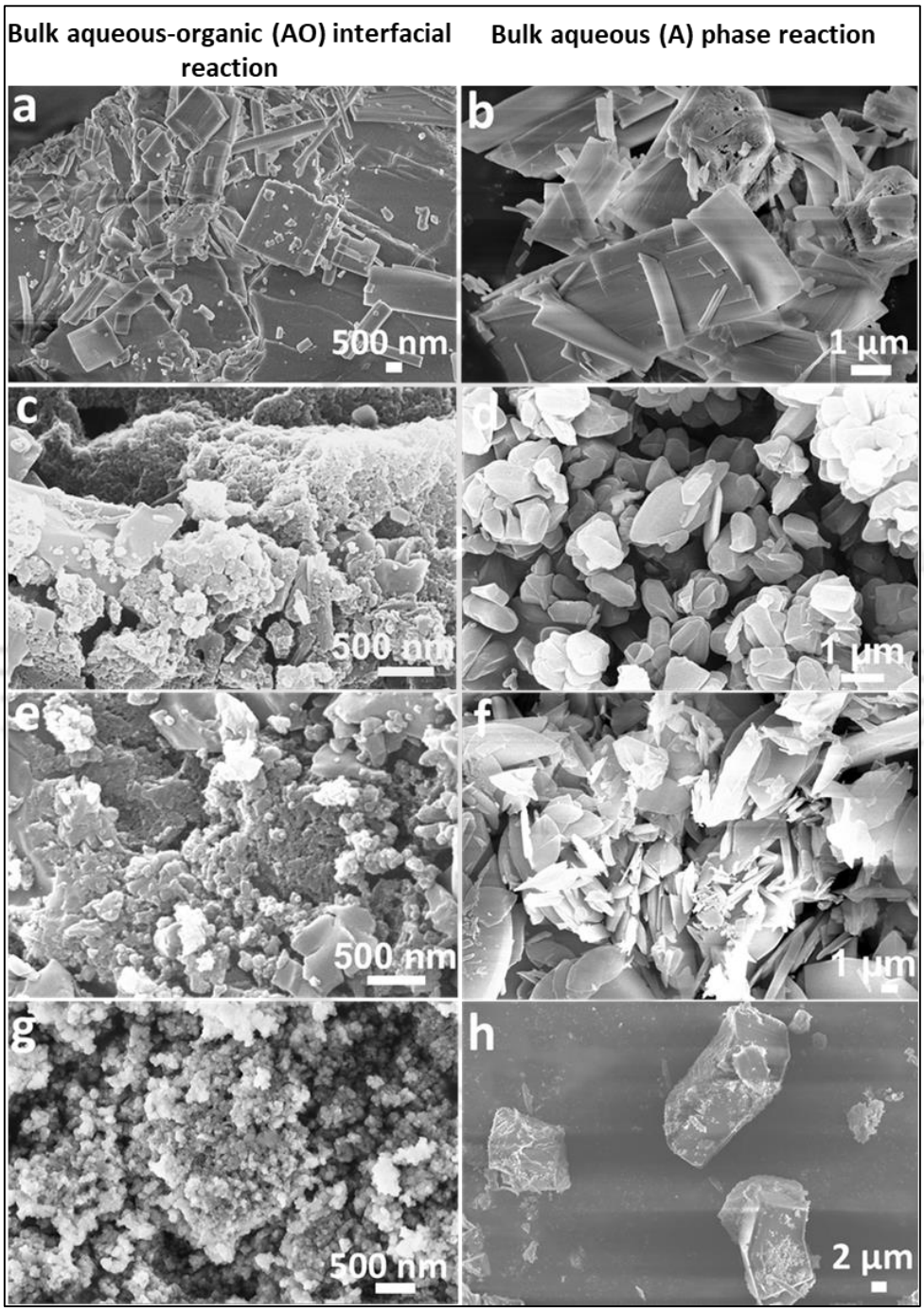

Figure 5.20. FESEM images of MOFs synthesized in bulk aqueous–organic (AO) and aqueous (A) phase reactions (without any hydrogel) for (a) $_{AO}$Cu(BTC) and (b) $_{A}$Cu(BTC); (c) $_{AO}$ZIF67 and (d) $_{A}$ZIF67; (e) $_{AO}$ZIF8 and (f) $_{A}$ZIF8; (g) $_{AO}$TM[R] and (h) $_{A}$TM[R].

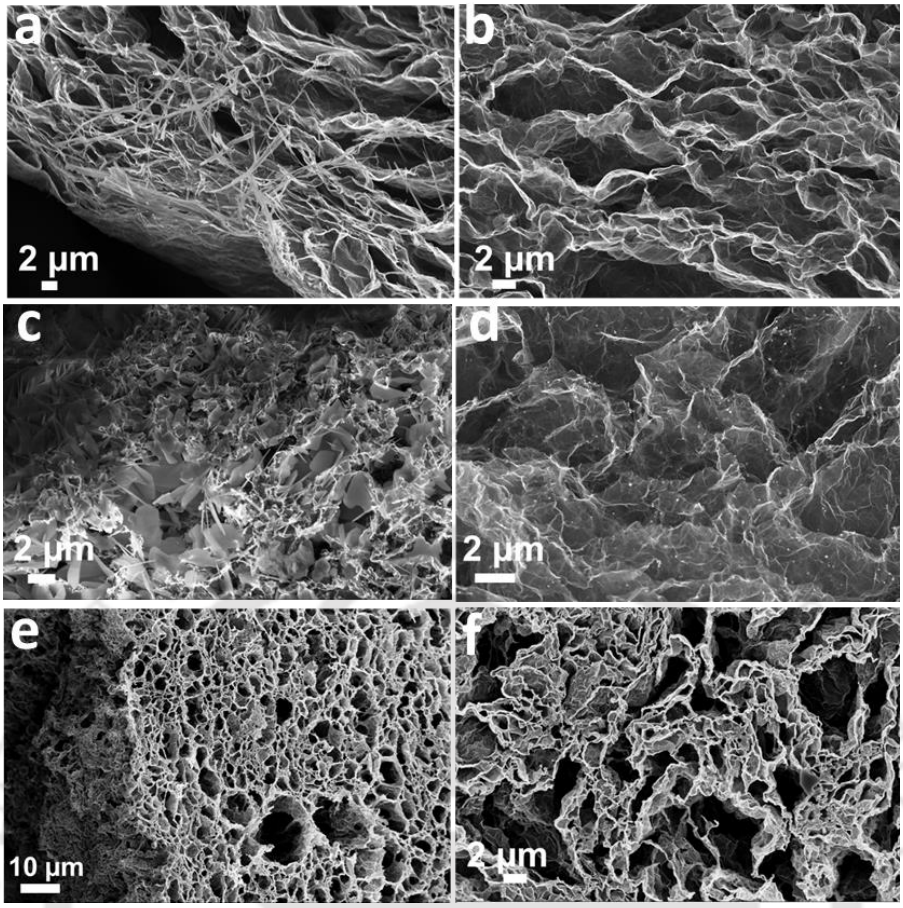

Figure 5.21. Surface confined water phase synthesis of (a)–(b) $_{AG}$Cu(BTC)–PG, (c)–(d) $_{AG}$ZIF67–PG and (e)–(f) $_{AG}$ZIF8–PG. Figure (a), (c) and (e) show the growth of MOFs just below the outer surface of PG and Figure (b), (d) and (f) show that the concentration of as grown MOFs decrease in the interior of the PG.

However, the MOFs grown via graphene hydrogel mediated aqueous phase reactions (for the cases of $_{AG}$Cu(BTC)–PG, $_{AG}$ZIF67–PG and $_{AG}$ZIF8–PG hybrids) exhibited a well–defined morphology (Figure 5.21.a–f) although different from that obtained via hydrogel–organic reactions. For instance, Cu(BTC) MOFs in $_{AG}$Cu(BTC)–PG hybrid showed nanobelt structure with several microns in length and ~200–500 nm in width, but the growth was found to be limited only within a depth of 10–15 μm from the hydrogel surface (Figure 5.21.a–b). For the case of $_{AG}$ZIF67–PG hybrid mixed nanosheet/particle morphology of ZIF67 was obtained (Figure 5.21.c–d) while in case of $_{AG}$ZIF8–PG hybrid ZIF8 exhibited rod–like structure (Figure 5.21.e–f). Interestingly, like Cu(BTC) MOFs in $_{AG}$Cu(BTC)–PG, both the ZIF67 and ZIF8 MOF particle density were found to decrease rapidly from the hydrogel surface to its core (Figure 5.21.c–f).

These results indicate that the narrow pore channels of graphene hydrogel alone can control the diffusion of reactant species and hence the growth kinetics of MOFs as observed in the case of $_{AG}$MOF–PG. However, the absence of the hydrogel–organic interface in $_{AG}$MOF–PG system leads to the rapid diffusion and hence the growth of the MOFs near the surface of the hydrogel. The rapid growth of MOFs near the graphene surface limits the further diffusion of reactants and thereby restricting the growth of MOFs near the surface of the hydrogel only. These results therefore highlight the significance of the controlled diffusion process at the hydrogel–organic interface which plays the key role in the development of morphology tuned MOF–PG hybridization.

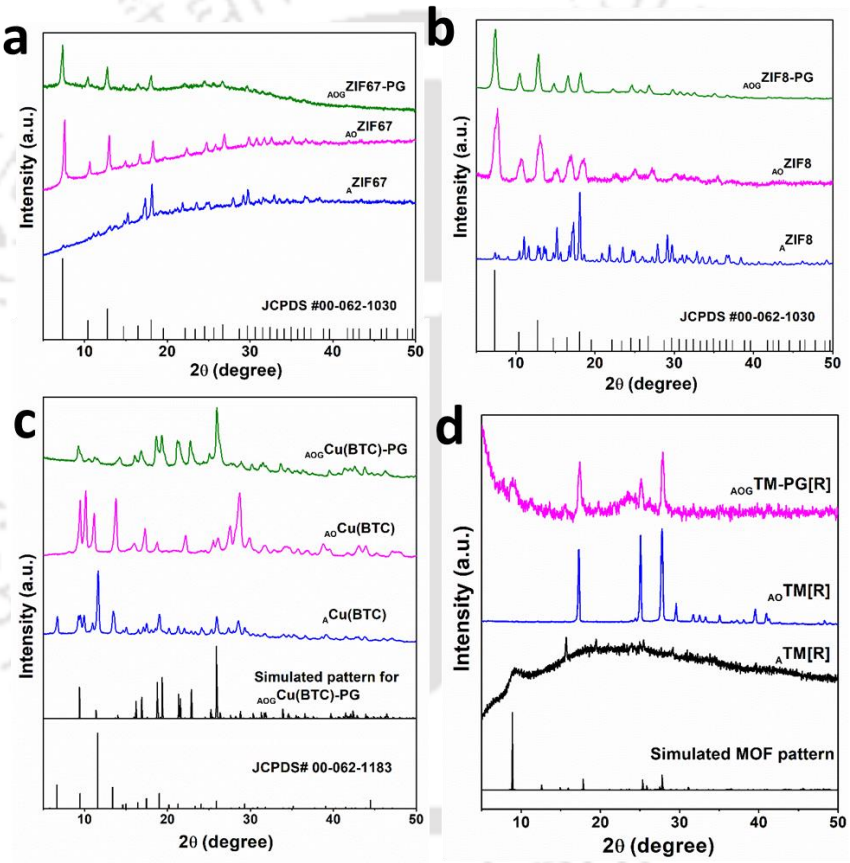

Figure 5.22. Comparison of XRD patterns of various MOFs and MOF–PG hybrids synthesized by different methods: (a) $_{AOG}$ZIF67–PG, $_{AO}$ZIF67 and $_{A}$ZIF67; (b) $_{AOG}$ZIF8–PG, $_{AO}$ZIF8 and $_{A}$ZIF8; (c) $_{AOG}$Cu(BTC)–PG, $_{AO}$Cu(BTC) and $_{A}$Cu(BTC) and (d) $_{AOG}$TM–PG[R], $_{AO}$TM[R] and $_{A}$TM[R].

Importantly, the crystal structures of the MOFs developed via different techniques as stated above, also possess different characteristics as examined from their XRD patterns

(Figure 5.22.a–d). For instance, although $_{AO}$ZIF67 and $_{AO}$ZIF8 had similar cubic crystal structure of ZIF67/ZIF8 of $_{AOG}$ZIF67–PG and $_{AOG}$ZIF8–PG respectively (Figure 5.22.a–b), $_{A}$ZIF67 and $_{A}$ZIF8 possessed orthorhombic crystal structures (*Pbam* space group) similar to the crystal structure of leaf–like ZIF67/ZIF8 MOFs as reported previously. [39, 40] While Cu(BTC) exhibited typical cubic crystal structure irrespective of the synthesis condition they possessed different space group symmetry. For example, bulk $_{AO}$Cu(BTC) and $_{A}$Cu(BTC) had a space group of *Fm–3m* different form the space group of HKSUT1 ($P\ 2_{1/c}$) in the hybrid $_{AOG}$Cu(BTC)–PG (Figure 5.22.c). In case of TM–MOFs prepared by different synthesis strategies, all the MOFs exhibited similar crystal structure (Figure 5.22.d).

Besides these transition metal based MOFs, platinum nanoparticle–PG hybrids ($_{AOG}$Pt–PG) was also developed to demonstrate the adoptability of this interfacial diffused induced synthetic protocol in controlled hybridization. The FESEM and FETEM images (Figure 5.23.a–b) confirmed the uniform distribution of Pt nanoparticles over the surfaces of graphene. SAED pattern (Figure 5.23.c) showed the presence of characteristic Pt planes namely, (111), (200) and (220). The HRTEM image (Figure 5.23.d) further revealed that Pt nanoparticles having size of ~3–5 nm form Pt–nanoclusters and inter–planer spacing of 0.23 nm corresponding to its (111) crystallographic planes. All these results further illuminate the insights of the controlled reaction kinetics for the synthesis of graphene–nanoparticles hybrids.

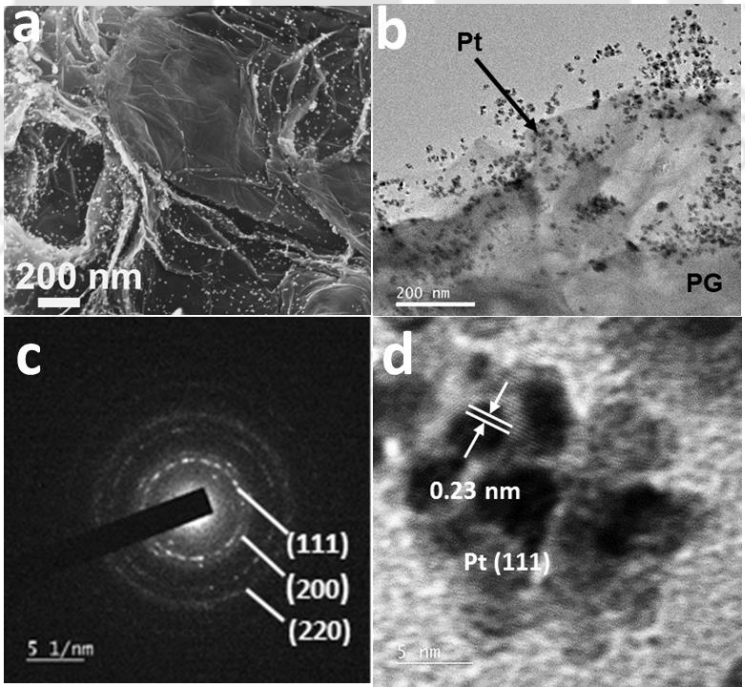

Figure 5.23. Characterization of $_{AOG}$Pt–PG: (a) FESEM, (b) FETEM, (c) SAED pattern and (d) HRTEM images of $_{AOG}$Pt–PG hybrid.

5.3.14 Electrochemical characterizations:

It is known that tri–metallic MOFs with BDC ligand exhibit good electrocatalytic activity toward OER process. Therefore, the tri–metallic–MOFs with tuned nanostructures in conjugation with the high conductivity and porosity of the PG are expected to deliver excellent OER activity. Linear sweep voltammetry (LSV) plots (Figure 5.24.a–b) show that the overpotentials (η) of OER to achieve a current density of 10 mA cm^{-2}, is 255 mV for $_{AOG}$TM–PG[R] which is much lower in comparison to the commercial catalyst RuO_2 (334mV) and also lower than the other MOFs or MOF–PG hybrids namely, bulk $_{AO}$TM[R] (266mV), $_{AOG}$TM–PG[S] (287mV) and bulk $_{AO}$TM[S] (301 mV). Besides, achieving a high current density (~100 mA cm^{-2}) at relatively low overpotential is very important for practical applications. The comparative bar diagram (Figure 5.25) and Figure 5.24.b indicate that the overpotentials required to deliver a current density of 100 mA cm^{-2} for the samples $_{AOG}$TM–PG[R], $_{AO}$TM[R], $_{AOG}$TM–PG[S] and $_{AO}$TM[S] are 300 mV, 317 mV, 338 mV and 346 mV respectively which are superior in comparison to RuO_2 electrocatalyst (402 mV). Furthermore, $_{AOG}$TM–PG achieved a large current density of 500 mA cm^{-2} at an affordable overpotential of 335 mV (Figure 5.24.a) indicating its superior performance over the other catalysts.

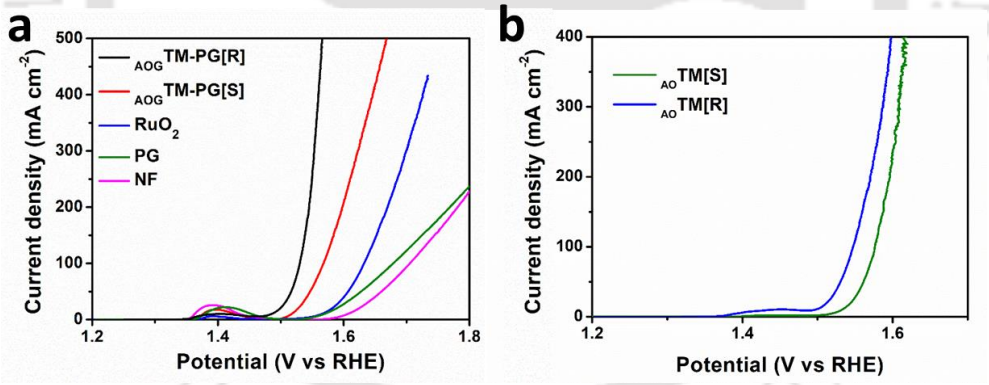

Figure 5.24. Electrocatalytic OER activity: (a)–(b) comparison of linear sweep voltammetry (LSV) curves of various electrocatalysts at a scan rate of 5 mV s^{-1}.

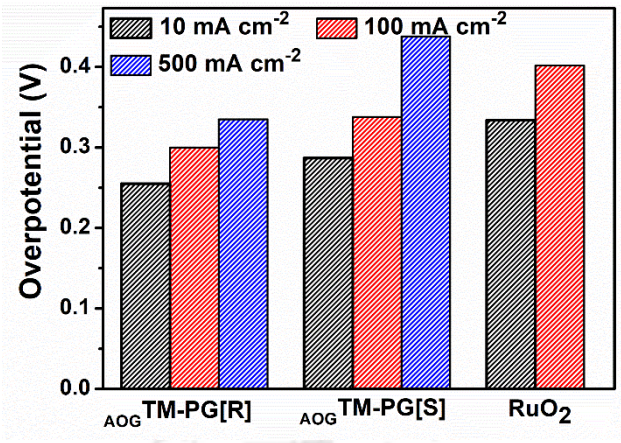

Figure 5.25. Comparison of overpotentials of $_{AOG}$TM–PG[R] and $_{AOG}$TM–PG[S] with commercial RuO_2 at different current densities.

The reaction kinetics of the electrocatalytic OER process, the samples were analyzed via Tafel equation (equation 1.20). Figure 5.26.a–b reveal that $_{AOG}$TM–PG[R] possesses the lowest Tafel slope of 44.3 mV dec^{-1} as compared to the $_{AO}$TM[R] (49.8 mV dec^{-1}), $_{AOG}$TM–PG[S] (52.1 mV dec^{-1}), $_{AO}$TM[S] (46.4 mV dec^{-1}) and RuO_2 (62.9 mV dec^{-1}). The low Tafel slopes as exhibited by the tri–metallic MOF nanostructures, suggest an intrinsically high activity and fast reaction kinetics of OER process.

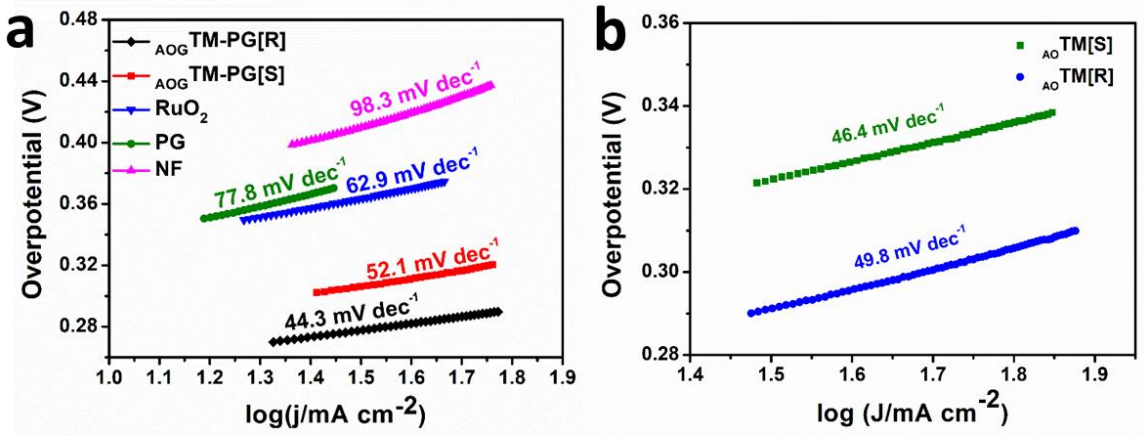

Figure 5.26. Electrocatalytic OER activity: (a)–(b) comparison of Tafel plots of various electrocatalysts.

As discussed in chapter 1, the mass activity of an electrocatalyst remains an important metric to quantitatively compare the OER activities of different samples. A compression of the mass activities of the hybrid catalysts at an overpotential of 300 mV (Figure 5.27) revealed that $_{AOG}$TM–PG[R] possessed the highest mass activity of 155.9 A g^{-1} which was significantly higher than the mass activities of $_{AOG}$TM–PG[S] and RuO_2 (~4 and 43 times respectively). It is to be noted that, the MOF content in the hybrids $_{AOG}$TM–PG[R] and $_{AOG}$TM–PG[S] were respectively close to 53% and 57% with respect to the total mass of the hybrids. As a result, the observed high mass activity of $_{AOG}$TM–PG[R] can be associated with the intrinsically high activity and the large number of exposed active sites of the hybrid heterostructure.

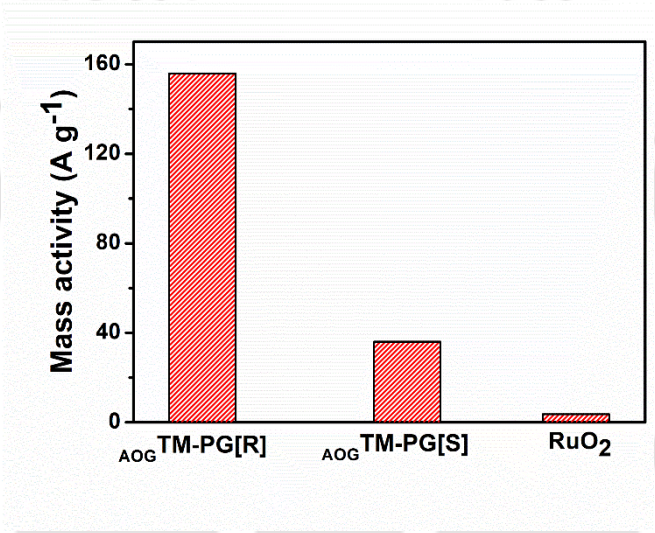

Figure 5.27. Comparison of mass activities of $_{AOG}$TM–PG[R] and $_{AOG}$TM–PG[S] with commercial RuO_2 at an overpotential of 300 mV.

It is worth mentioning that, not all the metal centers of MOF are OER active. Therefore, estimating the number of catalytic active sites is very important. For this we calculated the electrochemical surface areas (ECSA) by measuring the double layer capacitances (C_{dl}) from the CV profiles taken in the non–Faradaic region (Figure 5.28.a–d) which gives a direct estimation of the possible number of catalytically active sites. The C_{dl} values were calculated to be 11.7 mF cm^{-2}, 6.1 mF cm^{-2}, 23.1 mF cm^{-2} and 5.25 mF cm^{-2} for the samples $_{AOG}$TM–PG[R], $_{AO}$TM[R], $_{AOG}$TM–PG[S] and $_{AO}$TM[S] respectively (Figure 5.29.a–d). The very high C_{dl} value obtained for $_{AOG}$TM–PG[R] clearly indicates a high ECSA and hence a high number of exposed catalytic sites. Moreover, a high specific surface area of 110 m^2 g^{-1} was obtained for $_{AOG}$TM–PG[R] as measured from the Brunauer–Emmett–Teller (BET) analysis (Table 5.4

and Figure 5.30 for specific surface areas of various MOF–PG hybrids). Therefore, both the ECSA and BET results suggest that $_{AOG}$TM–PG[R] possessed a large specific surface area and very high number of exposed catalytically active sites. Furthermore, the observed high value of C_{dl} for $_{AOG}$TM–PG[S] than $_{AOG}$TM–PG[R] hybrid could be ascribed to the sheet–like structure (high surface area) of tri–metallic MOF in $_{AOG}$TM–PG[S]. Nevertheless, both the MOF–PG hybrids exhibited a high value of C_{dl} originating from the intrinsically high surface area of the tri–metallic MOFs as well as the presence of high surface area porous graphene framework.

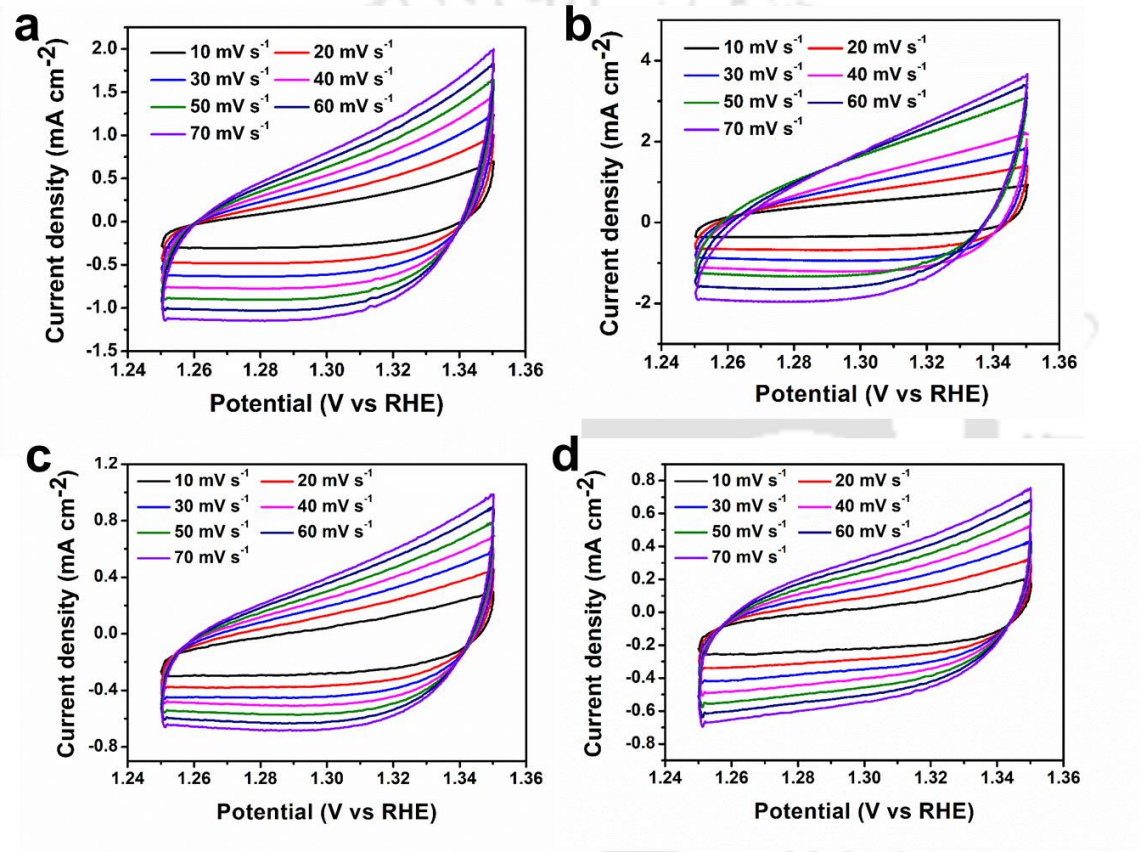

Figure 5.28. Cyclic voltammetry curves of (a) $_{AOG}$TM–PG[R], (b) $_{AOG}$TM–PG[S], (c) $_{AO}$TM[R] and (d) $_{AO}$TM[S] at different scan rates in the non–Faradaic region.

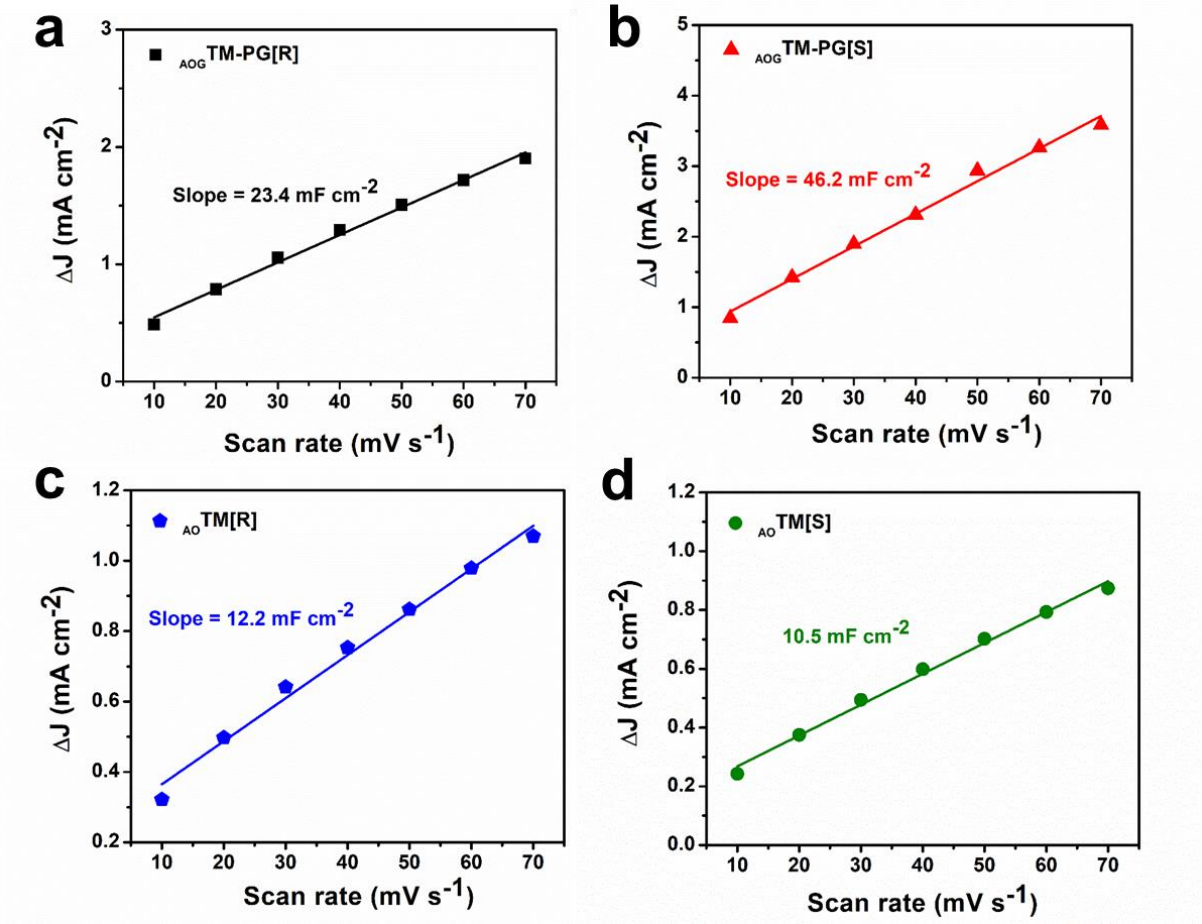

Figure 5.29. Linear plots of $\Delta J = (J_a - J_c)$ vs scan rates for (a) $_{AOG}$TM–PG[R], (b) $_{AOG}$TM–PG[S], (c) $_{AO}$TM[R] and (d) $_{AO}$TM[S].

Table 5.4. BET specific surface area of MOF–PG hybrids

	$_{AOG}$ZIF67–PG	$_{AOG}$Cu(BTC)–PG	$_{AOG}$TM–PG[R]	$_{AOG}$TM–PG[S]
BET specific surface area ($m^2\ g^{-1}$)	1105	85.9	111	83

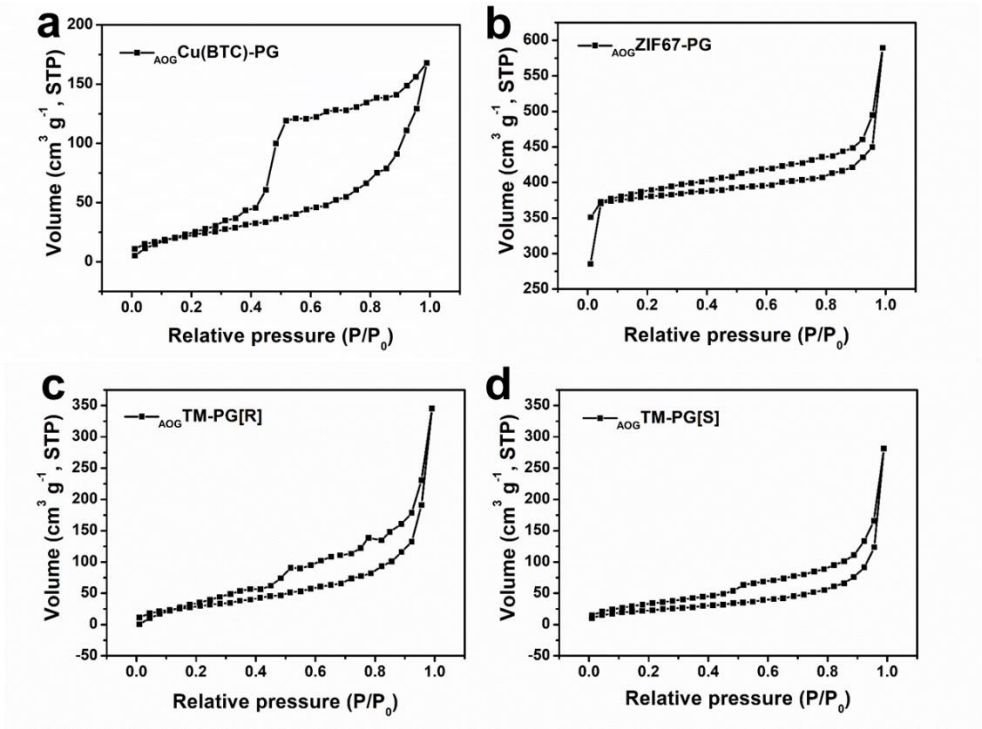

Figure 5.30. N_2 adsorption/desorption (BET) isotherms for (a) $_{AOG}$Cu(BTC)–PG, (b) $_{AOG}$ZIF67–PG, (c) $_{AOG}$TM–PG[R] and (d) $_{AOG}$TM–PG[S].

The reaction kinetics of the electrochemical OER process were further investigated by the electrochemical impedance spectroscopy (EIS). The Nyquist plots (Figure 5.31.a–b) were semicircular in nature revealing typical solution resistance (R_s) and the charge–transfer resistance (R_{ct}). It was found that, $_{AOG}$TM–PG[R] and $_{AOG}$TM–PG[S] possessed a low R_s of 0.84 Ω and 0.85 Ω respectively corresponding to the low R_{ct} of 1.61 Ω and 0.69 Ω as compared to the other samples, indicating efficient charge transfer kinetics of the electrode. The low resistances of the hybrid samples can further be attributed to the direct growth of MOFs over the conducting graphene sheets which favors efficient electron transportation and thereby results in the high OER activity by minimizing iR–loss.

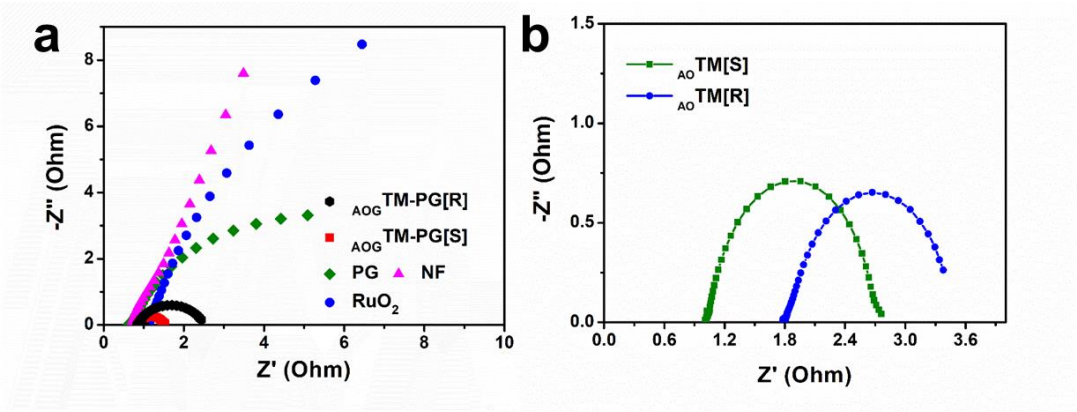

Figure 5.31. (a)–(b) Electrochemical impedance spectra (EIS) of various electrocatalysts.

To further study the possible dependency of the OER activity on the morphology of the MOF structure we compared the performance of $_{AOG}$TM–PG[R]$_{High}$ and $_{AOG}$TM–PG[R]$_{Low}$ with the $_{AOG}$TM–PG[R]. The LSV results showed that $_{AOG}$TM–PG[R]$_{High}$ and $_{AOG}$TM–PG[R]$_{Low}$ possessed a relatively high overpotentials (271 mV and 276 mV respectively) with corresponding Tafel slopes of 68.9 mV dec^{-1} and 41.6 mV dec^{-1} (Figure 5.32.a–c). The high overpotentials of $_{AOG}$TM–PG[R]$_{High}$ and $_{AOG}$TM–PG[R]$_{Low}$ in comparison to $_{AOG}$TM–PG[R] indicates very poor OER activity originating from the agglomerated or low density of the MOFs formed within PG as evident from the FESEM images (Figure 5.18.e–f).

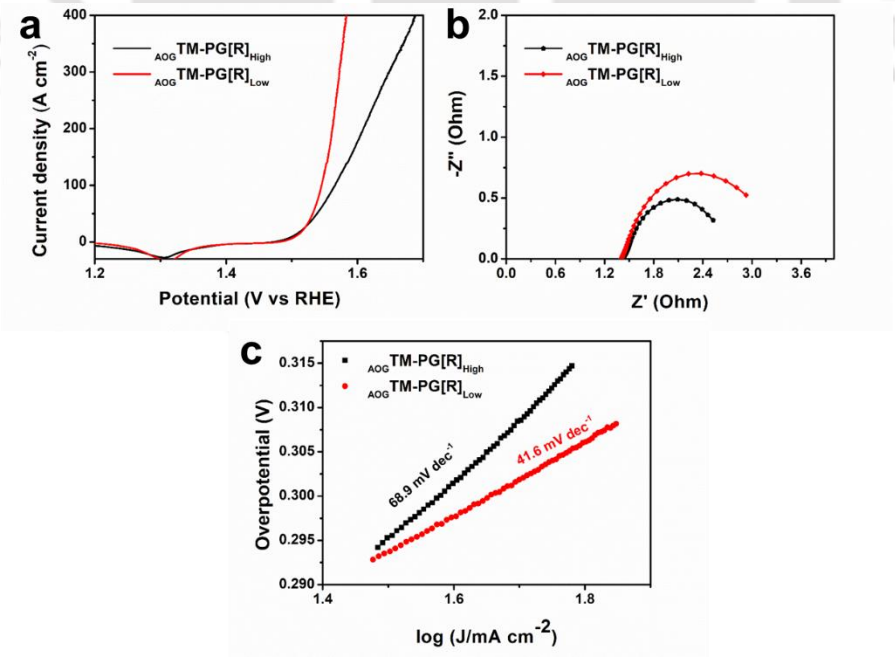

Figure 5.32. (a) LSV plot, (b) EIS spectra and (c) Tafel plots of $_{AOG}$TM–PG[R] prepared at different reactant concentrations.

To build OER based efficient energy storage/conversion systems the electrocatalyst should exhibit long term durability. To test the long term stability at high overpotential (280 mV vs RHE) chronoamperometry test was conducted for the hybrid catalyst $_{AOG}$TM–PG[R] (Figure 5.33). Interestingly, even after 24 hours of chronoamperometry test, no noticeable drop in the current density was observed. Moreover, the LSV performed before and after the durability test (inset of Figure 5.33) did not possess any obvious difference implying the long term stability of $_{AOG}$TM–PG[R] catalyst which is suitable for practical applications.

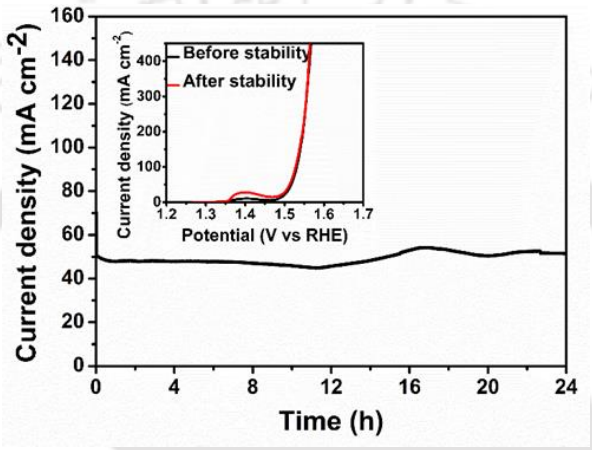

Figure 5.33. Durability test for $_{AOG}$TM–PG[R], the inset shows the LSV plots before and after the durability test.

The in–situ phase transformation of MOFs upon OER cycling has been established as the source of their high OER activity. [15, 16, 41] To associate the high activity of $_{AOG}$TM–PG[R] with the phase transformation, we studied the morphological, structural and electronic properties after a long term OER cycling. The FETEM image first suggests that the rod–like structure of the MOF in $_{AOG}$TM–PG[R] remained intact even after the OER process (Figure 5.34.a). However, nanopores were seen to generate over the rod structure indicating possible structural change. The HRTEM image (and supported by SAED pattern) (Figure 5.34.b) showed the evolution of crystalline domains with interlayer spacing of 0.25 nm and 0.24 nm which are related to the (101) crystal planes of nickel hydroxide ($Ni(OH)_2$) and (002) crystallographic planes of nickel oxyhydroxide (NiOOH) respectively. [16, 41]

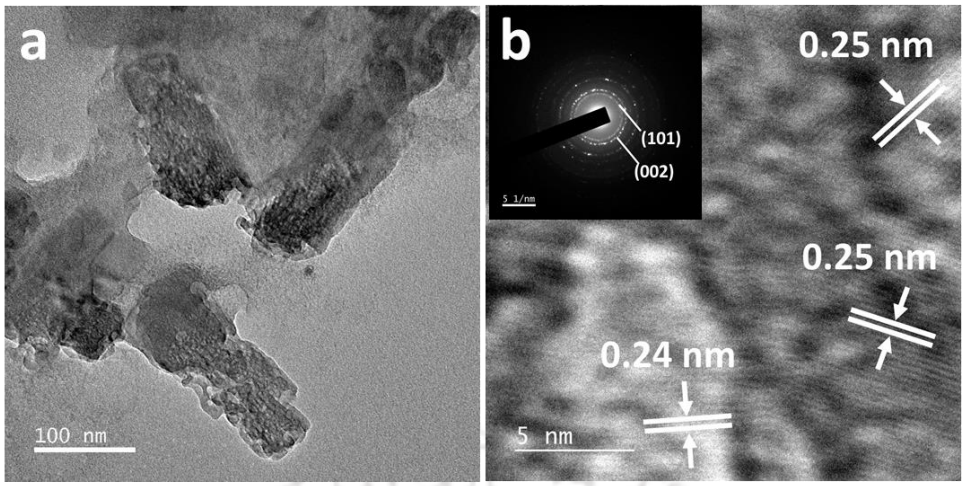

Figure 5.34. Study of origin of OER activity for $_{AOG}$TM–PG[R]: (a) FETEM image and (b) HRTEM image of $_{AOG}$TM–PG[R] after OER test.

This structural evolution of MOF structure however, did not alter the uniform distribution of the various atomic species of the MOFs (Ni, Co, Fe) as is evident from the scanning transmission electron microscope (STEM) elemental mapping results (Figure 5.35). The elemental composition of $_{AOG}$TM–PG[R] before and after OER cycling were analyzed by energy–dispersive X–ray spectroscopy (EDAX). It was found that, before OER cycling the atomic% of Ni, Fe and Co were calculated to be 1.85%, 2.95% and 1.47% (Figure 5.36.a). After OER cycling EDAX analysis (Figure 5.36.b) showed the presence of Ni, Co and Fe atomic species in the hybrid $_{AOG}$TM–PG[R]. Although, a decrement in the atomic% of Fe element was observed for OER treated $_{AOG}$TM–PG[R] (Figure 5.36.b) in comparison to the pristine hybrid owing to the possible etching of Fe atoms during the long OER cycling.

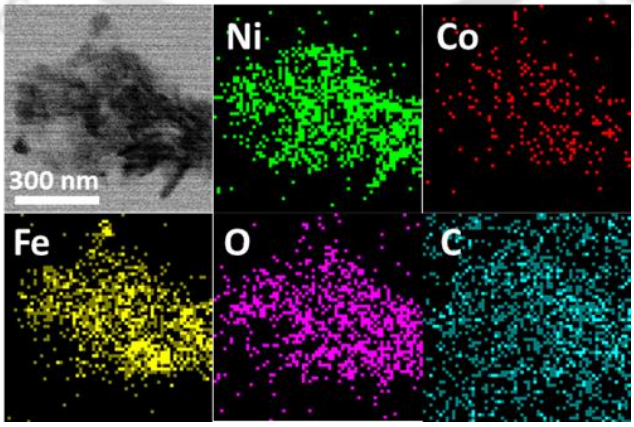

Figure 5.35. Study of origin of OER activity for $_{AOG}$TM–PG[R]: STEM elemental mapping of $_{AOG}$TM–PG[R] after OER test.

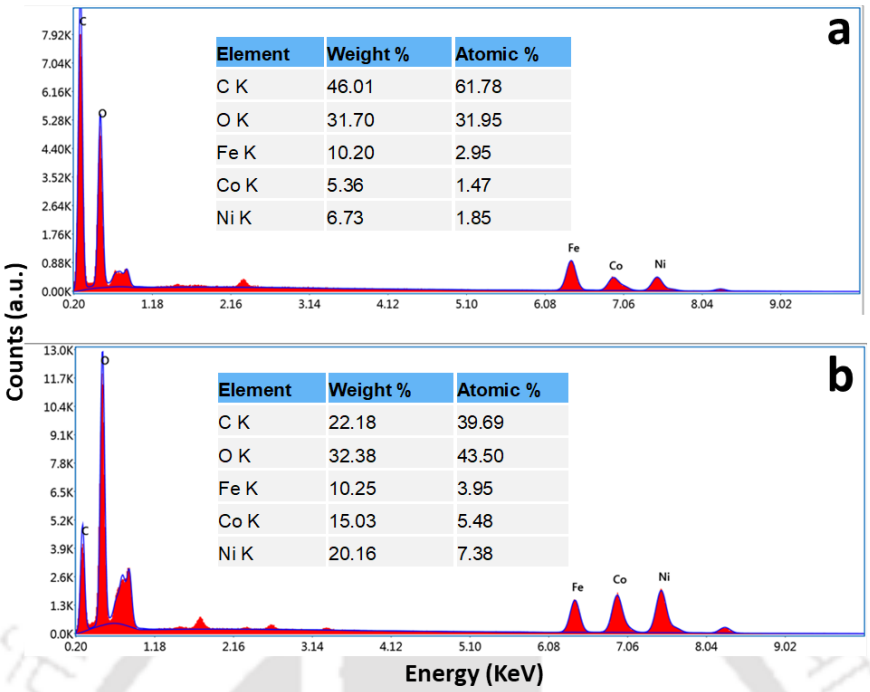

Figure 5.36. EDAX elemental analysis of $_{AOG}$TM–PG[R] (a) before and (b) after OER cycling.

The XPS analysis was conducted on the sample $_{AOG}$TM–PG[R] before and after the OER test to understand the electronic structure modification due to the structural evolution of MOF. From the energy positions of the high resolution XPS spectra of $_{AOG}$TM–PG[R] revealed that Ni (with Ni $2p_{3/2}$ at 856.4 ev and Ni $2p_{1/2}$ at 873.6 eV) (Figure 5.37.a) and Co (with Co $2p_{3/2}$ at 781.8 ev and Co $2p_{1/2}$ at 797.7 eV) (Figure 5.37.b) remained in +2 oxidation states, while the Fe (with Fe $2p_{3/2}$ at 711.9 ev and Fe $2p_{1/2}$ at 725.6 eV) (Figure 5.37.c) remained in the +3 oxidation state. [15, 20, 42] Furthermore, the deconvoluted high resolution Ni 2p XPS spectrum taken after OER test (Figure 5.37.a) showed four main peaks with the satellites of which the peaks at binding energies 855.8 eV, 873.1 eV were ascribed to the Ni^{2+} state of nickel hydroxide ($Ni(OH)_2$) whereas the peaks at 856.7 eV and 874.1 eV were related to the Ni^{3+} state of nickel oxyhydroxide (NiOOH). [16, 43] These results indicate electrochemical transformation of Ni sites of MOF into its various hydroxide/oxyhydroxide structures further supporting the results obtained by HRTEM and XRD analysis. Similarly, Co 2p XPS peak obtained after OER test (Figure 5.37.b) were fitted with peaks at binding energies 782.4 eV and 797.3 eV corresponding to the Co^{2+} state of cobalt hydroxide ($Co(OH)_2$) while the peaks at 780.2 eV and 795.5 eV could be associated with the Co^{3+} state of cobalt oxyhydroxide (CoOOH) suggesting in–situ transformation of Co species of the MOF. [44, 45] Importantly, a

shift in the Fe 2p peak toward the higher binding energy was observed after OER test (Figure 5.37.c). The components of Fe 2p centered at 713.3 eV (Fe $2p_{3/2}$) and 726.8 eV (Fe $2p_{1/2}$) (Figure 5.37.c) indicated the existence of Fe^{3+} state of FeOOH. [15]

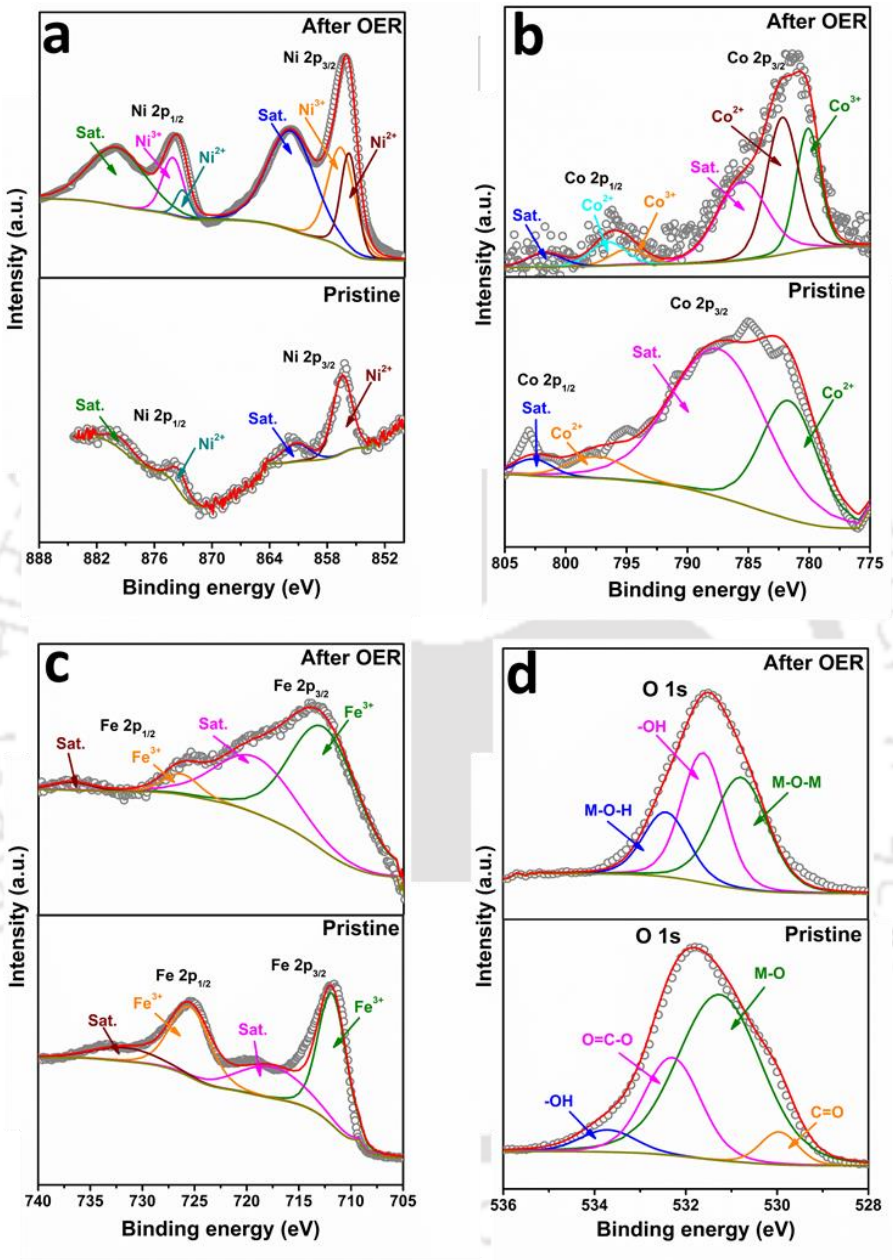

Figure 5.37. Study of electronic structural evolution of $_{AOG}$TM–PG[R] upon water oxidation: high resolution XPS spectra of (a) Ni 2p, (b) Co 2p, (c) Fe 2p and (d) O 1s for $_{AOG}$TM–PG[R] before and after OER test.

The phase transformation of MOF into various metal hydroxide/oxyhydroxides structures was further confirmed from the deconvolution of O1s XPS spectrum where the

appearance of new peaks at 530.8 eV and 532.4 eV were assigned to the oxygen in M–O–M bonding and M–O–H bonding states respectively (Figure 5.37.d). [16, 41] Therefore, the results obtained by FETEM, XRD and XPS analysis collaboratively revealed the in–situ phase transformatoon of MOF into various metal hydroxide/oxyhydroxides states having uniformly distributed Ni, Co and Fe centers and possessing +2/+3 mixed ionic state which served as the active species for the high OER activity. In this multimetallic hydroxide/oxyhydroxide states, the Ni^{3+} sites serve as the OER active sites while the role of the Co and Fe species in their +2/+3 states is to further enhance the activity of the Ni–sites by drawing away the electron cloud density from the Ni–sites which promotes the adsorption of OH^- and OOH^- species (OER intermediates). [19, 46]

In conclusion, the excellent OER activity of the $_{AOG}$TM–PG[R] hybrid can be attributed to the synergistic effect of a number of possible factors: (i) the rod–like structure of the MOF which possesses a large number of catalytically exposed active metal sites; (ii) electrochemically formed Ni/Co/Fe hydroxide/oxyhydroxide structure during the in–situ phase transformation of the MOF serve as the active species with favorable electrochemical kinetics; (iii) the high conductivity of PG framework which promotes rapid electronic mass transportion the OER process. Moreover, the porous framework of PG ensures high accessibility of the active sites by the electrolyte ions and the release of the gaseous specious during OER process. Table 5.5 compares the electrocatalytic OER performance of $_{AOG}$TM–PG[R] hybrid with other reported MOF and transitional metal based electrocatalysts.

5.4 Conclusions:

In summary, we have extended and generalized the unique concept of diffusion controlled hydrogel–organic interfacial reaction protocol for the morphology and structure tuned versatile MOF nanostructures hybridized with porous graphene framework. MD simulation study revealed that the control of monomer diffusion at the hydrogel–organic interface and within the hydrated pores of PG, in conjugation with the interaction effects of the graphene sheets of PG play major roles in controlling the morphology and crystal structures of the MOFs. The as developed rod–like $_{AOG}$TM–PG[R] hybrid demonstrated a remarkably high electrocatalytic activity and durability toward OER process, with a very low overpotential of 255 mV and a small Tafel slope of 44.3 mV dec^{-1}. We believe this work provides a novel direction for the synthesis of versatile MOF–PG hybrids and other functional nanohybrids with tunable structure in such a facile way.

Table 5.5. Comparison of electrocatalytic OER performances of existing MOF based and transition metal double hydroxide based water oxidation catalysts

Nature of catalyst	Catalyst	Mass loading (mg cm^{-2})	Electrolyte	Overpotential @10 mA cm^{-2} (mV)	Tafel slope (mV dec^{-1})	Ref
MOF based catalysts	$_{AOG}$TM–PG[R]	**0.64**	**1M KOH**	**255**	**44.3**	**This work**
	$Co_2(\mu–OH)_2(bbta)$ (MAFX27–OH)	1.13	1M KOH	292	88	[17]
	Co–ZIF–9	0.2	Potassium phosphate+KOH (pH= 13.4)	510 at 1 mA cm^{-2}	93	[47]
	CUMS–ZIF–67	0.1	0.5 M KBi (pH = 9.2)	410	185.1	[18]
	PANI–ZIF–67	0.6	1M KOH	330	37	[48]
	Ni–MOF@FeMOF	0.2	1M KOH	265	82	[41]
	$(Ni_2Co_1)_{0.925}Fe_{0.075}$–MOF	0.54	1M KOH	257	41.3	[16]
	$Ti_3C_2T_x$–CoBDC	0.21	0.1M KOH	410	48.2	[49]
	CoOx–ZIF	0.2	1M KOH	318	70.3	[50]
	3D Graphene/Ni–MOF	0.29	0.1M KOH	370	91	[51]
	2D CoZIF–9(III) sheets	0.21	1M KOH	380	55	[14]
	EG/Co(OH)2/ZIF–67		1M KOH	280	63	[52]
Other transition metal based electrocatalysts	NiV	0.143	1M KOH	300	50	[53]
	Ni–Co nanosheet	1	1M KOH	334	41	[54]
	Fe–Co LDH	0.21	1M KOH	323	85	[55]
	Ni–Fe LDH hollow nanoprisms	0.16	1M KOH	280	49.4	[56]
	MOF derived Co_3N@AN–C NCs	2.6	1M KOH	280	69.6	[57]
	$Ni_{0.7}Fe_{0.3}$ @$Ni_{0.7}Fe_{0.3}O$/NF	2	1M KOH	215	47.4	[58]

References:

1. K. Jayaramulu, F. Geyer, M. Petr, R. Zboril, D. Vollmer and R. A. Fischer, Shape Controlled Hierarchical Porous Hydrophobic/Oleophilic Metal-Organic Nanofibrous Gel Composites for Oil Adsorption, *Adv. Mater.*, 29 (2017), pp. 1605307.
2. L. Jiao, Y. Wang, H.-L. Jiang and Q. Xu, Metal–Organic Frameworks as Platforms for Catalytic Applications, *Adv. Mater.*, 30 (2018), pp. 1703663.
3. H. Li, K. Wang, Y. Sun, C. T. Lollar, J. Li and H.-C. Zhou, Recent advances in gas storage and separation using metal–organic frameworks, *Mater. Today*, 21 (2018), pp. 108-121.
4. A. Morozan and F. Jaouen, Metal organic frameworks for electrochemical applications, *Energy Environ. Sci.*, 5 (2012), pp. 9269-9290.
5. G. Xu, P. Nie, H. Dou, B. Ding, L. Li and X. Zhang, Exploring metal organic frameworks for energy storage in batteries and supercapacitors, *Mater. Today*, 20 (2017), pp. 191-209.
6. H. Yang, X.-W. He, F. Wang, Y. Kang and J. Zhang, Doping copper into ZIF-67 for enhancing gas uptake capacity and visible-light-driven photocatalytic degradation of organic dye, *J. Mater. Chem.*, 22 (2012), pp. 21849-21851.
7. M. H. Hassan, A. B. Soliman, W. A. Elmehelmey, A. A. Abugable, S. G. Karakalos, M. Elbahri, A. Hassanien and M. H. Alkordi, A Ni-loaded, metal–organic framework–graphene composite as a precursor for in situ electrochemical deposition of a highly active and durable water oxidation nanocatalyst, *Chem. Commun.*, 55 (2019), pp. 31-34.
8. M. Jahan, Z. Liu and K. P. Loh, A Graphene Oxide and Copper-Centered Metal Organic Framework Composite as a Tri-Functional Catalyst for HER, OER, and ORR, *Adv. Funct. Mater.*, 23 (2013), pp. 5363-5372.
9. X. Zheng, Y. Cao, D. Liu, M. Cai, J. Ding, X. Liu, J. Wang, W. Hu and C. Zhong, Bimetallic Metal–Organic-Framework/Reduced Graphene Oxide Composites as Bifunctional Electrocatalysts for Rechargeable Zn–Air Batteries, *ACS Appl. Mat. Interfaces*, 11 (2019), pp. 15662-15669.
10. J. Duan, S. Chen and C. Zhao, Ultrathin metal-organic framework array for efficient electrocatalytic water splitting, *Nat. commun.*, 8 (2017), pp. 15341.
11. J. Huang, Y. Li, R.-K. Huang, C.-T. He, L. Gong, Q. Hu, L. Wang, Y.-T. Xu, X.-Y. Tian, S.-Y. Liu, Z.-M. Ye, F. Wang, D.-D. Zhou, W.-X. Zhang and J.-P. Zhang, Electrochemical Exfoliation of Pillared-Layer Metal–Organic Framework to Boost the Oxygen Evolution Reaction, *Angew. Chem. Int. Ed.*, 57 (2018), pp. 4632-4636.
12. X. Zhang, J. Luo, K. Wan, D. Plessers, B. Sels, J. Song, L. Chen, T. Zhang, P. Tang, J. R. Morante, J. Arbiol and J. Fransaer, From rational design of a new bimetallic MOF family with tunable linkers to OER catalysts, *J. Mater. Chem. A*, 7 (2019), pp. 1616-1628.
13. S. Zhao, Y. Wang, J. Dong, C.-T. He, H. Yin, P. An, K. Zhao, X. Zhang, C. Gao, L. Zhang, J. Lv, J. Wang, J. Zhang, A. M. Khattak, N. A. Khan, Z. Wei, J. Zhang, S. Liu, H. Zhao and Z. Tang, Ultrathin metal–organic framework nanosheets for electrocatalytic oxygen evolution, *Nat. Energy.*, 1 (2016), pp. 16184.
14. K. Jayaramulu, J. Masa, D. M. Morales, O. Tomanec, V. Ranc, M. Petr, P. Wilde, Y.-T. Chen, R. Zboril, W. Schuhmann and R. A. Fischer, Ultrathin 2D Cobalt Zeolite-Imidazole Framework Nanosheets for Electrocatalytic Oxygen Evolution, *Advanced Science*, 5 (2018), pp. 1801029.

15. F.-L. Li, P. Wang, X. Huang, D. J. Young, H.-F. Wang, P. Braunstein and J.-P. Lang, Large-Scale, Bottom-Up Synthesis of Binary Metal–Organic Framework Nanosheets for Efficient Water Oxidation, *Angew. Chem. Int. Ed.*, 58 (2019), pp. 7051-7056.
16. Q. Qian, Y. Li, Y. Liu, L. Yu and G. Zhang, Ambient Fast Synthesis and Active Sites Deciphering of Hierarchical Foam-Like Trimetal–Organic Framework Nanostructures as a Platform for Highly Efficient Oxygen Evolution Electrocatalysis, *Adv. Mater.*, 31 (2019), pp. 1901139.
17. X.-F. Lu, P.-Q. Liao, J.-W. Wang, J.-X. Wu, X.-W. Chen, C.-T. He, J.-P. Zhang, G.-R. Li and X.-M. Chen, An Alkaline-Stable, Metal Hydroxide Mimicking Metal–Organic Framework for Efficient Electrocatalytic Oxygen Evolution, *J. Am. Chem. Soc.*, 138 (2016), pp. 8336-8339.
18. L. Tao, C.-Y. Lin, S. Dou, S. Feng, D. Chen, D. Liu, J. Huo, Z. Xia and S. Wang, Creating coordinatively unsaturated metal sites in metal-organic-frameworks as efficient electrocatalysts for the oxygen evolution reaction: Insights into the active centers, *Nano Energy*, 41 (2017), pp. 417-425.
19. M. Ding, J. Chen, M. Jiang, X. Zhang and G. Wang, Ultrathin trimetallic metal–organic framework nanosheets for highly efficient oxygen evolution reaction, *J. Mater. Chem. A*, 7 (2019), pp. 14163-14168.
20. D. Senthil Raja, X.-F. Chuah and S.-Y. Lu, In Situ Grown Bimetallic MOF-Based Composite as Highly Efficient Bifunctional Electrocatalyst for Overall Water Splitting with Ultrastability at High Current Densities, *Adv. Energy Mater.*, 8 (2018), pp. 1801065.
21. R. Ameloot, F. Vermoortele, W. Vanhove, M. B. J. Roeffaers, B. F. Sels and D. E. De Vos, Interfacial synthesis of hollow metal–organic framework capsules demonstrating selective permeability, *Nat. Chem.*, 3 (2011), pp. 382-387.
22. J. Huang and R. B. Kaner, A General Chemical Route to Polyaniline Nanofibers, *J. Am. Chem. Soc.*, 126 (2004), pp. 851-855.
23. Y. Shin, C. Lee, M.-S. Yang, S. Jeong, D. Kim and T. Kang, Two-dimensional Hyper-branched Gold Nanoparticles Synthesized on a Two-dimensional Oil/Water Interface, *Sci. Rep.*, 4 (2014), pp. 6119.
24. U. N. Maiti, J. Lim, K. E. Lee, W. J. Lee and S. O. Kim, Three-Dimensional Shape Engineered, Interfacial Gelation of Reduced Graphene Oxide for High Rate, Large Capacity Supercapacitors, *Adv. Mater.*, 26 (2014), pp. 615-619.
25. A. Sikdar, S. K. Deb, A. Gogoi, A. Majumdar, P. Dutta, K. A. Reddy and U. N. Maiti, Polyaniline–Graphene Hydrogel Hybrids via Diffusion Controlled Surface Polymerization for High Performance Supercapacitors, *ACS Applied Nano Materials*, 3 (2020), pp. 12278-12287.
26. M. D. Hanwell, D. E. Curtis, D. C. Lonie, T. Vandermeersch, E. Zurek and G. R. Hutchison, Avogadro: an advanced semantic chemical editor, visualization, and analysis platform, *J. Cheminformatics*, 4 (2012), pp. 17.
27. W. Humphrey, A. Dalke and K. Schulten, VMD: Visual molecular dynamics, *J. Mol. Graph.*, 14 (1996), pp. 33-38.
28. H. Tang, D. Liu, Y. Zhao, X. Yang, J. Lu and F. Cui, Molecular Dynamics Study of the Aggregation Process of Graphene Oxide in Water, *J. Phys. Chem. C*, 119 (2015), pp. 26712-26718.
29. X. Yang, L. Qiu, C. Cheng, Y. Wu, Z.-F. Ma and D. Li, Ordered Gelation of Chemically Converted Graphene for Next-Generation Electroconductive Hydrogel Films, *Angew. Chem. Int. Ed.*, 50 (2011), pp. 7325-7328.

30. H. Wang, J. T. Robinson, X. Li and H. Dai, Solvothermal Reduction of Chemically Exfoliated Graphene Sheets, *J. Am. Chem. Soc.*, 131 (2009), pp. 9910-9911.
31. C. V. McGuire and R. S. Forgan, The surface chemistry of metal–organic frameworks, *Chem. Commun.*, 51 (2015), pp. 5199-5217.
32. P. Pachfule, D. Shinde, M. Majumder and Q. Xu, Fabrication of carbon nanorods and graphene nanoribbons from a metal–organic framework, *Nat. Chem.*, 8 (2016), pp. 718.
33. G. Zheng, Z. Chen, K. Sentosun, I. Pérez-Juste, S. Bals, L. M. Liz-Marzán, I. Pastoriza-Santos, J. Pérez-Juste and M. Hong, Shape control in ZIF-8 nanocrystals and metal nanoparticles@ZIF-8 heterostructures, *Nanoscale*, 9 (2017), pp. 16645-16651.
34. A. Kojtari, P. J. Carroll and H.-F. Ji, Metal organic framework (MOF) micro/nanopillars, *CrystEngComm*, 16 (2014), pp. 2885-2888.
35. H. Wang, F. Yin, G. Li, B. Chen and Z. Wang, Preparation, characterization and bifunctional catalytic properties of MOF(Fe/Co) catalyst for oxygen reduction/evolution reactions in alkaline electrolyte, *Int. J. Hydrogen Energy*, 39 (2014), pp. 16179-16186.
36. D. Kim and A. Coskun, Graphene oxide-templated preferential growth of continuous MOF thin films, *CrystEngComm*, 18 (2016), pp. 4013-4017.
37. D. Kim, D. W. Kim, W. G. Hong and A. Coskun, Graphene/ZIF-8 composites with tunable hierarchical porosity and electrical conductivity, *J. Mater. Chem. A*, 4 (2016), pp. 7710-7717.
38. A. Schaate, P. Roy, A. Godt, J. Lippke, F. Waltz, M. Wiebcke and P. Behrens, Modulated Synthesis of Zr-Based Metal–Organic Frameworks: From Nano to Single Crystals, *Chem. Eur. J.*, 17 (2011), pp. 6643-6651.
39. R. Chen, J. Yao, Q. Gu, S. Smeets, C. Baerlocher, H. Gu, D. Zhu, W. Morris, O. M. Yaghi and H. Wang, A two-dimensional zeolitic imidazolate framework with a cushion-shaped cavity for CO2 adsorption, *Chem. Commun.*, 49 (2013), pp. 9500-9502.
40. J. Zhang, T. Zhang, D. Yu, K. Xiao and Y. Hong, Transition from ZIF-L-Co to ZIF-67: a new insight into the structural evolution of zeolitic imidazolate frameworks (ZIFs) in aqueous systems, *CrystEngComm*, 17 (2015), pp. 8212-8215.
41. K. Rui, G. Zhao, Y. Chen, Y. Lin, Q. Zhou, J. Chen, J. Zhu, W. Sun, W. Huang and S. X. Dou, Hybrid 2D Dual-Metal–Organic Frameworks for Enhanced Water Oxidation Catalysis, *Adv. Funct. Mater.*, 28 (2018), pp. 1801554.
42. X. Hu, H. Hu, C. Li, T. Li, X. Lou, Q. Chen and B. Hu, Cobalt-based metal organic framework with superior lithium anodic performance, *J. Solid State Chem.*, 242 (2016), pp. 71-76.
43. R. Wang, C. Xu and J.-M. Lee, High performance asymmetric supercapacitors: New NiOOH nanosheet/graphene hydrogels and pure graphene hydrogels, *Nano Energy*, 19 (2016), pp. 210-221.
44. J. Yang, H. Liu, W. N. Martens and R. L. Frost, Synthesis and Characterization of Cobalt Hydroxide, Cobalt Oxyhydroxide, and Cobalt Oxide Nanodiscs, *J. Phys. Chem. C*, 114 (2010), pp. 111-119.
45. S.-H. Ye, Z.-X. Shi, J.-X. Feng, Y.-X. Tong and G.-R. Li, Activating CoOOH Porous Nanosheet Arrays by Partial Iron Substitution for Efficient Oxygen Evolution Reaction, *Angew. Chem. Int. Ed.*, 57 (2018), pp. 2672-2676.
46. F.-L. Li, Q. Shao, X. Huang and J.-P. Lang, Nanoscale Trimetallic Metal–Organic Frameworks Enable Efficient Oxygen Evolution Electrocatalysis, *Angew. Chem. Int. Ed.*, 57 (2018), pp. 1888-1892.
47. S. Wang, Y. Hou, S. Lin and X. Wang, Water oxidation electrocatalysis by a zeolitic imidazolate framework, *Nanoscale*, 6 (2014), pp. 9930-9934.

48. M. Khalid, A. M. B. Honorato, H. Varela and L. Dai, Multifunctional electrocatalysts derived from conducting polymer and metal organic framework complexes, *Nano Energy*, 45 (2018), pp. 127-135.
49. L. Zhao, B. Dong, S. Li, L. Zhou, L. Lai, Z. Wang, S. Zhao, M. Han, K. Gao, M. Lu, X. Xie, B. Chen, Z. Liu, X. Wang, H. Zhang, H. Li, J. Liu, H. Zhang, X. Huang and W. Huang, Interdiffusion Reaction-Assisted Hybridization of Two-Dimensional Metal–Organic Frameworks and Ti3C2Tx Nanosheets for Electrocatalytic Oxygen Evolution, *ACS Nano*, 11 (2017), pp. 5800-5807.
50. S. Dou, C.-L. Dong, Z. Hu, Y.-C. Huang, J.-l. Chen, L. Tao, D. Yan, D. Chen, S. Shen, S. Chou and S. Wang, Atomic-Scale CoOx Species in Metal–Organic Frameworks for Oxygen Evolution Reaction, *Adv. Funct. Mater.*, 27 (2017), pp. 1702546.
51. A. Xie, J. Du, F. Tao, Y. Tao, Z. Xiong, S. Luo, X. Li and C. Yao, Three-dimensional graphene surface-mounted nickel-based metal organic framework for oxygen evolution reaction, *Electrochim. Acta*, 305 (2019), pp. 338-348.
52. J. Cao, C. Lei, J. Yang, X. Cheng, Z. Li, B. Yang, X. Zhang, L. Lei, Y. Hou and K. Ostrikov, An ultrathin cobalt-based zeolitic imidazolate framework nanosheet array with a strong synergistic effect towards the efficient oxygen evolution reaction, *J. Mater. Chem. A*, 6 (2018), pp. 18877-18883.
53. K. Fan, H. Chen, Y. Ji, H. Huang, P. M. Claesson, Q. Daniel, B. Philippe, H. Rensmo, F. Li, Y. Luo and L. Sun, Nickel–vanadium monolayer double hydroxide for efficient electrochemical water oxidation, *Nature Communications*, 7 (2016), pp. 11981.
54. F. Song and X. Hu, Exfoliation of layered double hydroxides for enhanced oxygen evolution catalysis, *Nature Communications*, 5 (2014), pp. 4477.
55. B. Zhang, X. Zheng, O. Voznyy, R. Comin, M. Bajdich, M. García-Melchor, L. Han, J. Xu, M. Liu, L. Zheng, F. P. García de Arquer, C. T. Dinh, F. Fan, M. Yuan, E. Yassitepe, N. Chen, T. Regier, P. Liu, Y. Li, P. De Luna, A. Janmohamed, H. L. Xin, H. Yang, A. Vojvodic and E. H. Sargent, Homogeneously dispersed multimetal oxygen-evolving catalysts, *Science*, 352 (2016), pp. 333.
56. L. Yu, J. F. Yang, B. Y. Guan, Y. Lu and X. W. Lou, Hierarchical Hollow Nanoprisms Based on Ultrathin Ni-Fe Layered Double Hydroxide Nanosheets with Enhanced Electrocatalytic Activity towards Oxygen Evolution, *Angewandte Chemie International Edition*, 57 (2018), pp. 172-176.
57. B. K. Kang, S. Y. Im, J. Lee, S. H. Kwag, S. B. Kwon, S. Tiruneh, M.-J. Kim, J. H. Kim, W. S. Yang, B. Lim and D. H. Yoon, In-situ formation of MOF derived mesoporous Co3N/amorphous N-doped carbon nanocubes as an efficient electrocatalytic oxygen evolution reaction, *Nano Res.*, 12 (2019), pp. 1605-1611.
58. Z. Yang and X. Liang, Self-magnetic-attracted NixFe(1−x)@NixFe(1−x)O nanoparticles on nickel foam as highly active and stable electrocatalysts towards alkaline oxygen evolution reaction, *Nano Res.*, 13 (2020), pp. 461-466.

Chapter 6

Summary and Outlook

Chapter 6

Summary and Outlook

6.1 Summary of the thesis:

This chapter highlights the brief summary and the key findings of this thesis work. This thesis implemented graphene hydrogel based approach to address some of the key challenges in the field of supercapacitive energy storage and water electrolysis. Besides addressing the requirement of high performance, the goal of this thesis was set to answer the questions regarding practical usability of the materials and techniques. Facile processing and ultimate scalability are the two practical criteria from the material development perspectives, whereas high mass and area specific performances are important considerations that have been taken care of in this thesis. In addition, a critical point for the entire work of the thesis is full ambient processing. Here, key findings of this thesis have been grouped into six points, namely i) Development of interfacial co–assembly strategy for functional hydrogel hybrid of graphene and polyaniline (PANI) nanowire; ii) development of new protocol for ultra–fast graphene hydrogel; iii) Scalable, casting based approach for the development of graphene–hydrogel and graphene–MXene hydrogel–hybrid, iv) Introducing the concept of biomimetic hydrogel–organic interfacial reaction for tunable hybridization with a molecular level of understanding; v) achievement for high areal, mass and volume specific energy storage metrics with high rate capability and vi) achievement of stable OER catalyst with low onset and Tafel slope from hydrogel derived MOF hybrids.

In points i)–iv), we shall discuss findings and importance of the developed materials and techniques, whereas the key outcome in terms of performance metrics of the functional hydrogel–hybrids will be discussed in point v) and vi).

i) Development of interfacial co–assembly strategy for functional hydrogel hybrid of graphene and polyaniline (PANI) nanowire:

In chapter 2, we have demonstrated a facile and scalable strategy for co–assembly of graphene and polyaniline nanowires over metallic zinc foil, resulting in graphene–PANI hydrogel hybrid at room temperature. When PANI nanowires were mixed with graphene oxide in aqueous dispersion, the nanowires got adsorbed and wrapped with GO due to $\pi - \pi$ interaction of aromatic rings of PANI and random graphitic domains of GO. On insertion of zinc plate within the GO–PANI mixed dispersion a spontaneous layer–by–layer co–assembly and reduction of

GO into reduced graphene oxide (graphene) occurred. This layer–by–layer co–assembly of graphene together with associated PANI, resulted in porous structure in which the water molecule associated with the residual functional groups of graphene helped to avoid complete face–to–face restacking. This spontaneous assembly and reduction was governed by the continuous electron transfer from zinc to GO due to the difference in reduction potential of GO and zinc plate. The facile processability of the technique was demonstrated by realizing a large size (~30 cm × 12 cm) freestanding hydrogel and directly integrating the hydrogel with carbon cloth during assembly process. Porosity of the hydrogel was tuned by mechanical compression without significant restacking of graphene sheets. As–developed hydrogel hybrid was used for supercapacitive energy storage performance with high performance metric. The importance of co–assembly induced gelation strategy is its ability to customize the size, composition and possibility to direct assembly over cloth substrate, and finally high energy storage performance.

ii) Development of new protocol for ultra–fast graphene hydrogel:

In chapter–2, we introduced co–assembly and graphene gelation strategy over zinc plate that took hours to obtain desired gel thickness. All the reported common strategies to prepare graphene based hydrogel also require hours of gelation. In an effort to make the gelation faster with easy tunability in thickness, a modified interfacial gelation technique was introduced in chapter 3. We found that by adding ammonia with GO, the assembly over immersed zinc plate took place at ultra–fast rate, and within 5 minutes a thick hydrogel was obtained. The thickness of the hydrogel was shown to be easily tuned by controlling the assembly time (starting from 1 minute). The ultrafast gelation resulted from the combined effect of forced assembly of negatively charged GO over zinc plate by in–situ generated positively charged zinc amino–complex, and reduction of assembled GO via electron transfer from zinc due to the difference in reduction potential. The ultrafast formation of porous graphene based hydrogel is expected to be suitable for commercial application.

iii) Scalable, casting based approach for the development of graphene–hydrogel and graphene–MXene hydrogel–hybrid:

Blade casting of molds is a very common and commercially used method for ultimately scalable films of polymer, polymer hybrids, graphene oxide, different composites, electrode materials and so on. All these methods relied on casting desired viscous material and then drying it to get the film. We inspected whether porous graphene hydrogel can also be developed by blade–casting method, if possible then the trivial processing can easily make entry into the

commercial techniques. It is to be noted that GO film can be made by casting, but that dried film will not preserve porous structure, or it will be of insulating nature only. To make a conducting, porous graphene hydrogel, we have successfully demonstrated a casting based approach in which GO mixed with zinc powered and could be cast into desired shape as discussed in chapter 4. The local reduction and assembly of GO around the mixed zinc particle gave rise to graphene based casted hydrogel. This process is versatile and can be used for hydrogel hybrid preparation by dispersing desired nanomaterials with GO. We choose to prepare graphene–MXene hybrid hydrogel, considering the high importance of newly discovered MXene, the nanosheets of transition metal carbides, and hydrogel structure in energy storage. We developed a graphene–MXene hybrid 3D hydrogel by casting a mixture of GO, MXene and zinc particles. High scalability, straightforward casting based approach, and easy processing of hybrids with MXene are the key importance of this hybrid which was also shown to display high performance energy storage.

iv) Introducing the concept of biomimetic hydrogel–organic interfacial reaction for tunable hybridization with molecular level of understanding:

The development of nanomaterials via biomimetic process is an important scientific field on behalf of its key ability to precisely control the morphology and the size of nanomaterials, but understanding this process is challenging due to the lack of knowledge on associated molecular diffusion and interactions. In chapter–4, we employed 'graphene hydrogel–organic media' biphasic system as a biomimetic platform for controlled interfacial molecular (aniline) diffusion and its subsequent polymerization into ultrathin polyaniline nanostructures over 3D hydrogel framework. In chapter 5, we have employed this concept for controlling the morphology of metal organic framework (MOFs) hybridized with porous graphene hydrogel. In this process, the hydrated pores of the hydrogel offered cell like environment, whereas pore walls made of graphene served as membrane to control the diffusion. Ultrafine PANI nanostructures, and diverse MOFs (Cu(BTC), ZIF67, ZIF8, tri–metallic (Ni, Co, Fe) MOF) were directly hybridized with graphene hydrogel with precise control over shape, size and morphology, which were hard to implement with other techniques. The molecular (aniline/organic ligand) diffusion processes across the hydrogel–organic media interface and within hydrogel were studied with molecular dynamics simulation (MD). MD simulation study revealed that hydrogel slowed down the diffusion process from outer organic phase into the porous hydrogel matrix. As slow and continuous release of precursor is known to be the key to develop size controlled nanomaterials, this slow and continuous phase transfer of aniline/2–

methyl imidazole from organic to hydrogel aqueous phase resulted in control growth of nanomaterials directly over GH. MD simulation results also revealed the existence of strong van der Waals and electrostatic interactions offered by the graphene sheets, which was the key for uniform nano–hybridization.

v) Achievement for high areal, mass and volume specific energy storage metrics with high rate capability:

Graphene–PANI, Graphene–MXene hybrid hydrogels, developed via co–assembly (chapter 2), interfacial diffusion (chapter 3) and co–casting (chapter 4), have been used to address some of the key challenges in the field of supercapacitive energy storage.

In chapter 2, the co–assembly strategy was proposed to address the customized need of supercapacitors having high areal or volumetric energy and power densities without sacrificing good rate capability. The PGH exhibited a high areal capacitance of 853 mF cm^{-2}, which was increased up to 2.2 F cm^{-2} via systematically increasing electrode mass loading (15.3 mg cm^{-2}). Further, a compressed gel hybrid was obtained by controlling the hydration level of the hybrid hydrogel (< 35 wt%) via electrolyte protected mechanical compression, which resulted in an excellent volumetric capacitance of 560 F cm^{-3}, while retaining high rate performances (81.3% at 20 mA cm^{-2}). Moreover, PGH was directly developed over a carbon cloth to fabricate a wearable device which exhibited excellent performance metrics and potential wearability. We reported this work in Electrochim Acta, 2020, 332, 135492. Continuous ion channels even in thick/compressed electrode ensured surface accessibility of PANI and graphene, thus effective contribution of pseudocapacitive and electrical double layer (EDLC) type charge storage respectively can be assessed from them, which gives high rate performance. The importance of this process lies in the scalability, and universality to use in high areal, volumetric energy density supercapacitors or wearable supercapacitors as per customize need.

In chapter 3, instead of co–assembly, uniform PANI nanostructures were directly grown over GH framework by diffusion limited process. By controlling the morphology of the PANI nanostructure in graphene hydrogel (PANI–GH), a high mass loading of 8.8 mg cm^{-2} was achieved. The as obtained PANI–GH demonstrated an excellent specific capacitance of 503 F g^{-1} at a high current density of 5 A g^{-1} with superb rate performance (retaining 88.6% at a current density of 30 A g^{-1}) and long term stability (95.8% retention after 3000 charge–discharge cycles). This work has been published in ACS Appl. Nano Mater. 2020, 3, 12, 12278. Together with the intrinsic structural advantage of hydrogel, direct connection of PANI

nanostructures over graphene provided a robust electronic interface for rapid charge transport. Besides, ultrafine nature of PANI with non–aggregated vertical orientation ensured significant utilization of its redox active surface resulting in high and stable performance. The importance of the work lies in the highly controlled polymer hybridization protocol utilizing hydrogel as confined reactor and resultant high energy storage performance.

In chapter–4, we developed graphene–MXene hybrid hydrogel via simple casting based approach and utilized it as negative electrode of an asymmetric supercapacitor. Graphene hydrogel produced via same casting approach was hybridized with PANI and this hybrid was used as positive electrode to complete the asymmetric supercapacitor device. The motivation behind the hybridization with MXene ($Ti_3C_2T_x$) was to restrict the restacking of MXene by locking them in the graphene hydrogel porous framework, thereby accessing predicted high pseudocapacitive metric of MXene. Further, asymmetric configuration of supercapacitor was utilized to increase the operation potential window up to 1.4 V, which exhibited improved energy density. As–developed Graphene–MXene/Graphene–PANI hydrogel asymmetric system displayed an ultra–high energy density of 30.3 Wh kg^{-1} at a high power density of 1.13 kW kg^{-1}. Most importantly, the exceptional capacity retention of MXene hybrids was demonstrated even at a high scan rate of 1V. These capacitor matrices are higher than most of the reports and particularly the retention at 1V beat most of the results.

vi) Achievement of stable OER catalyst with low onset and Tafel slope from hydrogel derived MOF hybrids:

In chapter 5, we developed a universal diffusion limited hybridization strategy for MOF and graphene hydrogel, and oxygen evolution performance (OER) was investigated for rod–like nickel–cobalt–iron tri–metallic MOF–porous graphene hybrid ($_{AOG}$TM–PG[R]) in alkaline medium. The porous aerogel derived from $_{AOG}$TM–PG[R] exhibited a remarkably low overpotential of 255 mV to achieve a current density of 10 mA cm^{-2} and a small Tafel slope of 44.3 mV dec^{-1} surpassing the performance of bulk MOF (without PG) $_{AO}$TM[R] (266 mV) and commercial RuO_2 catalyst (402 mV). Moreover, the activity of $_{AOG}$TM–PG[R] was found to vary significantly with the morphology of the MOFs. It was seen that the uniform rod like MOF in $_{AOG}$TM–PG[R] possessed a better performance than the agglomerated MOFs in $_{AOG}$TM–PG[R]$_{High}$ (271 mV) and very low density of MOFs in $_{AOG}$TM–PG[R]$_{Low}$ (276 mV). This work has been published in J. Mater. Chem. A, 2021 (DOI: 10.1039/D0TA09077H).

For MOF–graphene hybrid $_{AOG}$TM–PG[R], the excellent OER activity was ascribed to the synergistic effect of the (i) the rod–like structure of the MOF possessing numerous catalytically exposed metal sites; (ii) electrochemically formed Ni/Co/Fe hydroxide/oxyhydroxide during the in–situ phase transformation of the MOF, which served as the active species for OER process; (iii) the high conductivity of PG framework and its direct connection with MOFs, which promoted rapid electronic transportation the OER process and iv) open porous structure of the hybrid framework, that facilitated fast electrolyte ion diffusion kinetics which minimized ion diffusion resistance, and also helped to release the generated gases during water splitting process.

6.2 Future scope:

The focus of this thesis is to develop graphene–hydrogel based hybrids for supercapacitive energy storage and water electrolysis. Nanomaterials, like polyaniline (PANI), MXene, possessing Faradic activity, were primarily hybridized for electrochemical energy storage, whereas MOFs were linked with hydrogel for OER applications. However, these materials can immediately find widespread applications in diverse areas, namely gas storage, oil adsorption, or adsorption of contaminations from water. In particular, Cu(BTC) is known as one of the best material for CO_2 storage, thus Cu(BTC)–graphene aerogel which has been developed here is expected to show excellent storage capacity due to the high aspect ratio nanowire like structure of Cu(BTC) and porous framework of graphene aerogel. As–developed MOF based hybrids can also be used for diverse catalytic application such as oxygen reduction reaction, nitrogen reduction reaction and hydrogen evolution reaction, after carbonizing MOF at high temperature, in which the fine structure of MOF and porous framework of aerogel are expected to play key role in ensuring electronic and mass transport efficiencies.

The method of diffusion limited hybridization using hydrogel as confined reactor is a generic process, and can straightforwardly be extended to generate different functional hybrids beyond PANI and MOFs. For such generalization, one can revisit any reported bulk organic–aqueous interfacial reaction system, and replace the free aqueous phase with hydrogel, the hydrogel can act as additional diffusion controller for tunable nanohybridization. We have already shown the extendibility of this technique with platinum metal nanoparticles, and it is immediately extendable to other catalytic metal nanoparticle like gold, silver and alloys. Similarly, manganese oxide; which has already been synthesized via bulk organic–aqueous phase reaction, is expected to be easily linked with tunable size to graphene hydrogel.

The casting based approach for graphene–MXene hydrogel is another generic process, thus can be realized with other nanomaterials of interest. In particular, range of 2D materials of molybdenum sulfide, tungsten sulfide, boron nitride, etc. can be hybridized via same technique which can find applications in hydrogen evolution reaction, EMI shielding, thermal interface materials and so on. Furthermore, graphene–MXene hydrogel which has been presented in this thesis can also be applied for urea adsorption, and capacitive deionization.

Permissions and Attributions

- The content of the chapter 2 is based on the following published work:

Electrochim Acta, 332 (2020), pp. 135492, in collaboration with Abhisek Majumdar, Pronoy Dutta, Munu Borah, Sang Ouk Kim and Uday Narayan Maiti.

- The content of the chapter 3 is based on the following published work:

ACS Appl. Nano Mater. 3 (2020), pp. 12278, in collaboration with Sujit Kumar Deb, Abhijit Gogoi, Abhisek Majumdar, Pronoy Dutta, K. Anki Reddy and Uday Narayan Maiti.

- The content of the chapter 4 is based on an unpublished work in collaboration with Sujit Kumar Deb, Abhisek Majumdar, Pronoy Dutta and Uday Narayan Maiti

- The content of the chapter 5 is based on the following published work:

J. Mater. Chem A, 2021, DOI: 10.1039/D0TA09077H, in collaboration with Abhisek Majumdar, Abhijit Gogoi, Pronoy Dutta, Munu Borah, Soumen Maiti, Chiranjib Gogoi, K. Anki Reddy, Youngtak Oh and Uday Narayan Maiti.